1

ORNL-4350
UC-25 – Metals, Ceramics, and Materials

FUELS AND MATERIALS DEVELOPMENT PROGRAM

QUARTERLY PROGRESS REPORT

FOR PERIOD ENDING SEPTEMBER 30, 1968

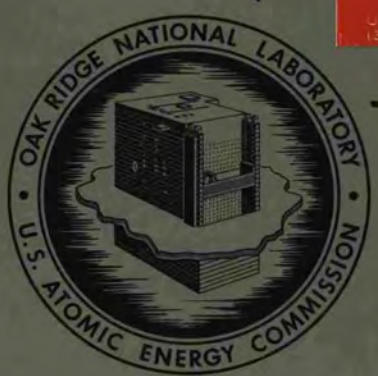

OAK RIDGE NATIONAL LABORATORY
operated by
UNION CARBIDE CORPORATION
for the
U.S. ATOMIC ENERGY COMMISSION

Printed in the United States of America. Available from Clearinghouse for Federal
Scientific and Technical Information, National Bureau of Standards,
U.S. Department of Commerce, Springfield, Virginia 22151
Price: Printed Copy $3.00; Microfiche $0.65

ORNL-4350

Contract No. W-7405-eng-26

METALS AND CERAMICS DIVISION

FUELS AND MATERIALS DEVELOPMENT PROGRAM QUARTERLY PROGRESS REPORT FOR PERIOD ENDING SEPTEMBER 30, 1968

Compiled by

P. Patriarca W. O. Harms

Edited by

D. J. Rucker

FEBRUARY 1969

OAK RIDGE NATIONAL LABORATORY
Oak Ridge, Tennessee
operated by
UNION CARBIDE CORPORATION
for the
U.S. ATOMIC ENERGY COMMISSION

FOREWORD

This quarterly progress report describes research and development on nuclear fuels and materials performed at the Oak Ridge National Laboratory for the U.S. Atomic Energy Commission. With several exceptions, as noted below in the listing of specific programs, the work is sponsored by the Fuels and Materials Branch of the Division of Reactor Development and Technology. Classified aspects of the Nitride Fuels Development activity and work on fuels and materials for isotope heat sources are covered in separate ORNL progress reports.

The report is presented in five parts according to AEC Activity titles provided by the Fuels and Materials Branch, RDT.

Program Title	ORNL Division(s)	Person in Charge	Principal Investigator(s)
	I. Fuels and Claddings		
Sol-Gel Fast Reactor Fuels	Metals and Ceramics Chemical Technology Reactor	P. Patriarca	A. L. Lotts J. L. Scott R. E. Brooksbank
Nitride Fuels Development	Metals and Ceramics Reactor	W. O. Harms	J. L. Scott H. C. McCurdy
Fission-Gas Release and Physical Properties of Fuel Materials During Irradiation	Reactor Chemistry	O. Sisman	R. M. Carroll J. G. Morgan
Zirconium Metallurgy	Metals and Ceramics	C. J. McHargue	P. L. Rittenhouse
	II. Coolants		
Alkali-Metal Corrosion Studies	Metals and Ceramics Reactor	W. O. Harms	J. H. DeVan A. P. Litman R. E. MacPherson

Program Title	ORNL Division(s)	Person in Charge	Principal Investigator(s)
III. Radiation Damage to Structural Materials			
Behavior of Refractory Materials Under Irradiation	Reactor Chemistry	G. M. Watson	G. W. Keilholtz
Fast-Neutron Irradiation Effects on Electrical Insulators*	Reactor Chemistry	G. M. Watson	G. W. Keilholtz
Mechanical Properties Research and LMFBR Cladding and Structural Materials Development**	Metals and Ceramics	C. J. McHargue	J. R. Weir
Radiation Effects in Alloys and Structural Materials	Solid State	D. S. Billington	M. S. Wechsler
IV. Techniques of Fabrication and Testing			
Tungsten Metallurgy	Metals and Ceramics	W. O. Harms	H. Inouye W. R. Martin G. M. Slaughter J. O. Stiegler J. R. Weir
Nondestructive Test Development	Metals and Ceramics	W. O. Harms	R. W. McClung
Joining Research on Nuclear Materials	Metals and Ceramics	G. M. Adamson	G. M. Slaughter
Fuel Element Fabrication Development	Metals and Ceramics	G. M. Adamson	J. V. Cathcart W. R. Martin R. W. McClung

*Sponsored by Reactor Power Systems Branch, Division of Space Nuclear Systems.

**Partially sponsored by Liquid Metals Branch, Division of Reactor Development and Technology.

Program Title	ORNL Division(s)	Person in Charge	Principal Investigator(s)
V. Engineering Properties of Reactor Materials			
Physical and Mechanical Metallurgy of Refractory Alloys	Metals and Ceramics	W. O. Harms	H. Inouye R. W. McClung D. L. McElroy G. M. Slaughter J. R. Weir

CONTENTS

Part II. Coolants

Part III. Radiation Damage to Structural Materials

SUMMARY

PART I. FUELS AND CLADDINGS

1. Sol-Gel Fast Reactor Fuels

We are assessing the potential of sol-gel-derived $(U,Pu)O_2$ fuel for use in the Fast Flux Test Facility. Emphasis this quarter has been on preparing materials and capsules for irradiation testing in the EBR-II.

Five Sphere-Pac-loaded EBR-II capsules are being fabricated and are scheduled to be completed by the first of November. After difficulties in preparing crack-free microspheres for the EBR-II capsules, we produced a sufficient quantity of spherical material with acceptable packing characteristics. Equipment for loading the EBR-II capsules by the Sphere-Pac process was installed and checked. Other equipment and procedures for preparing the EBR-II capsules were developed and checked and are being used in fabricating these capsules. We have continued to investigate methods of pressing and sintering pellets with controlled densities ranging from 80 to 95% of theoretical density.

A series of analyses is now available for characterizing finished fuel. We have developed a method for preparing stoichiometric UO_2 that is also applicable to the mixed oxides and will be used for preparing analytical standards. Construction is continuing on the new radial heat flow apparatus. Studies are under way to determine the thermal conductivity of LiF to its melting point. The thermal conductivity of LiF has been successfully calculated at room temperature in terms of phonon mean free path, but an expression for conductivity that is applicable at high temperatures is needed to compare conductivity values over the whole range of temperatures investigated. Isostatically pressed and die pressed UO_2 powders were found to have similar stress-strain curves at 1425°C. The stress leveled out at about 15,500 psi until the deformation exceeded 10%. We found the activation energy for creep in UO_2 to be 142 kcal/mole between about 2 and 6% deformation.

We began examining the fourth uninstrumented capsule in the ETR series. Burnup analysis of the fuel indicates the linear heat rating on these

four rods — three of Sphere-Pac UO_2 and one of pelletized UO_2 — was in excess of 20 kw/ft. This heat rating, which was higher than we anticipated, was probably caused by the flux in the irradiation position of this capsule being higher than advertised. There was no evidence of cladding strain in these rods, which achieved a burnup level of about 5% FIMA. Metallographic examinations have not yet been made. We have started developing a mathematical model to describe fuel densification by the evaporization-condensation mechanism.

Metallographic examination of the fuel from the first instrumented test of mixed-oxide Sphere-Pac fuel revealed attack of the central molybdenum thermocouple well. The fuel body contains a significant amount of a white deposit, probably Mo transported as the MoO_3 vapor and subsequently reduced.

We continued our evaluation of thermal neutron filters and of the heat-transfer medium for use in the transient test program. We will not use neutron filters on the first tests. Because of its significant effect on cladding temperatures, Na will be used in preference to NaK. The design for the five Series I EBR-II encapsulated test rods was completed, and the hardware has been procured. The required analysis of hazards for these rods is well under way.

2. Nitride Fuels Development

Characterization studies on UN powders produced by the traditional ORNL process have shown the powders to be acicular and smaller than 1 μ in diameter. X-ray analysis showed them to contain 20 to 30% higher nitrides.

An extensive effort to control gaseous impurity levels in our plutonium glove boxes has led to operating levels of less than 10 ppm O and 20 ppm water vapor at argon flow rates that change the atmosphere in the box five times per hour.

Kinetics studies on the reaction between UC_2 and N to form UCN showed that the process is controlled by the interface between UC_2 and UCN. The constant for the reaction rate, k_I, fits an Arrhenius relationship:

$$k_I = 85.9 \exp(-77{,}700/RT) \text{ cm/sec} .$$

Both single-phase UN with 400 ppm O and UN containing second-phase UO_2 (5000 ppm O) were found to have reacted with V–15% Cr–5% Ti after 100 hr at 1000°C. The reaction is thought to have been caused by the Ti in the alloy.

3. Fission-Gas Release and Physical Properties of Fuel Materials During Irradiation

We need to know the nonfission (NF) heating for calculating thermal diffusivity of fuel specimens during irradiation.

We have found that the NF heating of Cu in the C-1 position of the ORR can be represented by a linear function of the thermal neutron flux, ϕ:

$$\text{NF heating (w/g)} = (8.73 \times 10^{-14})\ \phi + 0.09 .$$

UN specimens developed many fine cracks during irradiation. The gas-release measurements reflected the physical condition of the specimen.

Specimens of $(U_{0.75}\ Pu_{0.25})O_2$ are being irradiated. We developed a method for handling $(U,Pu)O_2$ specimens on the bench. The specimen was coated with a protective layer of naphthalene to prevent the spread of plutonium contamination. After the specimen was encapsulated, the coating was evaporated by heat and vacuum.

4. Zirconium Metallurgy

Seven of the twelve schedules for the manufacture of Zircaloy tubing have been completed. These tubes have been reduced to final size by tube reduction, swaging, planetary swaging, and cold drawing. Grain size in the finished tubing depended only upon the degree of cold work in the final reduction.

Circumferential variation in texture intensity of up to 400% has been observed in tubing produced by experimental tube reduction. This variation is directly attributable to improper die shape, to the ratio of tube feed to rotation, and to the ratio of wall reduction to diameter reduction.

Texture gradients and texture developments have been examined in tubing fabricated by different techniques to identical dimensions from identical starting materials and starting dimensions. Heavy reductions in wall thickness promote texture gradients through the wall of the tubing and align basal poles parallel to the radial direction, whereas large reductions in diameter align basal poles at about ±60 deg from the radial toward the tangential direction with no texture gradient through the wall of the tubing.

PART II. COOLANTS

5. Alkali-Metal Corrosion Studies

The partitioning of O between V and Na was investigated in static capsules tested at 600 and 800°C for 500 hr. We found that V containing about 2000 ppm O has a much higher affinity for O in Na than do Nb and Ta containing ≤ 100 ppm O. Vanadium containing 2000 ppm O was not attacked by Na, in contrast to similarly doped Nb or Ta. Several thermal convection loop assemblies were fabricated to investigate the partitioning of C and N between V and 300 series stainless steels. The loops incorporate vanadium hot leg assemblies joined to stainless steel with dissimilar metal braze joints.

We began a two-year effort to guide the selection of containment piping and thermal insulation for LMFBR systems. This task includes a comprehensive study of the literature and tests of the compatibility of selected stainless steels and thermal insulation in air and inert gas, with and without the presence of Na. Our experimental program incorporates an investigation of the causes and cures of catastrophic oxidation, effects of small and large sodium leaks, and early leak detection.

We have completed our examination of two W–26% Re refluxing capsules that were operated 3000 hr with boiling K at 1200°C. One of the capsules showed no evidence of corrosion, but the other showed a tungsten deposit in the condenser and subsurface attack in the boiler. The latter capsule was fabricated from arc-cast material and had a higher as-received oxygen concentration than the unattacked capsule produced by a powder metallurgy process. A mechanism was presented to relate the corrosion observed to the higher initial oxygen content of the W–26% Re alloy. We also

completed our examination of a TZM natural-circulation loop that operated with boiling K for 4400 hr at a 1200°C boiler-condenser temperature. The loop showed no evidence of attack and only minor weight gains in the subcooler region.

A D-43 alloy loop with D-43 alloy test section (FCL-8) which operated with boiling K for 10,000 hr was removed from the vacuum chamber and sectioned for metallurgical examination. Detailed information is presented on liquid-metal removal, metal cleanup, and visual examination of boiler and condenser legs. No dimensional changes and no evidence of mass transfer have been found in examinations to date on the loop piping or specimens.

The role of O in the corrosion of Ta by K was evaluated at 800 and 1000°C. Tantalum specimens with pretest concentrations of 650 ppm O or higher were penetrated by K at 800°C. The same occurred for specimens with $\geq$ 1000 ppm O at 1000°C. The conditions for penetration are comparable in many respects to those for the penetration of contaminated Ta in Li. Oxygen contamination in the K did not lead to penetration but increased the apparent solubility of Ta in Na. Preliminary studies of the Nb-O-Na system show effects quite similar to the Ta-O-K system.

An analysis of the partitioning of O in the Zr-Na and Zr-K systems was carried out in conjunction with the use of the zirconium-gettering technique (GVF) for measuring the oxygen level of these alkali metal systems. We found the partitioning coefficient, (i.e., $\frac{\text{atom fraction of O in Zr}}{\text{atom fraction of O in K or Na}}$) at 815°C, to be greater than 10^3 for both systems. This means that, under our experimental conditions, the O picked up by our zirconium getter tab gives a direct measure of the O initially present in our alkali metal sample.

Examination of a T-111 loop that circulated Li for 3000 hr at 1350°C has revealed preferential transport of Hf from hot to cold regions. Chemical analysis of insert specimens, which initially contained 2.5% Hf, showed the hafnium surface concentration to be 1.4% at the hottest loop position compared with 58% at the coldest point.

Work continued on the T-111 alloy test-bed loop (FCLLL-1) for studying new refractory alloys, especially tungsten alloys, at temperatures to

1540°C in 20 fps liquid Li. All T-111 alloy assemblies have been fabricated, all welds have been vacuum annealed, and all control specimens with their furnace enclosures have been completed.

PART III. RADIATION DAMAGE TO STRUCTURAL MATERIALS

6. Behavior of Refractory Materials Under Irradiation

In-reactor thermal annealing reduced gross damage to explosion-pressed carbides of refractory metals (Ti, Zr, Ta, Nb, W) irradiated at 1000 to 1100°C as compared to damage at 300 to 700°C. Volume expansion was also reduced at 1000 to 1100°C except for the case of explosion-pressed WC, which expanded slightly more at high temperature. The data are generally consistent with results for hot-pressed and slip-cast carbides.

Cylindrical specimens of the nitrides of Zr, Ti, Ta, and Nb were irradiated at 1000 to 1100°C to fast-neutron fluences ranging from 0.4 to 2.3×10^{21} neutron/cm^2 (> 1 Mev). Gross damage to ZrN was much less at this temperature than at 150°C, whereas that to NbN was much greater than at 150°C. The nitrides expanded significantly less at 1000 to 1100°C than at 150°C. The expansion was decidedly greater in the axial direction than in the radial direction. We suggest that He from the (n,α) reaction diffused in such a way as to produce preferential axial expansion because the radial direction was constrained by the specimen containers.

7. Fast-Neutron Irradiation Effects on Electrical Insulators

A short-term and a long-term assembly containing three commercial Al_2O_3 products for evaluation for thermionic use, have been undergoing irradiation in the ETR at 600, 800, and 1100°C. The irradiation of the short-term assembly is now complete after fast-neutron doses between about 0.3 and 1.8×10^{21} neutrons/cm^2 (> 1 Mev). An assembly containing metal-clad Al_2O_3 units prepared at other installations was fabricated and inserted into the ETR for planned fluences ranging from 0.4 to 2×10^{21} neutrons/cm^2.

8. Mechanical Properties Research and LMFBR Cladding and Structural Materials Development

Results of postirradiation tests on standard and titanium-modified type 316 stainless steel continue to show that important thermally induced changes in the properties are occurring from 550 to 750°C. For the standard type 316 stainless steel, we observe that the reduction in tensile elongation is larger for the low-carbon alloy than for the high-carbon alloy. We observe an increased postirradiation creep rate due mainly to thermal aging and a reduced ductility due to neutron damage.

As the titanium content in 50-lb melts of type 316 stainless steel is increased, the postirradiation ductility exhibits a maximum in the range of 0.1 to 0.5% Ti in both high- and low-carbon compositions. Upon aging near 650°C, the ductility of the titanium-bearing alloys increases with time.

We are continuing to investigate the effects of tubing fabrication variables on the properties of the titanium-modified type 304 stainless steel and have successfully processed tubing from both the high- and low-carbon heats. The effects of processing variables on the tubing yield and its mechanical properties are now being studied.

Further work on the influence of titanium concentration on the postirradiation ductility of Incoloy 800 shows that the optimum titanium concentration occurs at 0.1% Ti in both high- and low-carbon melts. We find that the creep strength parameters are strongly influenced by the grain size and the composition, with the larger grain size and higher alloy content favoring higher strength.

The modifications to the composition of Hastelloy N that we are investigating have been found to introduce aging effects not found in the standard composition. It appears that at temperatures above about 700°C the microstructure formed with time has a deleterious effect on the properties that may be associated with compositional changes other than the titanium addition.

9. Radiation Effects in Alloys and Structural Materials

Several new techniques have now been employed in our study of the radiation hardening and embrittlement of reactor pressure-vessel steels. The impact machines in the laboratory and hot cell have been fitted with strain gages whose calibrated output registers the load applied to the sample during impact. The total energy to fracture determined from the strain-gage output agrees with that indicated on the scale of the impact machine. The general yield load, the maximum load, and the fracture load were evaluated as a function of test temperature for unirradiated A 212-B and A 533-B steel and for A 533-B steel irradiated at three temperatures. The temperature at which the general yield load curve intersects the maximum or fracture load curve appears to correlate well with the ductile-to-brittle transition temperature (DBTT) determined on a zero-fracture-energy criterion.

Unirradiated and irradiated steels have been observed by optical and electron microscopy including electron fractography by replication of the fracture surfaces. No major difference in appearance of the unirradiated and irradiated material has been detected. Thin foils of unirradiated and irradiated steel specimens were examined by transmission electron microscopy; the irradiated foils showed no evidence of defect clusters produced by radiation, although the exposure was sufficient to cause significant hardening and embrittlement.

In conjunction with the Heavy Section Steel Technology Program, we conducted impact and tensile tests on irradiated specimens from HSST plate 01, a 12-in.-thick plate of A 533-B steel. In comparison with other steels of the same general type, this steel displayed an intermediate degree of radiation-embrittlement sensitivity. We also performed impact and tensile tests on unirradiated specimens of several orientations taken from several depths in HSST plate 02. Specimens from the surface of the plate exhibited the lowest DBTT, and specimens of longitudinal orientation showed the greatest ductile fracture energy.

Three aspects of radiation hardening in Fe are described: temperature dependence, fluence dependence, and the effect of interstitial solutes. After a low-fluence irradiation (1×10^{16} neutrons/cm^2), the yield stress of vacuum-melted Fe is increased about the same amount

at all test temperatures; but after a higher-fluence irradiation (3×10^{19} neutrons/cm^2), the yield stress increase is larger at lower test temperatures. When the radiation hardening of several irons was analyzed on the basis of a square-root dependence on the fluence, the rate of hardening was found to decrease with increasing exposure. The amount of hardening was greater in samples with higher carbon concentrations. The effect of nitrogen content was studied in samples containing less than 1 and about 20 ppm N by weight irradiated below −50°C, where N is immobile. Upon postirradiation annealing to 250°C, the rate of radiation-anneal hardening was about the same for the Fe and Fe-20N materials. However, the magnitudes of the increase in flow stress and the drop in yield upon strain aging decreased sharply for Fe-20N annealed at 100°C, indicating that N is removed from solid solution by becoming trapped at defects produced by radiation.

Finally, measurements of resistivity and internal friction have been made on irradiated V. The results are similar to those for irradiated Nb in indicating that interstitial impurities (O and N) migrate to traps produced by radiation and are thus effectively removed from solid solution.

PART IV. TECHNIQUES OF FABRICATION AND TESTING

10. Tungsten Metallurgy

Four tungsten duplex extrusion billets have been fabricated to study the effect of prior work and extrusion preheat temperature on the microstructure of extruded billets. Installation of the high-capacity 450,000-lb Aetna-Standard tube reducer is near completion.

In our studies of chemical vapor deposition, modification of the substrate geometry has enabled us to produce two $3\frac{1}{4} \times 14$-in. sheets of the nominal W—5% Re alloy for mechanical property evaluation. The rhenium content was 3.8 to 4.1%, and the thickness was 0.033 to 0.041 in. over the central 10 in. of the deposit. Attempts to deposit V from VF_5, VCl_4, and VCl_3 have been unsuccessful up to 950°C because of the formation of stable intermediate phases. An induction-heated

deposition apparatus is being fabricated to enable deposition at higher temperatures.

The rate of recrystallization of wrought CVD tungsten is logarithmic, and recrystallization is 80% complete after 800 hr at 1800°C if the material is not annealed at high temperature before rolling. Grain growth at 1800°C is inhibited by small gas bubbles in fluoride CVD tungsten (deposited from WF_6) containing 7 ppm F but is not inhibited by the same fluorine content in material deposited from WCl_x.

11. Nondestructive Test Development

We are developing new techniques and equipment for the nondestructive testing of materials and components. The major emphasis has been on eddy-current, ultrasonic, penetrating radiation, and holographic methods.

In our analytical work on electromagnetic phenomena, we have continued to use closed-form solutions to integral equations applicable to a variety of eddy-current tests. This work has included determining induced voltage in a through-transmission test and producing graphical data relating sensitivity to defects to their relative position of the defects within a specimen. Probe coils were designed and built for drift-free operation at temperatures up to 175°C.

The mirror schlieren system has been tested and shown to have improved sensitivity and resolution over the previous lens system. The frequency-analysis system is being used both to analyze spatial characteristics in ultrasonic pulses from transducers as a function of frequency and to evaluate the effects of testing variables on the frequency spectrum of the pulse.

12. Joining Research on Nuclear Materials

Studies concerning the effect of minor quantities of selected elements on the susceptibility of Inconel 600 to hot cracking have been conducted under subcontract at Rensselaer Polytechnic Institute. They employed a newly developed weldability test, the TIGAMAJIG, to investigate the effects of S, P, Mn, Si, Ti, and Al. A full factorial experiment was conducted. They found that S and P both were detrimental.

The deleterious effect of S was minimized with either Mn and Si; when both were present, however, they were not as effective as was either one alone. The propensity toward hot cracking was reduced when Ti and Al were added. They attributed this result to the excellent deoxidizing capabilities of these elements.

An investigation of the effect of ferrite content and distribution on the mechanical properties of stainless steel welds has been initiated. A variety of ferrite contents will be achieved through variations in the chemical composition of the filler metals. Both the quantity and distribution will be studied as functions of welding parameters.

We have begun our joining efforts in support of the fabrication of the FFTF vessel. This is a thick-walled ($1\frac{1}{2}$ to 3 in.) vessel that may be fabricated by any one of a number of welding processes. Little is known regarding the mechanical properties of austenitic weld metal, particularly in the creep range, above 480°C. The program is concerned with the mechanical properties of weldments in both the unirradiated and irradiated conditions. Our efforts will include the evaluation of filler metals, the determination of unirradiated weldment properties, and the preparation of specimens for irradiation studies.

A program to determine the effect of defects on the mechanical properties of weldments is also under way. We intend to determine when a discontinuity becomes a flaw. Initially, we are working toward producing typical weldment discontinuities. We have been successful in producing microfissures in Inconel 600 using an electron-beam welder and an overlapping weld-pass technique. A scanning electron microscope has been employed to characterize the discontinuities produced.

13. Fuel Element Fabrication Development

Miniature fuel plates have been successfully prepared for the next series of ETR loop tests. Principal variables being studied are increased fuel loadings, higher burnups, increased percentage of fines, and the use of burned oxides. Both the burned oxide and the higher percentage of fines increased the ultrasonic attenuation and caused difficulty in the nonbond test. The void volume was considerably higher in the plate

containing the burned oxide. The rolled density, densification during rolling, and fabrication voids in the core appear to be independent of initial fines.

In a study of variation in clearance between both U_3O_8-Al and UAl_3-Al compacts and the aluminum frames during plate rolling, no blisters were found when clearances as large as 4% in either length or width had been present. The degree of core end thickening (dogboning) decreased with the better fits. It was, however, in all cases lower than normal. We attribute this to the thin cladding used on these plates. The spread in fuel cores during rolling was shown to vary directly with the core thickness.

It was shown that different rolling characteristics occur in rolling ATR fuel plates 8 and 19. As expected, severe dogboning was encountered with both types of plates, with 19 being much worse. Neither plate would meet ATR specifications for cladding thickness. In both cases, square ends without flaking were obtained. The amount of dogboning was determined by the scanner used for fuel homogeneity measurements as well as by densitometer measurements of radiographs and by metallography; good correlations were obtained between the methods.

The use of crushing rolls appears to be a much more efficient method for crushing UAl_3, the percentage of fines produced being by far less than with previous techniques. A fluid energy mill was also tried for such crushing but was found to be ineffective.

The inhibiting nature of Zr on the reaction between UAl_3 and Al was confirmed by the use of diffusion couples.

Rather than the large pores and cracks found in U_3O_8 produced by other techniques, that produced by a sol-gel process contains an abundance of minute voids distributed uniformly throughout the structure. Such an oxide is predominantly orthorhombic with traces of the hexagonal form. Characteristics of the oxide were determined. Such a material would appear to be very attractive from the viewpoint of radiation damage.

Electron micrographs show a pore structure is still present in the more corrosion-resistant anodic film formed on Al in oxalic acid

at 4°C. The pore size, density, and degree of interconnections were all reduced from those in films formed at room temperatures. When oxalic acid films formed at 16°C were exposed in a flowing loop with a high thermal gradient across the sample, thermal data from the loop indicated a reduction in corrosion rate. However, metallographic examination of the specimen after test failed to reveal any remnant of the original anodic film.

A report was issued demonstrating the feasibility of converting PuF_6 to PuO_2 by chemical vapor deposition. Work is now under way to modify the equipment for handling mixed PuF_6-UF_6 gases.

The economics of the process for producing UO_2 in a flame reactor have been improved by showing that it is possible to vary the stoichiometry of the reacting gases to produce a by-product HF with the desired water content. The H_2 and O_2 were varied from 2 to 20 times the stoichiometric amounts. Efforts to increase the particle size of the flame-produced oxides have not been successful. Heat treatments have broken up agglomerates and thereby appear to have increased the percentage of fines.

The feasibility of preparing duplex UO_2-W powders in a flame reactor was demonstrated. Pellets pressed and sintered from these powders contained defects that resulted in thermal conductivities lower than expected.

When SiC is deposited from silicon tetrachloride-methane-hydrogen mixtures, the primary process parameter is temperature, with other variables of only secondary importance. In general, the higher the deposition temperature, the more carbon-rich the deposit stoichiometry and the rougher the deposit morphology.

The study of the use of radiography and densitometry to determine fuel homogeneity has revealed a bias in such a procedure when a 0.078-in.-diam aperture was used to measure small areas of inhomogeneity. In some cases, errors as large as 33% were determined.

PART V. ENGINEERING PROPERTIES OF REACTOR MATERIALS

14. Physical and Mechanical Metallurgy of Refractory Alloys

The rate at which Hf is precipitated from solid solutions of Nb-Hf within the miscibility gap increases with the quenching rate from the annealing temperature due to vacancies produced by quenching. Quenched and aged alloys in the Nb-Hf, Ta-Hf, and Ta-Zr systems exhibit a Rockwell-C hardness range from 20 to 60. A general equation has been derived for ΔG_m, the free energy of mixing of spinodal alloys. The diffusivity of N in W is 4.5×10^{-8} cm^2/sec at 1600°C and increases to 8.9×10^{-8} cm^2/sec at 1800°C. The BET surface area of Haynes alloy No. 25 in vacuum increases with the stress and accounts for the increase in the evaporation rate of the alloy with stress. The creep strength of Haynes alloy No. 25 in vacuum decreases as the specimen thickness decreases.

The shear strengths of a number of brazing alloys developed in this program have been determined by the Miller-Peaslee test. Brazes made with Ta—10% W base metal were all stronger at room temperature than similar brazes made with TZM. This difference did not persist at elevated temperatures, and, in fact, the TZM brazes made with alloys from the titanium-zirconium system were stronger. In all instances the shear strength of the brazes were high even at temperatures within 200°C of the melting point of the brazing alloy.

Aging Ta—10% W brazements at elevated temperatures for 50 hr did not degrade the strength of the joints made with the Ti-Zr system alloys. Brazes made with alloys from the Ti-V system did not fare as well after a similar aging treatment; however, it should be noted that, regardless of the filler metal employed, the strengths did remain impressively high.

The thermal conductivities of W, W-Re alloys and W—1.5% Ta were estimated by five methods. Thermal conductivities based on one of the methods agreed reasonably well with the experimental values. A method is being developed to measure thermal conductivities to 1700 K from electrically heated wires.

PART I

FUELS AND CLADDINGS

1. SOL-GEL FAST REACTOR FUELS

A. L. Lotts

The purpose of this program is to obtain the technical data needed to assess the potential of sol-gel-derived $(U,Pu)O_2$ fuel for liquid-metal-cooled fast breeder reactors and to provide basic technology for the development of commercial fabrication plants. The primary requirement is to establish an economical fabrication procedure that is suitable for recycling irradiated fuel and that will produce a fuel rod that meets the criteria for reliable and safe operation in a fast breeder reactor. To meet this requirement, Sphere-Pac, pelletized, and extruded fuels are fabricated and characterized and irradiated in capsules in thermal and fast reactors to determine their operating limits.

Preparation of Sol-Gel $(U,Pu)O_2$ Fuels

W. T. McDuffee

We prepared mixed UO_2-PuO_2 (80:20) sols equivalent to 3.8 kg metal in efforts directed toward supplying dense microspheres for fabricating the fuels for the EBR-II and TREAT experiments. The eight 150-g lots of PuO_2 sols were prepared according to the standard flowsheet in the alpha facility, where this material was also blended with the UO_2 sols (prepared elsewhere). The enriched UO_2 sols for the EBR-II fuel were supplied in 300-g (U) lots; and, after blending with the appropriate volume of PuO_2 sol, these were cross blended to ensure uniform composition. Those sols prepared from natural U for the TREAT fuel were blended with PuO_2 sol in single batches. The mixed UO_2-PuO_2 sols were formed into microspheres: 70% were 420 to 595 μ in diameter, and the remainder were fines < 63 μ in diameter. Furnace malfunction resulted in a melt-down of the furnace tube and contamination of the fines fraction with Cr and Ni.

We made three attempts to prepare the microspheres needed for the EBR-II fuel. All resulted in products $> 96\%$ of theoretical density, but yields were lower than desired. In the first attempt, we obtained a

50% yield of spherical product, but metallographic examination revealed microcracks. Nevertheless, this material had high packing density. In the two subsequent attempts, the mixed sol feeds were prepared according to a different flowsheet to reduce or eliminate the cracking that had occurred earlier. The new process included a digestion at 100°C to increase the average crystallite size of the fundamental sol particles. The feed sols prepared by either method were difficult to form into microspheres. Although we obtained a crack-free product > 96% of theoretical density, the yield of spherical microspheres was only 5 to 10%.

Development of Fabrication Processes

J. D. Sease

Fast reactors operating at high specific powers will require small-diameter fuel pins containing a fuel of 80 to 90% of theoretical density with a high fissile loading. To satisfy the requirements of the fast reactor, we are investigating various fabrication processes for using sol-gel-derived $(U,Pu)O_2$ fuels. During the quarter, our fabrication development has been concentrated on Sphere-Pac for EBR-II irradiation capsules and pelletization for TREAT irradiation capsules.

Sphere-Pac (W. L. Moore)

Sphere-Pac loading of EBR-II irradiation capsules has been the main effort this quarter. A loading glove box in the Interim Alpha Laboratory was given cold check-out, and dummy EBR-II pins were loaded. The major difference in loading the EBR-II pins from previous Sphere-Pac loadings is that the 32-in. length of the EBR-II fuel pins requires vibration coupling to the top of the fuel pin to facilitate loading them in a glove box. We installed a well in the bottom of the box so that the top of the fuel pin could be positioned at a convenient glove-port height during loading. A vibrator with variable-angle stand was constructed and installed adjacent to the well. A scale and a shape separator were also installed in this box. To minimize gas absorption

during loading, we added a system to purge the helium atmosphere of the box. Using thoria microspheres, we successfully practice loaded dummy EBR-II pins in the glove box.

Pelletizing of Sol-Gel $(U,Pu)O_2$ (R. A. Bradley)

Irradiation experiments planned for the TREAT, ORR, and EBR-II reactors require sol-gel-derived urania-plutonia pellets of various sizes and densities. Our objective is to develop fabrication procedures and to produce the pellets for these irradiation experiments. Urania-plutonia pellets with 84 ± 0.8 and 91.3 ± 0.9% of theoretical density and oxygen-to-metal ratios of 1.980 ± 0.005 are required for transient tests in TREAT. Our main effort this quarter has been to establish a process that would reproducibly satisfy these requirements.

Material Preparation and Characterization. — The preparation of the sol-gel $(U_{0.8}, Pu_{0.2})O_2$ for TREAT has been described previously.[1] The preparation and characterization of this material are shown below:

Preparation	Tray-dried in argon-purged stainless steel tray for 36 hr at 38°C and 18 hr at 86°C.
	Ground in Ar in a fluid energy mill at 50 psi.
	Redried for 18 hr at 90°C.
	Pressed at 10,000 psi and granulated to −20 mesh.
Chemical Analysis	
Pu/(Pu + U) Ratio	0.200
NO_3 Content	0.065%
Oxygen-to-Metal Ratio	2.3 ± 0.1
Physical Properties	
Bulk Density	5.42 g/cm^3 = 49.0% of theoretical
BET Surface Area	57 m^2/g

[1]W. L. Moore and R. A. Bradley, Fuels and Materials Development Program Quart. Progr. Rept. June 30, 1968, ORNL-4330, pp. 7–8.

Pressing and Sintering. – Pellets were uniaxially pressed at 30,000 to 40,000 psi from the TREAT material and sintered at 125°C/hr to 1450°C in either CO_2 or Ar–4% H_2. The forming pressures, green densities, and sintered densities of pellets sintered in CO_2 and in dry Ar–4% H_2 are given in Tables 1.1 and 1.2, respectively. The linear relationship between green density and forming pressure is shown in Fig. 1.1(a) and (b), respectively. The two curves show the average densities of pellets sintered in CO_2 and in Ar–4% H_2 as a function of forming pressure. In both cases there is a linear relationship between sintered density and forming pressure, but the densities of pellets sintered in CO_2 are about 4% higher than those sintered in dry Ar–4% H_2. The variability in the green densities of pellets pressed at a given pressure is only about ±0.2%, but the variation in sintered density is 1.5 to 2.0%. Pellets sintered in Ar–4% H_2 tend to develop hairline, laminar cracks during sintering. Sintering in CO_2 eliminates the cracks but produces non-uniform shrinkage that may result in density variations within the pellets. Pellets sintered in CO_2 typically have 0.002-in. ovality at the top and flare to 0.005 in. at the bottom.

Although we have produced pellets in the 84% dense range from the tray-dried, jet-milled TREAT powder, it is very difficult to control the process. The very great surface area of the powder makes it difficult to control its moisture content and oxygen-to-metal ratio. The moisture content affects the consolidation of the powder during pressing, and the oxygen-to-metal ratio affects the sintering behavior. The high content of volatiles in the tray-dried powder (about 7% weight loss during sintering) leads to pellet cracking.

We believe that calcining the powder before pelletizing, to reduce the surface area to 5 to 20 m^2/g and to adjust the oxygen-to-metal ratio to about 2.1 to 2.2, would make it easier to control the sintered density and eliminate cracking. Studies are in progress to establish calcining conditions that will yield a stable powder for producing pellets.

Table 1.1. Forming Pressures, Green Densities, and Sintered Densities of Urania-Plutonia Pellets Sintered in CO_2

Sinter Number	Forming Pressure (psi)	Density, % of Theoretical	
		Green	Sintered
	$\times 10^3$		
45	30	43.2	82.6
	35	43.7	85.0
	40	44.4	86.7
46	30	43.2	84.1
	35	43.8	85.8
	40	44.5	88.0
47	30	43.0	84.1
	35	43.9	86.1
	40	44.6	86.6
48	28.5	43.0	84.8
	35	43.9	86.6
	40	44.6	87.2

Table 1.2. Forming Pressures, Green Densities, and Sintered Densities of Urania-Plutonia Pellets Sintered in Dry Ar–4% H_2

Sinter Number	Forming Pressure (psi)	Density, % of Theoretical	
		Green	Sintered
	$\times 10^3$		
36	30	43.7	80.5
	35	44.4	82.0
	40	45.0	82.5
38	30	43.5	80.3
	35	44.2	81.3
	40	44.3	82.0
42	30	43.2	79.0
	35	44.0	80.2
	40	44.8	81.3

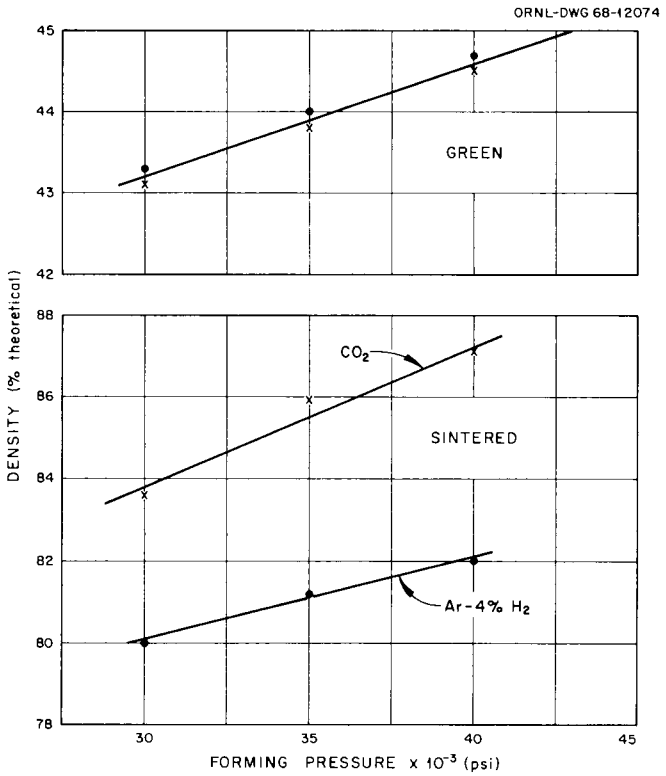

Fig. 1.1. Effect of Forming Pressure on Green and Sintered Densities of $(U,Pu)O_2$ Pellets Sintered in CO_2 and Ar–4% H_2.

Capsule Fabrication (J. D. Sease, M. K. Preston, W. L. Moore)

As part of our fast fuels irradiation program, we have commitments to fabricate three types of capsules: (1) EBR-II, (2) TREAT, and (3) ORR. We plan to build the complete capsules for EBR-II and TREAT. We shall fabricate only fueled portions of the ORR capsules.

EBR-II Capsules. – Fabrication of the five EBR-II capsules is in progress and should be completed by the first of November. A cross section of the EBR-II capsules is shown in Fig. 1.2. During this quarter, we procured all hardware for the capsules, developed welding procedures, and outlined and checked fabrication procedures.

We developed a procedure to keep the weld buildup on the outer capsule within the maximum specified limit of 0.0018 in. on the diameter. We improved the reliability of the tack weld of the fuel capsule to the outer capsule by designing a special joint for this weld.

Procedures and run sheets for fabrication of the EBR-II capsules were developed and checked with a dummy capsule.

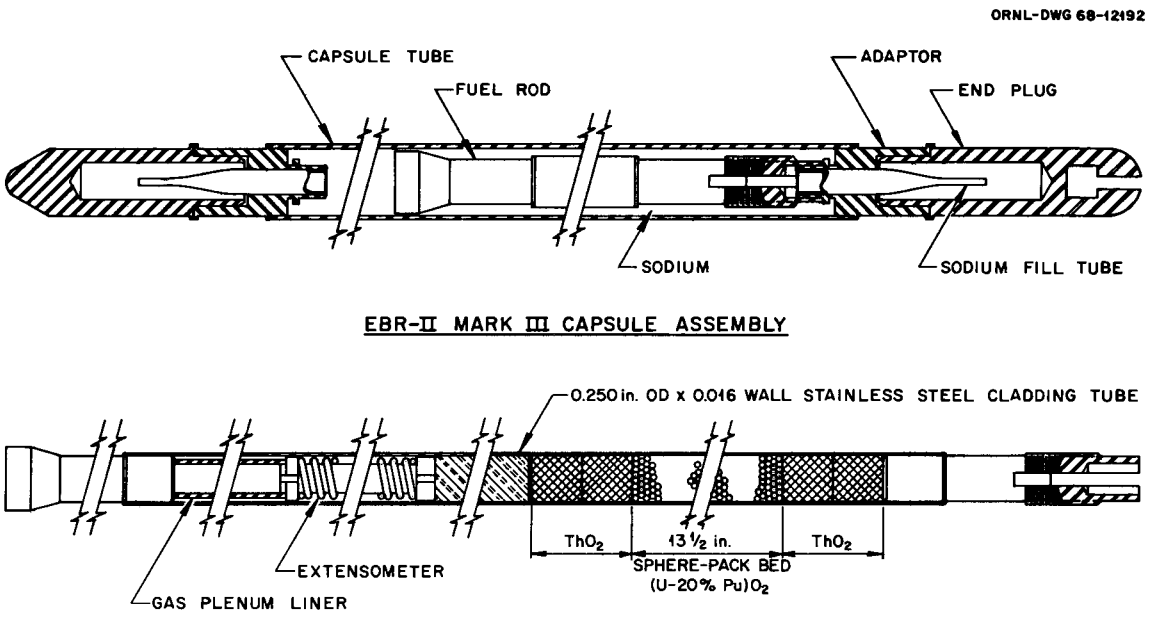

Fig. 1.2. Series I ORNL Oxide Fuels Tests in EBR-II.

TREAT Capsules. — We have completed detailed design of the TREAT capsules and procured essentially all the hardware. We have begun fabrication of selected hardware.

The major hardware items that have been completed are the pressure vessels for three TREAT capsules. We encountered difficulties due to the lack of a welder qualified to work with the 4130 steel and able to make the required joint and due to warping during final heat treating. A welder was finally qualified for the material and weld joint of the pressure vessel. The warping (about 1/8 in.) was corrected mechanically, and the final 455°C drawing treatment was repeated to ensure that warping would not reoccur during operation.

Sodium Filling System

The system for filling the heat-transfer annuli in the EBR-II and TREAT capsules has been completed, and initial cold check-out runs have been made. The completed sodium system without the protective shielding is shown in Fig. 1.3. The sodium rig is shown schematically in Fig. 1.4. The six major constituents indicated in the two figures are the (1) pressurized gas supply, (2) vacuum source, (3) sodium trap,

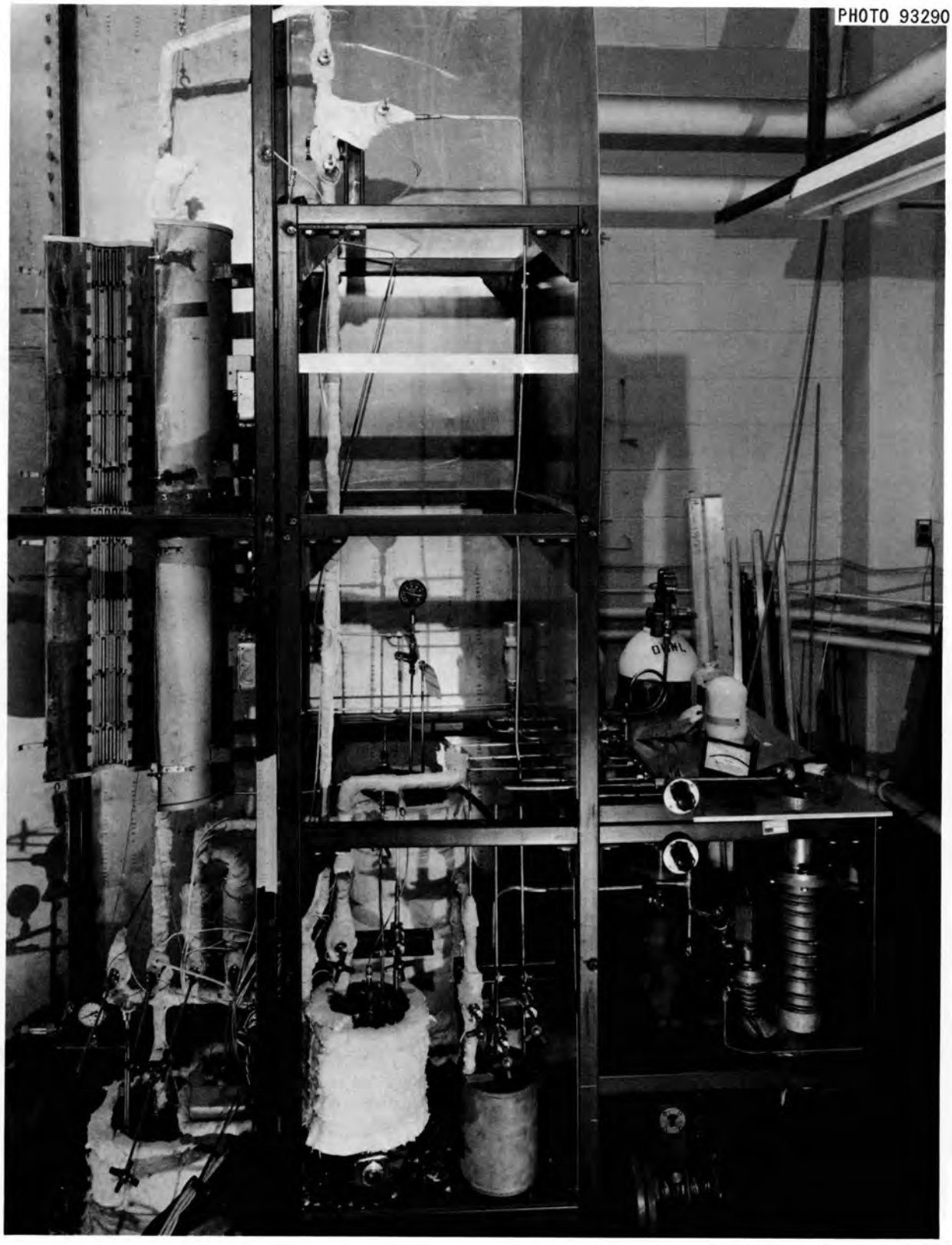

Fig. 1.3. Sodium Filling Apparatus Without Protective Shielding.

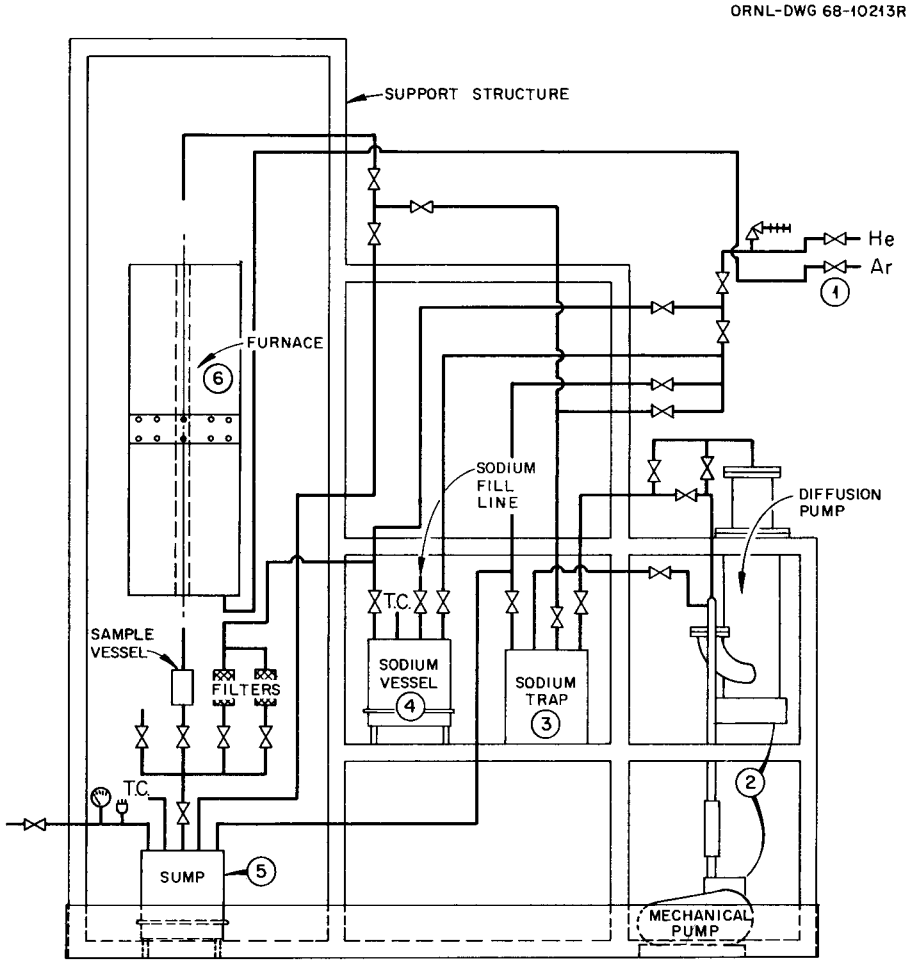

Fig. 1.4. Schematic of Sodium Filling Apparatus.

(4) sodium supply tank, (5) sump, and (6) capsule furnace. All tubing joints, with the exception of compression fittings on the gas supply header, are welded. The sodium filling system is shown with the protective shielding in place in Fig. 1.5.

We plan to first wet the walls of the capsule by flushing Na through the capsule at 540°C and then fill the capsule at 175°C. Vacuum will transfer Na in and out of the system.

In initial filling runs, we encountered a number of difficulties, most of them due to inadequate heat tracing of lines. Additional heat tracing solved most of these problems, and we are making additional cold runs.

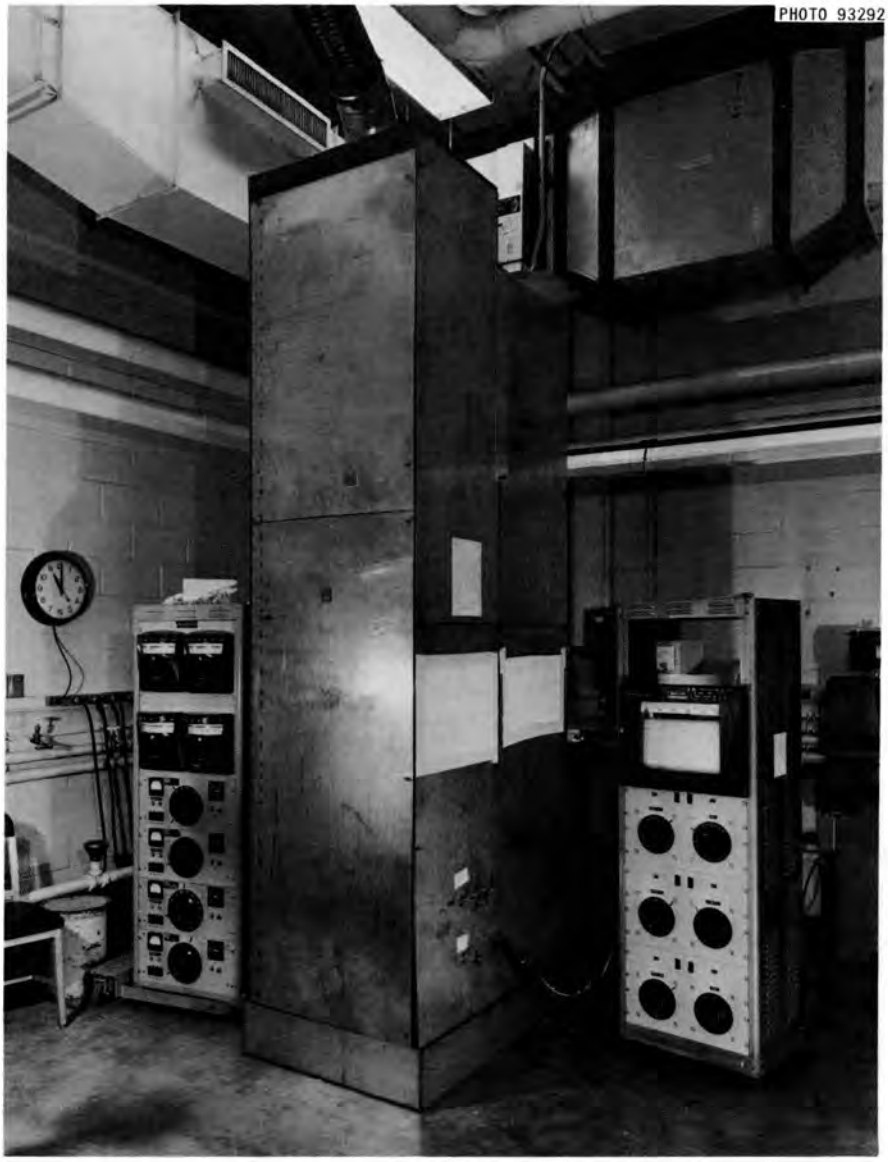

Fig. 1.5. Sodium Fill Apparatus With Protective Shielding in Place and With Relative Power Supplies and Instrumentation.

The eddy-current devices, which have been developed by the Nondestructive Testing Group for detecting sodium level and voids, appear to operate satisfactorily. The level probe, which is capable of operating at 150°C, has indicated the sodium level within 1/8 in. or better. The eddy-current void detector appears to be capable of discriminating a void smaller than 1/32-in. in diameter by 1/32-in. deep.

Characterization of $(U,Pu)O_2$ Fuels

W. H. Pechin

The development of sol-gel fuel fabrication requires characterization of the material to control the process and to determine which properties are important in the irradiation behavior. The characterization requires determination of both the chemical composition and the physical properties.

Analytical Chemistry (W. H. Pechin)

A series of chemical and physical analyses is now available for characterization of the preirradiated mixed-oxide fuel. These are summarized below:

Desired Constituent	Method
Pt	Coulometric titration
U	Coulometric titration
Isotopic	Mass spectrography
Oxygen-to-Metal ratio	Gravimetric oxidation – reduction
C	Combustion-gas chromatography
N	Spectrophotometry
F	Pyrohydrolysis – spectrophotometry
Cl	Pyrohydrolysis – spectrophotometry
Metallic Impurities	Spectrographic (carrier distillation)
Gas Release	Vacuum heating – mass spectrography
Density	Mercury porosimeter for microspheres, dimensions and weight for pellets.
Surface Area	BET analysis

The gravimetric determination of oxygen-to-metal ratio has been modified from that described by Lyons[2] in that the final reduction step is carried

---

[2]W. L. Lyons, The Measurement of Oxygen-to-Metal Ratio in Solid Solutions of Uranium and Plutonium Dioxides, GEAP-4271 (May 31, 1963).

out at 850°C in Ar–4% H_2. The determination of microsphere density by mercury displacement has been modified to correct for incomplete filling of the voids between spheres at low pressure. This modification involves plotting the volume displaced at increasing pressures. The volume will approach a constant value between the filling of intersphere voids and the filling of the pores in the spheres. The carrier distillation on the spectrographic analysis is required for the determination of B and Cd.

A problem of increasing interest is the characterization of powders from dried sols. At present, the measurement of surface area by the BET method is the primary comparison. Particle size analysis and differential thermal analysis-thermal gravimetric analysis will be available shortly, but the oxidation state of the metal ions in the powder is also of interest. We have made two trials of dissolving the powder and titrating the U(IV) in solution. Results indicate that only 50 to 60% of the U is present as U(IV), which would make the oxygen-to-metal ratio about 2:3. We are presently looking for a means to confirm these results.

Manufacture of Standard Samples of UO_2 (J. M. Leitnaker, K. E. Spear)

Since fissioning produces enough metal elements whose oxides are less stable than the oxides of the type 316 stainless steel used for cladding in an LMFBR, a stoichiometric oxide fuel, $(U,Pu)O_{2.00}$, would tend to oxidize the cladding. One current idea is to use a fuel with a very low oxygen potential so that the fuel itself will act as a tailoring agent. Since plans now call for irradiation of $(U,Pu)O_{1.98\pm0.01}$, we must be able to distinguish between oxygen-to-metal ratios of 2.00 and 1.98 in order to fix the oxygen potential of the fuel.

There is no concensus on analytical methods for determining the oxygen content of UO_2 and mixed oxides. In fact, at least two "round robins" are now being organized to compare results on the same samples from laboratories in this country and elsewhere.

Young et al.[3] recently expressed the variation of lattice parameter with varying oxygen content in UO_{2+x} by the equation

[3]W. A. Young, L. Lynds, J. S. Mohl, and G. G. Libowitz, An X-Ray and Density Study of Nonstoichiometry in Uranium Oxides, NAA-SR-6765 (1962).

$$a_0 = 5.4705 - 0.094x \quad (0 \leq x \leq 0.125), \tag{1.1}$$

where a_0 is the lattice parameter in angstroms. Since 5.4705 A for the room-temperature lattice parameter of $UO_{2.00}$ agrees with the work of Baldock et al.[4] (who considered a large amount of published data as well as their own work), we checked samples available to us against this value.

X-ray measurement[5] of two samples being used as standards in ORNL's Analytical Chemistry Division indicated lattice parameters of 5.46780 ± 0.00017 and 5.46831 ± 0.00023 A, respectively. Thus, the oxygen-to-metal ratios for these supposedly standard $UO_{2.00}$ specimens would, according to Eq. (1.1), be 2.02 or 2.03.

A number of hydrogen-reduced samples, believed to be of high quality since they had been made to close specifications for an oxide-fueled reactor, were available. X-ray analysis of inside, center, and outside portions of two of these gave results ranging from 5.4717 to 5.4708 A. According to the study of Young et al.,[3] portions of such samples could be nonstoichiometric by as much as 1.987 in the oxygen-to-metal ratio. Our analysis by combustion in O_2 at 850°C indicated oxygen-to-metal ratios that ranged from 2.02 to 1.995 for various parts of the samples.

Our experiences clearly illustrate the fact that standard materials for comparison are not available.

For our immediate problem of producing irradiation test specimens, we do not need to know the exact oxygen content. What we do need to know precisely is the difference between any given specimen and some fixed point. Therefore, we decided to try to establish such a reference point in terms of equilibration with a gas mixture of known oxygen activity and to relate other measurements from the literature to this fixed point for our own use.

---

[4]P. J. Baldock, W. E. Spindler, and T. W. Baker, The X-Ray Thermal Expansion of Near-Stoichiometric UO_2, AERE-R-5007 (1965).

[5]J. M. Leitnaker, "The Ideality of the UC-UN Solid Solution," pp. 317–330 in Thermodynamics of Nuclear Materials, 1967, International Atomic Energy Agency, Vienna, 1968.

To fix the oxygen composition for these samples, we chose to fix the thermodynamic oxygen potential in a furnace and then equilibrate UO_2 samples in this furnace. Markin and Roberts[6] have shown by measurements of electromotive force that an enormous change in oxygen potential, occurs close to the stoichiometric composition; at 850°C a $\overline{\Delta}G(O_2)$ value of −100 kcal represents the steepest slope of the curve for $\overline{\Delta}G(O_2)$ vs oxygen-to-uranium ratio. A CO_2-to-CO ratio of 1:10, which approximates this $\overline{\Delta}G(O_2)$ value, is a very useful choice for fixing the oxygen potential for small changes in the CO_2-to-CO ratio would not be detectable in the final product by any means now available. For example, even a change in the ratio from 1:10 to 1:1 or to 1:20 would change the oxygen-to-uranium ratio by only ±0.001.

Our starting material was a large (about 1 lb) batch of a laboratory sample of urania with an oxygen-to-uranium ratio of about 2.1. Spectographic analysis indicated < 100 ppm total impurities, principally Cu (20 ppm) and Fe (40 ppm). Samples were cold-pressed pellets 1/4 in. in diameter and weighing about 2 g. We used a simple muffle furnace and controlled the temperature to ±25°C. At the conclusion of an 18-hr run, the boat in which the samples were placed was manually pushed to the cold zone of the furnace where it cooled to below red heat within 2 min.

We used two techniques to examine the samples after this treatment. In an argon-filled dry box, we took two x-ray specimens of each sample, one from the surface of the pellet and one from near the center, so that inhomogeneities might be detected. Second, we made duplicate analyses for total uranium content by combustion to constant weight.

Results of the heat treatments are shown in Table 1.3. Two things are noteworthy. The last set of samples heated (at 1400°C) gives a precision in lattice parameter and analysis that is excellent and perhaps the limit of the measuring equipment. Thus, these samples almost certainly reached equilibrium throughout. The composition is about what

---

[6]T. L. Markin, L.E.J. Roberts, and A. Walter, "Thermodynamic Data for Uranium Oxides Between UO_2 and U_3O_8," pp. 693–711 in Thermodynamics of Nuclear Materials, International Atomic Energy Agency, Vienna, 1962.

Table 1.3. Results of Heating UO_2 for 18 Hr in a 10:1 Mixture of CO and CO_2

Sample	Heat Treatment Temperature (°C)	Oxygen-to-Metal Ratio[a]	Specimen Location in Sample[b]	Lattice Parameter, A		
				Determined[c]		Calculated[d]
				Value	Standard Deviation	Value
					$\times 10^{-5}$	
A-1	1000	2.0583[e]	S	5.46971	±24	5.4650
			C	5.47058	±18	
E-1	1000	2.0629[e]	C	5.47030	±17	
			S	5.46975	±17	
A-3	1200–1250	2.0052[e]	C	5.47092	±16	5.4700
			S	5.47085	±26	
E-3	1200–1250	2.0006[e]	S	5.47070	±19	5.4704
			C	5.47065	±12	
B-3	1380	1.9959 ± 10[f]	C	5.47079	±26	5.4709
			S	5.47064	±17	
D-3	1380		S	5.47073	±16	
			C	5.47065	±19	

[a]Uranium content determined by combustion to constant weight in O_2 at 850°C: product assumed to be U_3O_8, balance to be oxygen.

[b]S = surface; C = center.

[c]Determined from a Nelson-Riley extrapolation.

[d]Calculated from $a_0 = 5.4705 - 0.094x$, where x is defined by the data of the third column as $UO_{2\pm x}$. W. A. Young, L. Lynds, J. S. Mohl, and G. G. Libowitz, An X-Ray and Density Study of Nonstoichiometry in Uranium Oxides, NAA-SR-6765 (1962).

[e]Average of two measurements.

[f]Average of four measurements, two for sample B-3 and two for sample D-3.

is expected, being slightly on the low side. The lattice parameter corresponds to the best recent determinations by Baldock et al.[7] and by Young et al.[8] Thus, we conclude that the material prepared in this rather simple way can be used as a standard for all oxygen analyses in which a stoichiometry of essentially $UO_{2.000}$ is wanted.

The second observation concerning the data is interesting but is of less importance for our purpose. The samples heated at 1000°C had an oxygen-to-uranium ratio considerably higher than 2.00, but the lattice parameter, of the inside at least, was nearly that corresponding to $UO_{2.000}$. The work of Young et al. makes clear that oxidation must have taken place after the sample cooled. The lower lattice parameter of the specimens from the outside of the samples indicates some oxidation took place above 400°C, the lowest temperature at which oxidation produces an oxygen-rich single phase. Samples heated at 1000°C had a sintered density of only 70% of theoretical, while at 1200°C and above the densities were about 95% of theoretical. Clearly, reduced samples cannot be removed from the furnace into the laboratory atmosphere for weighing unless sufficient sintering has taken place so that reaction with the atmosphere is negligible.

Although with our present equipment samples are below red heat in a couple of minutes, the furnace is too hot to touch for several hours. We are assembling an apparatus which should allow us to quench samples more rapidly. With our new apparatus we should be able to prepare samples with a predetermined deviation from a stoichiometric ratio.

Thermal Conductivity of Sol-Gel Fast Reactor Fuels (Peter Spindler)

Equipment for temperature control of the new radial heat flow apparatus has arrived and is being installed. Eight new Pt–10% Rh vs Pt

---

[7]P. J. Baldock, W. E. Spindler, and T. W. Baker, The X-Ray Thermal Expansion of Near-Stoichiometric UO_2, AERE-R-5007 (1965).

[8]W. A. Young, L. Lynds, J. S. Mohl, and G. G. Libowitz, An X-Ray and Density Study of Nonstoichiometry in Uranium Oxides, NAA-SR-6765 (1962).

thermocouples were added to this system. A sample of single-crystal LiF was installed in the old radial heat flow apparatus to obtain thermal conductivity data to its melting point. These results will complement the studies completed between 80 and 420 K. Using data on LiF available in the literature, we completed a number of calculations to define phonon and photon heat conduction effects. For example, Dugdale and MacDonald[9] show that the mean free path, ℓ, of phonons for an insulator is

$$\ell \simeq \frac{a_0}{\alpha\gamma T} , \qquad (1.2)$$

where

a_0 = lattice parameter,
α = thermal expansion coefficient,
γ = Grüneisen constant,
T = temperature in K.

We calculated the thermal conductivity (λ) for LiF at room temperature to be 0.147 w cm^{-1} deg^{-1} from the well-known formula $\lambda = \frac{1}{3} c_v \ell v$ (c_v = specific heat per unit volume, v = velocity of sound). For a_0, α, γ, c_v, and v, we used literature data. Our measured value was $\lambda_{measured}$ = 0.139 w cm^{-1} deg^{-1}. Since we had to use experimental data from different authors, this is a very good agreement (6%). However, Dugdale and MacDonald indicated that the assumptions for ℓ are valid only around room temperature. At 85°C, for example, we find a deviation of 21%.

We believe this is due to combined uncertainties in the temperature dependencies of experimental quantities needed to obtain ℓ, c_v, and v. For instance, values for the elastic moduli versus temperature are needed to obtain γ and c_v versus temperature. Numerous studies show agreement for C_{11}, C_{12}, and C_{44} at room temperature; but at 1000 K only two sets of data exist, and these differ:

---

[9] J. S. Dugdale and D. K. MacDonald, Phys. Rev. 98, 1751 (1955).

	Haussühl[10]	Susse[11]
C_{11} (10^{11} dynes/cm^2)	10.5	4.0
C_{12} (10^{11} dynes/cm^2)	4.7	1.3
C_{44} (10^{11} dynes/cm^2)	6.1	4.9
c_v (cal g^{-1} K^{-1})	3.7	6.1

The greatly different c_v values indicate the dilemma for further calculation. Thus it seems necessary to find a similar semitheoretical expression for λ that is applicable for high temperatures in order to be able to compare the λ values over the whole temperature range investigated. This will be one of the important steps in determining the effects of infrared transmission and of vacancy formation with increasing temperatures.

Deformation of UO_2 (C. S. Morgan)

We have continued investigation of the deformation of polycrystalline UO_2 specimens prepared from sol-gel powder. Deformation studies involved compression under an Ar–4% H_2 atmosphere. At 1425°C, UO_2 specimens prepared by isostatically pressing sol-gel powder and those prepared by die pressing the same powder were found to have similar stress-strain curves at a constant strain rate. The stress leveled out at about 15,500 psi until the deformation exceeded 10%.

We have extended high-temperature deformation studies to include creep under constant stress. Deformation curves obtained under four conditions are shown in Fig. 1.6. The activation energy of the creep process between about 2 and 6% deformation was 142 kcal/mole based on data at a stress of 8000 psi (1525 and 1605°C) and was 120 kcal/mole based on data obtained at a stress of 20,000 psi (1225 and 1325°C). These values compare with an activation energy of about 100 kcal/mole for diffusion of U in UO_2.

---

[10]S. Haussühl, Z. Physik. 159, 223 (1960).

[11]C. Susse, Compt. Rend. 247, 1174 (1958).

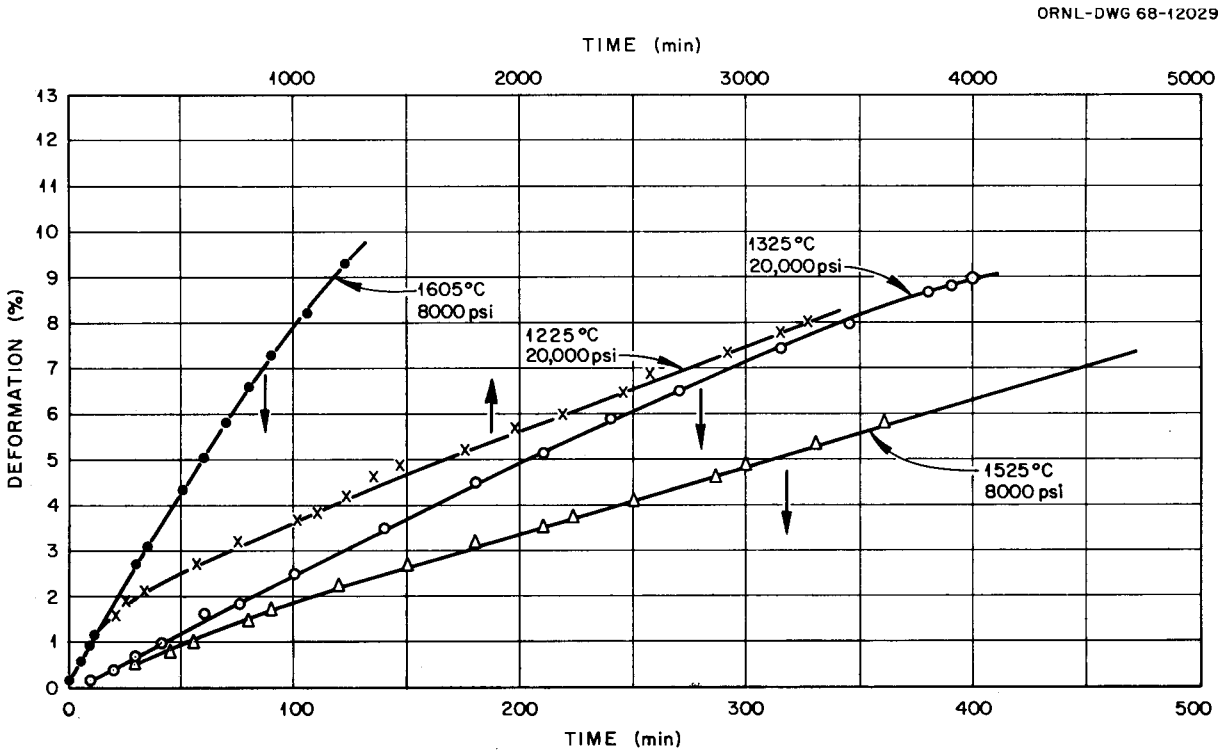

Fig. 1.6. Deformation of UO_2 Sol-Gel Specimens (92% Theoretical Density).

Further deformation tests will be made to determine long-term low-stress creep rates to provide a background for deformation studies of $(U,Pu)O_2$ specimens.

Irradiation Testing of Sol-Gel $(U,Pu)O_2$ Fuels

A. R. Olsen

The final evaluation of sol-gel-derived $(U,Pu)O_2$ fuels will be based upon their irradiation performance. The irradiation testing program is concentrating on comparative tests of the fabrication forms — Sphere-Pac, pellets, and extrusions. The program includes thermal flux irradiations of instrumented capsules to high burnup levels in relatively short times.

These tests will provide supplemental information essential to the analysis of the fast flux irradiations in which the profiles of radial fission-rate distribution and fuel temperature are more typical of anticipated LMFBR operating conditions. The test program also includes transient tests to investigate fuel performance under off-normal operating conditions. An integral part of the irradiation test program is the development of mathematical models to predict fuel behavior and computer programs to perform the associated calculations.

Uninstrumented Thermal Flux Irradiation Tests (A. R. Olsen, J. Komatsu,[12] R. B. Fitts)

Two capsules from a limited number of uninstrumented tests being irradiated in the ETR are undergoing postirradiation examination, and two are still being irradiated. The capsule design permits the simultaneous irradiation of four test rods, each containing a 3-in.-long fuel column.

We are still evaluating the microstructural changes in capsule 43-112, described previously.[13] We are considering several mechanisms of void migration and grain growth. Currently, we are concentrating on an evaporation-condensation model, based on the work of others,[14–17] for columnar grain growth in central regions of the fuel and are establishing the calculation procedures to evaluate this model.

---

[12] Guest Scientist from Power Reactor and Nuclear Fuel Development Corp., Tokai, Japan.

[13] A. R. Olsen, R. B. Fitts, and J. Komatsu, Fuels and Materials Development Program Quart. Progr. Rept. June 30, 1968, ORNL-4330 pp. 18–20.

[14] V. B. Lawson and J. R. MacEwan, Thermal Simulation Experiments with a UO_2 Fuel Rod Assembly, CRFP-915 (1960).

[15] P. R. DeHalas and G. R. Horn, J. Nucl. Mater. 8, 207 (1963).

[16] R. S. Barnes and R. S. Nelson, Theories of Swelling and Gas Retention in Reactor Materials, AERE-R-4952 (1965).

[17] F. H. Nichols, J. Nucl. Mater. 22, 216 (1967).

Although the evaluations are still in the early stages, one interesting fact has evolved. Using the equations of Nichols[18] and his parameters for UO_2 together with initial unrestructured temperature profiles for the four fuel rods in capsule 43-112, calculated by our PRØFIL program, we calculated rates of void migration for various radial positions in the fuel. We then compared these curves with the observed structures. We saw no columnar grain growth in rods 1 and 4, but there was significant columnar grain growth in rods 2 and 3. From these preliminary calculations and the constants used, we judge that columnar grain growth stopped when the void migration rate fell below about 5×10^{-6} cm/sec. Although these preliminary calculations are encouraging, the model requires modifications to accommodate changes in the rate of void migration as a function of prior restructuring and the consequent changes in temperature distribution.

Postirradiation examination of capsule 43-103, which contained three sol-gel UO_2 Sphere-Pac rods and one UO_2 pellet rod, has begun. We have gamma scanned the capsule and taken dimensional measurements from all fuel rods. All four rods were intact, and there is no indication of significant changes in the diameter of the cladding. The fission-gas sampling and the sectioning for burnup analysis and metallographic examination are complete.

The gamma scan for this capsule is reproduced in Fig. 1.7. The appearance of the scans for the three Sphere-Pac rods in positions 1, 3, and 4 is normal, showing the typical flux peaking near the center of the capsule. The scan of the rod fueled with UO_2 pellets, however, is not normal. The activity is excessively high at the bottom of the fuel column, and the high activity extends into both the top and bottom ThO_2 insulator regions.

The explanation for this unusual gamma scan is uncertain. As shown in Table 1.4, however, we have calculated the time-averaged linear heat ratings from the burnup analyses. Both the burnup levels and the heat ratings exceed those proposed and calculated for this capsule. It appears, from flux measurements made in adjacent locations while this capsule was being irradiated, that the peak, unperturbed flux in the ETR position

Photo R-44632

Slit width - 0.010 in.

Energy counter - $\int$ > 0.55 Mev

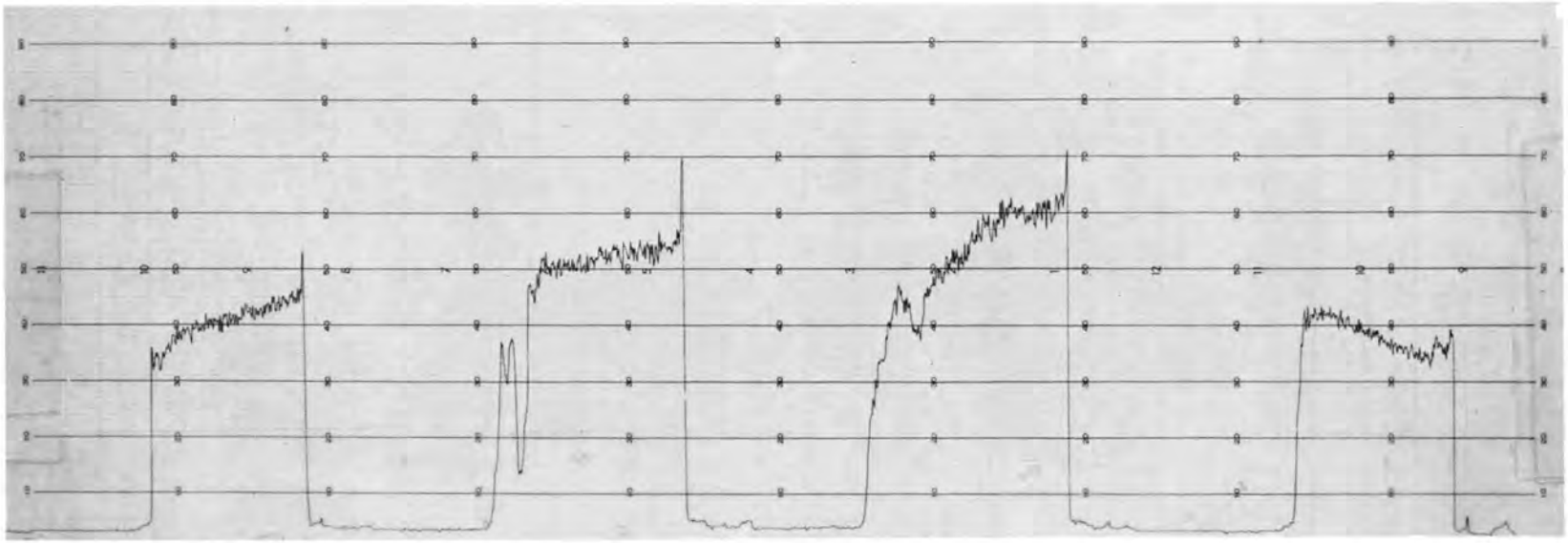

Rod No.	4	3	2	1
Fuel Form:	Sphere-Pac	Sphere-Pac	Pellets	Sphere-Pac
Smear Density:	8.09 g/cm³	8.03 g/cm³	9.58 g/cm³	8.06 g/cm³

Fig. 1.7. Postirradiation Gamma Scan of Test Capsule 43-103; All Fuel UO_2 (20% ^{235}U).

Table 1.4. Burnups and Time-Averaged Linear Heat Ratings for Experiment 43-103

Fuel Rod Identification	Fuel Form	Burnup[a] (% FIMA)	Linear Heat Rating[b] (kw/ft)
43-103-1	Sphere-Pac	4.10	15.6
43-103-2	Pellets	4.98	22.0
43-103-3	Sphere-Pac	5.44	20.7
43-103-4	Sphere-Pac	4.34	16.5

[a]Because of erratic and generally high burnup levels obtained from radiochemical analyses, we are using the burnup levels derived from changes in isotopic analysis for these UO_2 fuels (20% ^{235}U).

[b]The linear heat ratings are time-averaged over the total exposure time of 126 days of effective full power, assuming 177 Mev/fission.

where this capsule was irradiated was not, as we had requested, 0.86×10^{14} neutrons cm^{-2} sec^{-1}. The ETR Operations group is making a new flux measurement for this position, and we are measuring the activation of the capsule cladding. If the heat ratings were actually this much higher than planned, there may possibly have been some melting of the central portion of the fuel. The metallographic examination will have to be completed before this hypothesis can be confirmed.

The two capsules still in the reactor each contain three test rods of Sphere-Pac (^{238}U–15% Pu)O_2 and one of Sphere-Pac UO_2 (20% ^{235}U). Capsule 43-113 is operating at a calculated peak linear heat rating of 14 kw/ft with a target burnup of 10% fissions per initial metal atom (FIMA) and is at about the 5% burnup level. Capsule 43-115 has achieved about 50% of its target burnup level of 5% FIMA at a calculated peak linear heat rating of 16 kw/ft.

ORR Instrumented Tests (R. B. Fitts, V. A. DeCarlo)

Capsule SG-1. – This capsule, containing (U–15% Pu)O_2 Sphere-Pac fuel at 8.8 g/cm^3 smear density, was operated in the ORR Poolside Facility for about 1200 hr. Heat generation was selectively varied between 5

and 15 kw/ft. Operating temperatures compared favorably with design predictions.

Erratic behavior of the central thermocouple was described in the last quarterly report.[18] We believe this was caused by the reaction that we have observed metallographically between the Mo of the thermocouple well and some components of the fuel rod. A typical section from the wall of the molybdenum well before irradiation is shown in Fig. 1.8. The white material in the center of Fig. 1.9 is the Mo after irradiation. The structure in this cross section is typical of this fuel when it was operated at 15 kw/ft in other tests, except that a large amount of white deposit, probably Mo, is distributed throughout the fuel structure, as shown in Figs. 1.10 and 1.11. We hypothesize that the redistribution of Mo occurred by the formation of MoO_3 when the temperature and temperature gradient were raised enough to initiate significant oxygen migration in this fuel. This might be expected to occur in the temperature range where fuel restructuring by the evaporation-condensation mechanism becomes significant (about 1700°C). Reduction of the MoO_3 occurred as it moved to the cooler regions of the fuel. A similar mechanism has been proposed for molybdenum redistribution observed in a recent study of oxygen migration involving $(U,Pu)O_{2-x}$ in a molybdenum capsule.[19] Since the initial oxygen-to-metal ratio in the fuel would have a significant effect upon this reaction, and possibly a similar reaction with the W–26% Re to be used in the next capsule, we have requested a reanalysis of the oxygen-to-metal ratio using archive fuel samples.

Analysis of data from this capsule at selected times during operation has yielded "smeared thermal conductivity" values, defined as

---

[18]R. B. Fitts and V. A. DeCarlo, Fuels and Materials Development Program Quart. Progr. Rept. June 30, 1968, ORNL 4330, pp. 20–23.

[19]Sodium-Cooled Reactors, Fast Ceramic Reactor Development Program, 26th Quart. Progr. Rept., February–April 1968, GEAP-5631 (June 1968) p. 62.

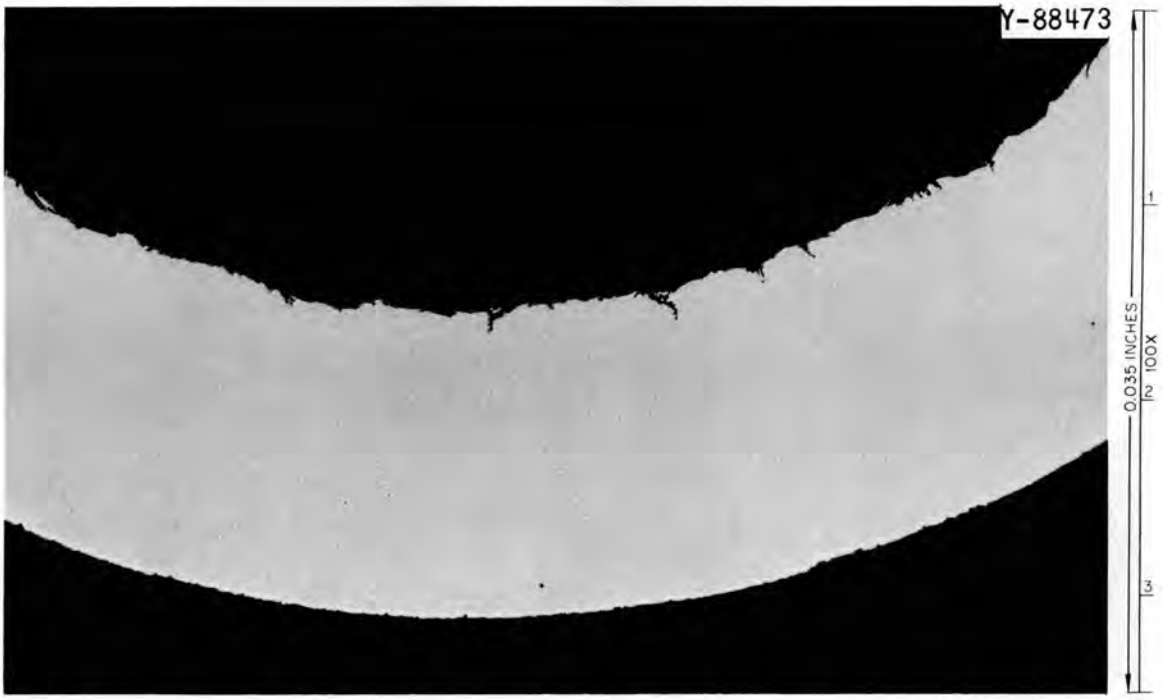

Fig. 1.8. Tube Wall of Molybdenum Thermocouple Well Before Irradiation.

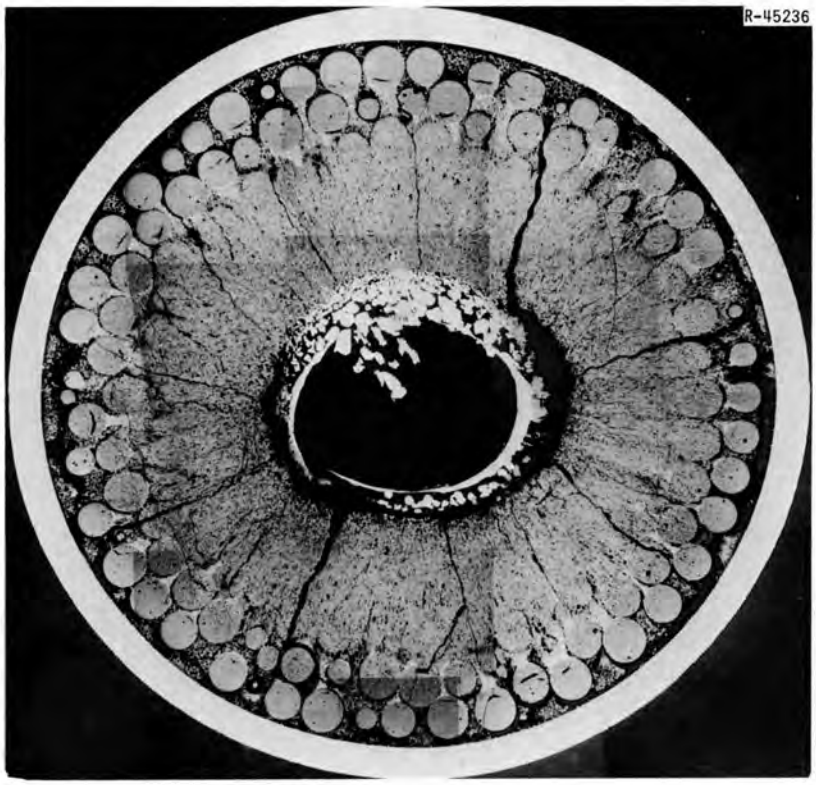

Fig. 1.9. Cross Section of (U–15% Pu)O_2 Fuel Rod from Capsule SG-1.

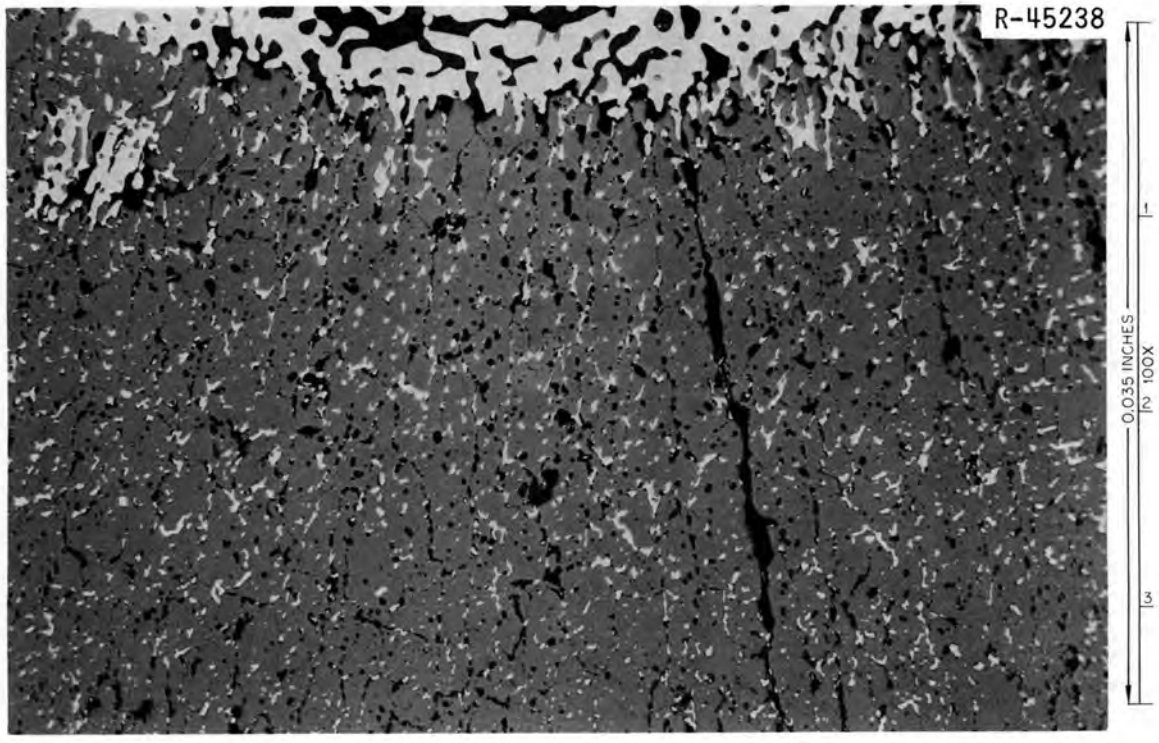

Fig. 1.10. Fuel and Molybdenum at Edge of Central Thermocouple Well in Capsule SG-1.

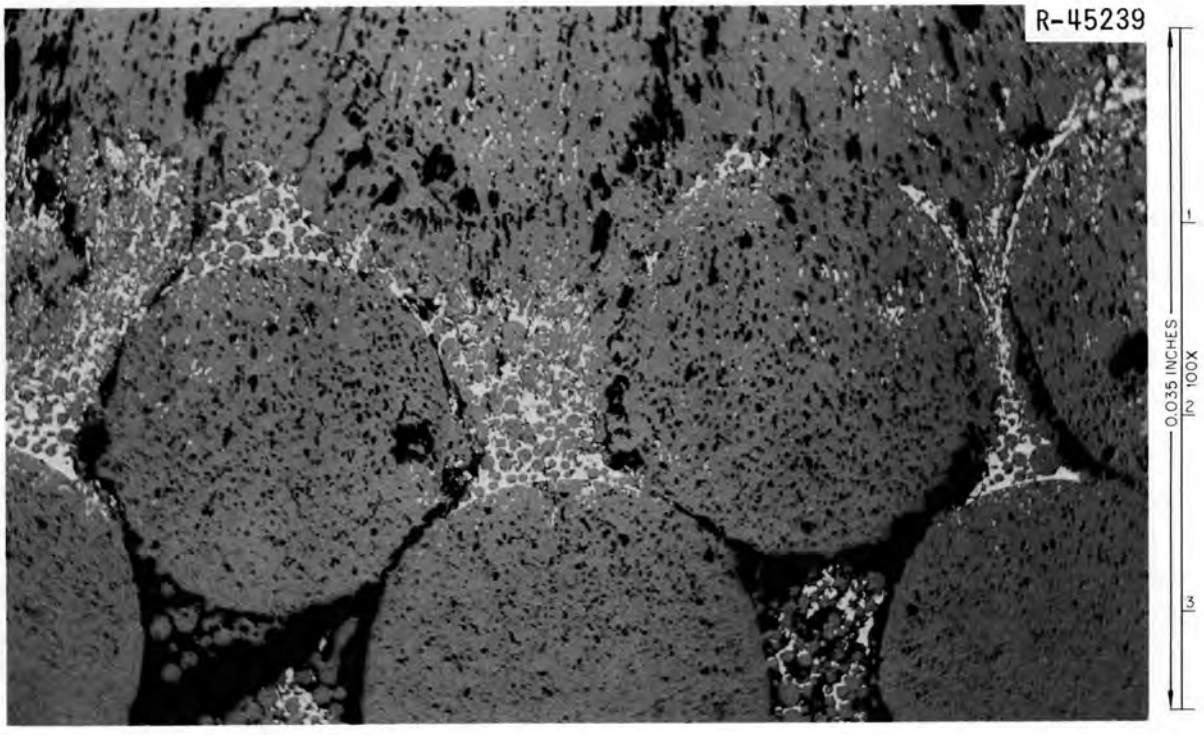

Fig. 1.11. Fuel and Molybdenum near Midradius in Capsule SG-1.

$$\bar{\lambda} = \frac{\int \lambda(T)\, dT}{T_{\mathfrak{L}} - T_s}, \qquad (1.3)$$

where

λ = thermal conductivity,

$T_{\mathfrak{L}}$ = fuel central temperature, and

T_s = temperature at inside surface of cladding.

These values range from 0.019 w cm^{-1} $°C^{-1}$ between 375 and 825°C and to 0.015 w cm^{-1} $°C^{-1}$ between 460 and 1300°C. These values increased with time of operation at center-line temperatures above 1200°C as would be expected if the density increased due to sintering at elevated temperatures. After operation at temperatures above 1600°C for 180 hr, the apparent thermal conductivity at temperatures below 1600°C increased 40%. The high-temperature operation included the period of erratic thermocouple operation. This effect may be explained by fuel sintering, but any explanation must also include the effects of the observed molybdenum permeation of the fuel structure.

Capsule SG-2. — Difficulty in procuring the W—26% Re thermocouple wells for this capsule has caused a delay. We are now hoping to insert the capsule into the reactor January 10, 1969.

Transient Testing of Sol-Gel-Derived $(U,Pu)O_2$ Fuels (C. M. Cox)

The purpose of the transient testing program is to investigate the behavior of sol-gel-derived $(U,Pu)O_2$ fuels under conditions simulating accidental power excursions. The initial transient experiments will be conducted at the TREAT this winter. The TREAT program outlined for this fiscal year includes four transient experiments with fuel that is not preirradiated and six capsules that will be inserted into the ETR for irradiation before transient tests. The fuel for all of these experiments will be nominally $(U_{0.8},Pu_{0.2})O_{1.98}$.

We continued our analysis of neutron filters and Na and NaK coolants for TREAT capsules by calculating transient heat transfer for a 155 Mwsec transient with a 200 msec initial reactor period. The shape

of the transient was assumed to coincide with that of TREAT transient[20] 554. The power density of an average specimen was taken as 9.3×10^{-5} w/cm^3 per watt of TREAT power from our earlier calculations for an unfiltered capsule, and the power profile for a cadmium-filtered capsule was normalized to the same power density. We had previously chosen Cd as being more effective than B or Eu.

We calculated temperatures for transient heat transfer with the TOSS program,[21] using physical properties appropriate for fuel of 81% smear density. The results are partially summarized in Table 1.5. For this particular case, the substitution of NaK for Na has a negligible effect on the fuel temperatures but causes the peak temperatures in the cladding to increase some 100°C. This would be undesirable in our study of failure thresholds and mechanisms, so we intend to use Na in all of our TREAT capsules. The flatter power profile associated with

[20]J. E. Hanson, J. H. Field, and S. A. Rabin, Experimental Studies of Transient Effects in Fast Reactor Fuels, Series II — Mixed Oxide (PuO_2-UO_2) Irradiations, GEAP-4805 (June 1965), pp. 3–4.

[21]D. Bagwell, TOSS, An IBM-7090 Code for Computing Transient or Steady-State Temperature Distributions, K-1494 (December 1961).

Table 1.5. Some Results from Calculations of Transient Heat Transfer for TREAT Capsule TR-1, Subjected to Transient 554

Case	Peak Temperatures, °C			
	Fuel Center	Fuel Average	Inner Cladding	Cladding Average
No filter-NaK	2850	2380	845	805
No filter-Na	2850	2385	725	695
0.005-in. Cd filter[a] Na	3015	2450	725	685

[a]Normalized to an average-specimen power density of 9.3×10^{-5} w cm^{-3} w^{-1} (equivalent to the no-filter cases).

a 5-mil-thick cadmium filter is predicted to have negligible effects on the cladding temperature. Although in the radial temperature profiles fuel temperatures are somewhat higher and less peaking is predicted, we do not judge the improvements to be sufficient to warrant the use of neutron filters with the initial capsules. They may be required in later experiments with highly enriched fuel that has been preirradiated in the EBR-II reactor.

The capsule and fuel pins have been designed for the first four capsules, and the drawings are being reviewed. We have begun preparing the hazards analysis for these experiments.

We have constructed an induction furnace to be used for experiments on thermal shock with sol-gel UO_2 microspheres. These experiments will initially investigate the mechanical stability of UO_2 microspheres subjected to severe temperature transients.

Fast Flux Irradiation Tests (A. R. Olsen, C. M. Cox)

The Series I encapsulated tests of Sphere-Pac sol-gel $(U,Pu)O_2$ fuels are scheduled to be inserted into the EBR-II at the start of cycle 32. The designs for fuel pin and capsule were shown in Fig. 1.2. All material for cladding and capsule components is on hand and has been inspected. Two of the fuel rods will have type 304 stainless steel cladding, and the remaining three will have type 316 stainless steel tubing, which we obtained from PNL. The 316 stainless steel tubing was the cleanest we have inspected. Only one ultrasonically detectable flaw in excess of our 0.001-in.-deep 0.030-in.-long reference notch was detected in the 35 ft we received.

We plan to include the five Sphere-Pac fuel rods in a reconstituted 19-rod subassembly for insertion into an EBR-II row 4 position. The hazards analysis for these tests is essentially complete, including revisions based on the new rates of heat generation for the row 4 positions with the EBR-II operating at 50 Mw.

The initial hazards analysis is based on the design parameters with an anticipated average burnup level of 5% FIMA in the position of highest heat rating in a row 4 subassembly. However, we have begun to make

preliminary physics calculations for a more detailed operational prediction. Using the GAM-II code,[22] we have prepared 18-group spectrum-averaged sets of EBR-II cross sections in format suitable for the ANISN neutron transport code.[23] A preliminary S_4 ANISN calculation of the EBR-II core, using P_1 scattering, predicted heat generation rates within 10% of the reported EBR-II rates. All of these calculations will be refined and compared with the empirical rates of fission-heat generation reported for the EBR-II. A set of 1-group spectrum-averaged cross sections was also prepared and used with the RIBD Program to calculate the content of fission products and rates of heat generation after irradiation for the hazards analysis.

Irradiation Test Calculations (C. M. Cox, F. J. Homan)

We have completed a draft of a report describing the PRØFIL code for computing steady-state radial temperature distributions in $(U,Pu)O_2$ fuel pins. This program includes an empirical model of fuel densification. We have begun work on an expanded version that accounts for thermal expansion and swelling due to fission products.

---

[22] G. D. Joanou and J. S. Dudek, GAM-II, A B_3 Code for the Calculation of Fast-Neutron Spectra and Associated Multigroup Constants, GA-4265 (September 1963).

[23] W. W. Engle, Jr., A User's Manual for ANISN, K-1963 (March 1967).

2. NITRIDE FUELS DEVELOPMENT

W. O. Harms J. L. Scott

The goals of this program are to investigate the properties and behavior of mixed uranium-plutonium nitrides and carbonitrides as LMFBR fuels and, through extension of irradiation conditions, to establish the ultimate limitations of UN as a space-nuclear fuel.

Our goal is to develop LMFBR fuel elements that can operate at linear heat ratings up to three times the limit now set for mixed oxides. It is almost certain that the economic benefits of these higher heat ratings will be profound.

The major problems associated with the use of mixed nitrides or carbonitrides as LMFBR fuels are (1) economical synthesis and fabrication, (2) compatibility with candidate cladding alloys, including the effects of fuel burnup, (3) model studies on carbide and nitride pins for LMFBR, and (4) irradiation behavior.

In dealing with these problems, we place high priority on developing a quantitative description of the thermodynamic properties and pertinent reaction kinetics in the materials systems of interest. This information is applied to the development of fabrication schemes and to the solution of compatibility problems. Promising combinations of fuel and cladding are irradiated under simulated service conditions.

Our work in synthesis, fabrication, and characterization of nitride fuels involves uranium nitride and carbonitride work for space-nuclear and fundamental studies and preparative work for mixed uranium-plutonium nitride and carbonitrides. For clarity, these two areas are described separately, though our experience with one guides our strategy on the other. Work on UN for space applications is described in classified monthly reports.

Synthesis, Fabrication, and Characterization of Nitride Fuels

Synthesis and Fabrication of UN (R. A. Potter)

We continued with the synthesis and fabrication of UN for distribution to groups concerned with irradiation test behavior and measurements of physical properties of these materials. Several problems were encountered.

Since our synthesis scheme is based on a batch process, we are confronted with slight variations from one powder batch to the next. These variations can be traced to a temperature gradient in the synthesis furnace that influences the final nitrogen content and particle-size distribution of the powder. Consequently, variations in the size of the charge and the physical configuration and location of the starting material (uranium metal) result in variations in the powder batches. Usually we can compensate for these differences during fabrication and sintering by adjusting pressing pressures, powder lubricant additions, and sintering schedules. The morphology of our UN powders is such that pressing faults, such as laminations, are inherent in samples formed by uniaxial cold pressing unless a powder lubricant such as camphor is employed during pressing and then made to sublimate by heating. Recently, however, we have produced batches of powders with extremely fine particle sizes. It is quite difficult to eject the lubricant from the samples cold pressed from these powders. Heating sufficient to drive out the tightly held lubricant can destroy the specimen if applied too rapidly. This happened during initial heat treating of a UN disk 3/4 in. in diameter × 1/4 in. in height containing 1% camphor. A photomacrograph of this specimen is shown in Fig. 2.1.

During our subsequent efforts to utilize the powder for a set of solid cylindrical test specimens, we tried cold pressing without the aid of a lubricant. Although the specimens were successfully formed and sintered to about 95% of theoretical density and appeared sound, during a grinding operation for dimensional sizing the ends flaked off because of built-in pressing faults. Ultimately, we were able to prepare the test specimens by reducing the lubricant from 1 to 1/2% and by

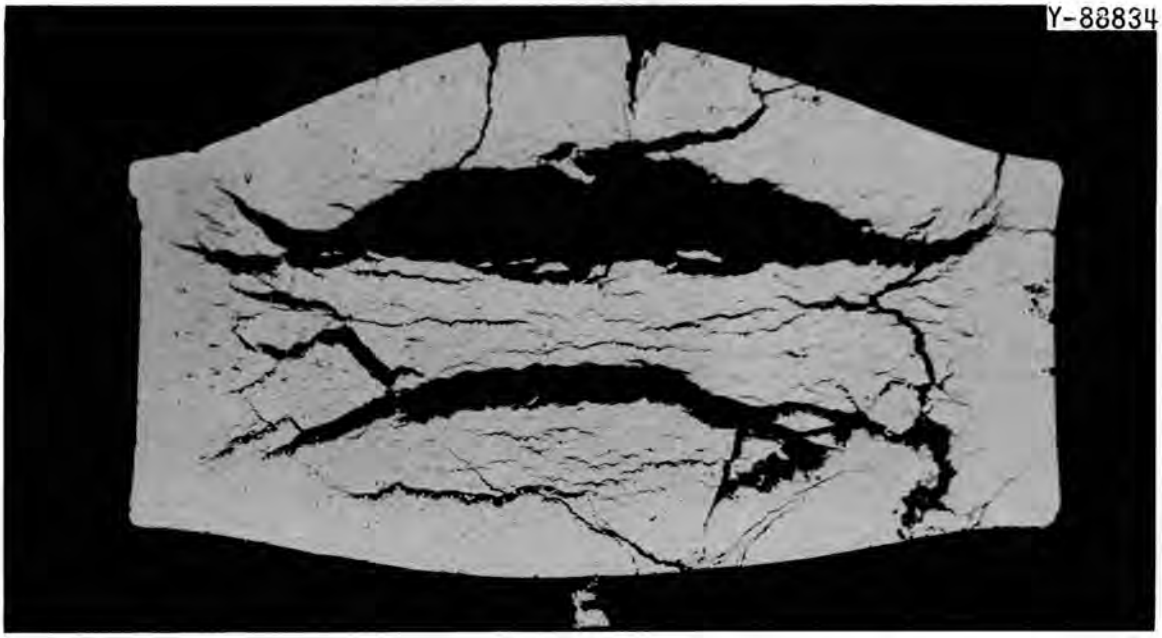

Fig. 2.1. Photomacrograph of UN Specimen Destroyed During Expulsion of 1% Camphor Lubricant. Specimen subsequently sintered at 2300°C in 1 atm N_2.

carefully controlling the initial heat treatment. Such problems emphasize the need for careful powder characterization, which will require an expansion of our facility.

In view of the foregoing and because of the increasing interest in nitride fuels, we have installed a second synthesis rig in which we can prepare powders for characterization. The new apparatus is equipped for atmospheres of N_2, H_2, Ar, and vacuum. The charge capacity will be about 1 kg.

Characterization of UN (V. J. Tennery)

Effort has been directed toward characterizing the UN powder produced by the hydride-dehydride-nitride process by determining the phases present in concentrations of about 3% or greater and the shape and size of the nitride powder particles. The procedure being developed for phase identification involves x-ray diffractometry and consists of preparing a dispersion of the nitride powder in a solution of 10% parlodian and 90% amyl acetate under an inert atmosphere in a glove

box and then spreading the dispersion onto a glass slide suitable for use in the x-ray diffractometer. Experiments conducted to date indicate that the nitride powder is adequately protected from oxidation to permit handling the nitride-parlodian film in air and that the nitride powders contain about 20 to 30 wt % of the higher nitrides $UN_{1.5+x}$, where x varies from 0 to about 0.5 depending upon certain processing conditions. The major phase is UN. The concentrations of the higher nitride phases and their relation to the final nitride reduction temperature used in producing the powder are being determined. The asymmetry of the (220) x-ray line group, and possibly others of the higher nitride, is being examined as a possible simple indicator of the general distribution of the higher nitrides in the nitride powder. These measurements are relatively simple and require little time when diffractometer methods are used.

A technique has been developed for suspending the nitride powder particles in a parlodian film that protects the particles from oxidation well enough that the film can be placed on grids and examined in an electron microscope. The particles as produced are agglomerated. Note in the typical particles shown in Fig. 2.2 that many of the ultimate particles are smaller than 1 μm in diameter. We do not know if the apparent roughness of the surface is an artifact due to agglomeration. We are developing a dispersion technique to disrupt the agglomerates so that the shapes and sizes of the ultimate particles of the nitride powders can be determined routinely. The correlation of the results with the processing parameters used in producing the nitride powders and the pressing and sintering characteristics of these powders should permit a rational approach to the manufacture and production of the advanced fuel, UN.

The gas-analysis system developed for the Interim Plutonium Facility was attached to our conventional UN glove boxes to determine contamination levels in this facility. Results showed, by volume, 100 ppm O_2 and 50 ppm moisture. Since these levels are considerably higher than those we have achieved in the plutonium laboratory, an inert-gas purifier has been ordered and will be installed on the glove

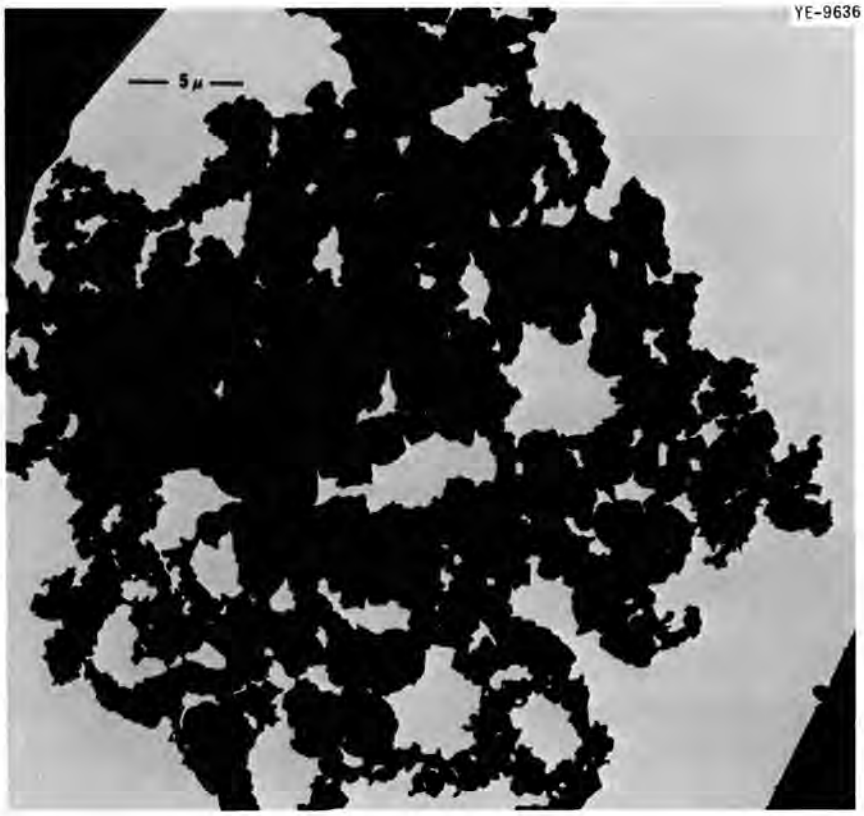

Fig. 2.2. Uranium Nitride Powder Cast in a Parlodian Film.

boxes in which the nitrides are handled in powder form. The strong affinity of the nitride for O_2 dictates the use of an essentially oxygen-free atmosphere in all boxes. We anticipate that the purifier will permit argon atmospheres with 10 ppm O_2 and 5 ppm moisture, by volume, to be maintained routinely. In addition, components for a gas-analysis system have been ordered and will be installed to permit the continuous analysis of the glove box atmospheres for O_2 and moisture.

Synthesis, Fabrication, and Characterization of Mixed Nitrides
(E. S. Bomar, Ji Young Chang)

The high-temperature furnace, built by the Richard D. Brew Company, was delivered and installed in the Interim Plutonium Facility during this period, and its performance was checked against purchase specifications. The furnace and vacuum system met each of the requirements for temperature, rate of pumping, and ultimate vacuum. This equipment will

let us experiment at temperatures to 3000°C in vacuum or to 2200°C in Ar and to 2400°C in N_2, each at 1 atm of pressure. The glove box to enclose the furnace for work with Pu is being built, but the furnace will be used in the interim for work with UN.

Work on the hot press in the Interim Plutonium Facility has progressed to the point of cold check-out. The first sample of UN was compacted in the hot press to a density of 99% of theoretical at 1400°C and 3 tsi for 1 hr. The press was also used to prepare high-density specimens of beryllium boride.

Several problems have been encountered in the facility for synthesizing mixed nitrides. Alterations in the seal where the vacuum lines from the tube furnace penetrate their glove box reduced the leakage of air into the box. We still find, however, an undesirably high impurity content, especially moisture, in the argon atmosphere of the box. While locating the source of the impurities, we have started the nitride synthesis. A mixture of Ar–4 vol % H_2 was used in the first hydriding experiment, but the rate of conversion of uranium metal to uranium hydride was too slow to be practical. Obviously, use of H_2 diluted with Ar is of interest for glove-box work since it eliminates any possibility of fire. We next passed undiluted H_2 into the tube furnace, which was vented to the box atmosphere, and adjusted the flow of Ar through the box to dilute the H_2 to at least 4 vol %. We converted the resulting hydride to metallic uranium powder by heating under vacuum at 400°C and then converted that to the nitride by slowly introducing N_2 at a pressure of 2 to 4 in. Hg. We raised the temperature in steps to 800°C and the nitrogen pressure to 1 atm. The resulting nitride was reduced to a nominal composition of UN by heating to 1300°C under vacuum.

Engineering drawings of the glove box for the equipment for measuring vapor pressure were completed, bids were requested for its construction, and a contract was let.

The hot-stage microscope was used to observe the behavior of three $^{238}PuO_2$ microspheres in individual heat treatments at 1200°C in an argon atmosphere. The particles were photographed at intervals as the

temperature was raised. The photographic film showed no dimensional change for the particles.

A piping system was designed for continuous sampling of the atmosphere from six locations. Any one of these samples can in turn be monitored quantitatively for O_2 and moisture and qualitatively for other impurities such as N_2. The console that contains the instruments for these analyses was described previously.[1] Experience to date shows that the oxygen content in the box atmospheres can be reduced to less than 10 ppm and moisture to less than 20 ppm at argon flow rates that change the atmosphere in the box five times per hour. Our argon supply contains, on the average, 5 ppm O_2 and 10 ppm moisture by volume.

Studies on Synthesis, Fabrication, and Thermodynamic Properties of Carbonitride Fuels

Manufacture of UC, UN, and U(C,N) from UO_2 (T. B. Lindemer, J. M. Leitnaker)

The kinetics of the conversion of sol-gel UO_2 to uranium carbides, nitrides, and carbonitrides is being studied to determine the rate-controlling mechanisms of the conversion processes. This information is fundamental to the design of the fuel cycle that will be used to manufacture the desired reactor fuels of this type.

Kinetics of the UC_2-N_2 Reaction. – We are studying the UC_2-N_2 reaction. (The UC_2 represents nominal uranium dicarbide; it is always substoichiometric with respect to C). The time-dependent conversion of 500-μm UC_2 microspheres to U(C,N) was fitted to a model based on rate control at the UC_2-U(C,N) interface.[2] This fit is demonstrated in Fig. 2.3; the metallographic determination of r (the diameter of the unreacted UC_2 core) and r_0 (the original diameter of the microsphere)

---

[1] J.D.L. Harrison, Fuels and Materials Development Program Quart. Progr. Rept. June 30, 1968, ORNL-4330, pp. 40–41.

[2] T. B. Lindemer, Fuels and Materials Development Program Quart. Progr. Rept. June 30, 1968, ORNL-4330, pp. 32–39.

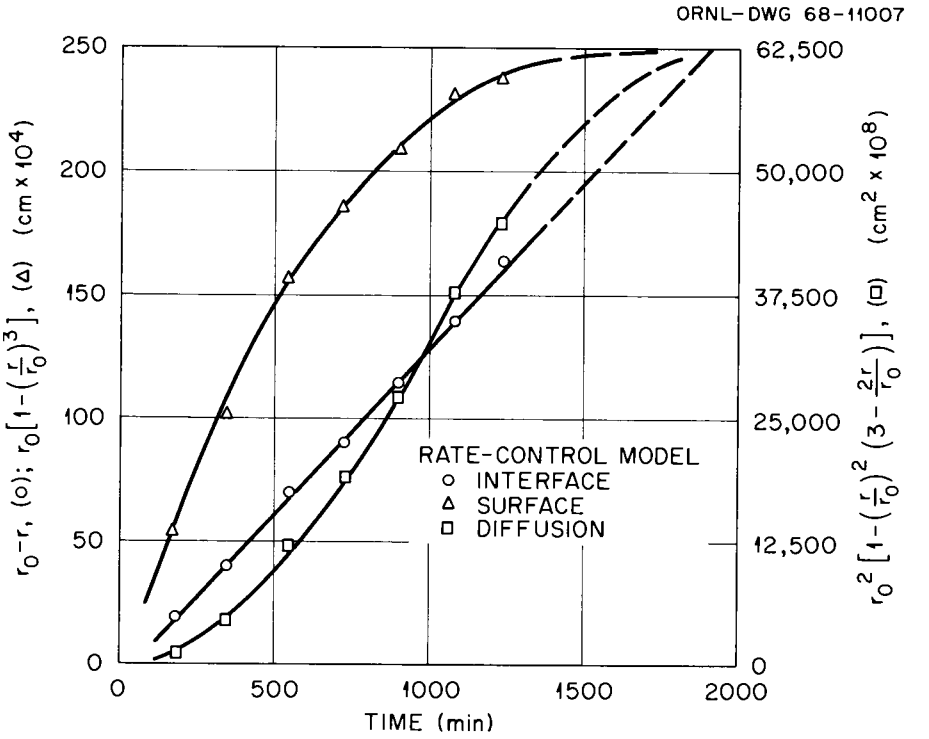

Fig. 2.3. The Time-Dependent Plots of the Functions for Surface, Interface, and Diffusion Control for the Reaction at 1700°C of UC_2 De-Aged for 20 hr in Ar with N_2 at a Pressure of 380 torr.

on each of 25 particles for a given reaction time was used to calculate the average values plotted in Fig. 2.3. The function will vary linearly with time for one model, thus permitting the determination of the general rate-controlling process. It can be seen that control of the reaction is occurring at the UC_2-U(C,N) interface, since the functions for the surface and diffusion control are definitely nonlinear. The slope of the linear plot is k_I, the proportionality constant for the interface-controlled reaction.

Representative photomicrographs demonstrating the progress of the reaction are shown in Fig. 2.4(a) through (h). These specimens were "de-aged" (i.e., the aging effect was counteracted by heating) in Ar at 380 torr for 30 min in a fluidized bed at 1700°C, then reacted in N_2 at the same temperature and pressure for the indicated times. Each figure shows an equatorial or near-equatorial cross section of the microsphere; the depth of the U(C,N) layer (the $r_0 - r$ of the interface-control model) is within two standard deviations of the average value determined from

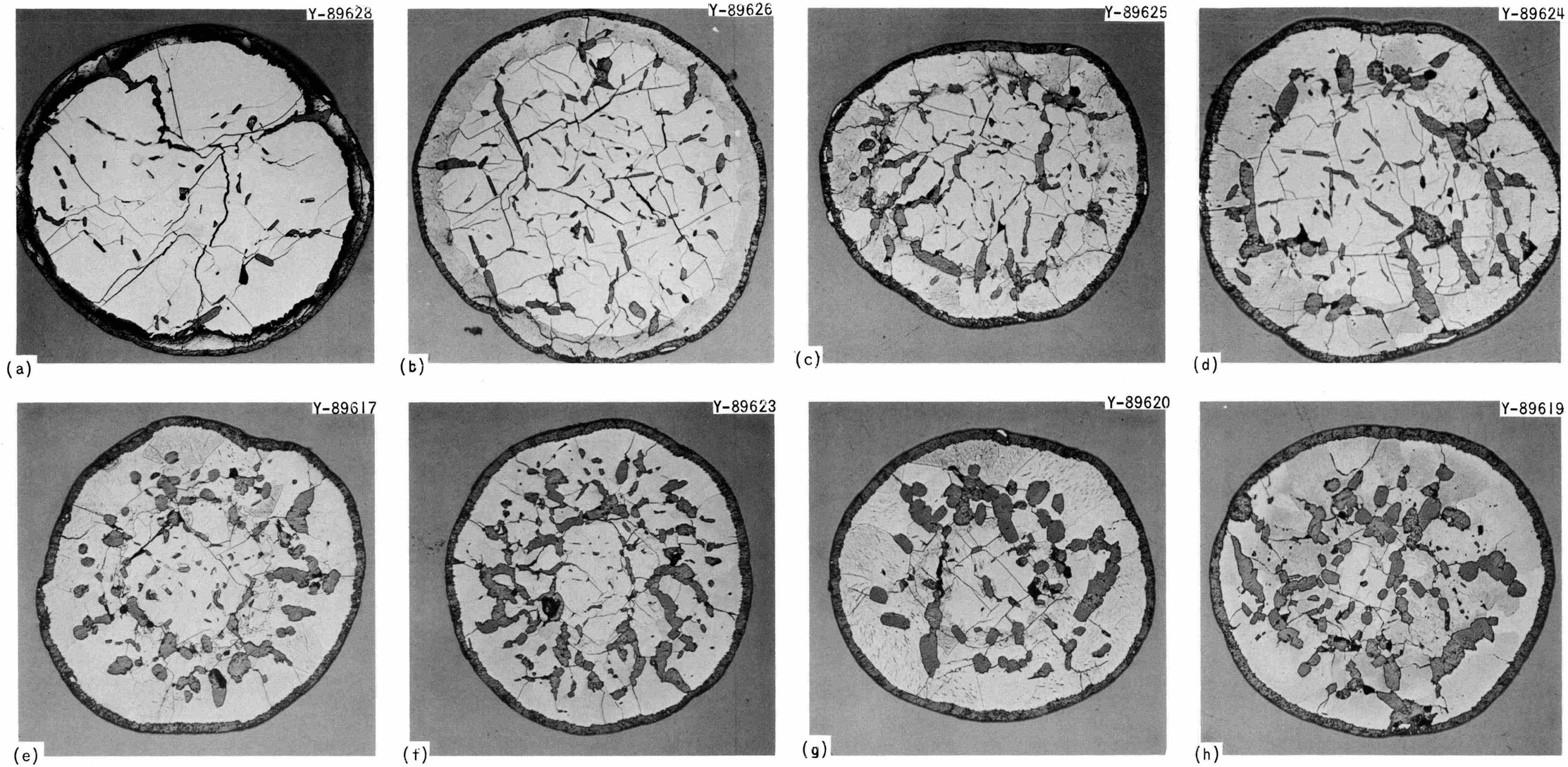

Fig. 2.4. Near-Equatorial Cross Sections of UC_2 Microspheres Reacted with N_2 at 1700°C for the Indicated Times. 150×. (a) 180 min; (b) 363 min; (c) 542 min; (d) 720 min; (e) 900 min; (f) 1080 min; (g) 1245 min; (h) 1440 min. The depth of the intermediate U(C,N) layer varies linearly with time. The outer layer is C, the core is UC_2. Etchant: $HAc-HNO_3-H_2O$.

the 25 microspheres measured for each indicated time. The features of these microstructures are generally observed at all reaction temperatures (1500 to 1700°C) and are important to several of the discussions that follow.

The interface-controlled reaction has been observed to obey the Arrhenius relation, $K_I = K_{I_0} \exp(-Q/RT)$. Table 2.1 lists the proportionality constant, k_I, obtained from each experiment, and also lists the other pertinent experimental data. Note that the effect on k_I of the various pretreatment times used to de-age the UC_2 in Ar has been ignored, since we do not believe the differences to be significant. The values of $\ln k_I$ were fitted against the reciprocal absolute temperature by least-squares methods, with all values of $\ln k_I$ weighted equally. The Arrhenius relation was thus

$$k_I = 85.9 \exp(-77{,}700/RT) \text{ cm/sec} . \qquad (2.1)$$

The standard deviation of the activation energy was 3660 cal/mole, and that of $\ln k_{I_0}$ was 0.993; thus k_{I_0} (plus one standard deviation) = 232 and k_{I_0} (minus one standard deviation) = 31.8. Equation (2.1) and the relation for an interface-controlled reaction, $r_0 - r = k_I t$, were used

Table 2.1. Experimental Parameters for the Interface-Controlled UC_2-N_2 Reaction at a Nitrogen Pressure of 380 torr

Specimen Number	Temperature (°C)	De-Aging Time in Ar (hr)	Proportionality Constant, k_I (cm/sec)	Standard Deviation (cm/sec)	Number of Points Used to Determine Standard Deviation
			$\times 10^{-8}$	$\times 10^{-8}$	
A5164-42	1500	0.50	2.293	0.093	8
A5164-26	1500	0.50	2.586	0.219	4
A5164-63	1500	26.0	2.064	0.160	5
A5163-84	1600	0.50	7.793	0.287	8
A5163-103	1600	24.0[a]	5.969	0.182	8
A5163-129	1600	76.0[a]	7.860	0.159	8
A5164-12	1700	0.50	20.98	0.770	8
A5164-54	1700	20.0	22.60	0.390	7

[a]De-aged in a vacuum of 10^{-5} torr.

to calculate the times necessary for complete conversion of UC_2 microspheres having a radius of 250 μm; this time was 307 hr at 1500°C, 95 hr at 1600°C, and 33 hr at 1700°C.

Another important result is shown in Fig. 2.5; this particle is from the same sample as that shown in Fig. 2.4(a). About 1% of the microspheres in the original UC_2 material contain an interconnecting network of free C. These particles react very rapidly: the particle in Fig. 2.5 is about 98% U(C,N) and was converted in about one-tenth of the time required to convert the particles shown in Fig. 2.4(a) through (h). They were converted rapidly because the carbon network has the twofold function of providing a short-circuit diffusion path for the N_2 and dividing the UC_2 into small subparticles that can be completely converted in a shorter time. This observation substantiates the assumed mode of reaction in the conversion of UO_2-carbon sol-gel shards to U(C,N) by reaction with N_2.

Fig. 2.5. A Microsphere from the Same Sample as that Shown in Fig. 2.4(a). The particle has been completely converted to U(C,N). 150×. Etchant: HAc-HNO_3-H_2O.

We also continued to study the effect of H_2 on this reaction; from this study we inferred additional information about the distribution of C. Our objective here was the removal of C from the completely converted

particle. Particles of UC_2 were converted in the fluidized bed to U(C,N) at 1700°C at a nitrogen pressure of 380 torr and then reacted in a N_2–4.33% H_2 mixture at the same pressure and temperature. Within 2 or 3 min, more than 80% of the volume of C originally in the particle was removed, as can be seen from a comparison of Figs. 2.4(h) and 2.6. Hydrogen stripping is apparently a very efficient method for removing the C precipitated by this reaction and may be just as useful for removing excess free C from the U(C,N) produced by the reaction of N_2 with the UO_2-C sol-gel material.

Fig. 2.6. A U(C,N) Microsphere that Has Been Reacted for 2 min in N_2–4.33% H_2 at 1700°C to Remove 80% of the C Produced by the UC_2-N_2 Reaction. 150×. Etchant: HAc-HNO_3-H_2O.

These results also indicate that the C that deposited in the particles shown in Figs. 2.4(a) through (h) and 2.6 becomes interconnected. This C thus apparently provides a short-circuit path from the particle surface to the vicinity of the UC_2-U(C,N) interface. Since the reaction was controlled in the vicinity of this interface, the diffusion of N_2 through the C is not the rate-limiting step in the conversion process. Because of this short-circuiting behavior, however, all of the other

rate-controlling steps that are postulated for this reaction occur in the vicinity of the interface:

1. $N_2 \rightarrow 2\ [N]_{U(C,N)}$ (Ref. 3) at U(C,N)-C interface,
2. [N] diffusion to UC_2-U(C,N) interface,
3. $y\ [N] \rightarrow UC_2 \rightarrow U(C_{1-y},N_y) \rightarrow (1+y)\ [C]_{U(C,N)}$ at UC_2-U(C,N) interface,
4. $[C]_{U(C,N)}$ diffusion to U(C,N)-C interface,
5. $[C]_{U(C,N)} \rightarrow C_{(free)}$.

Thus it is not possible to determine the rate-limiting mechanism from these experiments alone. On the other hand, we reported[4] that the reaction of carbon-free UC_2 did not exhibit these internal precipitates; instead, all the C precipitated on the surface of the sphere. We have ordered material of this type for a new series of experiments that will help us to better differentiate the rate-controlling mechanisms.

We also determined the carbon distribution in the U(C,N) and UC_2 phases typified by those in Fig. 2.4(a) through (h) by quantitative metallography on ten particles at each reaction time for a series (specimen set A5163-84) that was reacted at 1600°C at a nitrogen pressure of 380 torr. The results are given in Table 2.2 and Fig. 2.7 in terms of the volume percent of C in each phase. The statistical analysis follows that of Hilliard and Cahn.[5] The carbon content can be seen to increase in both phases as the reaction progresses. This is especially interesting in the case of the UC_2 phase; the C in solid solution produced by the reaction at the U(C,N)-UC_2 interface apparently establishes a carbon gradient in the UC_2 that leads to diffusion of C from the interface to the free-carbon sites within the UC_2.

---

[3] Brackets indicate a species in solid solution.

[4] T. B. Lindemer, Fuels and Materials Development Program Quart. Progr. Rept. June 30, 1968, ORNL-4330, pp. 32–39.

[5] J. E. Hilliard and J. W. Cahn, Trans. Met. Soc. AIME 221, 344–352 (1961).

Table 2.2. Free Carbon in UC_2 and U(C,N) Phases as Functions of Extent of Reaction of UC_2 in N_2 at 1600°C

Reaction		U(C,N) Phase		UC_2 Phase	
Extent (%)	Time (min)	Free Carbon Content (vol %)	Standard Deviation (vol %)	Free Carbon Content (vol %)	Standard Deviation (vol %)
0	0			1.0[a]	
28.8	485	7.45	2.2	5.1	1.0
45.4	966	15.9	2.5	12.5	1.8
64.1	1440	19.4	2.3	16.3	2.6
74.9	1920	22.9	2.3	20.2	3.1
83.8	2400	24.4	2.0	22.1	3.5
93.5	2880	27.5	2.0	21.3	3.3
96.1	3313	28.4	2.0	21.2	3.7

[a]Based on chemical analysis and verified qualitatively by metallography.

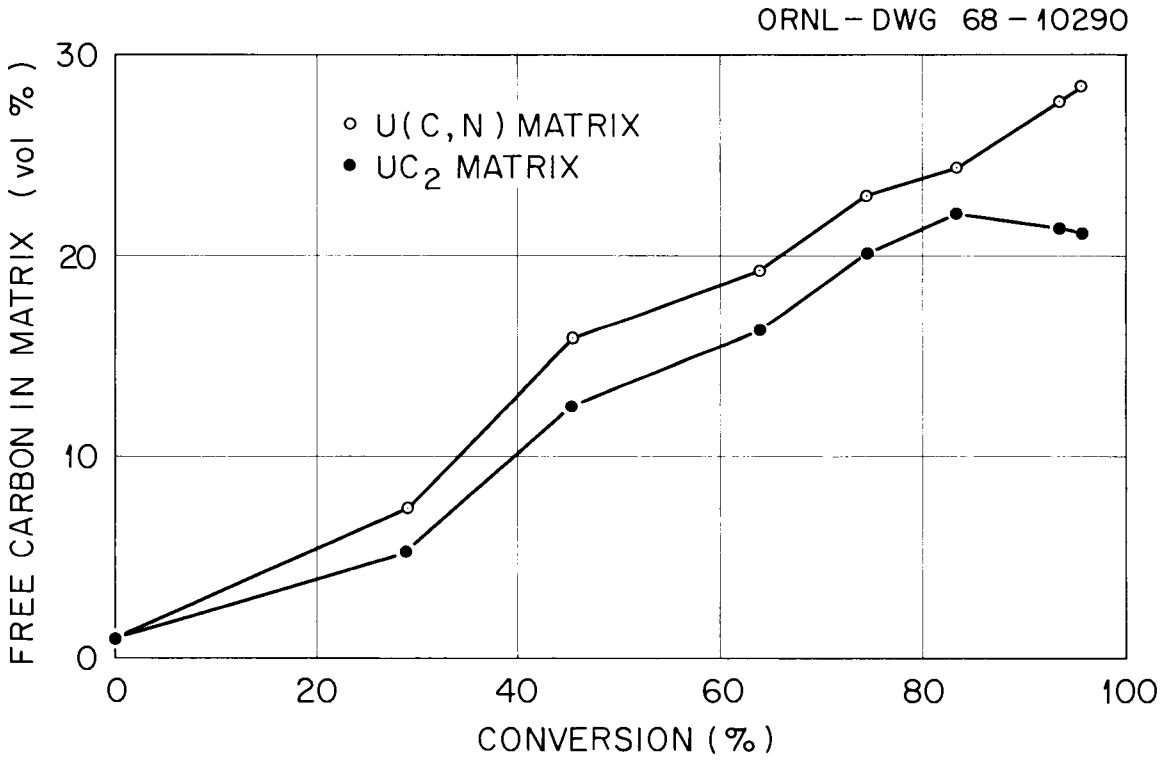

Fig. 2.7. The Volume Percent Free Carbon in the U(C,N) and UC_2 Phases as a Function of the Percent Reaction of UC_2 Microspheres in N_2 at 1600°C.

Effect of Nitrogen Exposure on UC_2 Lattice Parameter. — Another study involved the change of the lattice parameter of UC_2 during the initial stages of the reaction, since we noticed that metallographically prepared, as-received UC_2 microspheres responded differently to etching than did UC_2 that was exposed to N_2. We ran an experiment at 1600°C on UC_2 that was first de-aged 0.5 hr in Ar at 380 torr and then reacted in N_2 at the same temperature and pressure. We sampled the UC_2 after every hour of exposure to N_2 up to a total of 6 hr; this time is just sufficient for a measurable U(C,N) layer to form on the surface of the microsphere. We then analyzed the six samples to determine the UC_2 lattice parameter as shown in Table 2.3. These data demonstrate that the a_0 lattice parameter definitely decreases with longer exposure to N_2 and suggest that this effect is caused by the solution of N in UC_2. Limited additional work is planned to determine whether UC_2 is actually dissolving N.

Table 2.3. Effect of Nitrogen Exposure on UC_2 Lattice Parameter at 1600°C and a Nitrogen Pressure of 380 Torr[a]

Exposure Time (min)	Lattice Parameter a_0, A		Lattice Parameter c_0, A	
	Value	Standard Deviation	Value	Standard Deviation
		$\times 10^{-5}$		$\times 10^{-5}$
0[b]	3.519	100	5.979	200
67	3.51705	45	5.98239	227
123	3.51734	60	5.97636	312
184	3.51676	54	5.97474	315
255	3.51550	105	5.97185	485
300	3.51411	77	5.98006	344
361	3.51317	54	5.97360	291

[a]Run A5164-24.

[b]Lattice parameter from Edmund K. Storms, The Refractory Carbides, p. 187, Academic Press, New York, 1967.

Studies on Compatibility of Mixed-Nitride and Carbonitride Fuels with LMFBR Cladding Alloys

Compatibility of Vanadium Alloys with Nitride Fuels (K. E. Spear, J.D.L. Harrison[6])

The compatibility of the vanadium alloy V–15% Cr–5% Ti with single-phase UN and UN containing second-phase UO_2 has been investigated by means of isothermal sandwich experiments at 1000°C for 100 to 500 hr. Some results of these relatively short-term tests are presented in this report.

Experimental. – The composition of the 0.020-in.-thick specimens of the vanadium alloy used in this investigation is given below:

Element	Content, wt %
Cr	15.19
Ti	5.0
C	0.0253
O	0.0770
N	0.0107
H	0.0033

These specimens, supplied by the Metallurgy Division of the Argonne National Laboratory, had been annealed at 900°C for 1 hr at several stages during the rolling process and after the final pass. Circular disks, 0.25 in. in diameter, were then punched out, and the surfaces were ground to an 8-μin. root-mean-square (RMS) finish on both sides. One side was then metallographically polished with MgO powder and water.

Sintered UN pellets, 0.25 in. in diameter, of two different compositions and with bulk densities between 90 and 95% of theoretical, were cut into 0.1-in.-thick slices and polished on each side. The compositions of the UN pellets are given in Table 2.4. Note that composition 1 was substantially purer than composition 2 with respect to C and O. Only the mononitride phase was visible metallographically in composition 1, while oxide was present as 2- to 5-μm-diam particles in composition 2. No metallic phases were visible.

---

[6] On loan from Atomic Energy Research Establishment, Harwell, England.

Table 2.4. Composition of UN Specimens Used in Vanadium Alloy Compatibility Studies

Element	Content, wt %	
	Composition 1	Composition 2
U	94.55	94.53
N	5.15	5.12
C	0.015	0.048
O	0.012	0.22

Both the UN and vanadium-alloy specimens were degreased in acetone before being assembled as alternate layers, usually five, in the stainless steel capsules shown in Fig. 2.8.

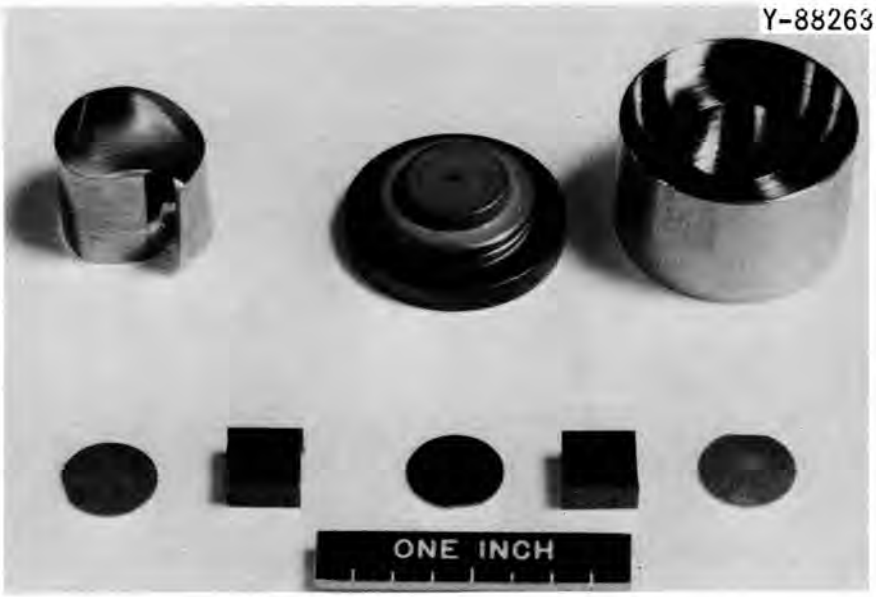

Fig. 2.8. Compatibility Capsule Components. Disks and foil are V–15% Cr–5% Ti, squares are UN, the bellows are type 321 stainless steel, and the capsule body is type 316 stainless steel. The polished faces appear black.

In order to limit the possibility of unwanted interactions through the gas phase, each capsule contained UN of only one composition and the vanadium alloy. To limit interaction between the sandwiches and the capsule bodies, each of which was made of types 316 and 321 stainless

steel, each sandwich was surrounded by a 0.005-in. annular wrap of the same alloy used in the sandwich.

Contact was maintained between the layers of the sandwiches in each capsule by an axial compressive load of about 20 lb. This load was sufficient to deform the bellows so that the load was properly transferred to the contents of the capsule. Several capsules were stacked together with the use of spacers, as shown in Fig. 2.9, and were placed inside a loosely fitting Inconel tube, as shown in Fig. 2.10. This tube served the dual purpose of enclosing the capsules in an atmosphere of pure, flowing Ar and of acting as the tension member that applied the compressive load through an internal spring and push rods to the stack of capsules.

Two capsules of each combination of metal and nitride were assembled and welded in a vacuum of 5×10^{-5} torr, as measured in the welding chamber. One capsule was heated for 100 hr and the other for 500 hr at 1000°C.

After the heating period, the capsules were slit with an abrasive wheel, vacuum impregnated with epoxy resin, sectioned transversely, and polished and etched. The surfaces were then examined metallographically and with an electron microprobe analyzer. Microhardness indentations at a 50-g load were made on the layers of vanadium alloy in some sandwiches to see if this technique yielded any indication of changes in the character of the layer that could not be detected by the other two methods.

Results. — Reaction with both UN compositions was observed at the UN-vanadium alloy interface after 100 and 500 hr. While all of the results have not been critically analyzed, the reactions appear to be independent of the second-phase oxide present in UN of composition 2. Accordingly, only the results of the couples involving UN of composition 1 are presented and discussed below.

Metallographic examination. Reaction at the interface was observed after 100 and 500 hr. As shown in Fig. 2.11, this reaction took the form of a metallic layer next to the nitride that was partially separated from the vanadium alloy by a broken layer of a blue-purple phase. The

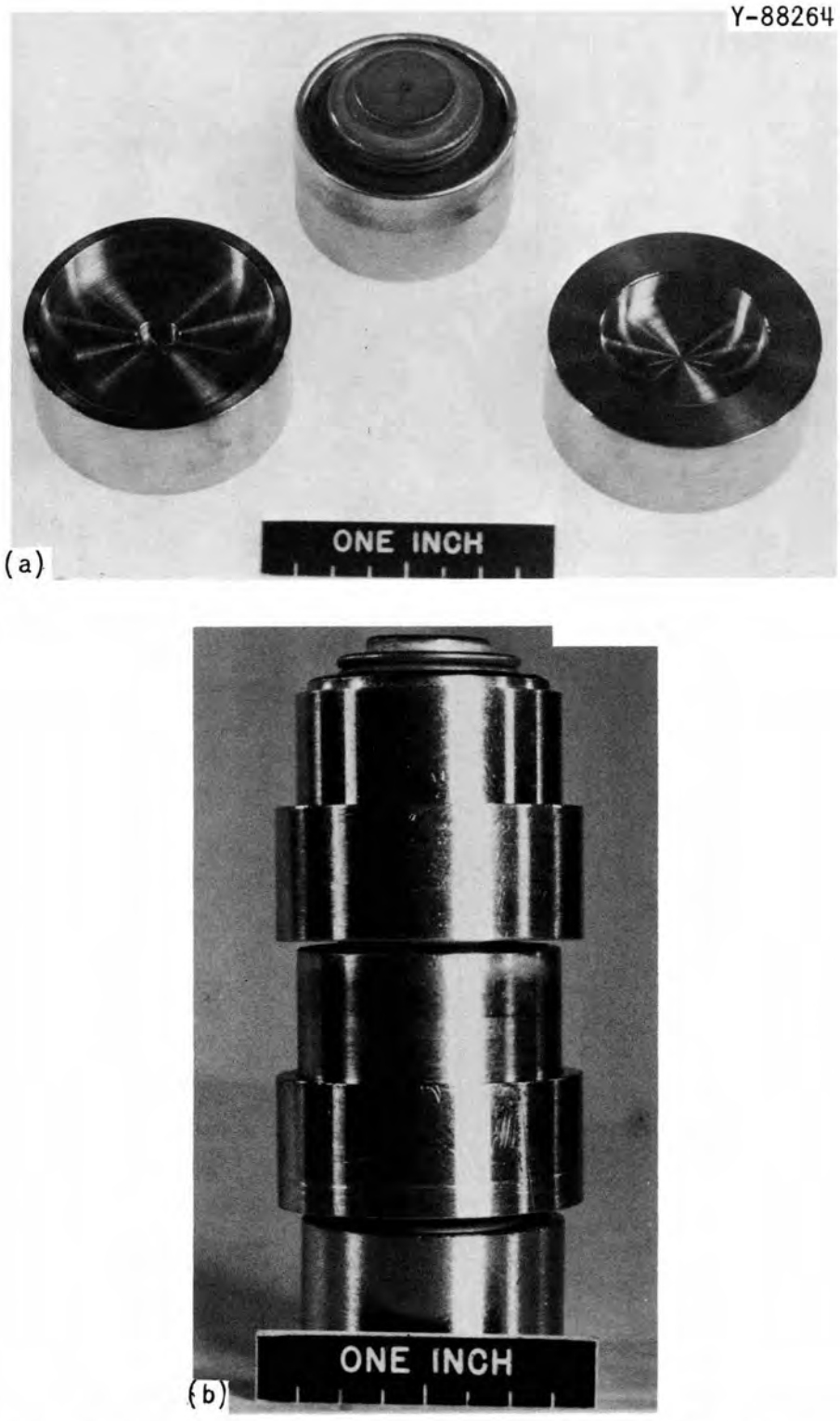

Fig. 2.9. Method for Stacking Several Compatibility Capsules. (a) Top and bottom view of spacer and a loaded capsule. (b) The stacking of three capsules and two spacers.

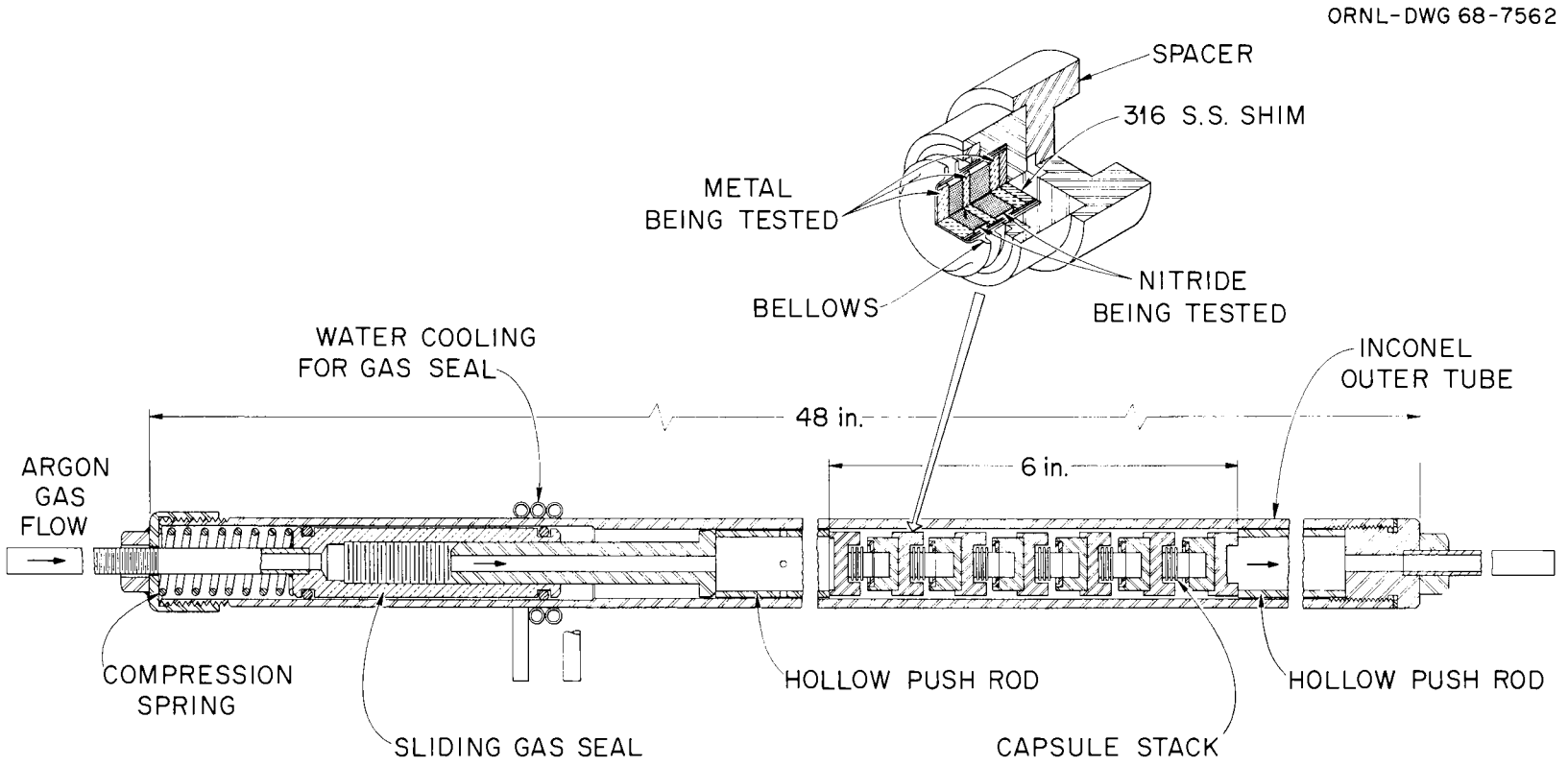

Fig. 2.10. Compatibility Capsule Assembly.

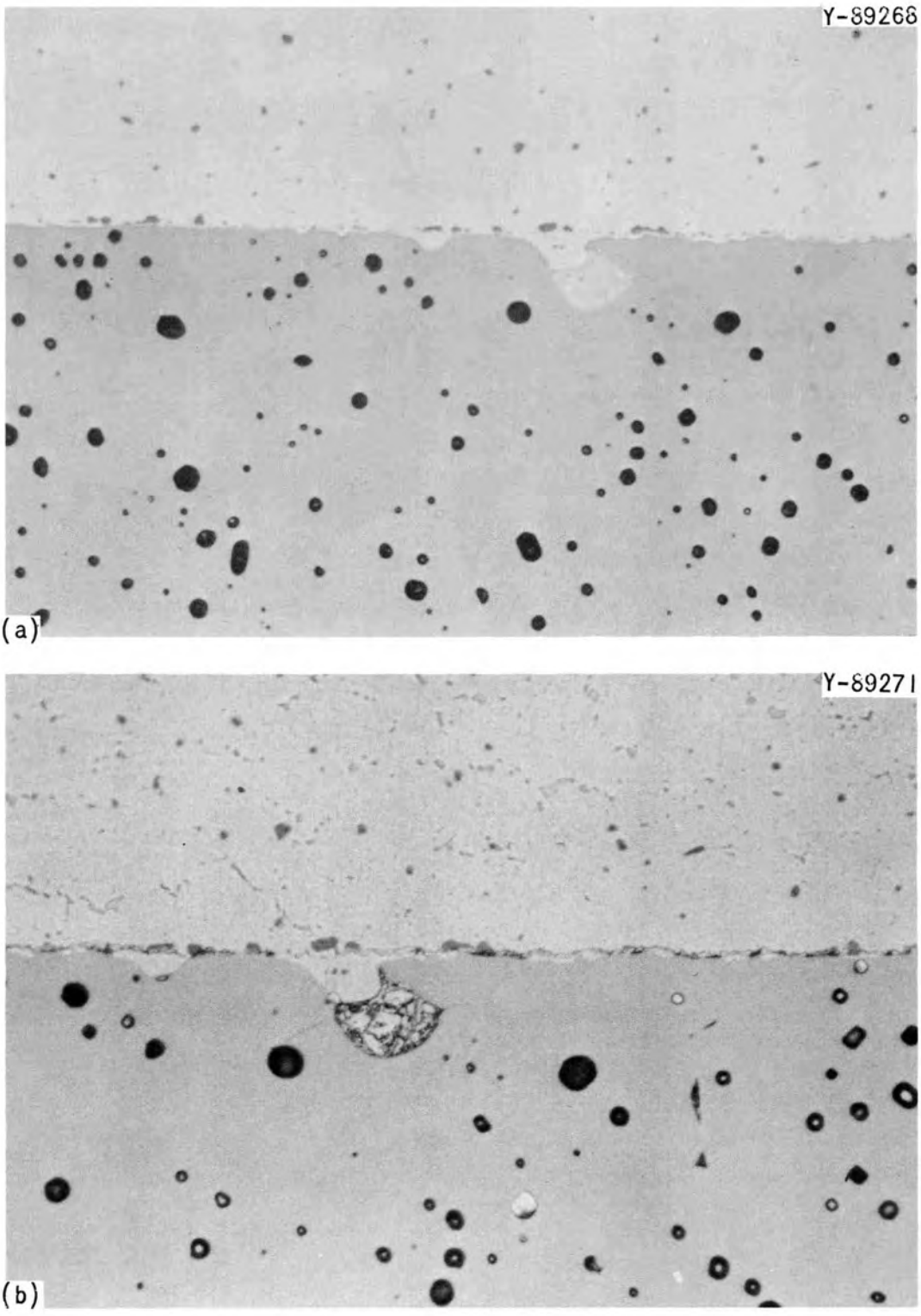

Fig. 2.11. Vanadium Alloy (V–15% Cr–5% Ti)–Uranium Nitride (Composition 1) After 500 hr at 1000°C. (a) Unetched. 500×. (b) Etched with Lactic, HNO_3, HF acid solution. 750×.

blue-purple phase extended 60 μm into the alloy as isolated grains about 2 μm in diameter. The metallic layer showed some signs of penetrating the nitride more deeply at the grain boundaries, as shown in Fig. 2.12. A colorless platelet phase was also visible in the vanadium alloy after etching. This phase extended into the alloy for some 150 μm from the interface and had a platelet size of about 1 μm in diameter and probably about 0.1 μm thick. In isolated instances it appeared that this phase had merged into certain grains of the blue-purple phase.

An extensive reaction zone was observed between the vanadium alloy and the capsule and spacers of type 316 stainless steel, as shown in Fig. 2.13. After 500 hr the total width of the zone was about 120 μm, extending 100 μm into the steel and 20 μm into the vanadium alloy. The material in this zone appeared to be brittle, as judged by its extensive cracking, and very hard (DPH at 50-g load of 1000 ± 100 kg/mm^2).

Electron microprobe analysis. Microprobe analysis showed that the metal layer next to the nitride was generally low in U and high in Cr and V. In some cases, there was uranium metal in small pockets next to the nitride with the layer rich in Cr and V outside it. The composition of the blue-purple phase was high in U and Ti and low in Cr and V. Uranium had diffused into the vanadium alloy for a distance corresponding to the extent of the colorless platelet phase (about 150 μm). It was not possible to identify positively the platelets as having high uranium content, but over the 150-μm region where the platelets were observed in uniform concentration the uranium concentration was almost constant; it dropped sharply in the center of the metal disk where the platelets were absent.

Microhardness measurements. Microhardness measurements showed an increase in hardness of the vanadium alloy from 230 ± 20 kg/mm^2 in areas where the platelet phase was absent to 310 ± 20 kg/mm^2 where it was present.

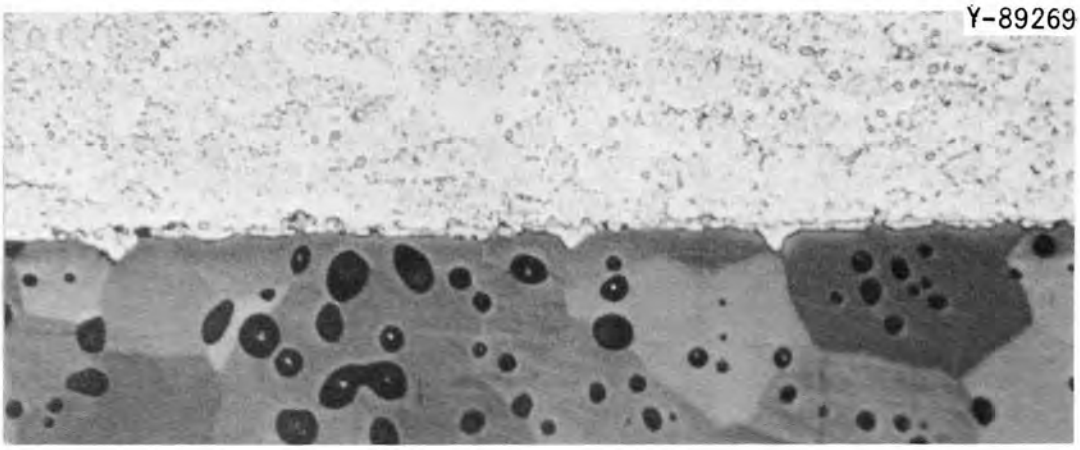

Fig. 2.12. Vanadium Alloy (V–15% Cr–5% Ti)–Uranium Nitride (Composition 1) Interface after 500 hr at 1000°C. Etched with lactic, HNO_3, HF acid solution. 500×.

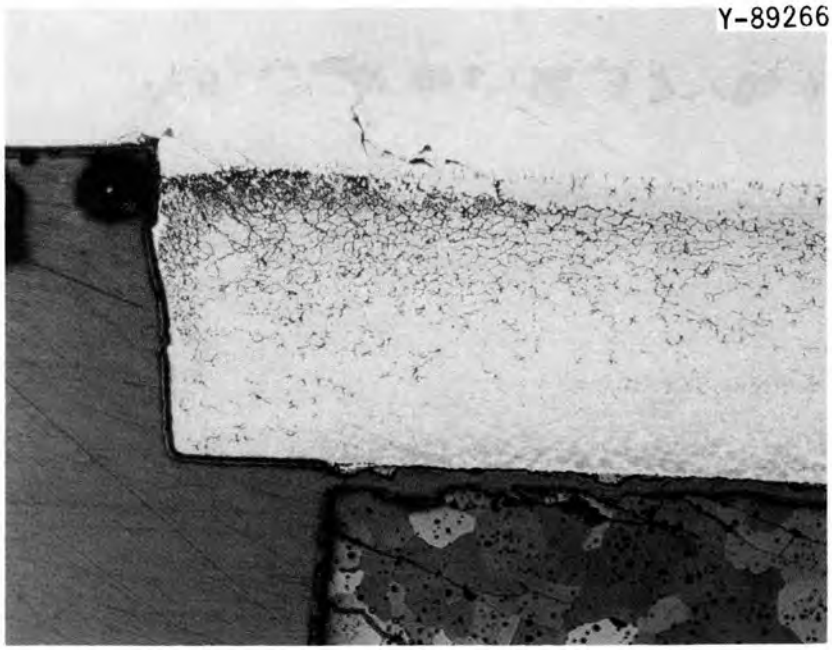

Fig. 2.13. Vanadium Alloy (V–15% Cr–5% Ti)–Type 316 Stainless Steel Reaction Zone. From bottom to top are uranium nitride, vanadium alloy, and the stainless-steel capsule shim. Etched with lactic, HNO_3, HF acid solution. 200×.

Discussion. – The results have not yet been critically evaluated in the light of available equilibrium phase diagrams and diffusion rates. However, titanium metal can reduce UN to form TiN and uranium metal according to available thermodynamic data, while UN is stable in the presence of either V or Cr. Therefore, the observed reaction of UN with the V–15% Cr–5% Ti alloy is interpreted as having been caused by the Ti in the alloy.

One explanation of the observed results is that reaction of Ti in the alloy first releases free U at the nitride interface and precipitates a titanium-uranium nitride (the blue-purple phase). Some of the U then diffuses rapidly into the alloy and reacts, probably with Ti, to give the platelet phase containing Ti and U. Nitrogen diffuses more slowly and is "fixed" as $(Ti_xU_y)N$ particles. The ratio x:y may vary, with a nitride being formed only when the ratio is large.

Fuel-Cladding Thermal Conductance (D. L. McElroy, R. K. Williams, T. E. Banks)

Our objective is to improve the ratings for permissible power generation in fuel elements by finding ways to decrease the thermal contact resistance associated with the fuel-cladding interface. Study of the thermal contact resistance is particularly applicable to carbide and nitride fuels that have relatively high thermal conductivities. In these materials, the interfacial temperature drop represents a very significant portion of the total center-to-edge temperature drop and thus governs the center temperature obtained at a given rate of power generation. This is illustrated by the calculations shown in Table 2.5.

The thermal contact resistance is defined as the temperature drop produced at the interface by unit heat flux:

$$R_c = \Delta T_i / q \ , \qquad (2.2)$$

where

R_c = thermal contact resistance in deg·cm^2/w,
ΔT_i = interfacial temperature drop in °C, and
q = heat flux in w/cm^2 .

Table 2.5. Calculated Temperature Drops in 0.200-in.-ID Stainless Steel-Clad Fuel Rods for Heat Rating of 12 kw/ft (400 w/cm)[a]

Fuel	Temperature Drops, °C			
	Fuel	Interface[b]	Cladding[c]	Total
$(U,Pu)O_2$	1590	250	50	1890
(U,Pu)N	175	250	50	475

[a] J. W. Prados, private communication.

[b] Fuel-cladding interface is a 1-mil gap filled with He.

[c] Cladding thickness: 0.015 in.

In general, heat can be conducted across an interface by thermal radiation, by conduction and convection due to gases present in areas that are not in intimate contact, and by conduction across the areas of solid-solid contact. The resistance to heat flow due to the solid-solid contacts seems to be the most likely place to seek improvements. Therefore, the initial phase of this study has been concentrated in this area. Available literature[7] indicates that the solid-solid contact resistance is sensitive to many variables and cannot be reliably predicted. This is especially true when the solid-solid contact involves two dissimilar materials. Previous studies have shown that thermal contact resistance varies with compressive stress, temperature, surface topography, the mechanical properties and thermal conductivities of the two contacting materials, and the presence of corrosion films. These facts have led to the adoption of a semiempirical approach in this study. The objectives of this approach are to determine the relative importance of the variables for systems of interest and to show which are the most likely avenues to pursue for minimizing the contact resistance.

We are measuring thermal contact resistance in vacuum at temperatures around 50°C to study solid-solid contact resistance without the additional complications of gas conduction and convection or thermal

[7] M. L. Minges, Thermal Contact Resistance, Volume 1 — A Review of the Literature, AFML-TR-65-375, Vol. 1 (April 1966).

radiation transfer. Data are being obtained in an apparatus that was originally designed for thermal conductivity measurements near room temperature. This apparatus, which has been described by Moore et al.,[8] uses two Armco iron heat-meter bars to determine the heat flux and temperature difference across a sample sandwiched between the two bars. Since previous work showed that compressed indium foil was useful for reducing the thermal contact resistance at the interfaces of sample and meter bar, a system for compressing the test column was included.

For the experiments on contact resistance, the single uninstrumented sample and its two indium foils were replaced by two instrumented samples and three foils. The top and bottom foils, at the interfaces of specimen and meter bar, are 0.020-in.-thick Pb and are used to compensate for misalignment in the test column. The third foil, located between the two 1-in.-long samples, simulates the cladding material. The two samples, which are each instrumented with three Chromel-P vs Constantan thermocouples, simulate the fuel material. The thermal conductivity of these two specimens is determined in a separate experiment, and with these data four values for the heat flux, q, are obtained at different positions along the test column. The variation in q indicates the uniformity of the heat-flow pattern and the importance of heat losses. The temperature drop across the two simulated fuel-cladding interfaces, $2\Delta T_i$, is obtained by extrapolating the three temperatures measured on each sample to the two interfaces, subtracting, and making a correction for the relatively small temperature drop across the cladding material. This temperature drop and its corresponding heat flux are then used to calculate the thermal contact resistivity [Eq. (2.2)].

A significant effort was required to convert the thermal conductivity apparatus for experiments on thermal contact resistance. The loading mechanism was rebuilt and calibrated to provide much more reproducible compressive loads on the test column. The total load is now

---

[8] J. P. Moore, T. G. Kollie, R. S. Graves, and D. L. McElroy, Thermal Conductivity Measurements on Solids Between 20 and 159°C Using a Comparative-Longitudinal Apparatus: Results on MgO, BeO, ThO_2, $Th_xU_{1-x}O_{2+y}$, and Al-UO_2 Cermets, ORNL-4121 (June 1967).

obtained from readings on a Baldwin load cell, and the calibration was obtained by replacing the test column with a second load cell. The results of several calibrations indicate that the compressive load is known to within ±10 psi.

Several runs were made to determine the best axial positions for the specimen thermocouples. These experiments indicated that uniform contact pressures are not easily obtained and showed the importance of having multiple temperature sensors for detecting these difficulties. Further modification of the experimental setup to minimize these difficulties and increase the accuracy of the measurements is now being planned.

Some characteristics of the materials obtained for these tests are shown in Table 2.6. The hardened, high-speed tool-steel samples were obtained because the hardness and thermal conductivity of this material

Table 2.6. Characteristics of Materials for Study of Thermal Contact Resistance

Material	Condition	DPH Hardness (kg/cm^2)	RMS Surface Roughness (μin.)	Thermal Conductivity at 25°C ($w\ cm^{-2}\ deg^{-1}$)
0.005-in. copper foil	Annealed 2 hr, 250°C in H_2	58 (50-g load)	14–15	4.01
0.005-in. type 302 stainless steel foil	"Half hard"	368 (50-g load)	10–12	0.12
T-1 tool steel[a]	Quenched and drawn	836 (1-kg load)	3–4	0.157
UN[b]	Pressed and sintered	525[c]	6–8	0.137

[a]Carpenter Steel Company startenith grade.

[b]Material was 95% of theoretical density with some oxide inclusions.

[c]E. Speidel and D. L. Keller, Fabrication and Properties of Hot-Pressed Uranium Mononitride, BMI-1633 (1963).

match those of UN fairly well at room temperature. These samples are being used for checking the apparatus and were required because the UN samples were not available when the work was begun. Microstructural examination and hardness traverse indicated that these samples were quite homogeneous. The ends of these samples were lapped optically flat before the tests, and the surface roughness values were determined with a profilometer. The pressed-and-sintered UN specimens described in Table 2.6 are now available and will be used in future tests. The simulated cladding materials, Cu and type 302 stainless steel, are commercial materials obtained from laboratory stores.

An extensive set of measurements on the interface between tool steel and annealed Cu was obtained and is shown in Fig. 2.14. These data show that the thermal contact resistance at 47°C decreases approximately linearly with increasing compressive stress and may show a further slight decrease on cycling from low to high stresses. This stress dependence is in agreement with the results of several other studies[7] but does not agree with the stress dependence previously obtained for other foils in this apparatus.[8] The maximum determinate error bands shown were computed by assuming that $\delta q = \pm 0.05\ q$, $\delta T_i = \pm 0.1°C$, $\delta x_i = \pm 6.35 \times 10^{-3}$ cm, $\delta K_f = \pm 0.06$ w cm^{-2} $°C^{-1}$, $\delta \Delta x_f = 2.54 \times 10^{-4}$ cm, where

T_i = temperature at axial position x_i,
K_f = thermal conductivity of the foil, and
Δx_f = thickness of the foil.

These calculations show that the temperature uncertainty is critical and thus suggest methods for improving the measurements.

Attempts to determine the temperature variation of thermal contact resistance at constant stress were inconclusive because the measured effects were slightly smaller than the maximum uncertainties calculated above. The data did indicate that the contact resistance decreases with increasing temperature, and this point will be investigated further.

The effect of He on the contact resistance was also investigated, but these experiments were also inconclusive and were discontinued. In the experiments, the test column was insulated with alumina wool, but

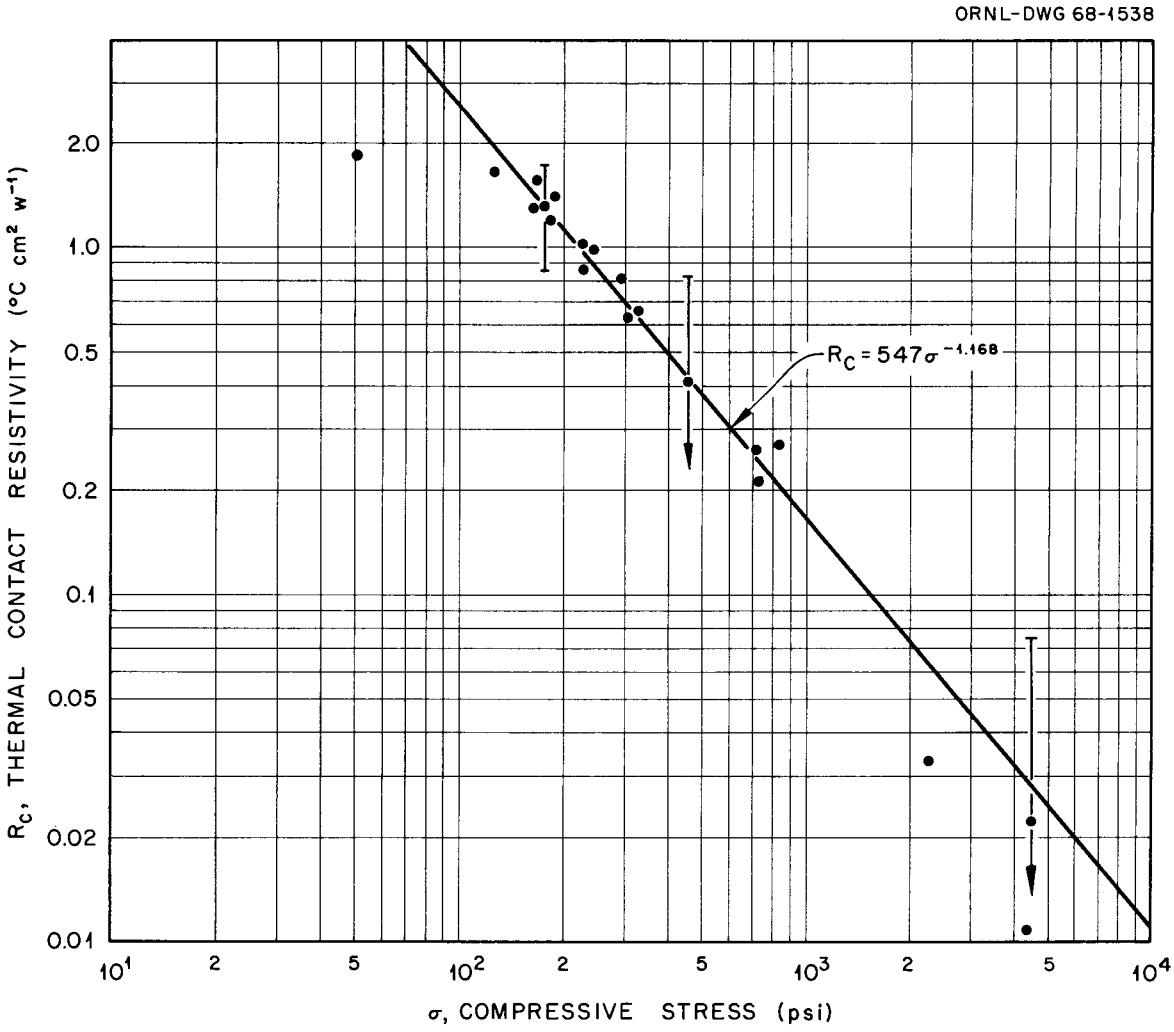

Fig. 2.14. Effect of Compressive Stress on the Thermal Contact Resistivity of the Interface Between Tool Steel and Copper. Interface temperatures vary from 43.8 to 47.5°C.

the insulation would not eliminate heat losses from the test column by gas conduction and convection. These losses could probably be reduced to acceptable levels by installing guard heaters, but the considerable effort required to produce effective thermal guarding would not be justified at this stage of the investigation.

The properties of the annealed copper foil were determined before and after the test of contact resistance, and no changes could be detected. Microhardness tests (DPH at 50-g load) showed no change in the foil and uniformity across the contact area. Surface roughness tests gave an indication that the root-mean-square (RMS) roughness of

the copper surface may have decreased from 14 or 15 μin. to about 10 μin., but these results were obtained in two different profilometers and may not be significantly different.

The interfacial conductance between UN and steel and stainless steel has also been tested to see if hardness of the stainless steel would markedly affect the contact conductance. Results are shown in Table 2.7. We found that data collected to date fit the equation

$$R_c = A\ \sigma^n\ , \qquad (2.3)$$

where σ is the compressive stressing in pounds per square inch; appropriate A and n values are shown in the table. The results show that the thermal contact resistance for interfaces between stainless steel and UN is not very sensitive to the hardness of the stainless steel and indicate that a soft and/or high thermal conductivity interface material can significantly reduce the thermal contact resistance.

The data in Table 2.7 can be used to predict what will happen if a loss of sodium bond occurs followed by fuel swelling which is eventually restrained by the cladding at an assumed pressure of 1000 psi. If the sodium bond were designed for the maximum allowable heat flux of 600 w/cm^2, loss of sodium bonding would result in a temperature rise of about 1200°C across this interface. Use of a soft metal, such as Cu, at the interface would reduce the temperature drop to about 110°C. If the Na in the bond wet the fuel and cladding, its presence would also result in a marked reduction in the contact resistance.

Irradiation Testing of Nitride Fuels

S. C. Weaver

We began selecting variables for irradiation testing of mixed nitride fuels. We plan to compare the relative merits of type 316 stainless steel and vanadium-base alloys with emphasis on VANSTAR-7 (V–9% Cr–3% Fe–1.3% Zr–0.05% C). Both sodium- and helium-bonded pins will be included. Fuel variables will include density, pellet shape, oxygen and carbon impurity levels, and heat ratings.

Table 2.7. Conditions and Results of Thermal Contact Resistance Measurements in Vacuum at 50°C

Contacting Materials[a]	Hardness[b] (DPH)	RMS Surface Roughness (μin.)	Thermal Conductivity at 50°C (w cm^{-1} $°C^{-1}$)	Contact Resistance R_c at Compressive Stress[c] of 1000 psi ($°C \cdot cm^2/w$)	Materials Constants[c]	
					A	n
Copper	50	14–15	4.0	0.17	550	−1.17
T-1 tool steel	835	3–4	0.16			
Type 302 stainless steel[d]	340	3–4	0.1	1.16	1156	−1.00
T-1 tool steel	835	3–4	0.16			
Type 302 stainless steel[e]	415	5	0.1	2.16	620	−0.82
UN	525	6–8	0.14			
Type 302 stainless steel[d]	340	3–4	0.1	2.29	1510	−0.94
UN	525	6–8	0.14			
Type 302 stainless steel[f]	166	5	0.1	1.71	750	−0.88
UN	525	6–8	0.14			

[a] First material listed in given couple was a thin foil and the second was a bulk specimen.

[b] 50-g load for foils; 1-kg load for bulk specimens.

[c] From relationship $R_c = A\sigma^n$, where σ is the compressive stress in pounds per square inch.

[d] Mill designation: Half hard.

[e] Mill designation: Full hard.

[f] Mill designation: Annealed.

The steps involved with irradiation testing on EBR-II have been assessed, and critical path items have been identified. Work was begun on a facility for the sodium bonding of fuel pins.

Model Studies on Nitride Fuel Pins

J. L. Scott

The excellent thermal conductivity of mixed (U,Pu)N creates the potential for a much higher linear heat rating than is possible for mixed $(U,Pu)O_2$. For the latter material, the linear heat rating to produce center melting is 20 to 23 kw/ft. For mixed nitrides, on the other hand, the maximum allowable linear heat rating is not governed by center melting, but is limited by one of the following:

1. nucleate boiling of Na at coolant-cladding interface,
2. thermal stresses in irradiation-embrittled cladding,
3. film-boiling of sodium bond at full-cladding interface,
4. excessive swelling of fuel,
5. melting of the cladding.

The problem of nucleate boiling of the Na is ameliorated by increasing the pin diameter for a given heat rating, increasing the coolant pressure or flow rate, and decreasing the temperature at the coolant inlet. The heat flux is normally limited to about 600 w/cm^2 at coolant-cladding or fuel-cladding interface. An alternative solution for long-range LMFBR designs is to use Li as a coolant.

For an elastic material the maximum (or tangential) thermal stress, σ_t, for a tube with diameter D, the hours t and linear heat rating H is approximated by the equation

$$\sigma_t = \frac{\alpha E H}{2\pi K (1 - \nu)} \left(\frac{t}{D}\right), \qquad (2.4)$$

where α is the linear coefficient of thermal expansion, E is Young's modulus, ν is Poisson's ratio, and K is the thermal conductivity. In selecting a material with maximum resistance to thermal stresses, one seeks a low coefficient of thermal expansion, a low Young's modulus,

a high yield or creep strength, and a high thermal conductivity. We can define a factor of merit, F, as

$$F = \frac{2\pi K\,(1-\nu)}{\alpha E}\,\sigma_c\,, \tag{2.5}$$

where σ_c is the stress to produce 1% second-stage creep strain in 10,000 hr. We can use this to compare various cladding materials on a relative basis. Table 2.8 shows such a comparison. A high factor of merit corresponds to improved resistance to damage from thermal stress.

Table 2.8. Relative Resistance to Thermal Stress Damage at 700°C

Material	Thermal Conductivity (w cm^{-1} $°C^{-1}$)	Coefficient of Thermal Expansion (cm cm^{-1} $°C^{-1}$)	Young's Modulus (psi)	10,000 hr Creep Stress (psi)	Factor of Merit
		$\times 10^{-6}$	$\times 10^{6}$	$\times 10^{3}$	
Type 304 stainless steel	0.23	18	21	6	16
Type 316 stainless steel	0.22	18	21	7	18
Hastelloy X	0.20	15	23	13	33
Nb–1% Zr	0.54	7.7	14	30	660
VANSTAR-7[a]	0.37	11.5	18	9	71

[a] V–9% Cr–3% Fe–1.3% Zr–0.05% C.

In the calculations in Table 2.8, Poisson's ratio was assumed to be 0.3 for all materials. The results are not very sensitive to changes in Poisson's ratio.

Table 2.8 demonstrates the decisive improvement in resistance to thermal stress in vanadium-base alloys typified by VANSTAR-7 (V–9% Cr–3% Fe–1.3% Zr–0.05% C). A heat rating of 42 kw/ft will produce the same effect in this material as 10 kw/ft in stainless steel. Hastelloy X also is better than stainless steel because of its higher creep strength but is not as good as vanadium-base alloys. Niobium-base alloys are markedly superior to vanadium-base alloys, but neutron

absorption effects preclude their use. They do offer the potential of service at extremely high heat ratings if a better coolant such as Li is used. Comparing the properties of Nb–1% Zr with type 304 stainless steel, one begins to see why a number of carbide pins with Nb–1% Zr cladding survived irradiation to burnups beyond 10%, whereas sister pins clad with stainless steel failed.[9]

Returning to our list of factors that might limit the allowable heat rating for sodium-cooled pins, we see that the next factor listed is film-boiling of sodium bond. As stated earlier, this factor sets a design limit of 600 w/cm^2 at the fuel-cladding interface. Since the pressure within a fuel pin will increase with increasing burnups, this process becomes less likely with increasing burnup. Against the reduced chance of boiling there exists a corresponding hazard that a pinhole will develop in the bottom of a pin and that gas pressure will blow the Na out of the capsule. This process could lead to overheating of the fuel and rapid swelling until the fuel-cladding gap closes. At this point the fuel will cool somewhat, but the contact resistance to heat conduction will result in a higher temperature drop across the interface than will exist with sodium bonding.

Excessive swelling of the fuel is the next factor to be considered to establish the maximum allowable heat rating. This limit will be reached earlier for gas-bonded pins than for sodium-bonded pins. The effect may be lessened by use of low density fuel, dished pellets, or annular pellets, but there are insufficient data at this time to assess this problem. This will receive major attention in our program.

The last item, melting of the cladding, will occur before carbide or nitride fuels will melt. It will probably be caused by loss of coolant either due to sodium boiling or to flow constriction. Because of their high thermal conductivities, carbide or nitride fuels will probably be much more forgiving than oxide fuel. Transient tests in TREAT will be required to demonstrate this design advantage.

---

[9]A. Strasser et al., "Uranium-Plutonium Carbide Fuels for Fast Breeder Reactors," paper presented at the American Nuclear Society National Topical Meeting, "Fast Reactor Technology," Detroit, Michigan, April 26–28, 1965.

3. FISSION-GAS RELEASE AND PHYSICAL PROPERTIES OF FUEL MATERIALS DURING IRRADIATION

O. Sisman

The purpose of this work is to measure the parameters that control the release of fission gas from highly characterized nuclear fuels. These parameters are evaluated in terms of a generalized model to predict release from operating fuel materials. Thermal diffusivity is measured in-reactor in analogous experiments.

Effect of Fission Density on Release of Fission Gas from Enriched Single-Crystal UO_2 Spheres

R. M. Carroll R. B. Perez

Irradiation and evaluation have been completed.[1]

Determination of Amount of Nonfission Heating Required for In-Reactor Thermal Diffusivity Measurements

R. M. Carroll R. B. Perez

The total amount of heat generated in a fuel specimen during irradiation is the sum of the fission heating plus the heating caused by beta, gamma, and neutron scattering and absorption. To determine the thermal diffusivity of fuels during irradiation, it is necessary to know the heat generation from all sources.

We made an experimental determination of the nonfission heating in the C-1 position of the ORR reactor. The apparatus (see Fig. 3.1) and experimental methods used have been reported.[2] The time-temperature response for the copper slug and the brass holder have been fed into a computer program, and we have found that a curve of the form

$$T(t) = A_o - A_1 e^{-rt} = \text{time rate of temperature rise} , \quad (3.1)$$

---

[1]R. M. Carroll, O. Sisman, and R. B. Perez, Nucl. Sci. Eng. 32(3), 430–431 (1968).

[2]R. M. Carroll et al., Fuels and Materials Development Program Quart. Progr. Rept. June 30, 1968, ORNL-4330, pp. 57–58.

gives a good fit. We found that transients produced by sudden movement or change in cooling rate would obscure the results unless the computer analysis was started from 20 to 100 sec after the capsule was perturbed. Each test produced transients of different time durations. For each test,

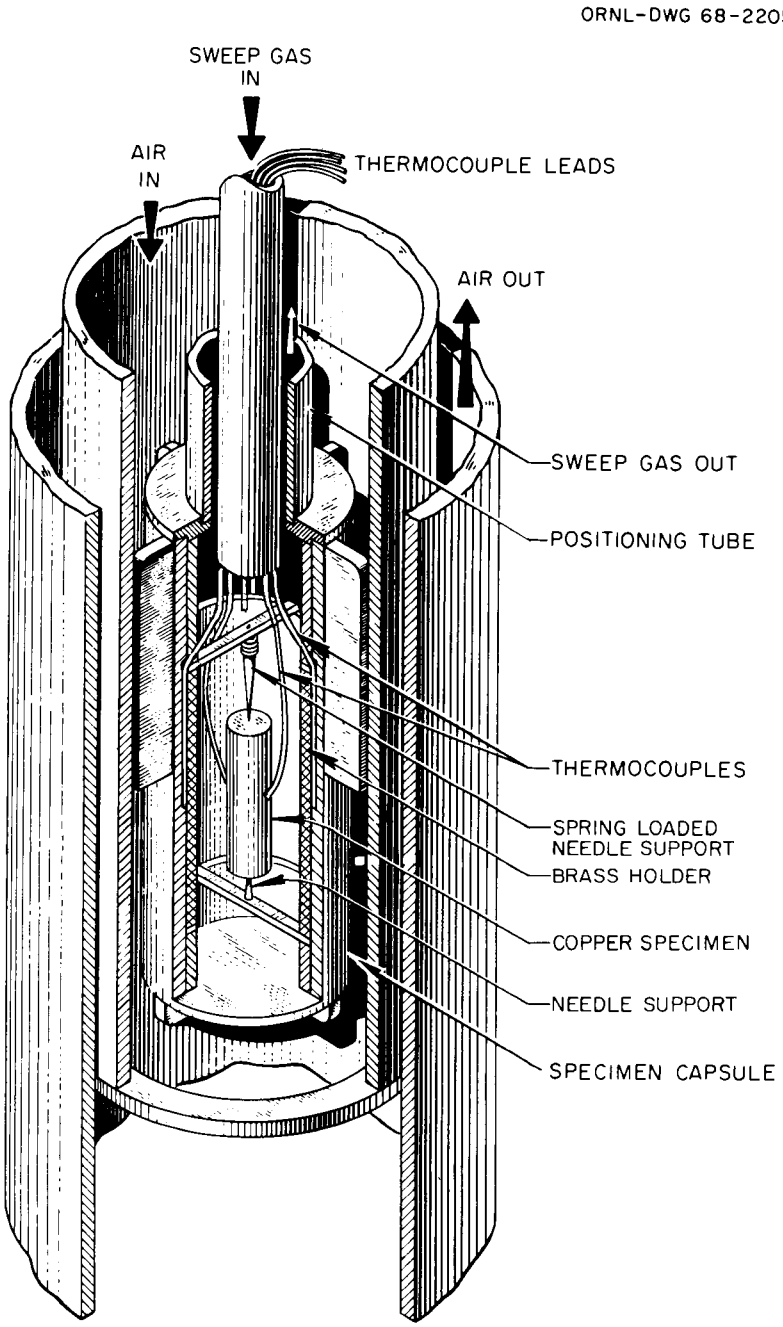

Fig. 3.1. Capsule for Measurements of Nonfission Heating.

we could determine when the transients had decayed by comparing the parameters A_o, A_1, and r for the copper slug and the brass holder, since at that time the value of r was the same for the copper slug and the brass holder.

During the measurements, a sweep gas composed of 99% He and 1% Ar was passed through the sweep system. The Ar was neutron activated as it passed through the capsule, and the thermal neutron flux at any time was measured by the amount of argon activation. Because the heating rate of the Cu was more than we anticipated, we could not place the specimen closer than 20 cm from the reactor center line without overheating the copper specimen. Therefore, the reactor power was raised at the start of a new reactor cycle to only 10 Mw, and measurements were made from near the center line of the reactor core to about 28 cm away, thus overlapping positions where measurements were made at full 30-Mw power. These measurements were then multiplied by 3.0.

The measured neutron flux as a function of reactor position is given in Fig. 3.2. The time interval of the data covers a reactor cycle, and there was some variation of the position-flux relation as the cycle progressed because the control rods were shifted to compensate for fuel burnup.

The nonfission heating is shown in Fig. 3.3 as a function of neutron flux. The solid line through the data, although not necessarily the best fit to the data points, was fitted graphically to the functional form

$$\text{Nonfission heating (w/g)} = (8.73 \times 10^{-14})\,\phi + 0.09 \,. \quad (3.2)$$

The data of Fig. 3.3 fit the above equation very well up to the edge of the fuel elements. Deeper in the core, the data of the first cycle show more heating than predicted while the data of the new core show less heating. This means that within the core the nonfission heating is influenced by factors — most likely the control rod positions — that are not directly proportional to the measured thermal neutron flux but that do reflect the core burnup.

A likely cause for the scatter of data within the core is that the nonfission heating is mostly from gamma rays produced by fissions in adjacent fuel elements. However, the thermal neutron flux within the

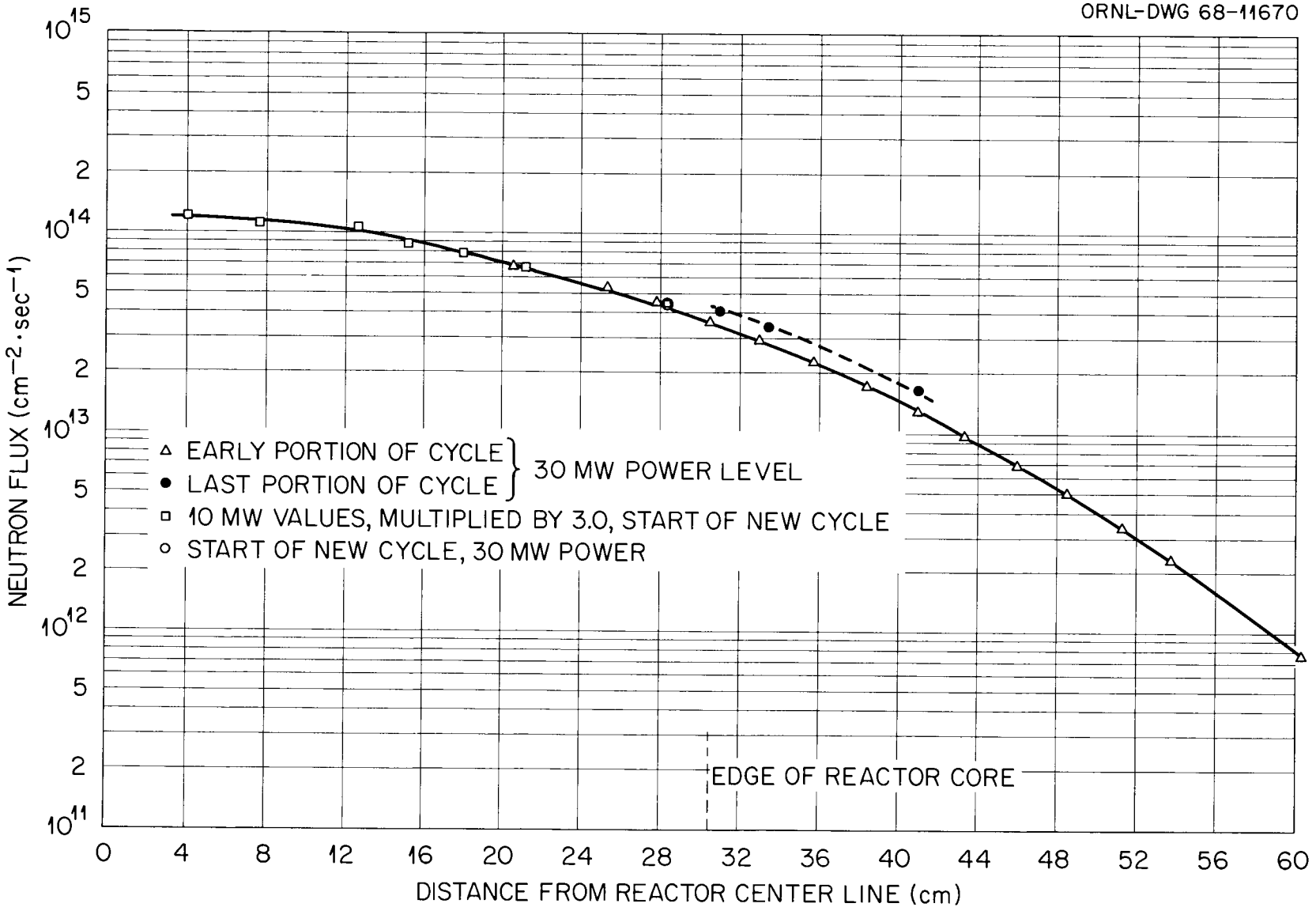

Fig. 3.2. Neutron Flux in C-1 Position of ORR Reactor, Measured by Argon Activation.

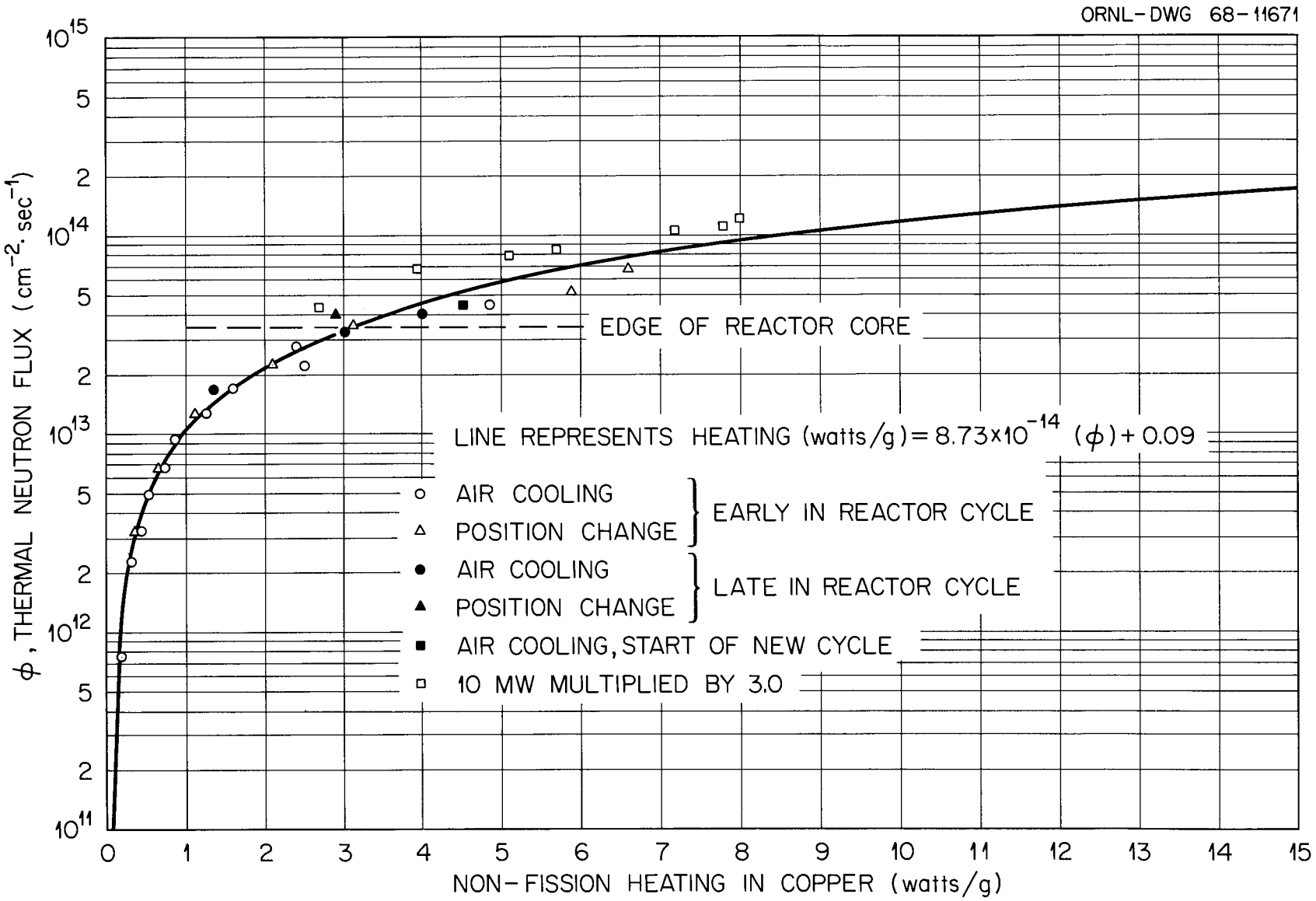

Fig. 3.3. Nonfission Heating in Cu as a Function of Neutron Flux in the C-1 Position of the ORR Reactor.

capsule may not be proportional to the fission rate that is occurring in the nearest fuel elements, which is several centimeters away. At a distance from the core, the thermal neutron flux within the capsule represents an average over a bigger portion of the core.

We can conclude that the nonfission heating above the reactor core is well represented by Eq. (3.2). Even within the core, the measured nonfission heating in Cu is given by Eq. (3.2) to within 25% accuracy if the reactor has been at power for at least one day.

Effect of Temperature, Fission Density, and Burnup on the Thermal Diffusivity and Fission-Gas Release of UN

R. M. Carroll J. G. Morgan

Three UN bushings (2.28 cm long, 0.649 cm in outer diameter, and with a 0.252-cm-OD axial hole) were stacked in an Al_2O_3 holder and irradiated at various temperatures and fission rates. At 200 to 1500°C a total burnup of 0.31% U and 9.8×10^{19} fissions/cm^3 was attained.

The irradiation was begun at low temperatures and fission rates to determine the surface release activated by recoil, since this is a sensitive indication of surface area. Early in the irradiation, after only 4×10^{18} fissions/cm^3 burnup at temperatures less than 600°C, we detected a step increase of gas release that could only be caused by cracking of the specimen. This was unexpected because of the low thermal stresses, low temperatures, and low burnup.

When the UN specimen was irradiated at higher temperatures, we found that the gas release behaved more like classical diffusion than the trapping process that we usually observe in UO_2. The gas release was proportional to the production rate and was an exponential function of temperature with a 35 kcal/mole activation energy.

As irradiation progressed there were more and more step increases of gas release, showing that cracking was occurring. At about 1300°C, however, the gas release decreased with time, showing that some of the cracks were healing. One would not expect cracks to heal at 1300°C during irradiation unless the cracks were almost microscopic.

Each time the UN specimen was heated or cooled, there were large bursts of gas release. Such a burst, when the specimen was cooled from

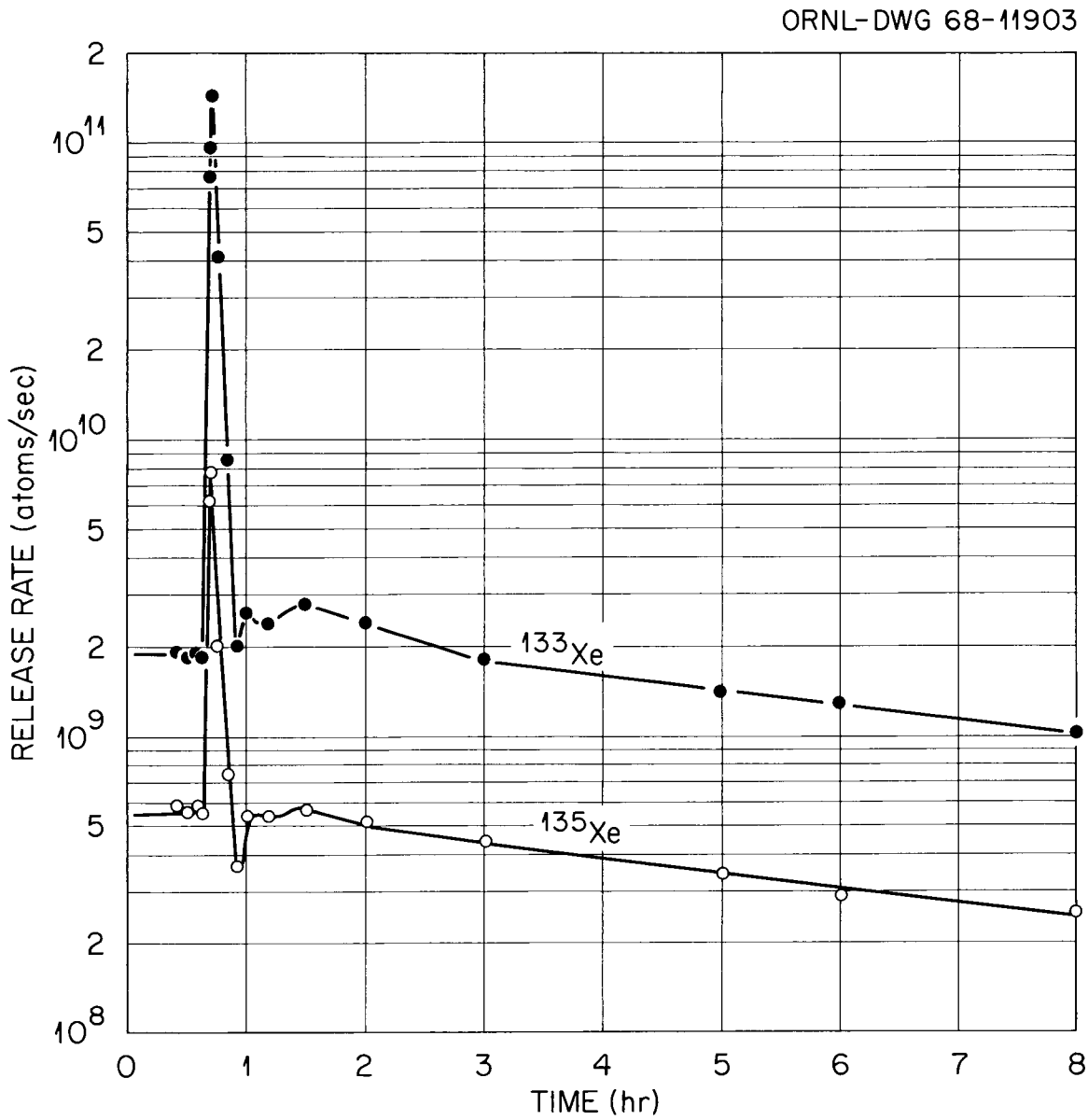

Fig. 3.4. Cooling Burst When UN Specimen (C1-23) was Cooled Quickly from 1340 to 200°C.

1340 to 200°C by withdrawing the specimen from the neutron flux, is shown in Fig. 3.4. Just before withdrawal, the ratio of ^{133}Xe to ^{135}Xe was about 3.5, the proper ratio for a diffusion process. During the cooling burst, this ratio was about 17, indicating that trapped gas was suddenly released. Thereafter, the gas release varied similarly for several hours. One can conclude from this that the UN cracked during cooling and that the liberated gas slowly escaped from the cracks for several hours. The slow escape implies that many of the cracks were very small.

A sweep gas containing 0.5% N_2, 3% H_2, and 96.5% He was used when the specimen was at 1400 to 1500°C. We found, however, no significant change in the gas-release characteristics whether or not the sweep gas contained N_2.

The irradiation has been terminated and the capsule opened in the hot cells. The physical appearance of the UN was just as we predicted: the pellets were nearly intact, but a fine network of cracks covered the surface (see Fig. 3.5). We suspect that most of the gross breaking occurred during the process of sawing the capsule open and removing the pellets from their container. Metallographic examinations are in progress that we hope will show whether there was a chemical cause for the cracking of the UN pellets.

Thermal diffusivity data were taken at intervals but have not yet been processed. In view of the cracking that occurred in the pellets, it is doubtful if such data will have any real significance.

Effect of Temperature, Fission Density, and Burnup on the Fission-Gas Release from Sol-Gel $(U_{0.80}Pu_{0.20})O_2$ Microspheres

R. M. Carroll H. E. Robertson

About 100 microspheres produced by the Chemical Technology Division (batch PUM-4) were selected individually by microscopic examination. After these were annealed at 1450°C in an atmosphere of Ar and 4% He, we selected 51 particles and placed them in a tungsten holder. The particle diameters were determined by x-ray techniques to be 546 ± 17 μ. This fuel is being held for future irradiation.

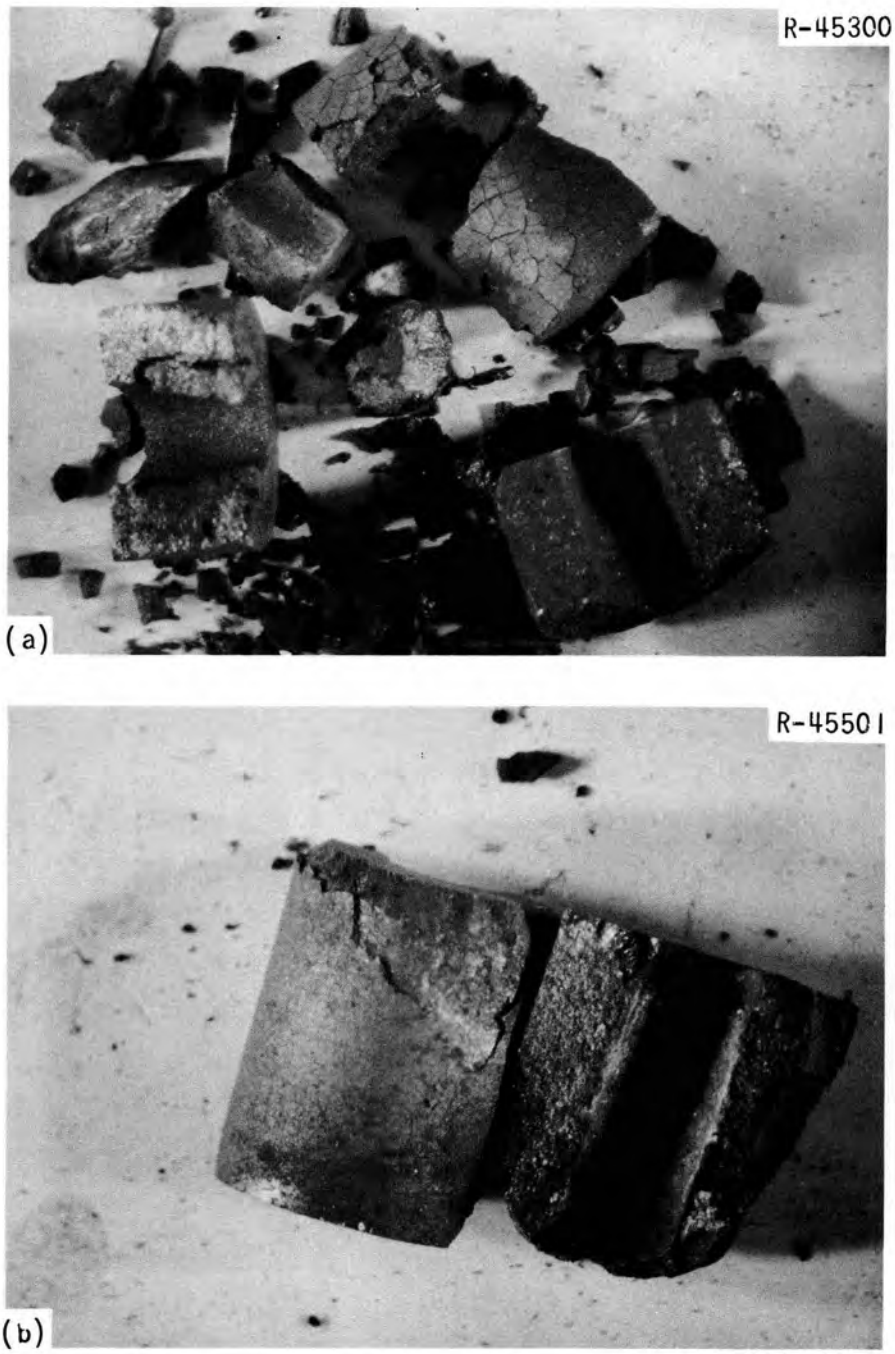

Fig. 3.5. UN Pellets after Irradiation (C1-23). (a) Top pellet of capsule. (b) Center pellet of capsule.

Effect of Temperature, Fission Density, and Low Burnup on Fission-Gas Release from $(U_{0.75}Pu_{0.25})O_2$

R. M. Carroll H. E. Robertson
J. G. Morgan

High-density (97% of theoretical density) pellets of $(U_{0.75}Pu_{0.25})O_2$ were obtained from Pacific Northwest Laboratory. These pellets were made to Fast Flux Test Facility specifications, but they have slightly higher density. Two 0.54-cm-OD × 0.58-cm-long pellets with 0.127-cm-diam axial holes were loaded into a tungsten holder and installed into a capsule as described below. The irradiation has just begun, and the initial data have not yet been evaluated.

A Technique for Handling PuO_2 Specimens Outside Glove Boxes (R. M. Carroll, H. E. Robertson)

We had the problem of loading a $(U,Pu)O_2$ specimen into a capsule for an in-reactor experiment. The assembly techniques for the 20-ft-long insert used in the experiment were developed over a period of years and involve delicate hand operations on a bench assembly located in a noncontamination area. We did not wish to attempt to assemble a 20-ft-long rig in a glove box or to change our successful assembly techniques.

An alternative method was to apply a temporary coating on the $(U,Pu)O_2$ specimen so that it could be handled without spreading plutonium. Naphthalene was selected for the coating material because it has a low melting point (80°C), forms a hard coating, is relatively nontoxic, and yet can be vaporized without leaving a residue.

The $(U,Pu)O_2$ specimen consisted of two pellets described above. The pellets were placed in a glove box and slid into a tungsten holder that had been machined into a hollow cylinder 0.60 cm in inner diameter and about 2.2 cm long with one end open and the other closed. A drill rod was placed into the axial hole of the pellets so as to leave a hollow space so that a thermocouple could later be inserted. Molten naphthalene was then poured into the tungsten holder, covering the specimen and

filling the holder. The filled holder was then removed from the glove box by the usual plastic-bagging method.

The contaminated glove box had contributed some activity to the naphthalene coating, so the specimen was removed from the bags in a relatively clean toxic hood and redipped in a series of four baths of clean naphthalene. This resulted in a very slightly contaminated outer coating with the contamination firmly fixed. The dipped specimen was stored in a closed bottle containing naphthalene crystals to prevent the coating from evaporating before installation in the capsule.

The specimen was loaded into the capsule by the usual techniques. A portable hood and constant monitoring were used, but only surgical gloves and laboratory coats were used to protect personnel. The central rod was extracted from the capsule by twisting it until the naphthalene bond was broken. Surprisingly, this released no contamination.

After the capsule was assembled, a weld was made within 1 in. of the coated specimen. We kept the naphthalene from melting by cooling the capsule between short welding periods. The welding required a continuous purge of Ar over the interior of the assembly, and there was some concern that this might cause loose contamination to be carried out into the room. There was no detectable release, however.

After the welding was completed, the assembly was evacuated, and the capsule was warmed to about 80°C. The warming and pumping was continued overnight. Bench tests had shown this to be more than sufficient time to ensure evaporation of the naphthalene. A filter was placed in the pump line to see if any Pu was released during the evaporation of the naphthalene.

Through the entire operation, no contamination was detected on any of the equipment, the handling gloves, or the tools. Air monitors placed very close to all operations detected no activity. All smears and filter readings had zero count level.

The ease of applying and removing naphthalene suggests that it might serve as a protective coating for many types of specimens, especially those of a friable nature, during handling and storing.

Fission-Gas Release Studies on Fine-Grained High-Density Spheres of $(U,Pu)O_2$

Specimens have been obtained from Battelle-Northwest.

4. ZIRCONIUM METALLURGY

P. L. Rittenhouse

The object of this program is to optimize the properties of zirconium alloy tubing used in nuclear reactors by study of fabrication procedures and their interaction with crystallographic deformation modes. Rather than following the usual practice of designing fuel element cladding on the basis of minimum strength values, we are attempting to control the crystallographic texture in the tubing to permit the strongest direction in the tubing to be matched against the highest service stress. This technique can also be used to control the orientation of potentially embrittling hydride platelets that form from absorption of H_2 that is released by corrosion. Success in this program can reduce the cost of producing nuclear power by making possible longer core life, higher operating temperature, and the use of tubing with thinner walls.

Fabrication and Texture Control of Zirconium Tubing

T. M. Nilsson

We have now planned in detail a total of twelve schedules for the manufacture of Zircaloy tubing. Four schedules in which the reduction to final size (0.59-in. outside diameter × 0.52-in. inside diameter) occurs by tube reducing alone have been finished and are being examined and evaluated. Grain sizes in some of the finished tubes are shown in Table 4.1. In addition, grain sizes for two of the intermediate sizes of tubes (3-3a and 5-3a) are given. The table also shows parameters that might influence the grain size. Clearly, the only important parameter is the amount of cold work. The reduction in area before annealing must be $> 20\%$, but $< 54\%$, to obtain fine-grained tubing. Neither reversing the lead ends of tubing in successive passes nor varying the Q-number (i.e., ratio of wall reduction to diameter reduction) seems important.

Table 4.1. Grain Size of Tube-Reduced and Annealed Zircaloy-4 Tubing

Schedule Number	Tube Number	Outside Diameter (in.)	Last Pass			ASTM Grain Size
			Reduction in Area (%)	Q-Number[a]	Direction[b] Sequence	
I	2-402a	0.591	54	0.91	F-F-F	9
	6-16	0.591	54	0.91	F-F-R	9 1/2
	6-3	0.591	54	0.91	R-R-R	9 1/2
II	3-3a	0.635	73	1.49	F-F	10
	3-4a	0.591	20	2.06	F-F-F	7 1/2
	5-3a	0.635	73	1.49	F-F	9 1/2
	5-4a	0.591	20	2.06	F-F-F	5 1/2
	6-2	0.591	20	2.06	F-F-R	7
	6-4	0.591	20	2.06	R-R-R	7
III	4-401a	0.587	65	1.44	F-R-F	9
	4-401b	0.587	65	1.44	F-R-R	9
	4-3	0.587	65	1.44	F-F-F	9
IV	7-101	0.592	18	1.81	F-F-F	7 1/2
	7-102	0.592	18	1.81	F-R-R	7 1/2
	7-103	0.592	18	1.81	F-R-F	7 1/2

[a] Q = wall reduction/diameter reduction.

[b] F indicates that the front end of the extrusion was the lead end in the tube reduction. R indicates that the rear of the extrusion was the lead end.

In addition to the four tube-reduced materials, three other schedules have been completed. These schedules started with tube-reduced tubing of intermediate size (0.636-in. outside diameter × 0.540-in. inside diameter) and were processed to final size (0.59-in. outside diameter × 0.52 inside diameter) by either swaging, planetary swaging, or cold drawing. The reduction in area, about 40%, was accomplished in four equal steps with intermediate anneals at 730°C for 2 hr. In the drawing schedule we also reversed lead ends between passes. In each case, most of the reduction is by wall thinning.

Three of the five remaining schedules will be cold drawn from tube-reduced material of the following sizes: 0.886-in. outside diameter × 0.786-in. inside diameter, 0.886-in. outside diameter × 0.736-in. inside diameter, and 0.886-in. outside diameter × 0.576-in. inside diameter. The other two schedules will reduce material to final size from 0.886-in. outside diameter × 0.786-in. inside diameter by swaging and planetary swaging. The deformation in these last five schedules will be primarily sinking (i.e., little wall thinning). The schedules are planned so that the tubes are annealed for 2 hr at 730°C after every 20% reduction (two passes).

Texture Effects, Texture Development, and Anisotropy of Properties

D. O. Hobson E. Tenckhoff

Circumferential Texture Variations in Zircaloy Tubing (D. O. Hobson)

Efforts continue in the examination of fabricated tubing to determine the causes of texture variations. We have examined tubing fabricated by the special procedures described by Nilsson and Rittenhouse,[1] and have obtained concise texture and texture variation data on this material from the forged billet to the finished tubing. We have found several instances of large variations in the fabricated tubing. These variations could be ascribed to a number of incidents in the history of the tubing including improperly shaped dies, the ratio of tube feed to tube rotation during reduction, and the amount of wall reduction relative to diameter reduction. Changes of 400% in radial basal pole intensity, based on values of random intensity, have been found at some stages of the tubing reduction schedule and were directly attributable to the bad dies, the markings on the tube surfaces corresponding closely to the observed intensity maxima. These large variations are of interest since we have found that a variation of 100%, again based on random intensity, produced large diametral strain variations around the circumference of a tube tested in tension.

---

[1]T. M. Nilsson and P. L. Rittenhouse, Fuels and Materials Development Program Quart. Progr. Rept. June 30, 1968, ORNL-4330, pp. 59–60.

Although individual texture variations existing in the forging from which the extrusion billets were machined and variations found in the tube shells after extrusion could not be followed during further fabrication steps, it is unquestionable that they affected the textures formed during the final steps of tube reduction. We found, though, that the major part of the variation was directly attributable to the procedures used for tube reduction.

Texture Gradients in Thin-Walled Zircaloy Tubing (E. Tenckhoff)

These examinations have been continued in greater detail for several especially interesting tubes. Basal (0002) and prism $\{10\bar{1}0\}$ pole figures for Zircaloy-2 tubing were determined after extrusion and after final reduction (ball swaging and tube reduction) on different layers of the tube wall. In tubing fabricated to the same size from extrusion billets of identical dimensions, different processing conditions (predominant reduction in diameter, R_D, or in wall thickness, R_W) cause markedly different final textures. Figures 4.1 and 4.2 show, respectively, the influence of predominant R_D and predominant R_W on the development of texture and the texture gradients across the wall thickness. The angle between the radial and tangential directions on a (0002) pole figure, Φ, is shown on the abscissa. The ordinate gives the ratio of measured intensity, $I_{(0002)}$, to the random intensity of a powder sample, $I^{\circ}_{(0002)}$. The third axis gives the position in the wall of the tube.

The results of these studies can be summarized as follows.

1. Predominant R_D leads to a split of basal poles with a tilt angle, ψ, (the angle, measured from the radial toward the tangential direction, at which the maximum basal pole intensity occurs) of about $\pm 60°$. Heavy R_W centers the basal poles with the ψ between 0 and 30 to 40°. In practical tube reduction these effects are in competition.

2. Predominant R_W also leads to a texture gradient across the wall thickness. This does not appear after predominant R_D.

3. Essentially similar textures are formed by tube reducing and ball swaging with high R_W.

4. Because of possible texture gradients, a single texture measurement — regardless of the layer it is taken from — does not necessarily give a representative texture.

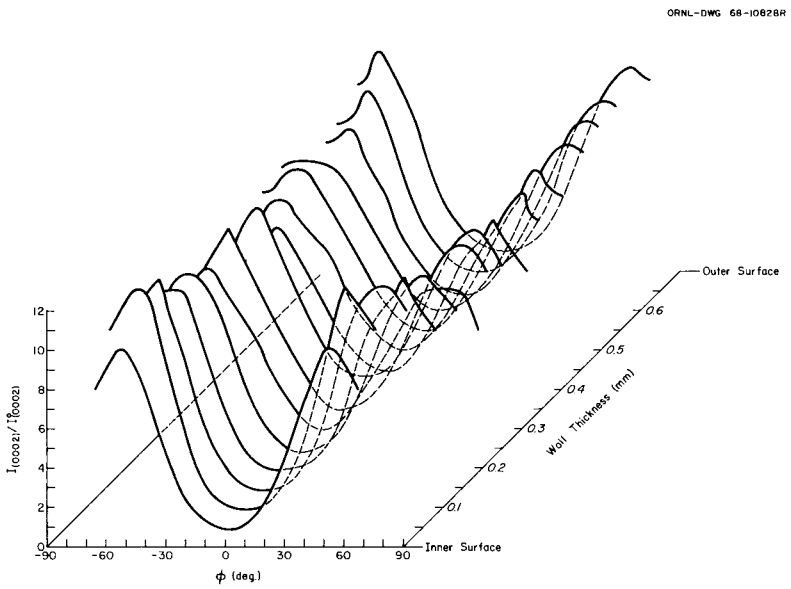

Fig. 4.1. Basal Plane Intensity Distribution Over the Wall Thickness of Tube 11W. Tube reduced to 58% reduction in area, R_D = 40%, R_W = 31%.

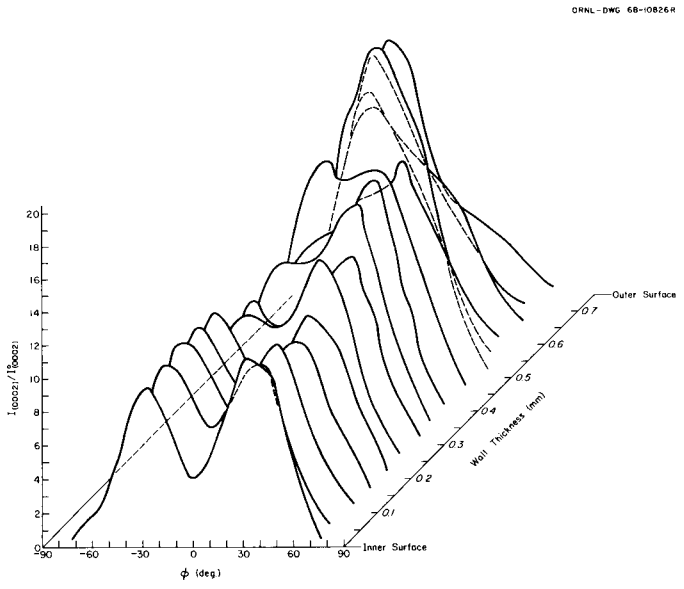

Fig. 4.2. Basal Plane Intensity Distribution Over the Wall Thickness of Tube 10W. Tube reduced to 58% reduction in area, R_D = 25%, R_W = 44%.

PART II

COOLANTS

5. ALKALI-METAL CORROSION STUDIES

W. O. Harms R. E. MacPherson

The purpose of this program is to investigate the chemical and metallurgical effects produced in structural materials during exposure to alkali metals. The program is designed to guide the selection of container materials for sodium-cooled fast breeder reactor (LMFBR) systems and lithium-cooled space power reactor systems in which K serves as the Rankine-cycle working fluid. Forced circulation loop experiments of engineering scale are included in the test program.

Mass Transfer of Interstitial Impurities Between Vanadium Alloys and Sodium

J. H. DeVan R. L. Klueh
D. H. Jansen R. L. Wagner

Although vanadium alloys are highly resistant to dissolutive attack by Na, they are quite reactive with nonmetallic impurities in Na, particularly with C, N, and O. Accordingly, we have begun an investigation of the mechanisms by which vanadium alloys are attacked in Na at impurity levels typical of reactor service conditions. Our program is concerned with four basic aspects of the oxidation process for vanadium alloys in Na: (1) the partitioning of O between vanadium alloys and Na; (2) the effects of alloying additions of Cr and Zr on the diffusion coefficient of O in V; (3) the effects of Cr and Zr in V on oxide scale formation and on the dissolution of the alloys in Na; and (4) the solubility of V in Na as affected by the presence of O in either metal. We are also examining the kinetics of carbon and nitrogen transfer between vanadium alloys and types 304 and 321 stainless steel in a sodium circuit.

Oxygen Effects on the Compatibility of Vanadium and Sodium (R. L. Klueh)

We have conducted a series of static capsule tests to evaluate the oxygen partitioning characteristics of pure V and Na and have compared these results with our previous findings for the Nb-Na and Ta-Na systems.

This comparison was of interest because of the much greater solid solubility of O in V than in Ta or Nb.

The experimental system used for these studies consisted of a vanadium specimen in contact with Na in a vanadium container. The capsule, pictured in Fig. 5.1, was made from 0.75-in.-OD × 0.63-in.-ID seamless tubing, and the end caps and specimens were made from 0.060-in.-thick sheet. The results of chemical analysis of the vanadium components are presented in Table 5.1.

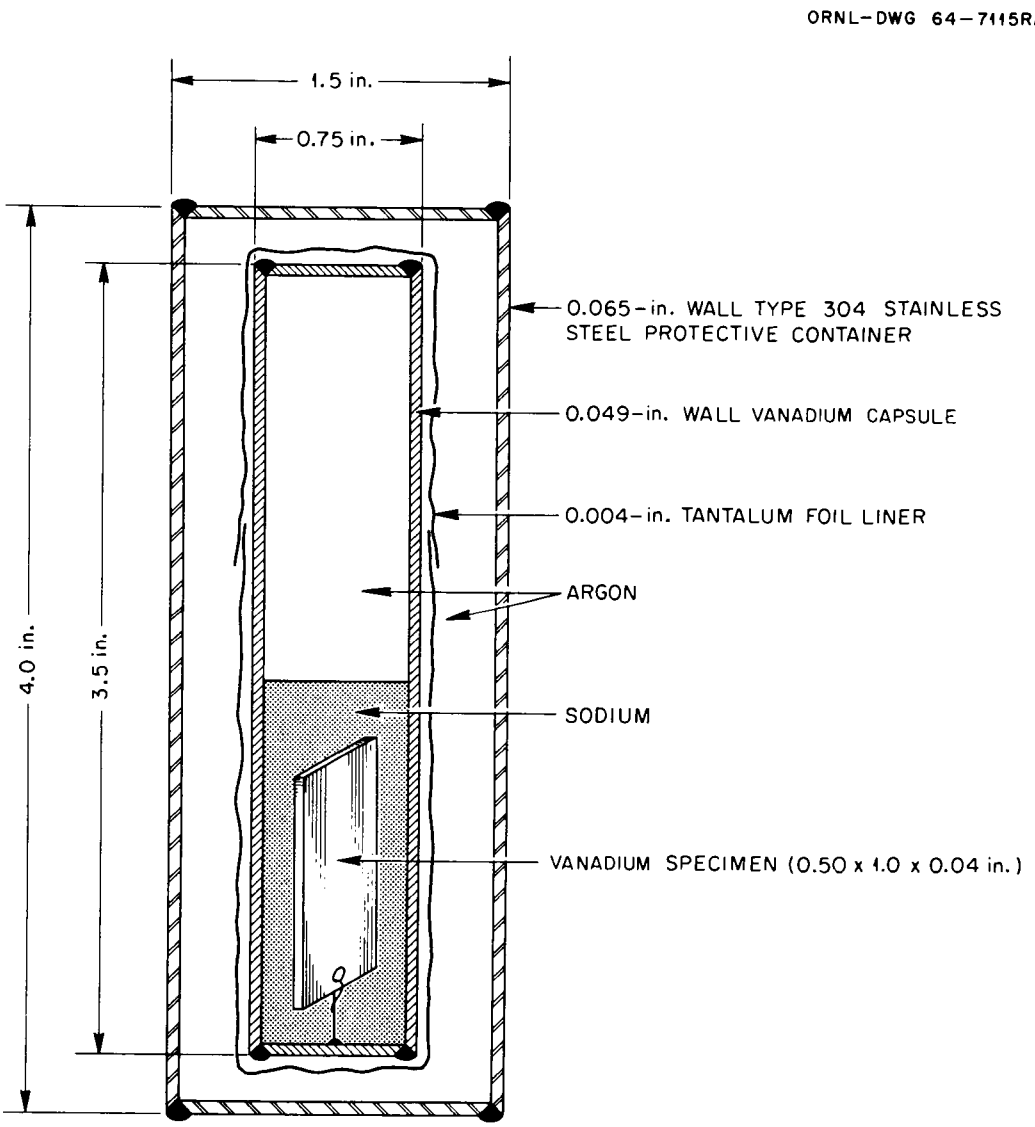

Fig. 5.1. Schematic Drawing of Corrosion Test Capsule Used to Study Oxygen Effects in Vanadium-Sodium Systems.

Table 5.1. Chemical Analysis of Vanadium Components Used in Sodium Compatibility Experiments

Impurity Element	Concentration,[a] ppm	
	Tubing	Sheet
O	1300, 1600	1900
H	2, 10	< 1
N	500, 580	570
C	170, 180	470
Ni	< 10	100
Si	80	80
Ti	40	20
Zr	10	20
Cr	< 4	40
Cu	10	20
Fe	200	500
Mg	20	40
Mn	4	80

[a]Two values indicate duplicate determinations.

The vanadium capsule was protected by an outer container of type 304 stainless steel, and both capsules were sealed under 1 atm of purified Ar. We varied the concentration of O in the Na of the different capsules by adding weighed amounts of Na_2O to the Na and conducted tests at each purity level for 500 hr at 600°C and for 100 hr at 800°C. After testing, each capsule was inverted and quenched in liquid N. The concentration of O in the vanadium specimens and capsules was determined by vacuum fusion analysis; the concentration of O in the Na was calculated by an oxygen mass balance; the vanadium dissolved in Na was analyzed by reacting the Na with isopropyl alcohol and spectrographically determining the concentration of V.

Table 5.2 shows the weight changes and concentrations of O in specimens after exposure to Na. Weight was gained in proportion to the amounts of Na_2O added to the Na before test. A mass balance for O showed that essentially all of the O added had transferred to the

Table 5.2. Weight Changes and Oxygen Analyses of Vanadium Specimens Exposed to Sodium Containing Various Amounts of Na_2O

Temperature (°C)	Initial Oxygen Content of Sodium (ppm)	Specimen Weight Gain[a] (mg)	Final Oxygen Content of Specimen[b] (ppm)
600	50	0.2	1900
	250	0.3	1900
	550	0.4	2100
	850	1.1	2200
	1300	1.6	2300
800	50	0.0	1900
	250	0.0	1900
	550	0.2	1900
	850	0.6	2000
	1250	1.1	2000

[a]Specimen dimensions: 1 × 0.5 × 0.040 in.

[b]Initial oxygen content of vanadium specimen was 1900 ppm.

vanadium specimen and capsule during test. The results differ significantly from those obtained for Nb at 600°C under similar test conditions. As shown elsewhere,[1] Nb containing 70 ppm O acquired O only when the concentration of O in the Na exceeded 1000 ppm, and even then the amount of O transferred was only a small fraction of the total amount present. Thus, the oxygen partitioning coefficient (i.e., $\frac{\text{ppm O in solid metal}}{\text{ppm O in alkali metal}}$) is considerably greater for the V-Na system than for the Nb-Na system.

The amount of V present in the Na after these tests showed little dependence on the amount of O initially added to the Na, but the vanadium concentration did change with test temperature. At 600°C the Na contained only about 40 ppm V, while at 800°C the level was about 200 ppm V. This behavior is in contrast to that of the Nb-Na system,

[1]R. L. Klueh, "Oxygen Effects in the Niobium-Sodium System," pp. 125–126, this report.

in which metal concentrations in the Na increase sharply with additions of O to Na (ref. 1). This further indicates that the O added to Na was rapidly gettered by the vanadium capsule and specimen.

One further distinction between Nb and V concerns the effect of the initial concentration of O in the refractory metal on its attack by Na. At concentrations as high as those initially present in our vanadium samples (1600 to 1900 ppm O), Nb and Ta at 600°C undergo rapid intergranular attack by Na. Vanadium samples in these tests, however, showed no evidence of attack by Na. We believe this difference in behavior reflects the difference in the solid solubility of O in the two materials. At 600°C, 1900 ppm O in Nb is above the solubility limit, whereas this level is only about 20% of the solubility limit of V.

Interstitial Mass Transport Between Type 300 Series Stainless Steels and Vanadium Alloys (J. H. DeVan, D. H. Jansen)

Shown in Fig. 5.2 is the design we have adopted for a thermal convection loop to evaluate the transport rates of N and C between vanadium alloys and stainless steels in a sodium circuit. Heated portions of the loops are being constructed of V or its alloys, and the isothermal and cooled portions are of either type 304 or 321 stainless steel. Brazed bimetallic joints are used to couple the dissimilar loop sections. Figure 5.3 shows the joint design, which is patterned after that used for earlier Nb–1% Zr–stainless steel bimetallic loop studies. Several joints fabricated by this technique have been examined metallographically, one after four thermal cycles between room temperature and 800°C. All of the joints appeared sound, and all passed a leak check with a helium mass spectrometer.

Mass transfer rates and interstitial effects on mechanical properties will be monitored in these loop systems by means of insert specimens placed in both the heated and cooled sections of the loop. The inserts, shown in Fig. 5.4, are small, round tensile specimens (1/8-in.-diam gage section) that are joined end-to-end to form a continuous, concentrically positioned rod running the entire length of each vertical loop section.

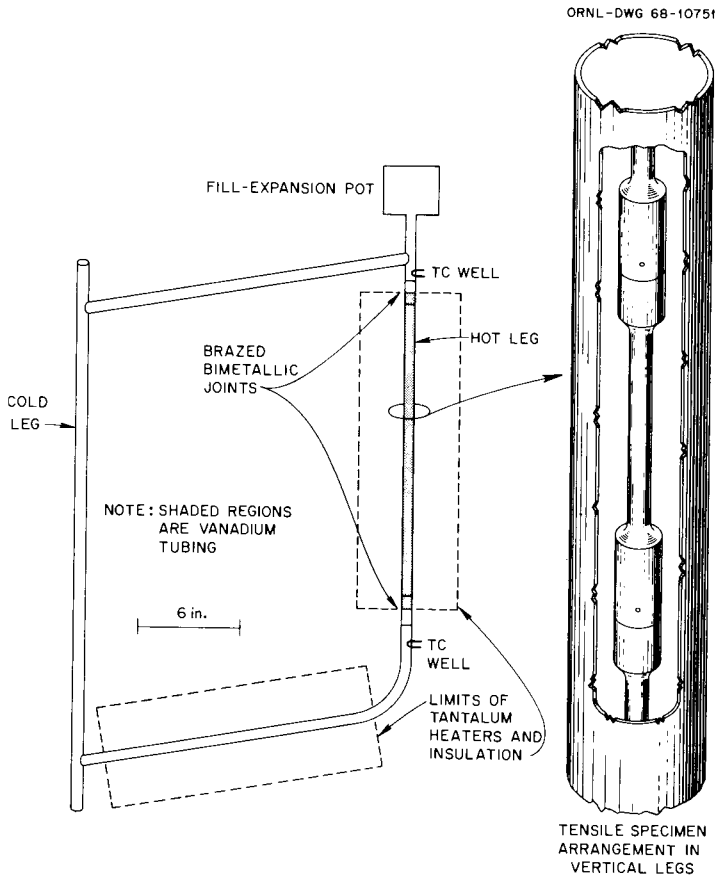

Fig. 5.2. Bimetallic Thermal Convection Loop Designed to Study Interstitial Mass Transport Between Vanadium Alloys and Sodium.

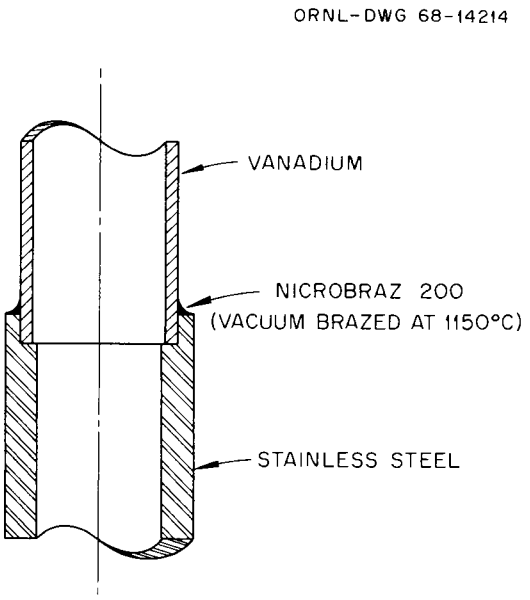

Fig. 5.3. Braze Joint Design for Vanadium-Stainless Steel Thermal Convection Loop System.

Fig. 5.4. Insert Specimen Designed for Bimetallic Thermal Convection Loop Studies.

We have completed the fabrication of three loops with hot-leg sections of pure V and cold-leg sections of type 304 stainless steel. Two similar loops with type 321 stainless steel cold legs are also being constructed. Operation of these loops is awaiting the fabrication at ORNL of developmental V-Cr alloys and the delivery of Westinghouse Vanstar alloys. Both types of materials will be used as insert specimens.

Interstitial Effects on Mechanical Properties of Vanadium Alloys
(R. L. Wagner)

As discussed above, the pickup of interstitial impurities from Na is a critical consideration in the development and use of vanadium alloys for LMFBR cladding. Of special concern are the effects this contamination may have on creep properties and the ductile-to-brittle transition temperature of candidate alloys. For this reason, mechanical properties rank very high in the list of effects to be evaluated in our analysis of corrosion specimens. To supplement this effort, we are also

planning investigations of the mechanical properties of specimens to which contaminants have been added from a low-pressure ($< 10^{-9}$ torr) gas. This possibility was suggested in conjunction with absorption studies that are under way to provide oxygen-doped vanadium samples for corrosion testing. We plan to correlate the creep properties of alloys contaminated with single impurities from a gaseous atmosphere with the effects on creep brought about by corrosion exposures.

Data recently published by Hörz[2] show that above 900°C engassing kinetics for pure V in rarified O_2 are controlled by the rate at which O_2 arrives at the vanadium surface and that the reaction rate is therefore directly proportional to pressure. We are extending these findings to temperatures of interest for our creep studies, 500 to 900°C.

Compatibility of Stainless Steel and Insulation in LMFBR Systems

A. P. Litman

This new task is a two-year effort designed to guide the selection of containment piping and thermal insulation for LMFBR systems and is in direct support of the Fast Flux Test Facility (FFTF). The structural materials for the FFTF closed sodium loops, while not yet fixed, will probably be types 304, 316, or 321 stainless steel operating at 370 to 760°C. A question not yet factored into the criteria for selection of materials for these loops is the extent to which the long-term oxidation resistance of these stainless steels will be affected by interaction with thermal insulating materials or a sodium leak. This task includes a comprehensive study of the literature and tests of the compatibility of stainless steels and thermal insulation in air and inert gas, with and without the presence of Na.

---

[2]G. Hörz, Z. Metallk. 59, 180 (1968).

Effect of Insulation on Oxidation of Stainless Steel (C. D. Bopp)

Years of experience have led to reliable insulation practices for dynamic sodium systems constructed of stainless steels; but most of this is highly empirical, and information is lacking in the areas of long-term, cyclic, and transient effects.

Table 5.3 shows some of the typical insulation materials used at ORNL and their chemical compositions, basically silica and alumina. The insulations are generally manufactured by jet blasting a molten mixture of minerals to produce relatively short ceramic fibers. Spinning produces longer fibers. By combining different lengths of fibers with or without a binder by various techniques, manufacturers can produce papers, blankets, felts, ropes, braids, boards, blocks, textiles, tubes, and cast shapes. In addition to the materials detailed in Table 5.3, a wide variety of more expensive insulations are available, suitable for LMFBR service to 760°C. These include almost pure oxides [i.e., SiO_2 (Glasrock, Min-K 1301, Refrasil, Astroquartz)], porous Al_2O_3, and porous ZrO_2.

Oxidation and Catastrophic Oxidation of Stainless Steel. — The resistance of stainless steels to mildly oxidizing conditions is well known and is attributed to the protective nature of chromium-rich oxides that form on the surface of the metal. Experience and examination of available thermodynamic data indicate that in the temperature range of interest, to 760°C, no reaction should occur between the oxides of Fe, Cr, or Ni on stainless steel and pure alumina or silica. However, the presence of low-melting and volatile oxides, S, and the halogens, combined or in elemental form, can lead to catastrophic oxidation at the interface between base metal and oxide. One of the possible causes is believed to be the formation of liquid or semiliquid phases that destroy the protective oxides. The result is the onset of extremely rapid corrosion accompanied by the formation of voluminous corrosion products. Numerous studies have demonstrated that oxidation occurs at normal, often parabolic, rates up to the melting point of binary or ternary eutectic mixtures (including the foreign substance). Above these definite temperatures, oxidation occurs at a linear or accelerating

Table 5.3. Typical Thermal Insulating Materials Presently Used for Stainless Steels

Aluminum Silicate Fibers Trade Name	Calcined Diatomaceous Silica Trade Name	Nominal Analysis, wt %							
		Al_2O_3	SiO_2	Fe_2O_3	B_2O_3	TiO_2	Na_2O	CaO	MgO
Fiberfrax[a]		51	47		0.6				
Kaowool[b]		45	51	1	0.1	2	0.2	0.1	Trace
Thermoflex[c,d]		42	50			6			
	Superex[c]	6	81	5		0.1		1	6

[a]Total Fe_2O_3, CaO, and MgO = 0.5 wt %. Manufactured by Carborundum Company.

[b]Manufactured by Babcock & Wilcox Company.

[c]A Johns-Manville Company product.

[d]Total other impurities which probably consist of Fe_2O_3, B_2O_3, Na_2O, CaO and MgO = 2 wt %. The analysis does not include a small amount of organic binder.

rate and is catastrophic. There are several other mechanisms by which oxidation may be accelerated by impurities. A common one is an increase in the semiconductivity of the oxide film, which may enhance reactions at the interface of oxide and gas.[3] Another possibility is an increase in the number of cation vacancies, although it has been shown that a number of thermodynamic variables must be considered in this case.[4] Though several postulates have been proposed to explain the actual details of the corrosion mechanism(s), much disagreement still exists. This is not surprising, since even the normal oxidation behavior of stainless steels still has not been described by a unified mechanism.

Numerous examples of catastrophic oxidation have been reported, including the corrosion of boiler tubes because of the presence of V or Na in low-grade fuels and Na or S in the atmosphere. Water vapor in the air has been found to aggravate this type of corrosion.[5] Furnace manufacturers have long been plagued with extensive corrosion of heater elements due to the presence of impurities such as PbO, MoO_3, WO_3, V_2O_5, Na_2O, Na_2SO_4, and NaCl in the furnace insulation. At ORNL, certain types of Sauereisen cements containing Na_2SiO_3 have produced catastrophic oxidation of type 316 stainless steel at 760°C (Fig. 5.5).

Oxidation resistant alloys that are particularly susceptible to catastrophic oxidation include types 316 and 317 stainless steel, 19-9 DL, N-155, Refractaloy B, and 16-25-6 alloy. All of these alloys contain Mo, and the 19-9 DL and N-155 alloys also contain 1 to 2% W. Both Mo and W form highly volatile, mobile oxides. It is believed that the molybdenum oxide vapors that evolve on heating accumulate in stagnant atmospheres cause catastrophic attack.

Experimental Approach. — Because of the short time allowed for this portion of the program, our experimental approach for determining the effect of insulation on the oxidation of stainless steel is reduced to an investigation of whether various commercial thermal insulations will

---

[3]J. H. Eriken and K. Hauffe, Z. Physik. Chem. 59, 332 (1968).

[4]K. Hauffe, Oxidation of Metals, p. 304, Plenum Press, New York, 1965.

[5]H. L. Logan, Corrosion 17, 185t (1961).

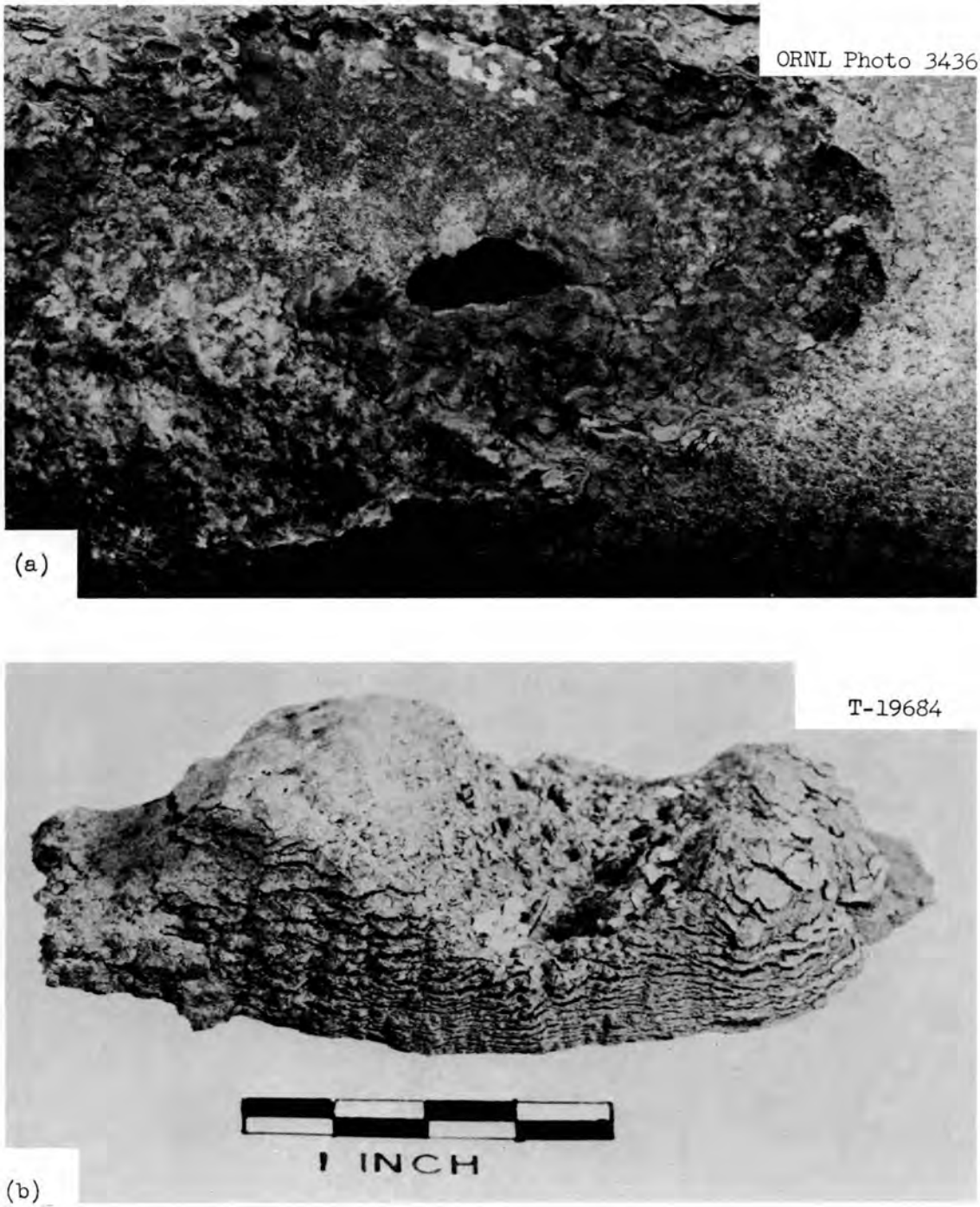

Fig. 5.5. Area of Catastrophic Oxidation Induced by Contact with Sodium Silicate that Produced Failure of Type 316 Stainless Steel 2-in. Sched-40 Pipe at 760°C. (a) Zone of failure after removal of oxide products; (b) oxide products.

induce catastrophic oxidation. If we find this, we will identify the impurity responsible. If the condition is only active during local atmosphere stagnation, we will characterize the system to determine preventative conditions.

A schematic of our experimental setup — almost complete at the time of this writing — is shown in Fig. 5.6. Specimens (coupons or tubes)

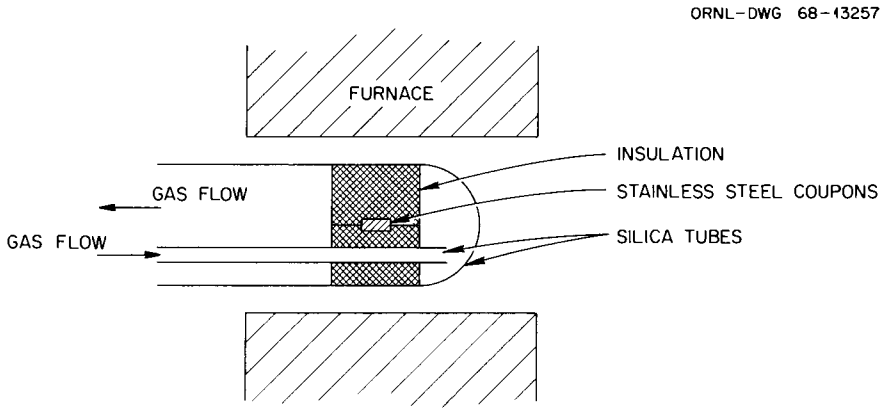

Fig. 5.6. Experimental Arrangement for Determining Compatibility of Stainless Steel with Thermal Insulation.

will be packed in insulation and oxidized isothermally in air or other atmosphere with a given moisture content. In some instances, the permeability of the insulation will be controlled by compressing it to various extents, and air will be forced to flow through the insulation at a given rate. In other tests, the space between the insulation and the specimens will be varied. The amount of oxidation will be determined by oxygen consumption, weight change after descaling, standard metallographic techniques, electron microprobe traces, and/or other means as necessary.

The effect of surface condition — often important in oxidation studies — will be investigated by pretreatment of the specimens. It is already known that work hardening affects the chromium content (and therefore the protective nature) of the scale that initially forms when stainless steels are heated. We will study the effect of moisture by regulating the moisture content of the gas, and in most cases we will remove moisture from the insulation with circulating dry air at about

300°C before test. Thermal cycling will be used to test the resistance of the surface scale to spalling. In some experiments, we will study the effect of stress by the use of C-ring specimens fabricated from tubing.

Effect of Sodium on Oxidation of Stainless Steel — Insulation Couples (C. D. Bopp)

Because leaks are always possible in closed sodium systems, we intend to record and categorize the events that take place during a sodium leak in stainless steel containment lagged with insulation. It is well known that the presence of sodium liquid or vapor greatly aggravates the oxidation of high-temperature alloys. As previously discussed, the fluxing of previously formed protective scales is a particularly destructive mode of attack. In this respect, the mixtures with relatively low melting points (shown below) that may form by interaction of Na, O, aluminum silicate insulation, and metal in LMFBR systems are important:

Components	Melting Temperature, °C
Na_2O-Fe_2O_3-SiO_2	800
Na_2O-Fe_2O_3-Al_2O_3-SiO_2	715, 728
Na_2O-FeO-SiO_2	667
Na_2O-FeO-Al_2O_3-SiO_2	< 667
Na_2O-MoO_3	510

For simplicity, we have omitted consideration of Na_2O_2 and NaOH, although these compounds could also form under the proper conditions. The Na_2O_2 is most likely to be present at lower temperatures (< 550°C), and some NaOH will be formed in moist gases. The presence of these additional components may lower the melting points substantially below the values listed above.

Small Leaks. — In the lower range of temperatures for LMFBR systems, a small leak may be self-sealing. (This possibility would be a function of the absorbency of the insulation.) In such cases the attack on stainless steel would be minimized. At these lower temperatures, a small leak — even if it were not sealed by Na soaking into the insulation — would probably be less destructive, be more localized, and require less

extensive repair to the affected areas. In any event, corrosion will be minimized if the leak is detected at the earliest possible moment and the affected insulation is replaced.

We will examine the problem of small leaks with the test device shown in Fig. 5.7. The leak is simulated by unplugging a small hole in a stainless steel capsule containing Na. After a given time, the amount of corrosion of the capsule is determined. Leakage will be studied in Ar as well as in air, since the data for Ar will be applicable to installations where an inert cover gas is used. It is possible that in Ar the Na may react with the insulation to produce products that corrode stainless steel, although in air it is likely that most of the corrosion will be produced by Na_2O and Na_2O_2.

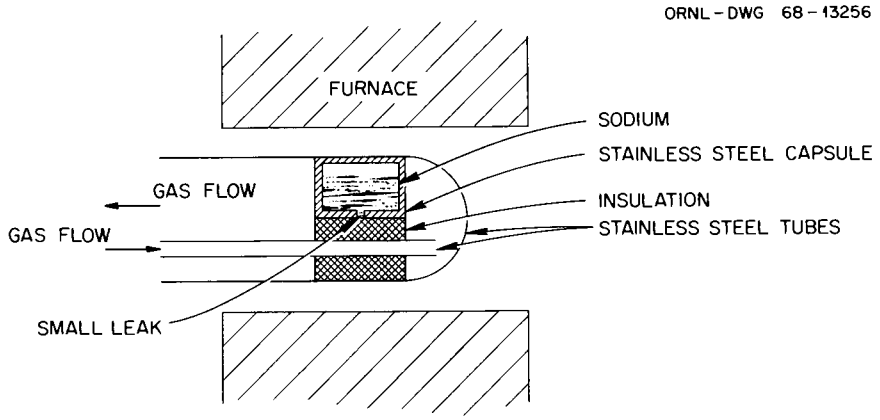

Fig. 5.7. Experimental Setup for Evaluating the Effects of Small Sodium Leaks in Stainless Steel–Thermal Insulation Systems.

Large Leaks. — It is probable at higher temperatures in LMFBRs that any leak will soon become a large leak. In order to test this and the influence of various insulations in proximity to the leak, we are constructing the test device shown in Fig. 5.8. In order to simulate as closely as possible LMFBR and FFTF conditions, we will heat the test pot with an immersion heater. This will induce temperature gradients similar to LMFBR conditions. The sodium pressure against the leak (and the sodium flow) will be maintained by inert gas pressure.

Leak Detection. — Early detection of leaks is important in LMFBR systems, and continuous sampling of the air confined by the insulation

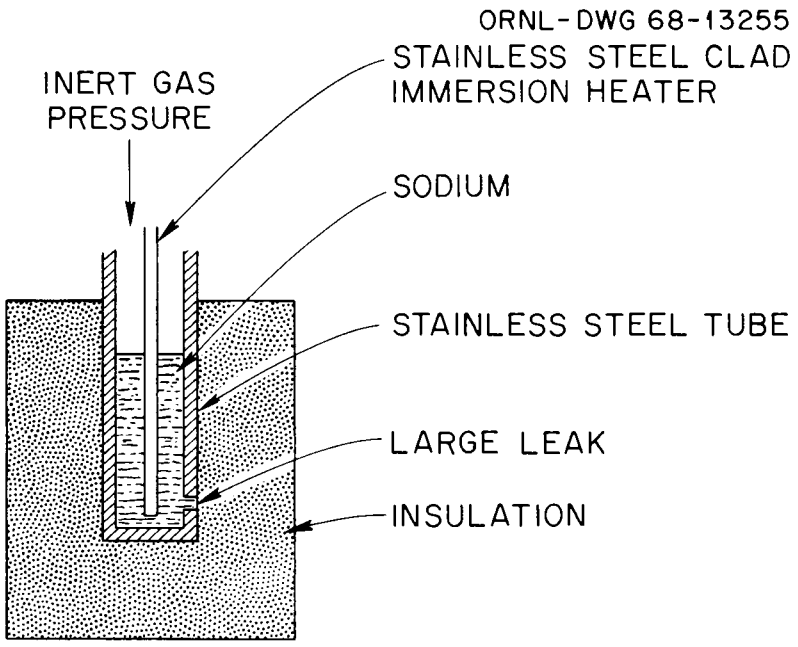

Fig. 5.8. Schematic of Pot Test for Determining Effect of a Large Sodium Leak in Stainless Steel Containment Lagged with Thermal Insulation.

may accomplish this. There are several possibilities for the sensing device for such a system, but perhaps a standard coulometric instrument[6] sensitive to oxidizing vapors will prove satisfactory. We will investigate the sensitivity of this method by using it to monitor the Na_2O aerosol produced in some of the experiments already described.

Corrosion of Refractory Alloys in Lithium, Potassium, and Sodium

J. H. DeVan A. P. Litman W. R. Huntley

Auxiliary electrical or ion-propulsion requirements for space vehicles necessitate power plants of high efficiency that will operate at high temperatures. For these applications, nuclear power systems have been proposed in which alkali metals are used to transfer heat, drive a turbogenerator, and lubricate rotating components. Accordingly, we are investigating the corrosion properties of candidate alkali metals,

[6]R. L. Chapman, Instr. Control Systems 41, 79 (1968).

primarily Li and K, under conditions of interest for space applications. Because of the relatively high temperatures (> 1000°C), the investigation is concerned largely with refractory metal container materials.

Compatibility of Boiling Potassium with Refractory Alloys

Refluxing Capsule Experiments (J. R. DiStefano). — We have reached a logical termination point in our study of the effects of refluxing K on refractory metals. Accordingly, although two tests in operation will be continued to 5000 hr, we plan no additional tests. A topical report has been written[7] covering all but the most recent tests, some of which are discussed below.

We have examined two W–26% Re refluxing capsules which, as reported last quarter,[8] operated for 5000 hr at a boiler-condenser temperature of 1250°C. The two capsules were of similar dimensions (0.86 in. outside diameter × 0.040 in. wall thickness × 12 in. long), but one was fabricated from a powder metallurgy product and the other from an arc-melted ingot. Both were tested in the as-extruded condition.

Our examination of the powder-product capsule showed no measurable corrosion effects in either the condenser or boiler sections. However, the capsule fabricated from arc-melted material, as shown in Fig. 5.9, contained a ring of crystalline deposit in the condenser section about 1/2 in. below the top end cap. Figure 5.10 shows the metallographic appearance of the wall of this capsule at several positions along its length. The deposit is clearly visible in the upper-left photomicrograph and is seen to be integral with the condenser wall. The boiler wall has undergone subsurface attack, the depth increasing with distance down the boiler. An electron-probe microanalysis of the deposit showed it to consist of almost pure W. Results of the microprobe scan are shown

---

[7] J. R. DiStefano, Refluxing Capsule Experiments with Refractory Metals and Boiling Alkali Metals, ORNL-4323, in preparation.

[8] J. R. DiStefano, Fuels and Materials Development Program Quart. Progr. Rept. June 30, 1968, ORNL-4330, p. 82.

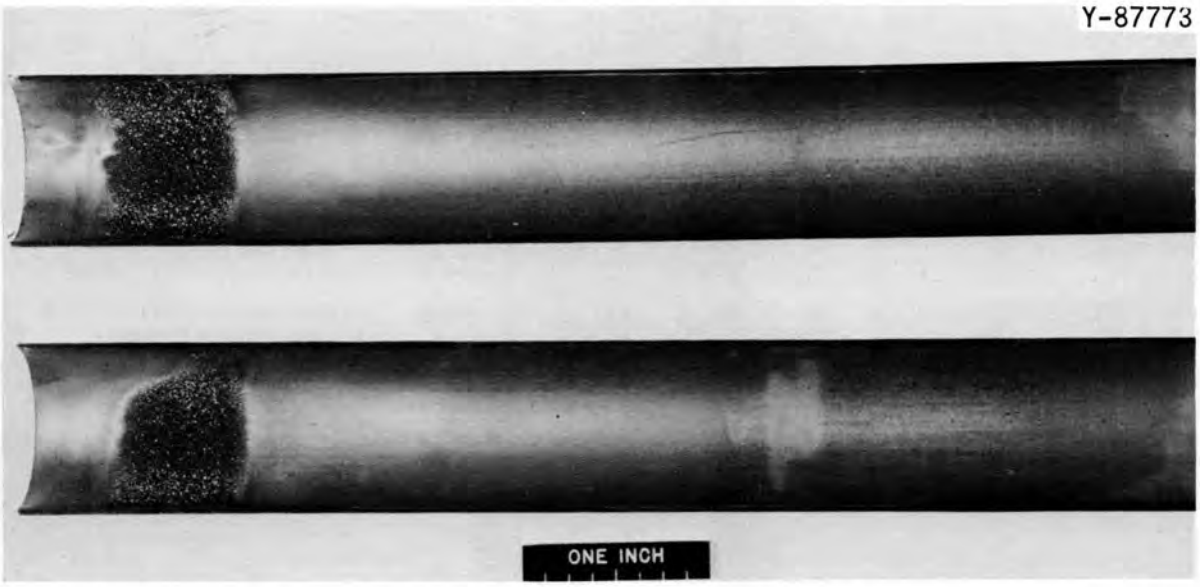

Fig. 5.9. Tungsten Mass Transfer Deposit in Condenser Section of Arc-Melted W–26% Re Capsule Containing Boiling Potassium for 5000 hr at 1250°C.

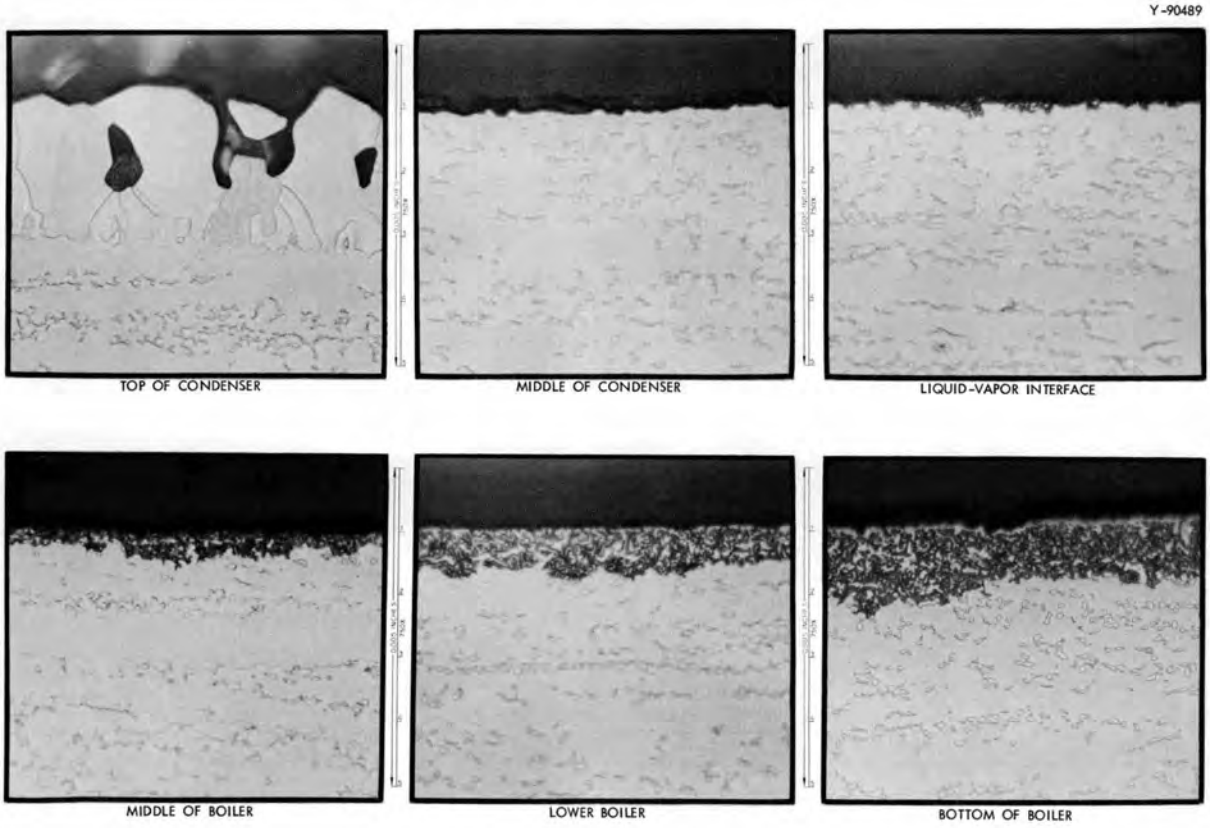

Fig. 5.10. Metallographic Appearance of W–26% Re Refluxing Capsule that Operated with Boiling Potassium for 5000 hr at 1250°C. (Capsule was made from an arc-cast extrusion.)

in Fig. 5.11. This result correlated with analysis of the boiler wall, which, as shown in Fig. 5.12, was depleted of W and enriched in Re in the attack zone.

In speculating as to the cause of the preferential tungsten mass transfer in this capsule, we must account not only for the inverse nature of the deposition (i.e., in the condenser rather than the boiler), but also for its occurrence in only one of the two W–26% Re capsules tested. We believe that none of the classical solution-deposition modes put forth for refluxing potassium systems is compatible with our observations and that some other mechanism must be operating. Results observed in our pure niobium capsules, reported last time,[9] may give a clue to this other mechanism. We noted in the case of pure Nb that, as a consequence of depletion of O from the condenser regions, we acquired a small amount of O in the K in the boiler region. Based on Nb-K static capsule tests, the level of O in the K was still far below that which should have led to migration of O into the Nb or to serious oxidative corrosion. Nevertheless, we have observed both effects in refluxing systems. This strongly suggests that, because of the boiling process, the activity of O at the boiler surface locally exceeds that associated with the "mixed-mean" concentration of O. Such an effect could also explain the deposits of W at the top of the capsule. Free energy considerations suggest that, at 1200°C, the oxygen activity needed to form WO_2 is considerably below the activity reached in a saturated solution of O in K. If the local oxygen activity were sufficient to form WO_2, it is not unreasonable, in view of the relatively high vapor pressure of this oxide, that WO_2 molecules could be swept along with potassium vapor to the condenser.[10] Once outside the region of locally high oxygen activity, any WO_2 molecules would encounter strongly reducing conditions. So long as they

---

[9] J. R. DiStefano, Fuels and Materials Development Program Quart. Progr. Rept. June 30, 1968, ORNL-4330, pp. 75–84.

[10] A similar conclusion could be drawn for thermally stable compounds of the type $K_x W_y O_z$. [See H. Kessler, A. Hatterer, and A. Herald, "Action of Alkali Metal Vapours on the Trioxides of Molybdenum and Tungsten," pp. 465–473 in The Alkali Metals, Chem. Soc. (London) Spec. Publ. 22. The Chemical Society, London, 1967.]

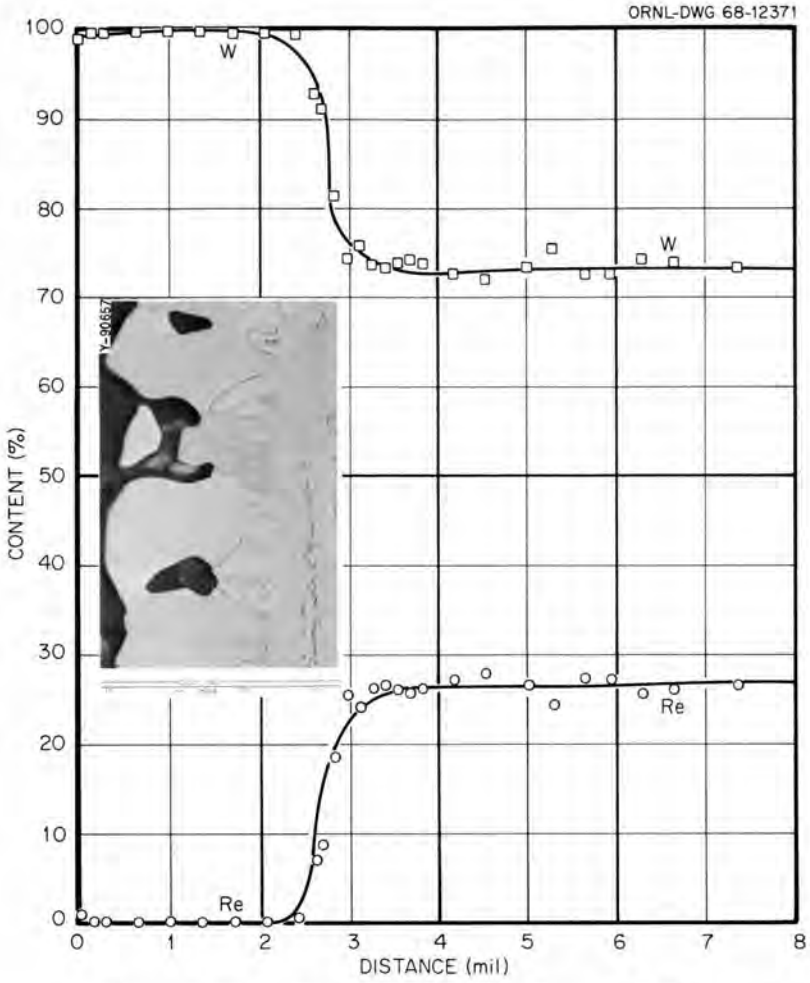

Fig. 5.11. Electron-Probe Scan of Condenser Section of W–26% Re Capsule After 5000 hr in Potassium at 1250°C.

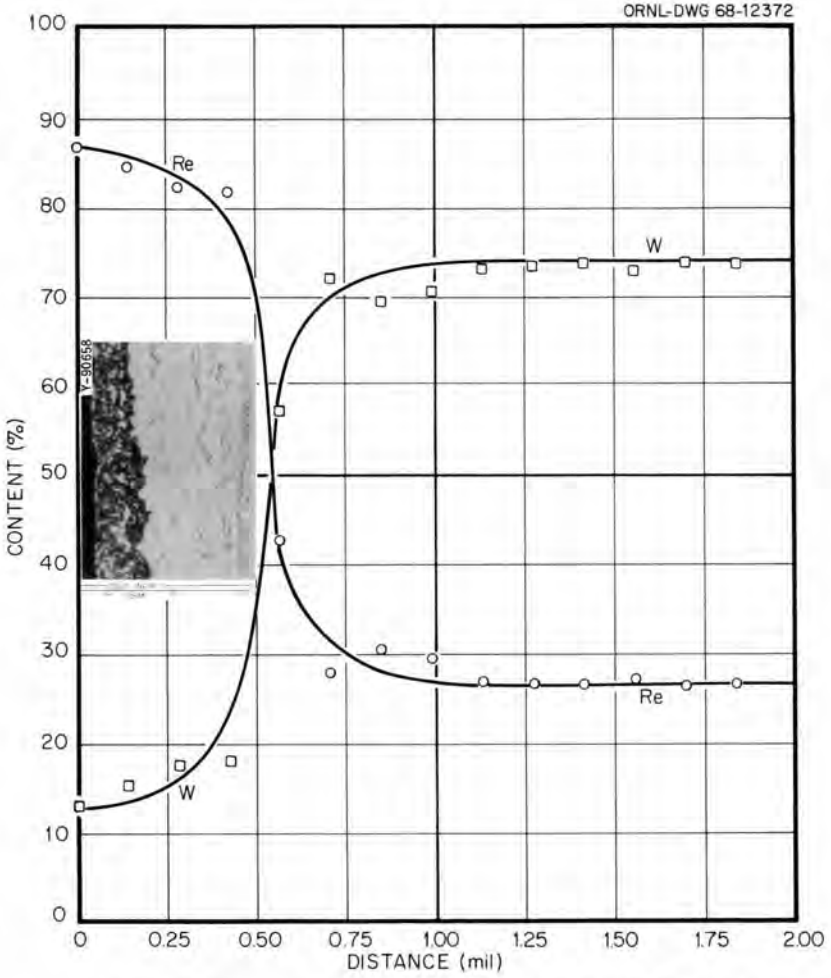

Fig. 5.12. Electron-Probe Scan of Boiler Region of W–26% Re Capsule After 5000 hr in Potassium at 1250°C.

were surrounded by vapor, however, reaction would be dependent on collisions in the gas state, a process sufficiently slow that some of the WO_2 molecules (acting as a noncondensible) could conceivably reach the top of the capsule. Here they would remain trapped until reduction occurred, probably as a heterogeneous reaction at the capsule wall. Oxygen would then be recycled via the condensate back to the boiler region.

Whatever the reasonableness of the above speculation, there is evidence to support the belief that O contributed to the observed mass transfer. This is based on the fact that the arc-melted W–26% Re capsule in which mass transfer was found originally contained about three times more O (about 60 ppm) than the deposit-free capsule (about 20 ppm O). As a consequence of this, the level in the boiler wall in the former capsule increased to almost 140 ppm O, while that in the latter capsule did not increase measurably above the starting level of about 20 ppm O. Neither test showed any measurable amount of W or Re in the K after operation.

Natural Circulation Boiling Potassium Loops (D. H. Jansen). – As reported last quarter,[11] we have concluded a series of natural circulation boiling loop experiments designed to evaluate the effects of boiling K on refractory metals. The final loop in this series was constructed of the molybdenum-base alloy TZM and was operated under the following test conditions.

Boiler-condenser temperature	1200°C
Subcooler temperature	650°C
Condensing rate	R total = 42 g/min
	$\frac{dR}{dA} = (0.13\ g\ min^{-1}\ cm^{-2})$

The loop completed 4400 hr of a scheduled 5000-hr test run and was stopped by a creep failure in the vapor line.

The condition of the loop after operation is shown in Fig. 5.13. Only the upper left-hand corner of the loop, where the failure occurred,

[11] D. H. Jansen, Fuels and Materials Development Program Quart. Progr. Rept. June 30, 1968, ORNL-4330, pp. 84–85.

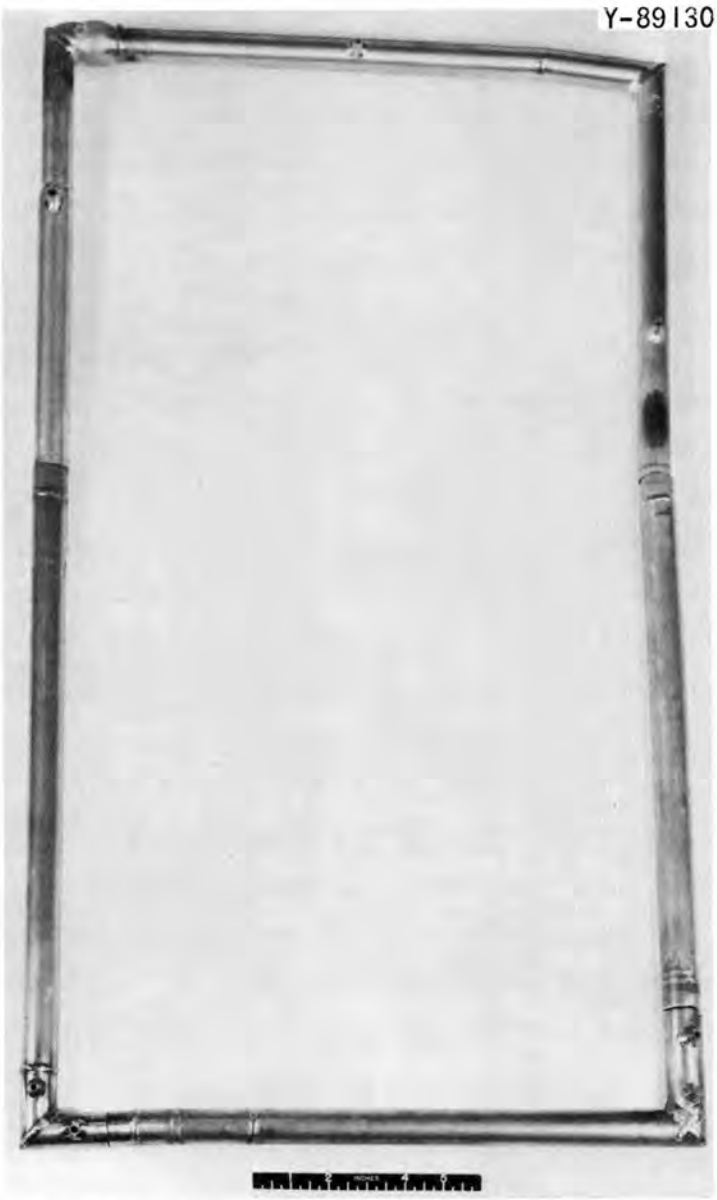

Fig. 5.13. Alloy TZM—Boiling Potassium Loop Showing Configuration of Mitered Corners. Rupture is at upper left-hand corner.

showed any change in macroscopic appearance. As shown at a higher magnification in Fig. 5.14, the failure occurred in a short section of tubing that joined the horizontal dryer section to the vertical condenser leg. This short tubing section was part of an original dryer segment that had to be replaced after 1300 hr of operation because of a similar creep failure under the dryer heater upstream of the later failure. The short section was left in place because (1) it was located well away from the

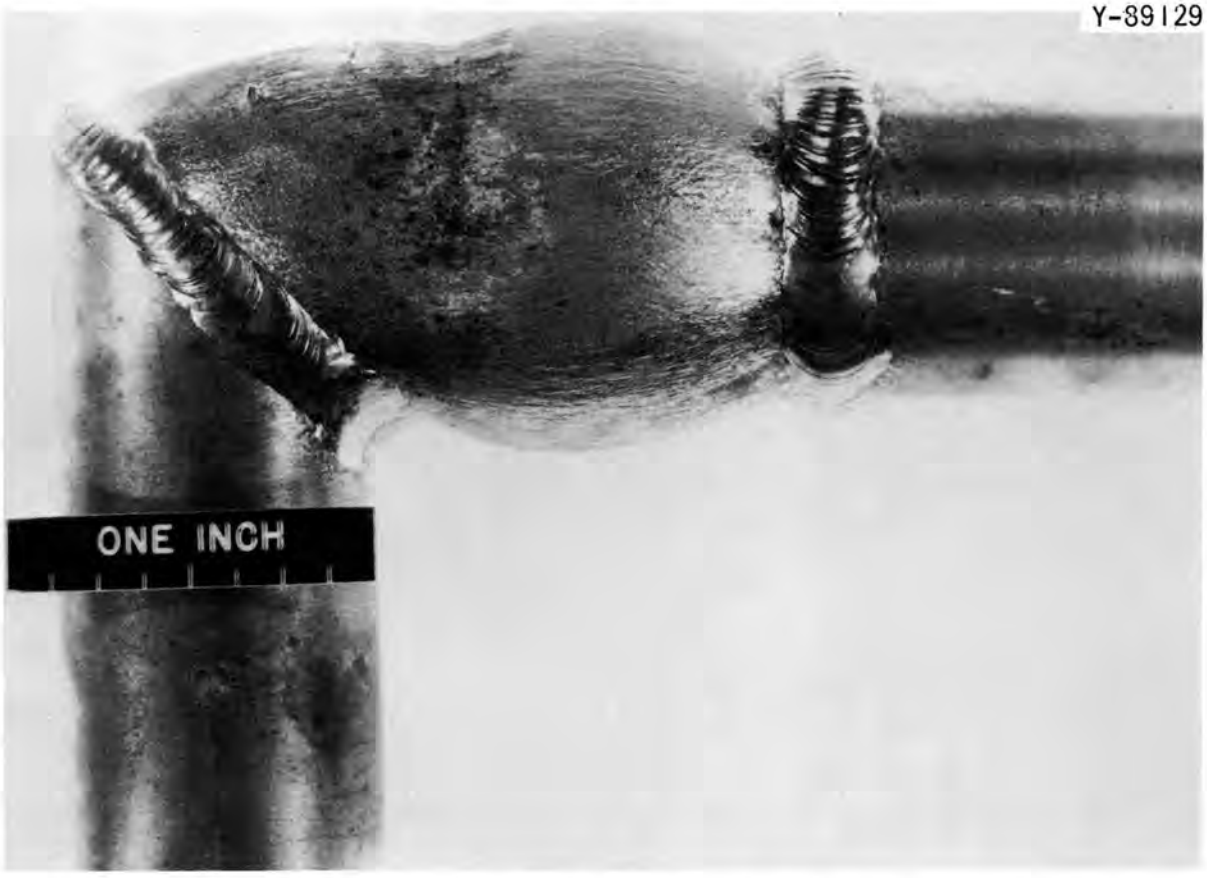

Fig. 5.14. Failure Area of TZM Loop Showing Deformation of Tubing Comprising the Vapor Carryover Line. Vertical leg is top of condenser area.

dryer heater, (2) it had shown no deformation in 1300 hr, and (3) the new dryer section was more easily attached by not running it all the way to the miter joint (Fig. 5.14). However, this short section of the original dryer did constitute a weak link, since it had less wall thickness than either the new dryer line or the adjoining condenser leg. Although long-term creep data on TZM are limited, the available data suggest that the failure of this section can be explained by time-temperature-stress conditions without recourse to a weakening effect of the K.

Weight changes of insert specimens contained in the condenser and subcooler sections of this loop were discussed last quarter.[11] Specimens from the condenser showed little weight change, while subcooler specimens gained an average of 10 mg/cm^2. The metallographic appearance of representative inserts from these respective loop sections is compared in Fig. 5.15. Note that recrystallization took place in both regions with

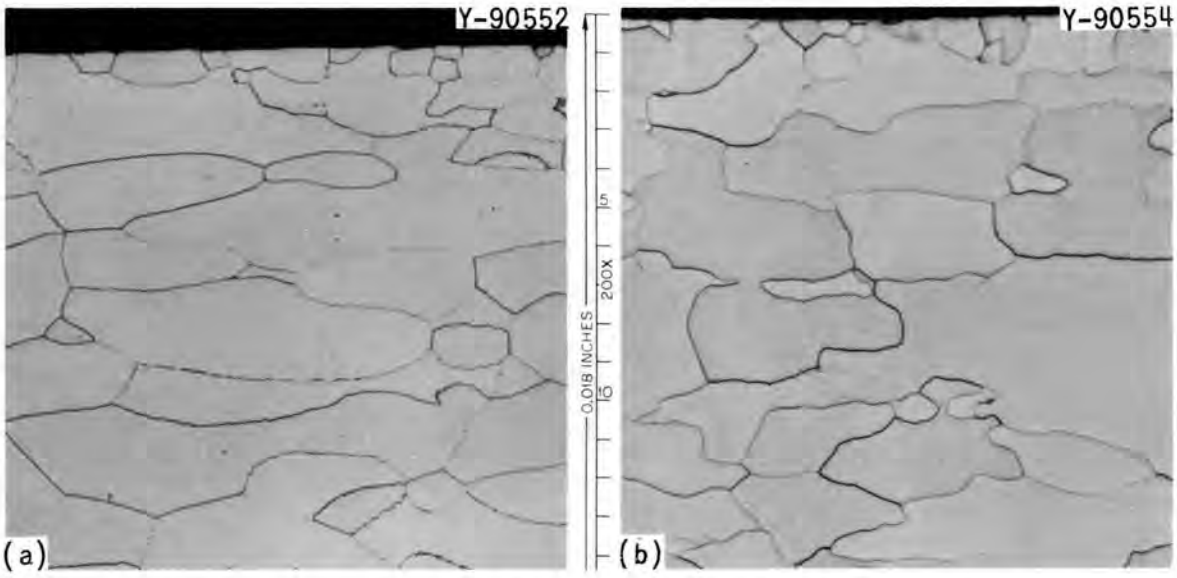

Fig. 5.15. Views Showing Inside Surface of (a) Boiler at Approximate Liquid-Vapor Interface, About 1250°C, and (b) Horizontal Vapor Line, About 1200°C. The material in (b) was from a more recent and purer heat. Etchant: H_2O-H_2O_2-H_2SO_4.

the exception of a narrow zone bordering the exposed surface. We are examining this region to determine what chemical changes may have occurred to cause the apparent grain stabilization.

Specimens from the boiler and dryer regions showed no changes from before-test specimens other than recrystallization and grain growth (Fig. 5.16). Specimen temperatures in the lower subcooler region were apparently below the recrystallization threshold, and these specimens were entirely similar in appearance to before-test specimens.

Forced Circulation Boiling Potassium Loop Tests (FCL-8) (B. Fleischer, C. W. Cunningham). — For several years we have been evaluating the corrosion and erosion properties of refractory alloys in K using forced convection loop systems. A D-43 alloy loop with D-43 test section (FCL-8) was the third in a series of loops designed to evaluate the effects of boiling potassium liquid and high velocity potassium vapor on niobium-base alloys and on TZM. Operating conditions of this loop were discussed last quarter.[12] During this reporting period the loop was removed from

[12]B. Fleischer and C. W. Cunningham, Fuels and Materials Development Program Quart. Progr. Rept. June 30, 1968, ORNL-4330, pp. 85–97.

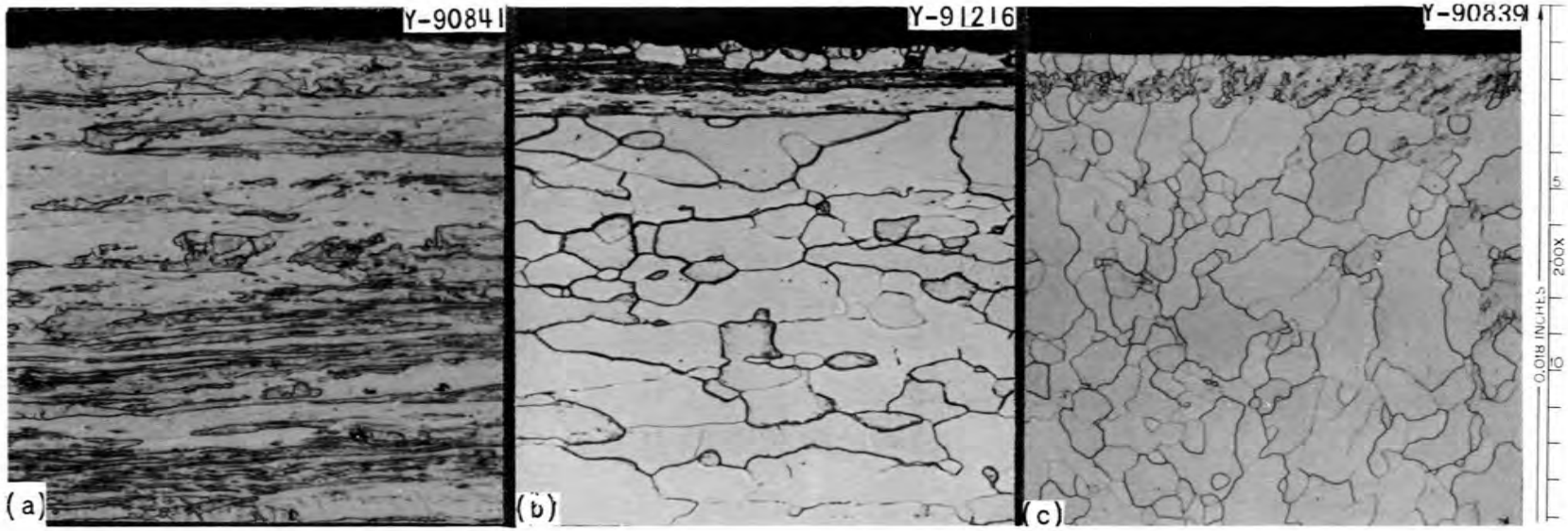

Fig. 5.16. Insert Material (a) Before Test, (b) After Test, and (c) at the Approximate Liquid-Vapor Interface. Etchant: H_2O-H_2O_2-H_2SO_4.

the vacuum chamber in which it was operated and sectioned for metallurgical examination. We are now modifying the vacuum system in preparation for the next test loop.

Liquid metal removal. The potassium inventory was drained into an evacuated tank at the end of the 10,000-hr operating period. Just before draining, the loop operating conditions were adjusted to ensure a maximum removal of the K to the dump tank:

1. The boiling conditions were adjusted to 871°C and 38.2 psia.
2. The vapor in the dryer was superheated to 996°C to supply heat to the test section.
3. The rate of heat removal to the NaK circuit was reduced to hold the condenser inlet conditions at 732°C and 12 psia.
4. The drain valve was opened to allow passage of the liquid K, driven by the combined forces of gravity and vapor pressure.
5. The potassium pump was then reversed to improve removal of liquid trapped in the helical flow passages of the pump.
6. The high temperature and the stored heat in the boiler leg, crossover line, and condenser leg dried residual pockets of K.
7. The drain valve was closed, and the loop was allowed to cool to ambient temperature to leave the loop under vacuum with only traces of condensed K.
8. The NaK economizer circuit was drained by gravity and left filled with Ar at atmospheric pressure.

We originally planned to remove any residual traces of K by distillation, but we could not do so because of a leak discovered in the NaK coolant system when the vacuum bell jar was removed. However, subsequent sectioning of the boiler and condenser revealed them to be free of K so that the distillation step was not essential.

Visual examination of boiler and condenser legs. The loop was initially sectioned into three parts as shown in Fig. 5.17. The dryer wall with its thermocouple well and heater support tabs is shown in Figs. 5.18 and 5.19. While we were trying to stabilize the loop flow, the temperature of this section reached 1370°C for a brief period. Dispite this, we saw no dimensional changes, and the only external effect noted was a general brightening of the outer surfaces.

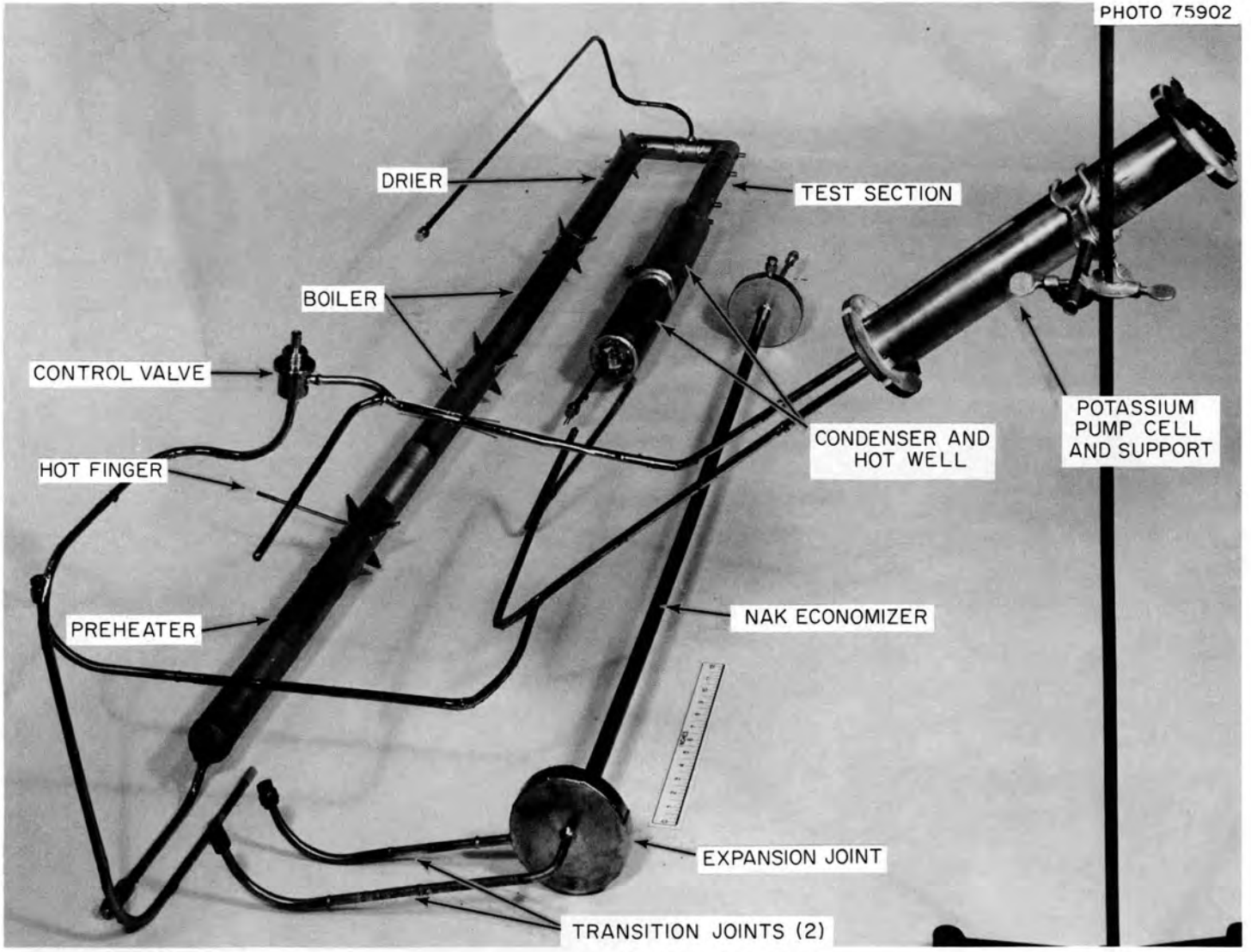

Fig. 5.17. Partially Disassembled D-43 Alloy Loop (FCL-8) After 10,000 hr of Test.

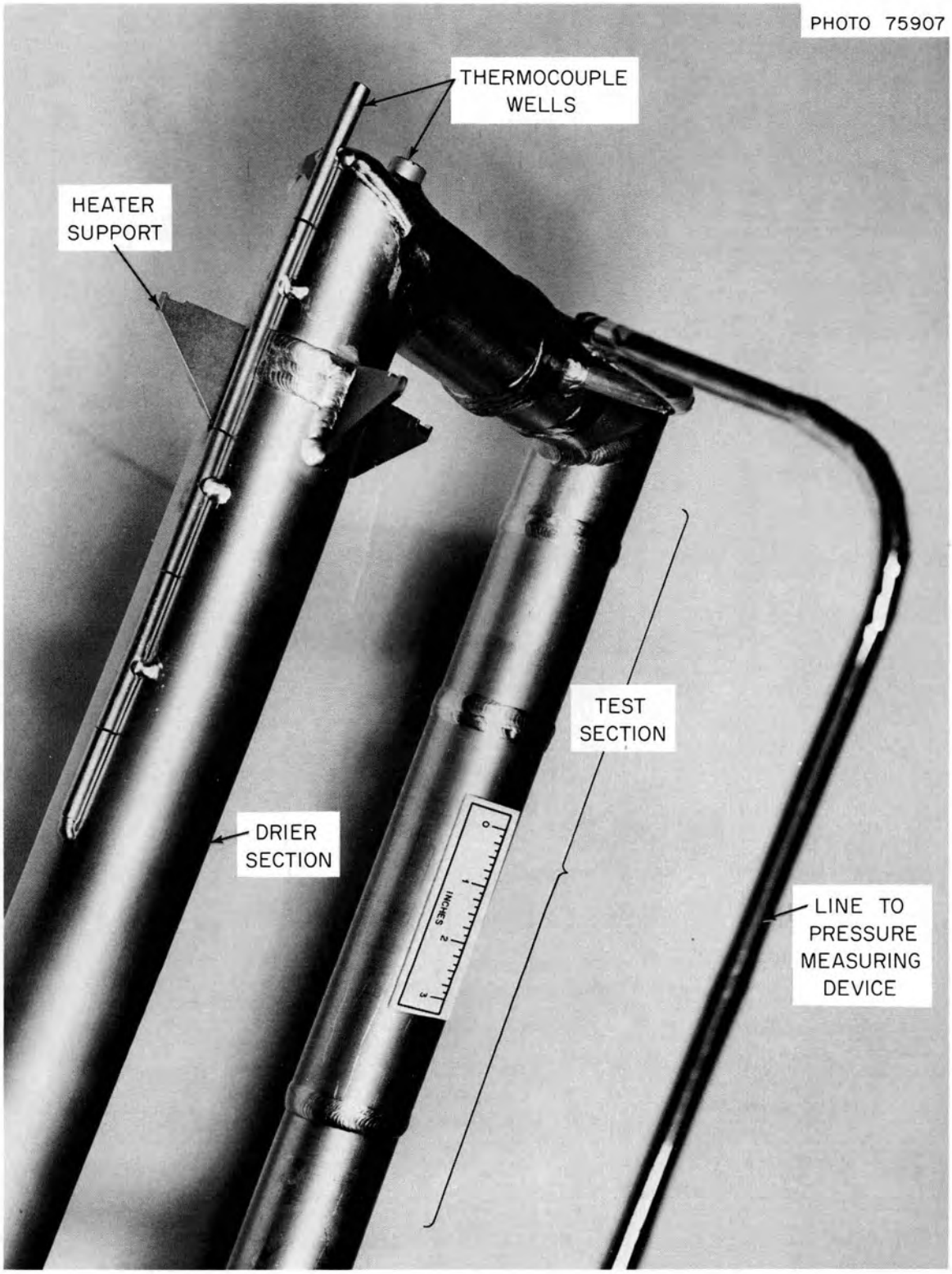

Fig. 5.18. Dryer and Test Sections of D-43 Alloy Loop (FCL-8) After Test.

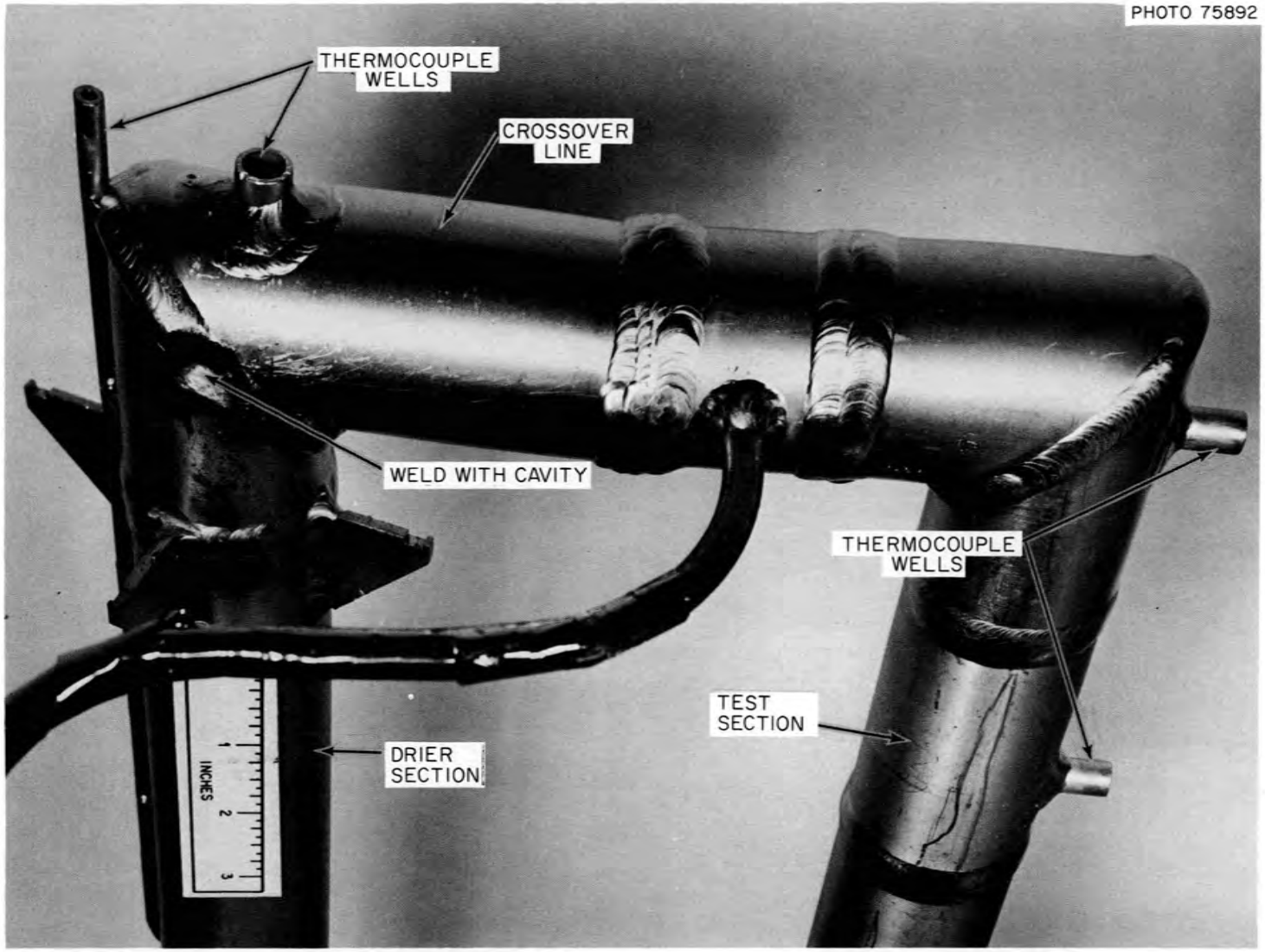

Fig. 5.19. Crossover Line Between Dryer and Test Sections of D-43 Alloy Loop (FCL-8) After Test Showing Weld Joint Complexity.

A groove apparent in one of the miter welds was made before test to eliminate a dye penetrant indication found after preoperational annealing.

Evaluation of pump. During the 10,000-hr operating period of this loop, it was necessary to increase the voltage to the potassium pump gradually to maintain a constant rate of flow in the loop. Our examination after the test disclosed decreased pump efficiency. The diameter of the exterior shell of the pump cell had increased in some areas as much as 1/32 in. X rays of the pump cell confirmed that a radial clearance of about 0.015 in. had developed between the wall and an internal helical core. The growth of the outer shell allowed bypass flows within the helical pump cell and gradually decreased the pump performance. The pressure stress on the outer shell of the pump cell would appear to have been too low to cause this extreme amount of creep. Our study of the cause of this phenomenon is still in progress.

Analysis of NaK leakage. As reported last quarter,[13] a NaK leak was detected when the vacuum chamber was opened. Visual inspection showed that the leak was very small. After we removed the protective tantalum foil wrap from the outlet line of the NaK economizer, it appeared that NaK might have leaked from the extruded Nb–1% Zr–stainless steel transition joint shown in Fig. 5.20. Dye penetrant inspection of this piece revealed a small defect on the outer surface at the interface between the Nb–1% Zr and stainless steel. X-ray inspection also showed a delamination type of defect on the interior surface. The joint was removed from the piping system, thoroughly washed in alcohol and boiling water, and then checked for leakage on a helium leak detector. No leak was indicated, but we cut the joint longitudinally and found that the interior surface was indeed delaminated at several areas where the Nb–1% Zr tapered into the stainless steel. Hence we would conclude that the leakage of NaK occurred because of this defective area in the transition joint. The rate of leakage was probably quite small, and therefore it is conceivable that NaK had been leaking into the vacuum vessel long before the end of the test.

---

[13]B. Fleischer and C. W. Cunningham, Fuels and Materials Development Program Quart. Progr. Rept. June 30, 1968, ORNL-4330, pp. 85–97.

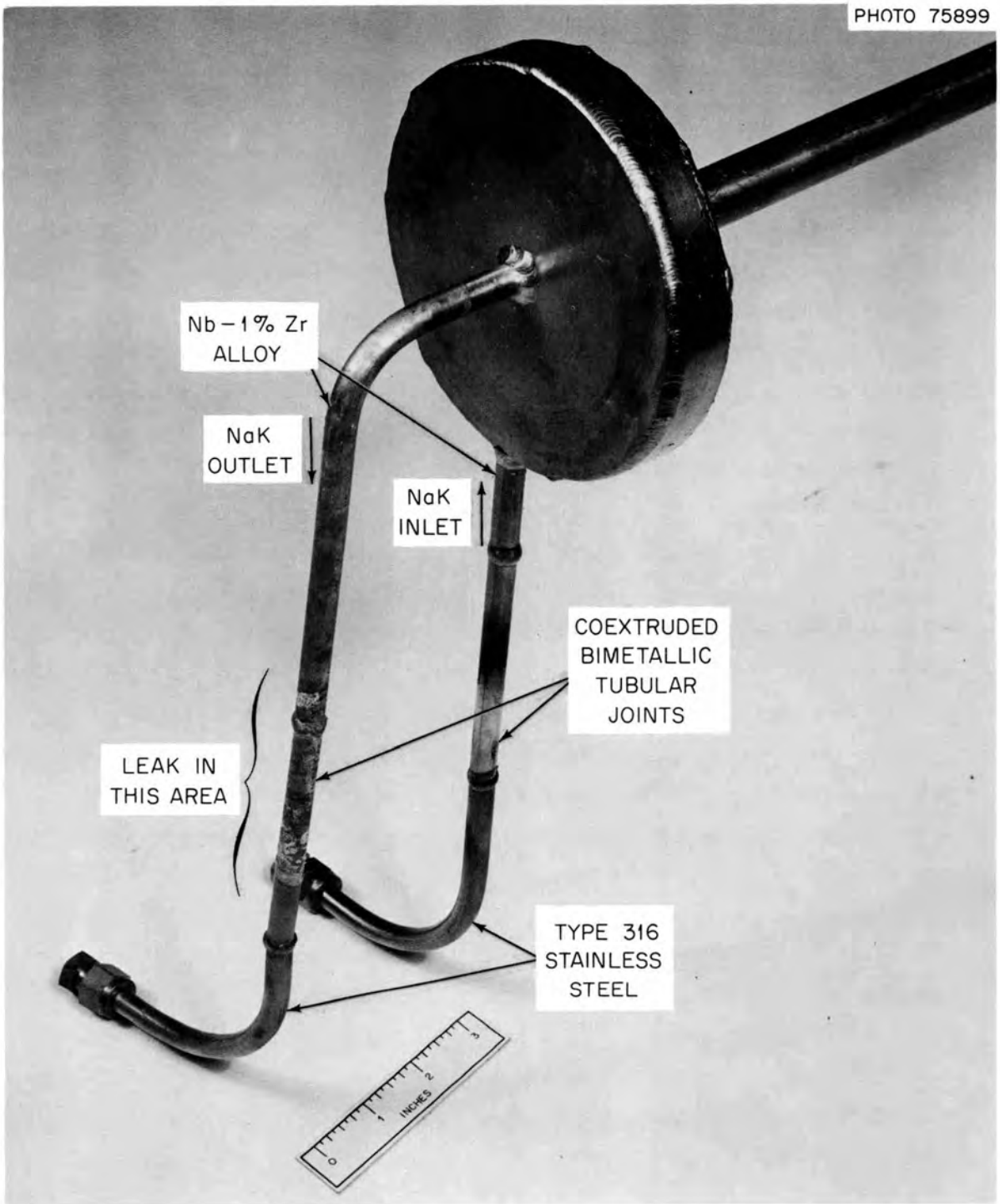

Fig. 5.20. Region of Small NaK Leak in D-43 Alloy Loop (FCL-8). Leak due to metal delamination in extruded Nb–1% Zr–stainless steel transition joint from economizer.

Inspection of vacuum chamber. During the test, we found an air leak in the area where the ion pump wells were welded to the vacuum chamber wall. However, the ion pumping capacity was sufficient to hold the chamber in the low (10^{-8} torr) range. A dye penetrant examination after test revealed a defect extending completely across this weld. A second defect was found in another weld. Both welds are being repaired and strengthened by overlaying weld metal around the entire joint. The nitrogen component observed in the residual gas during loop operation can be explained by this leak. The oxygen component was missing; we believe it was effectively consumed by the leaking NaK. The argon component can be explained in part by the air leak and in part by a possible leak from an argon-filled thermocouple assembly.

Refurbishing of triode ion pumps. The triode ion pumps were reconditioned at the vendor's plant, where the cathode construction was changed. The titanium wire and the supporting stainless steel of the cathode were replaced by an all-titanium expanded-metal-screen cathode construction. The vendor has found that the elimination of sputterable stainless steel is advantageous.

Interim vacuum test. Preparations are being made for a vacuum test before installing the next test loop into the chamber. This test will serve to verify the leak-tightness of the chamber, to determine the performance of the reconditioned ion pumps, and to evaluate the integrity of both new and old penetrations that are required for the next test.

Posttest examination. The main loop was sectioned as shown in the diagram in Fig. 5.21. Each section was cleaned with butyl, methyl, and ethyl alcohols to ensure safe removal of all unreacted K. No residual potassium metal was found during this cleaning. All parts were then rinsed 30 min with hot flowing water, dried with an alcohol rinse, and capped to await further examination.

All auxiliary piping lines were examined for residual K. Any K found was removed by melting under kerosene. These lines and the pump cell, valve, and economizer were then cleaned as previously described for the main loop.

Visual inspection of all pieces before and after cleaning showed no evidence of mass transfer. When the test pieces were removed, a

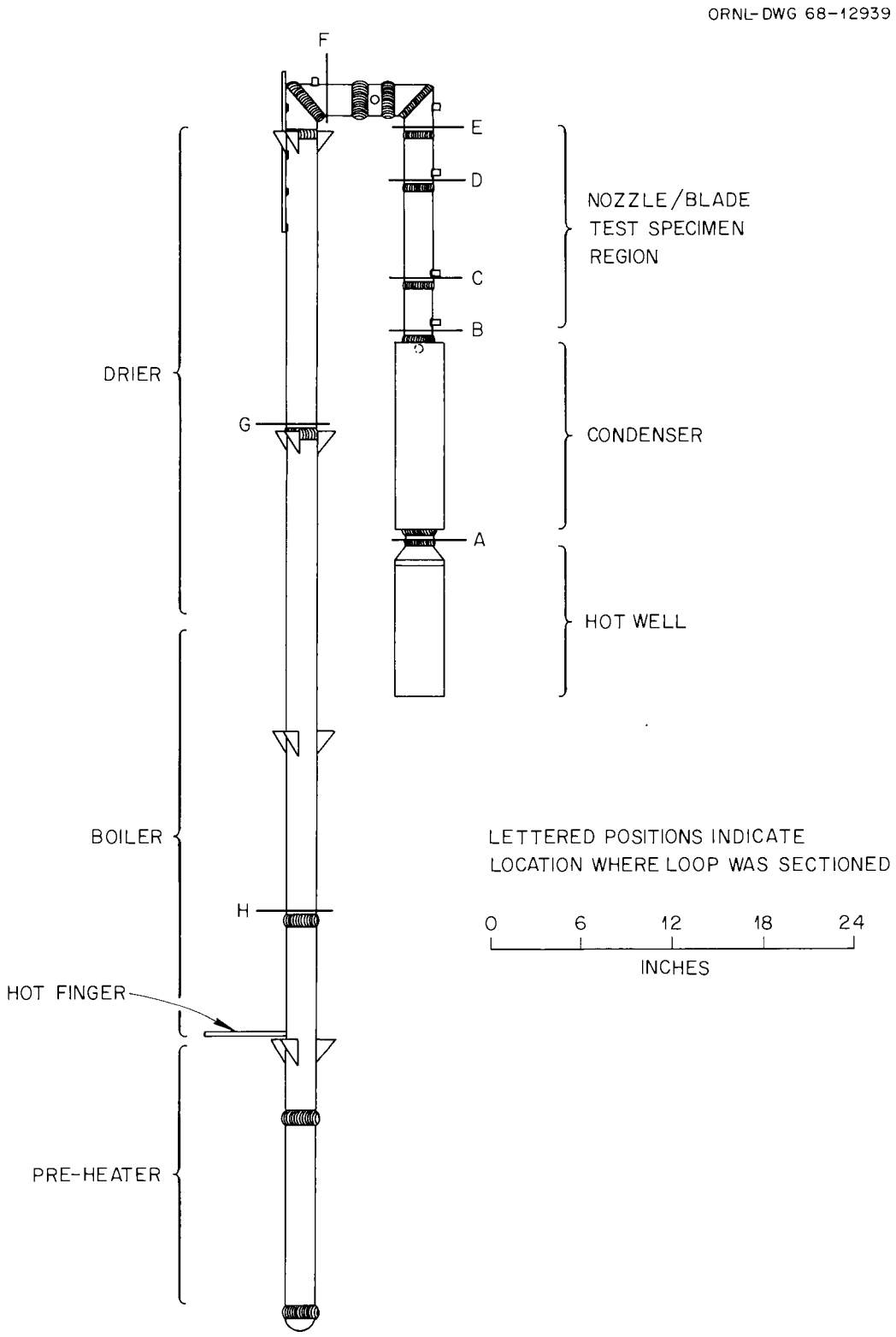

Fig. 5.21. Sketch of D-43 Alloy Loop (FCL-8) Showing Loop Sectioning Plan for Posttest Inspection.

small discolored area was noted on blade 2 at the vapor stream impingement point.

Effect of Oxygen on Compatibility of Refractory Metals and Alkali Metals (R. L. Klueh)

Oxygen Effects in the Tantalum-Potassium System. — We have completed our evaluation of the Ta-O-K system at 800 and 1000°C (ref. 14). The studies supplement those completed earlier on the Nb-O-K system.[15] In addition to providing data on equilibrium states, the tests were designed to yield data on the kinetics of weight changes of the tantalum specimens resulting from oxygen diffusion and tantalum dissolution. However, because of the rapid dissolution and because the specimens in some cases were penetrated by the K, the kinetics data are, at best, qualitative.

Table 5.4 shows the temperature, time, and oxygen conditions investigated in this test series. Potassium penetrated all but one of the tantalum specimens to which O had been added before testing (i.e., specimens containing $\geq$ 650 ppm O). Figures 5.22, 5.23, and 5.24 show the appearance of tantalum specimens containing 680, 1200, and 1800 ppm O after exposure to K at 800°C; each of the specimens exhibits attack preferentially along grain boundaries. Figure 5.24 is especially interesting because of the unusual grain structure of the Ta (i.e., the elongated grains parallel to the "flat" edge of the specimen). Compare the relatively deep penetration in the longitudinal direction with the shallower penetration in the transverse direction. Attack in the latter direction was confined to a band of small, equiaxed grains near the surface and was halted by grains elongated in the direction of rolling — confirmation that only grain-boundary attack is occurring. We believe that attack proceeds with the formation of a ternary oxide which then dissolves in K as the system tends toward equilibrium. This, as well as loss during metallographic preparation, could explain the apparent absence of corrosion products in the after-test microstructures.

---

[14]R. L. Klueh, Fuels and Materials Development Program Quart. Progr. Rept. June 30, 1968, ORNL-4330, pp. 142–146.

[15]A. P. Litman, The Effect of Oxygen on the Corrosion of Niobium by Liquid Potassium, ORNL-3751 (July 1965).

Table 5.4. Effect of Oxygen on Compatibility of Tantalum and Potassium

Temperature (°C)	Time (hr)	Oxygen in Potassium (ppm)	Oxygen in Tantalum (ppm)		Weight Change (mg/cm^2)	Tantalum in Potassium (ppm)
		Before	Before	After		After
800	1	1900	50	43	−0.0585	1890
	3	2000	50	29	−0.0594	2990
	5	1880	50	26	−0.0741	3200
	100	2000	50	19	−0.1520	2640
	100	490	680	34	−1.950	2480
	100	1970	650	36	−1.880	3120
	100	1950	1200	36	−3.240	7570
	100	1980	1800	32	−6.650	6850
1000	0.5	2020	50	39	−0.0460	3860
	1	1930	50	38	−0.0645	3830
	2	2020	50	50	−0.0745	4620
	50	2010	50	48	−0.202	14,120
	0.5	100	1600	120	−5.91	3680
	1	100	1600	210	−5.86	4980
	2	100	1600	36	−6.06	5110
	50	100	1700	23	−6.28	6830
	50	450	620	39	−1.92	9640
	50	1980	660	43	−1.86	15,070
	50	1970	1000	53	−3.23	7780
	50	1930	1900	53	−6.50	20,600

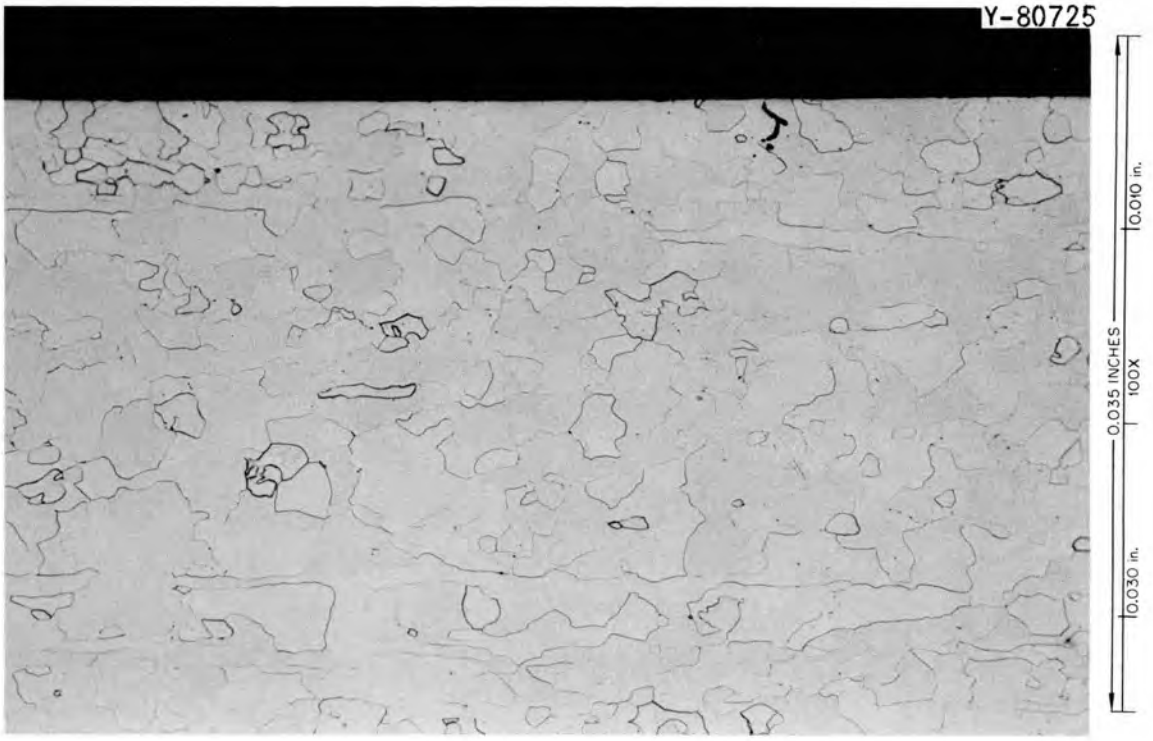

Fig. 5.22. Tantalum, Which Initially Contained 680 ppm O, After Exposure to Potassium for 100 hr at 800°C. Etched in a solution of H_2O, HNO_3, and NH_4HF.

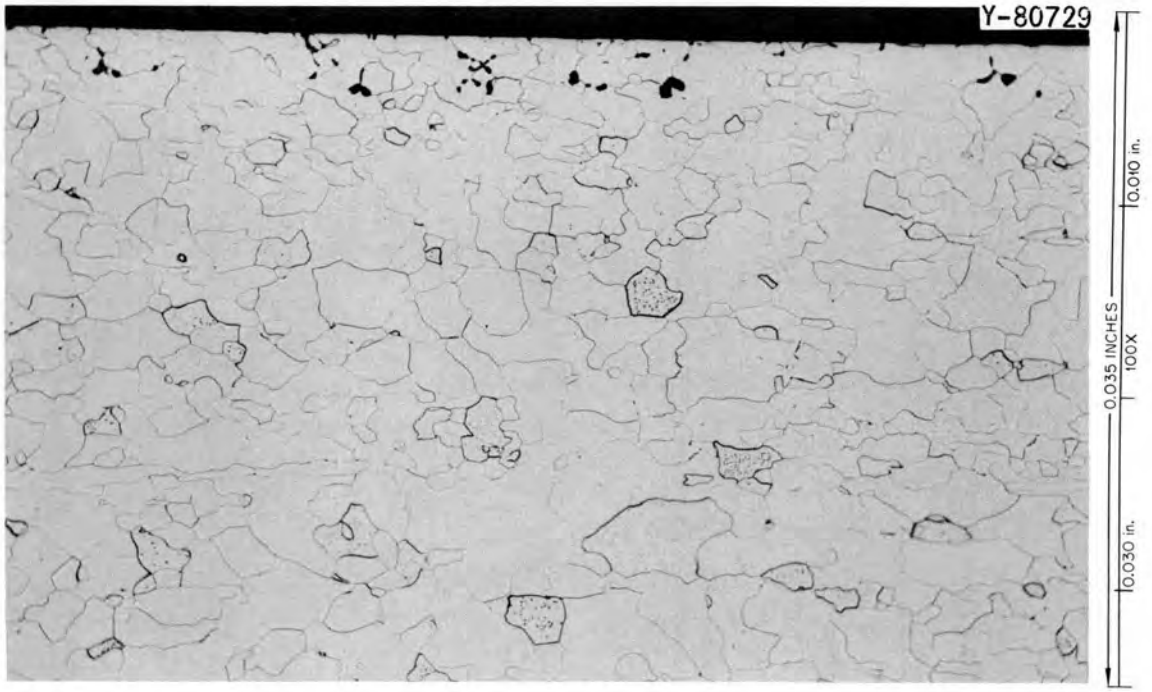

Fig. 5.23. Tantalum, Which Initially Contained 1200 ppm O, After Exposure to Potassium for 100 hr at 800°C. Etched in a solution of H_2O, HNO_3, and NH_4HF.

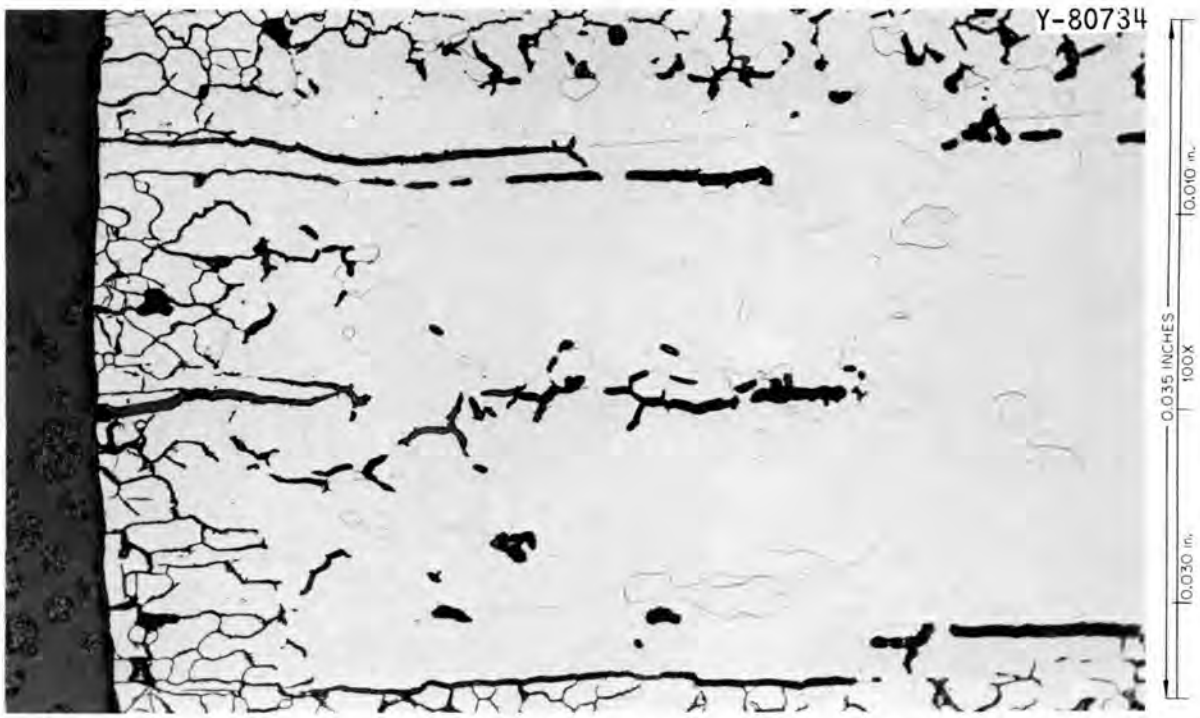

Fig. 5.24. Tantalum, Which Initially Contained 1800 ppm O, After Exposure to Potassium for 100 hr at 800°C. Etched in a solution of H_2O, HNO_3, and NH_4HF.

At 1000°C, the addition of 660 ppm O to Ta did not affect attack by K, and little attack (similar to Fig. 5.22 at 800°C) was noted for the specimen containing 1000 ppm O. Heavy attack at 1000°C resulted for a tantalum specimen containing 1600 ppm O after 1 hr exposure to K, as shown in Fig. 5.25.

These results are qualitatively similar to those obtained by DiStefano[16] for the Nb-O-Li and Ta-O-Li systems: (1) a threshold concentration of O in the Ta must be exceeded before penetration occurs (this level increases with increasing exposure temperature); (2) above this threshold level, the amount of attack (i.e., depth of penetration) increases with an increase in the initial concentration of O in the Ta; (3) the attack is not affected by the concentration of O in the K; (4) when O_2 diffuses out of the specimen rapidly, as at 1000°C, it

[16]J. R. DiStefano, Corrosion of Refractory Metals by Lithium, ORNL-3551 (April 1966).

Fig. 5.25. Tantalum, Which Initially Contained 1600 ppm O, After Exposure to Potassium for 0.5 hr at 1000°C. As polished.

limits the depth of penetration. The chief difference between the present studies and DiStefano's studies of Li is that the latter showed attack to occur in Ta at 815°C with as little as 300 ppm O (ref. 16). This would indicate that the threshold concentration is higher for penetration by K than by Li.

As shown in Table 5.4, the concentration of Ta in the K increased as the level of O in the K increased. (The final concentration of O in the K is somewhat larger than that shown in Table 5.4 because of O donated by the Ta of the container and specimen.) Since we believe penetration involves the formation of a compound containing O, the final concentration of O in the penetrated specimens may include O in the form of a corrosion product as well as O dissolved in the Ta.

The specimens exposed to K with a high concentration of O contained a dark scale. When we tried to identify the scale by x-ray diffraction, we detected only tantalum metal. Furthermore, within experimental error, removal of the scale from the specimen did not change the oxygen content of the specimen.

Oxygen Effects in the Niobium-Sodium System. — The results of the Ta-O-K system discussed above, together with previous studies[16,17] at ORNL, indicate that there is a marked difference in the effect of O on the compatibility of refractory metals and alkali metals depending upon whether O is present in the refractory metal or the alkali metal. We are attempting to categorize these different effects in the Nb-O-K, Ta-O-K, Nb-O-Na, Ta-O-Na, Nb-O-Li, and Ta-O-Li systems. For these studies we are using static capsules of the configuration previously described for studies of Ta-O-K (ref. 18). All tests are being conducted at 600°C, since this temperature is of direct interest in sodium-cooled fast breeder reactor applications.

Our first tests in this series were conducted on the Nb-O-Na system. Four capsules containing unoxidized niobium specimens were exposed to Na with several oxygen levels, and two capsules containing niobium specimens with 950 and 1600 ppm O, respectively, were exposed to Na with about 50 ppm O.

All tests were conducted for 500 hr. Results are shown in Table 5.5. Although the specimens appeared dull after test, none of them appeared to have a scale. All specimens showed weight losses. The two oxidized specimens showed considerable oxygen loss, while the unoxidized specimens showed little oxygen change. Diffusion calculations and microhardness profiles of the unpenetrated specimens indicated that the oxygen concentration was near equilibrium after 500 hr at 600°C.

Metallographic examination of the two oxidized specimens indicated that they had been penetrated by the Na. The penetration was much less severe than for similarly oxidized tantalum specimens exposed to K at 600°C (ref. 19). As in the case of these Ta-O-K tests, the final oxygen concentration in the Nb-O-Na tests may include O present as an internal corrosion product as well as O in solid solution.

---

[17]A. P. Litman, The Effect of Oxygen on the Corrosion of Niobium by Liquid Potassium, ORNL-3751 (July 1965).

[18]R. L. Klueh, Fuels and Materials Development Program Quart. Progr. Rept. June 30, 1968, ORNL-4330, p. 142.

[19]R. L. Klueh, "Oxygen Effects in the Tantalum-Potassium System," pp. 120–124, this report.

Table 5.5. Effect of Oxygen on Compatibility of Niobium and Sodium at 600°C

Oxygen in Sodium[a] (ppm) Before	Oxygen in Niobium (ppm) Before[b]	Oxygen in Niobium (ppm) After[b]	Weight Change[c] (mg)	Niobium in Sodium (ppm) After
50	70	59	−0.1	400
300	70	62	−0.5	800
700	70	64	−2.0	1400
1000	70	83	−1.7	2200
50	950	540[d]	−1.7	500
50	1600	440[d]	−6.2	1000

[a]Oxygen added as Na_2O to Na containing about 50 ppm O.

[b]Determined by vacuum-fusion analysis.

[c]All specimens were 1 × 0.5 × 0.04 in.

[d]Microstructures show that Na penetrated these specimens.

Partitioning of Oxygen Between Potassium and Zirconium and Sodium and Zirconium. — As noted in the previous report[20] we have re-examined the value originally assigned to the equilibrium distribution coefficient for the distribution of O between Zr and K (i.e., $\kappa^O = \frac{\text{atom fraction of O in Zr}}{\text{atom fraction of O in K}}$). Below we will demonstrate why we believe that the equilibrium distribution coefficient at 815°C is much larger than originally thought and then show how this new coefficient affects the gettering-vacuum-fusion (GVF) method for determining oxygen concentrations in K (and Na).

Zirconium containing 1 wt % O, when exposed at 815°C to triple-gettered K (< 10 ppm O), gained a small amount of weight and increased in O (ref. 21). This result can be used to set limits on the distribution coefficient, κ^O, at 815°C. Taking 10 ppm O as the upper limit for

[20]R. L. Klueh, Fuels and Materials Development Program Quart. Progr. Rept. June 30, 1968, ORNL-4330, p. 146.

[21]A. P. Litman, private communication.

the after-test concentration of O in the K, it follows that $\kappa^{O}_{815°C} > 2 \times 10^{3}$. But since the concentration was probably closer to 1 ppm O after test, $\kappa^{O}_{815°C}$ more reasonably approaches 10^{4} or higher.

Using the oxidation data of Mackay[22] for Zr in Na along with recent solubility data for O in Na (ref. 23) and following the same argument as above, we find that κ^{O} for Na at 635°C must be greater than 5×10^{4}. This is in accord with Mackay's results, which showed that Zr could be oxidized at 635°C in Na that had an oxygen concentration determined by a cold trap operating at 160°C. Theoretical calculations of κ^{O} suggest that the coefficient should not change by more than an order of magnitude at 800°C, the temperature of the GVF anneal.

Once κ^{O} has been established as being very much larger than unity, it follows, under the conditions of our GVF analysis technique, that when pure Zr is exposed to K or Na containing O, essentially all of the O is gettered by the Zr. Therefore, the amount of O originally present in the liquid, $C_{O}^{(A)}$, is given by

$$C_{O}^{(A)} = \Delta C_{O}^{(Zr)} \frac{W_{Zr}}{W_{A}} \quad , \tag{5.1}$$

where $\Delta C_{O}^{(Zr)}$ is the O gettered by the Zr and W_{Zr} and W_{A} are the weights of the Zr and alkali metal, respectively. The distribution coefficient, being effectively infinite, does not enter into the calculation.

We are now conducting recovery tests designed to verify Eq. (5.1).

Corrosion of Refractory Alloys by Lithium

Thermal Convection Loop Tests (J. H. DeVan). — The sixth in a series of lithium thermal convection loop tests designed to study mass transfer of refractory metals was terminated after completing a 3000-hr test run. This loop, TCL-6R, was fabricated of the tantalum-base alloy T-222 and operated at a maximum hot-leg temperature of 1350°C. Compositions of the

---

[21] T. L. Mackay, Oxidation of Zirconium and Zirconium Alloys in Liquid Sodium, NAA-SR-6674 (February 1962).

[22] V. J. Rutkauskas, Determination of the Solubility of Oxygen in Sodium by Vacuum Distillation, LA-3879, Los Alamos Scientific Laboratory (September 17, 1968).

loop tubing and insert specimens are given in Table 5.6, and flow rate and temperature conditions for the test are shown below:

Maximum hot-leg temperature, °C	1350
Minimum cold-leg temperature, °C	1140
Lithium flow rate, g/min	240
Lithium velocity, cm/sec	2.5
Test duration, hr	3000

After operation, the loop was drained to collect a sample of Li and was then flushed with liquid ammonia to remove residual Li. Eighty-two sheet specimens were then removed and tested for weight change, chemistry, and metallographic condition.

The weight-change results are shown in Fig. 5.26. The weight change around the loop was analogous to that observed for Nb–1% Zr and D-43 at 1200°C, where about two-thirds of the loop surface lost weight and one-third gained weight. Also, as in the niobium alloy loops, specimens from the weight gain region of this loop were covered by a thin, gold-colored film. As would be expected from the small magnitude of the weight changes for the T-222 specimens, no dimensional changes could be detected on any of the specimens.

Chemical analyses of the insert specimens, although not complete, have shown a significant transport of Hf from the hotter to the cooler loop surfaces. X-ray fluorescence was used to evaluate the concentration of Hf near the surface of the insert specimens; the results are shown in Fig. 5.27. Note that the profile of the hafnium surface concentration around the loop mirrors the weight-change profile shown in Fig. 5.26:

Table 5.6. Compositions of T-222 Components Used in Loop TCL-6R

Loop Component[a]	Chemical Composition, wt %					
	W	Hf	O	N	C	Ta
Insert Specimens (0.030 × 1 × 0.8 in.)	10.2	2.3	0.005	0.004	0.014	Bal
Loop Tubing (1 in. outside diameter × 0.065 in. wall thickness)	10.3	2.2	0.003	0.002	0.013	Bal

[a]Loop annealed after assembly for 2 hr at 1300°C.

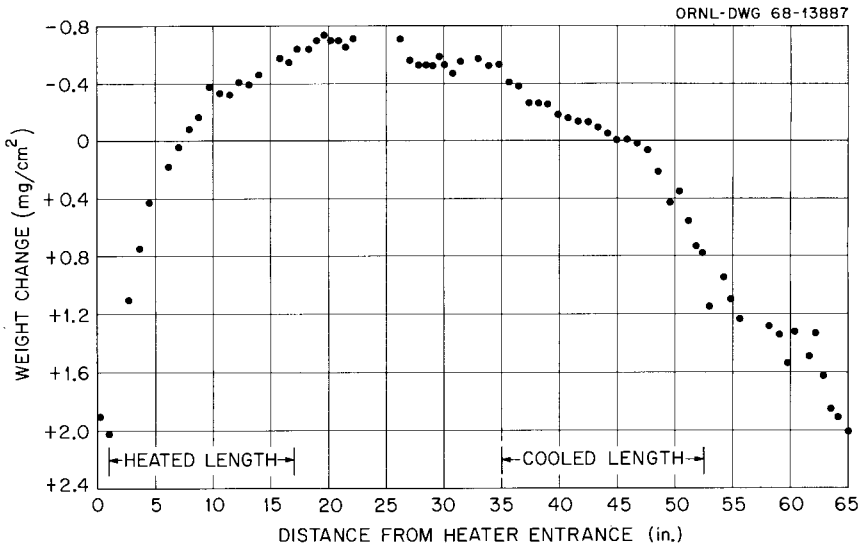

Fig. 5.26. Weight Change of T-222 Thermal Convection Loop After Operating with Lithium for 3000 hr at 1350°C.

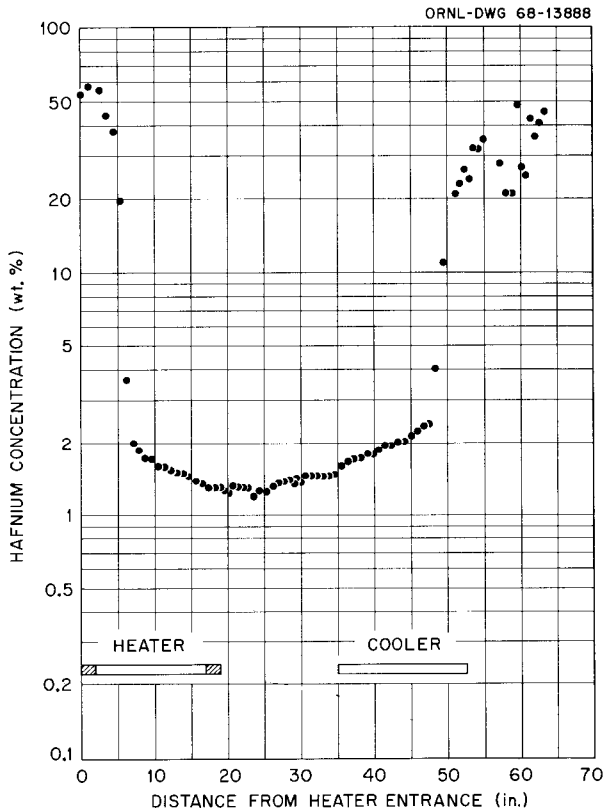

Fig. 5.27. Hafnium Concentration Near Surfaces of T-222 Insert Specimen After Operation with Lithium. Analyzed by x-ray fluorescence.

regions of weight loss reflect hafnium depletion while regions of weight gain reflect hafnium enrichment.

Additional metallographic and chemical analyses of loop sections and insert specimens are in progress.

T-111 Forced Circulation Loop (FCLLL-1). – Loop equipment and design. (D. L. Clark) All design work has been completed, and drawings have been issued for construction. Work has continued on the T-111 alloy test-bed loop for studying new refractory alloys at very high temperatures in high-velocity liquid Li. Installation of component parts and assemblies is being delayed until completion of the preliminary check-out of the reworked triode ion pumps. All available vacuum penetrations are being installed for check-out during this period. Included will be the 3000-amp electrical feedthrough, the flange penetration for the fill and drain, and sampling systems, the part for the optical pyrometer, and the can and flange for the helical induction pump.

Fabrication of T-111 assemblies. (B. Fleischer) We completed welding of the radiator, heater section, economizer, and pump lines. We fabricated the radiator coil by butt welding straight pieces of tubing together and then bending them. All welds were inspected after bending and found to be free of cracks. The ends of the coil were then cut off and prepared as subassemblies to facilitate welding of thermocouple wells, end caps, and inlet and outlet tubing. The subassemblies were then butt welded to the main coil.

The economizer, heater section, and pump lines were constructed by welding of component parts previously bent and machined in accordance with detail drawings. We experienced considerable difficulty in attempting to achieve dimensional tolerances and proper alignment. To check for proper mating of the economizer, radiator, and heater sections, we placed the parts on the test stand and aligned them with respect to the copper bus assembly. Additional bending of portions of the economizer and heater sections was required to properly mate the parts.

Annealing of T-111 welds. (B. Fleischer) Welds of T-111 severely contaminated with O will fail rapidly when exposed to Li. This problem can be alleviated by annealing the welds for several hours at 1315°C before exposing them to Li. Even though the welds we made in assembling

FCLLL-1 were performed under clean, inert conditions in a dry box, the possibility of undiscovered weld contamination made it prudent to anneal. The cost of this insurance is inconsequential compared to the cost of materials and labor already invested in the assemblies.

Accordingly, we prepared the assemblies for annealing by an outside contractor. The loop surfaces were wiped with lint-free cloths soaked in alcohol and then wrapped spirally at about 3/4-in. pitch with 0.060-in.-diam tantalum wire. Tantalum foil 0.001-in. thick by 2-in. wide was wrapped at half lap over the wire, which serves as a spacer to prevent welding of the foil to the parts. The foil acts as a mechanical barrier to minimize environmental contamination.

We annealed these subassemblies in a 12-ft-long by 4-ft-diam vacuum furnace located in the Refractory Metal Center, Materials Systems Division, Union Carbide Corporation, Kokomo, Indiana. The annealing cycle is described in Table 5.7. The temperature of the parts was determined by placing Pt–6% Rh vs Pt–30% Rh thermocouples at anticipated heat-lag locations. Sample coupons of T-111 were placed at various locations to check contamination.

After annealing, all the foil and parts were still bright. An unwrapped T-111 control specimen was bent 90° without any evidence of cracking. Analysis of the control specimens reported in Table 5.8 showed no contamination of wrapped or unwrapped specimens.

Fabrication of control specimen units. (D. L. Clark, B. Fleischer) Furnaces for the exposing of control specimens have been fabricated. The units are shown in Fig. 5.28. Figure 5.29 shows the control specimen material mounted on the holders. One of the furnaces will be used to expose the specimens at 1370°C while the other will operate at 1205°C. The units will be mounted on the top of the test stand. These specimens will be used for comparison of mechanical properties of the same material exposed at the same temperature to Li inside the loop.

Table 5.7. Vacuum Annealing Cycle for FCLLL-1 T-111 Loop

Time (pm)	Description of Operation	Temperature, °C			Vacuum Pressure (torr)
		Furnace	Parts[a]		
			Position 1	Position 2	
					$\times 10^{-7}$
12:30	Start heatup				200.0
1:00	Start 260°C hold	260			270.0
1:25	End 260°C hold	260			80.0
1:35		315			290.0
2:10	Start 540°C hold	540	305	345	120.0
2:35	End 540°C hold	540	420	445	44.0
3:00		705			330.0
3:15	Start 815°C hold	815	670	705	170.0
3:30	End 815°C hold	815	760	780	73.0
3:40	Realign vacuum instruments	870			90.0
		870			190.0
4:05	Start 1095°C hold	1095	1010	1030	320.0
4:20	End 1095°C hold	1095	1060	1070	210.0
4:35		1315	1250	1270	650.0
4:45	Start 2-hr anneal	1330	1290	1300	540.0
5:05		1330	1310	1315	230.0
6:45	End 2-hr anneal (start controlled cool down)	1330	1310	1315	63.0
7:20	Cut off all furnace power	815	860	860	7.5
7:35		540			5.6
8:35		260			5
11:55		95			6.7

[a]Thermocouples placed arbitrarily at anticipated heat-lag positions.

Table 5.8. Interstitial Element Concentration of Control Samples During FCLLL-1 Anneal

Specimen Description	Concentration, ppm							
	Unwrapped				Wrapped[a]			
	C	O	N	H	C	O	N	H
Unexposed control specimen	90	140	12	3	70	140	7	4
Exposed at top of furnace	80	150	7	12	70	140	8	1
Exposed at bottom of furnace	70	140	10	7	70	140	13	1

[a]These specimens were wrapped with two layers of 0.001-in.-thick tantalum foil.

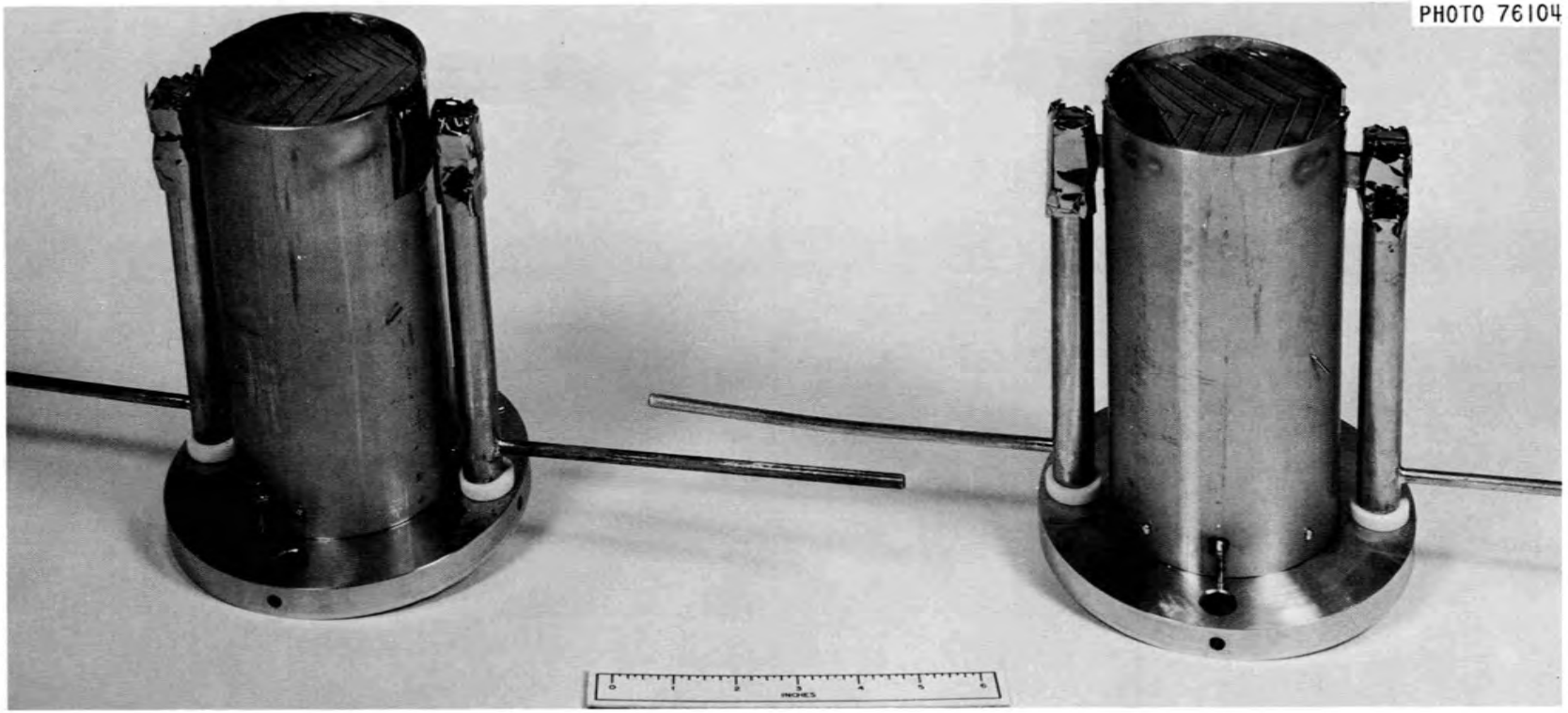

Fig. 5.28. Furnaces for FCLLL-1 Control Specimens.

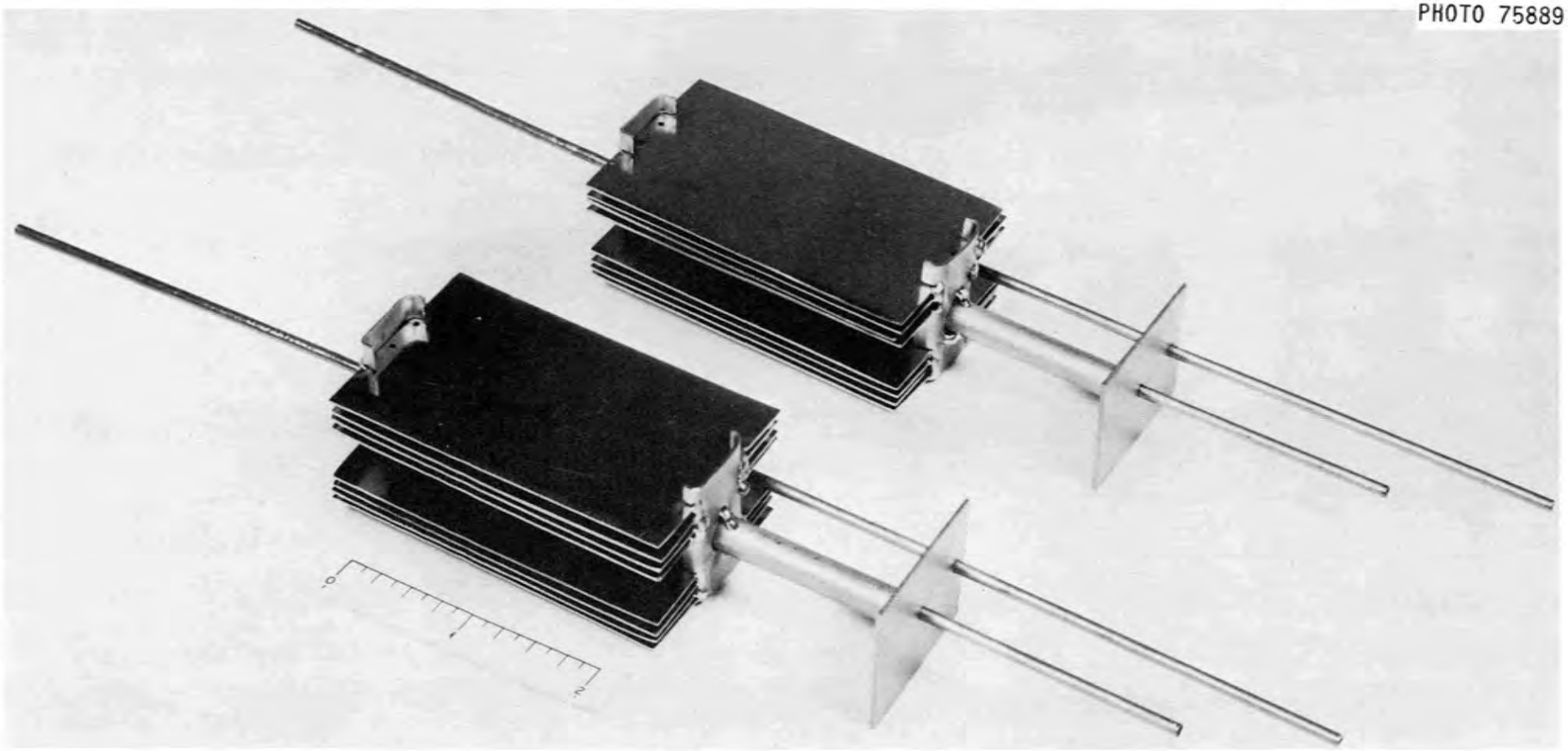

Fig. 5.29. Control Specimens of T-111 Alloy for FCLLL-1.

PART III.

RADIATION DAMAGE TO STRUCTURAL MATERIALS

6. BEHAVIOR OF REFRACTORY MATERIALS UNDER IRRADIATION

G. W. Keilholtz R. E. Moore
D. A. Dyslin[1]

The purpose of this program is to evaluate the effects of high fast-neutron fluences at temperatures from 150 to 1100°C on the properties of refractory nuclear materials for both space and civilian power reactors. While we emphasize nonfissionable ceramic materials such as the carbides, nitrides, and silicides of refractory metals, we have extended the scope of the work to include irradiation of fuels of interest to fast breeder reactors.

Irradiation Damage to Nonfissionable Refractory Materials

Refractory Metal Carbides

Irradiation of Explosion-Pressed Carbides at 1000 to 1100°C. — An in-reactor thermal annealing effect on gross damage and volume expansion had been previously observed[2] in irradiations of hot-pressed and slip-cast carbides at 1000 to 1100°C. Recent results from another high-temperature assembly indicate that thermal annealing also reduces damage to explosion-pressed carbides during irradiation at 1000 to 1100°C. The assembly, which was irradiated in the ETR, consisted of seven temperature-controlled capsules, each of which contained a pair of specimens of the same material, as shown in Table 6.1.

The pair of specimens of WC that received fast-neutron fluences of 1.6×10^{21} neutrons/cm^2 and the two pairs of specimens of NbC were found to be inseparably bonded together after irradiation. We also observed this phenomenon in some hot-pressed and slip-cast carbides irradiated at high temperature. It may result from a combined effect of atomic cascades produced by fast neutrons at contact areas and thermal

---

[1]General Engineering Division.

[2]G. W. Keilholtz, R. E. Moore, and D. A. Dyslin, Fuels and Materials Development Program Quart. Progr. Rept., June 30, 1968, ORNL-4330, pp. 151–158.

Table 6.1. Explosion-Pressed Carbide Specimens Irradiated in Pairs at 1000–1100°C

Capsule	Specimen	Fast-Neutron Dose [neutrons/cm^2, (> 1 Mev)]	Condition After Irradiation
		$\times 10^{21}$	
1	NbC	1.4	No damage
	NbC	1.4	No damage
2	NbC	2.5	No damage
	NbC	2.5	No damage
3	WC	1.6	No damage
	WC	1.6	No damage
4	WC	2.5	No damage
	WC	2.5	No damage
5	ZrC	2.4	No damage
	ZrC	2.4	No damage
6	ZrC	1.5	Badly damaged
	ZrC	1.5	Badly damaged
7	TiC	2.3	No damage
	TiC	2.3	No damage

annealing of these partially disordered cascade regions. All specimens survived without significant gross damage over the range 1.4 to 2.5×10^{21} neutrons/cm^2 except a pair of specimens of ZrC irradiated to 1.5×10^{21} neutrons/cm^2. The general appearance of the capsule containing these specimens strongly suggested that overheating had caused a reaction between the specimens and the TZM sleeve with which they were in contact. If it is assumed that this damage did result from overheating, it can be concluded, when results in Table 6.1 are compared with results from tests at lower temperature,[3] that in-reactor thermal annealing reduces gross damage to explosion-pressed carbides at 1000 to 1100°C.

Explosion-pressed carbides of Ti, Zr, and Nb expanded less during irradiation at 1000 to 1100°C than at 300 to 700°C. Figure 6.1 shows

[3]G. W. Keilholtz, R. E. Moore, and M. F. Osborne, Nucl. Appl. 4, 330 (1968).

ORNL-DWG 68-12062

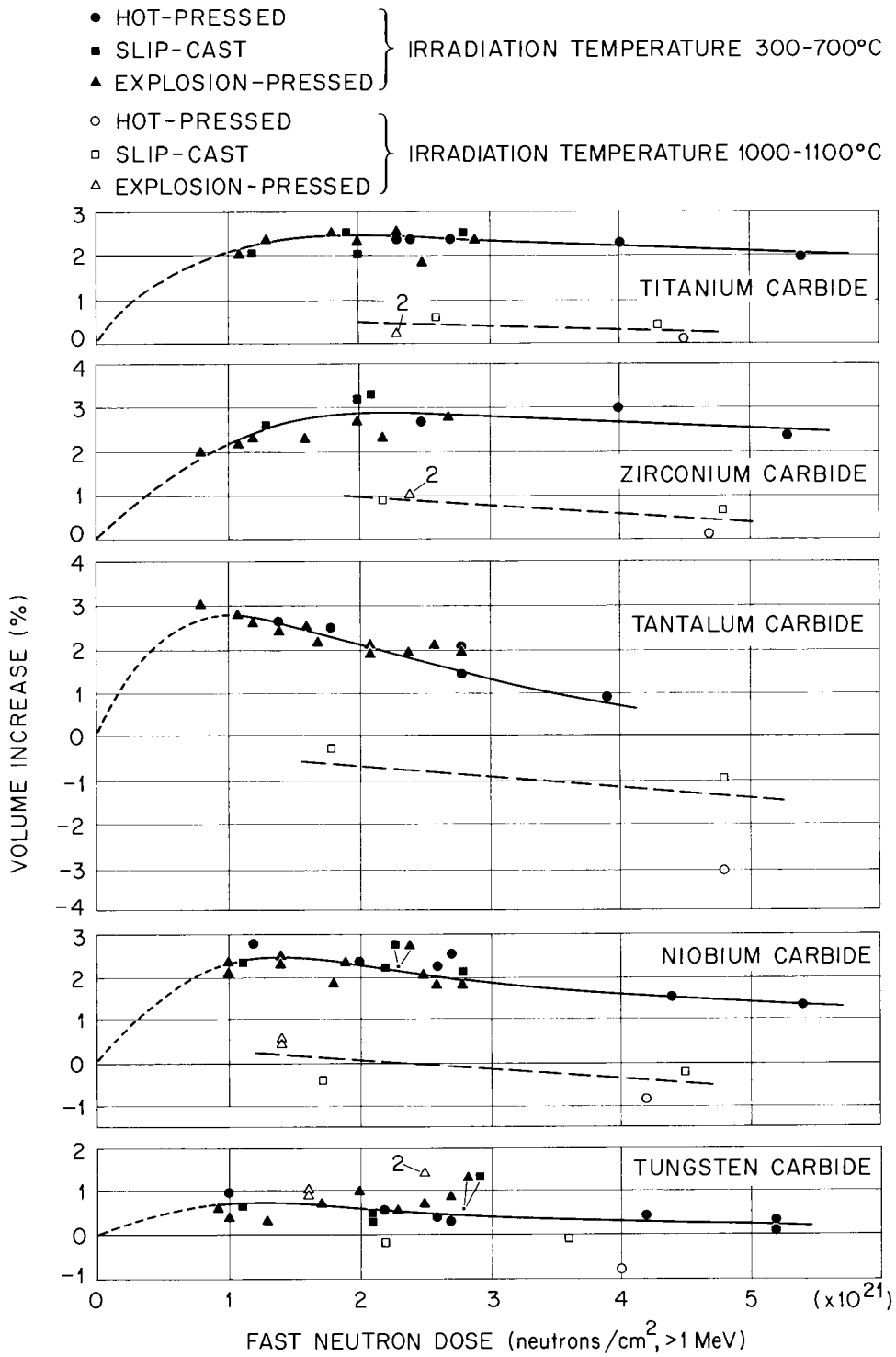

Fig. 6.1. Gross Volume Increase as a Function of the Fast Neutron Fluence for Monocarbides of Ti, Zr, Ta, Nb, and W at 300 to 700°C and 1000 to 1100°C.

that high-temperature data for explosion-pressed carbides of Ti, Zr, and Nb agree with data for hot-pressed and slip-cast specimens. Unexplainably, explosion-pressed WC expanded more during irradiation at 1000 to 1100°C than specimens of WC made by the other two processes. The irradiated carbides are being examined by metallography, x-ray diffraction, and replication electron microscopy to establish the mechanisms of damage.

Effects of Fast Neutrons on Carbides at Low Temperature. — Dimensional measurements of refractory metal carbides irradiated at low temperature (300 to 700°C) showed[2,3] an initial expansion that reaches a maximum between 1 and 2×10^{21} neutrons/cm^2 (> 1 Mev). Higher fluences produced shrinkage that appears to approach a constant net expansion value in each case (see Fig. 6.1). We proposed a simple model to explain the swelling-shrinkage phenomenon. We assumed that fast neutrons produce atomic cascades that leave regions of low density within the specimens and that fast-neutron strikes on atomic nuclei in or near these regions will anneal them to produce new regions of higher density. The simplest equation for volume expansion derived from this model is

$$\Delta V/V = (K_2 - 1) - (K_2 - 1)\, e^{-\bar{\sigma}_s N_d(\phi t)} + (K_1 - K_2)\, \bar{\sigma}_s N_d(\phi t)\, e^{-\bar{\sigma}_s N_d(\phi t)}, \tag{6.1}$$

where

$\Delta V/V$ = fractional volume increase,

ϕt = fast-neutron fluence,

K_1 = density of original crystalline material per density of primary disordered regions,

K_2 = density of original crystalline material per density of secondary disordered region,

$\bar{\sigma}_s$ = average scattering cross section for atoms of the carbides for fast neutrons of the neutron energy spectrum,

N_d = average number of displaced atoms per collision of a fast neutron with an atomic nucleus.

It can be shown that this equation fits the low-temperature data for carbides with physically realistic constants if the volume expansion between 0 and 1×10^{21} neutrons/cm^2(ϕt) is assumed to follow the dashed lines in Fig. 6.1. However, it is necessary to obtain low-dose data as one of the tests of the damage model and, assuming the data do not contradict the model, to obtain information helpful for evaluating the constants of the equation. If the equation for volume expansion is differentiated, the expression for the change in $\Delta V/V$ with change in (ϕt) is

$$\frac{d(\Delta V/V)}{d(\phi t)} = (K_1 - 1)\,\bar{\sigma}_s N_d\, e^{-\bar{\sigma}_s N_d(\phi t)} - (K_1 - K_2)(\bar{\sigma}_s N_d)^2\,(\phi t)\, e^{-\bar{\sigma}_s N_d(\phi t)}. \tag{6.2}$$

If we let (ϕt) approach 0, the initial slope change is

$$\frac{d(\Delta V/V)}{d(\phi t)} = (K_1 - 1)\,\bar{\sigma}_s N_d\,. \tag{6.3}$$

This value can be used for evaluating constants in the equation for volume expansion for the various carbides.

We are planning a short (one ETR cycle) irradiation of explosion-pressed and slip-cast carbides at low temperature to obtain the information discussed above and a low-temperature irradiation in the EBR-II to separate the effects of absorptions of slow neutrons on the carbides. The EBR-II neutron energy spectrum consists almost entirely of fast neutrons.

Refractory Metal Nitrides

Commercial nitrides of Zr, Ti, Ta, and Nb have been irradiated as 1/2- × 1/2-in. solid cylinders at 1000 to 1100°C in the ETR. The fast-neutron fluence ranged from 0.4 to 2.3×10^{21} neutrons/cm^2 (> 1 Mev).

There was not as much gross damage to ZrN at 1000 to 1100°C as in previous irradiations[4] at about 150°C. Four of five specimens irradiated to fluences ranging from 0.4 to 2.3×10^{21} neutrons/cm^2 survived

[4]G. W. Keilholtz and R. E. Moore, Reactor Chem. Div. Ann. Progr. Rept. December 31, 1967, ORNL-4229, p. 143.

without significant gross damage, whereas all specimens irradiated at 150°C fractured. Niobium nitride, on the other hand, did not stand up as well at high temperature. Four of six specimens of NbN fractured, while no significant gross damage occurred at 150°C for fluences less than 3.8×10^{21} neutrons/cm^2. The results for TiN do not indicate whether there is a difference in gross damage for the two temperature ranges.

There is definitely an in-reactor thermal effect on the volume expansion of nitrides. Table 6.2 compares the volume expansion data at 150°C and 1000 to 1100°C for specimens that could be measured. The only case in which a dependence on neutron fluence was apparent was the high-temperature irradiation of TiN.

Table 6.2. Comparison of Volume Increases in Nitrides Irradiated at About 150°C and 1000 to 1100°C

Nitride	Dose Range [neutrons/cm^2, ($>$ 1 Mev)]	Volume Increase, %	
		at About 150°C	at 1000 to 1100°C
	$\times 10^{21}$		
ZrN	1.6–4.4	~ 3	
	0.4–2.2		~ 0.5
TiN	0.7–4.8	2–3	
	0.7–2.3		0.1–0.7
TaN		a	
	2.3		0.5
NbN	1.1–4.9	2–3	
	0.7–2.3		~ 1

[a]Not determined.

Volume increases were calculated from diameter and length measurements by using the equation $\Delta V/V = 2\Delta d/d + \Delta \ell/\ell$. The fractional increase in length of the nitrides irradiated at 1000 to 1100°C was from 2 to 16 times more than the fractional increase in diameter. This preference

for axial expansion, which did not occur at 150°C, can be explained by the constraint on radial expansion imposed by the TZM sleeves in which the specimens were enclosed and the absence of constraint on axial expansion. This phenomenon can be most easily understood if gas generation within the specimens is responsible for the observed expansion. Helium gas, produced randomly in nitrides through the (n,α) reaction, would, of course, diffuse in the direction of least resistance. Any helium gas in excess of that which can diffuse out of the specimen or into voids within grains must align itself to expand the entire specimen in the direction of least constraint. The greater mobility of atoms at high temperatures would facilitate preferential alignment.

The nitride irradiations were initiated as a preliminary survey, for their technology, unlike that of the carbides which we had begun investigating earlier, was relatively undeveloped. The specimens, bought from commercial sources, show a generally poor microstructure and stoichiometry, but the results provide hope that nitrides may prove useful as high-temperature nuclear materials. Several questions pertinent to the use of nitrides for the LMFBR program, however, have been raised from this work. Improvements in nitride technology may make it possible to prepare nitrides of higher quality with which experiments can be specifically designed to answer such questions as the role of the (n,α) reaction in producing damage and whether an improved microstructure will reduce fracturing.

Effects of Irradiation on LMFBR Fuels

Irradiations of Depleted UN, UC, and U(C,N) Fuels

These experiments are aimed at determining the effect of the generation of He through the (n,α) reaction on nitride fuels. The first irradiation assembly is being fabricated, and the specimens of depleted fuel are being prepared.

7. FAST-NEUTRON IRRADIATION EFFECTS ON ELECTRICAL INSULATORS

G. W. Keilholtz R. E. Moore
D. A. Dyslin[1]

The purpose of this program is to establish the effects of fast neutrons on materials suitable for use as electrical insulators in thermionic converters and to evaluate mechanisms of neutron damage in these materials from 150 to 1100°C.

General Survey of Fast-Neutron Effects on Electrical Insulators

This task is aimed at determining fast-neutron effects on a variety of materials with properties that are required for thermionic insulators. A low-temperature (150°C) assembly containing 1/2- × 1/2-in. cylindrical specimens of large-grain (25 μm) translucent Al_2O_3, sintered MgO, and Si_2ON_2 is being irradiated[2] in the ETR. This assembly will be removed from the ETR on December 2, 1968. A high-temperature (600, 800, 1100°C) assembly containing the same types of specimens as well as other materials of thermionic interest will be irradiated starting in the last half of FY 1969.

Irradiation of High-Density Commercial Al_2O_3 Products Considered for Thermionic Insulators

Irradiations in ETR

A short-term assembly and a long-term assembly containing three commercial types of Al_2O_3 in the form of both solid cylinders and thin-walled cylindrical shells were irradiated[2] in the ETR at 600, 800, and 1100°C. The short-term irradiation has been completed, and the specimens will soon be examined. The fast-neutron fluence ranges from 0.3 to 1.8×10^{21} neutrons/cm^2 (> 1 Mev). The long-term assembly will be removed from the ETR late in FY 1969.

---

[1]General Engineering Division.

[2]G. W. Keilholtz, R. E. Moore, and D. A. Dyslin, Fuels and Materials Development Program Quart. Progr. Rept., June 30, 1968, ORNL-4330, pp. 160–164.

Irradiations in EBR-II

The same types of specimens of Al_2O_3 irradiated in the ETR will be irradiated in the EBR-II to test the effect of neutron energy on damage. Three columns of specimens will be irradiated simultaneously with different capsule parameters for each column determined in such a way that when gamma-heating rate uncertainties are considered the temperatures of the three columns will bracket 800°C. The specimens are being prepared, and the irradiation assemblies are being designed.

Irradiations of Metal-Clad Al_2O_3 Specimens

Units consisting of cylindrical shells of metal-clad Al_2O_3, fabricated at other installations, are now undergoing irradiation in the ETR. This assembly will be removed from the ETR for postirradiation examinations in March 1969. The fast-neutron fluence will range from about 0.4 to 2×10^{21} neutrons/cm^2 (> 1 Mev).

8. MECHANICAL PROPERTIES RESEARCH AND LMFBR CLADDING AND STRUCTURAL MATERIALS DEVELOPMENT

C. J. McHargue J. R. Weir, Jr.

Work in this program includes studies of the high-temperature irradiation embrittlement and other technologically important aspects of radiation damage to fuel cladding materials at high neutron fluence. The work centers around types 304 and 316 stainless steel, Incoloy 800, and Hastelloy N and the effects of titanium concentration in these alloys on radiation damage, with emphasis on LMFBR applications. Associated with the program are studies of the effects of tubing fabrication variables on the properties of types 304 and 316 stainless steel and related compositions.

Development of Titanium-Modified Type 304 Stainless Steel

G. A. Reimann T. M. Nilsson

Tubing of titanium-modified types 304 and 304L stainless steel has been drawn to final size (0.250-in. outside diameter × 0.218-in. inside diameter) from several tube shells and two heats of material. This tubing has been submitted for nondestructive testing.

Recovery of usable material from extruded tube shells has averaged 75.5% for the modified type 304 stainless steel. About 65% of the finish-machined tube shells have been converted to 1/4-in.-diam tubing. Final recovery rates of tubing that will meet specifications for the Fast Flux Test Facility will not be known until the completion of nondestructive testing.

About 240 ft of tubing was examined with the borescope after drawing. Although this technique gives qualitative results only, it appears that about half the tubing may be acceptable.

The planetary swager was placed in operation, and we used it for the final pass on part of the tubing. This technique appears to have certain advantages over conventional methods of tube drawing, and we will investigate it further.

Several problem areas are apparent in the fabrication schedule: (1) large grain size, (2) duplex grain structures, (3) eccentricity, (4) straightness, and (5) scratches. Possible solutions that will increase the yield of acceptable tubing are being evaluated in further drawing tests.

We are also examining the influence of processing variables on grain size, since it is essential to have a uniformly fine-grained microstructure. The grain sizes of the tubing (0.250-in. outside diameter × 0.016-in. wall thickness) we first examined are shown in Table 8.1. The first batch was mandrel drawn in 26 passes, each of about 15% reduction, with a 20-min anneal at 1200°C between each pass. The annealing schedule for the last four passes (27 to 30) varied. One-third of the tubing was annealed after the first two passes, one-third was annealed after the first three passes, and the remaining third was not annealed at all (43% reduction). The processing of both the first and second batches has been reported earlier.[1] Table 8.1 shows that the grain sizes range from ASTM Nos. 5 through 8. Grain size decreases with increasing cold work and decreasing annealing temperatures, which is in agreement with the general recrystallization behavior of metals. Larger amounts of cold work also tend to eliminate variations in grain size through the tube wall.

Development of Titanium-Modified Types 316 and 316L Stainless Steel

E. E. Bloom

We are investigating the effects of small titanium additions on the mechanical properties of types 316 and 316L stainless steel. The alloys included in this investigation are from 50-lb heats melted by vacuum induction and have the compositions listed in Table 8.2. Baseline or reference data have been obtained from two commercial heats, melted in air, of types 316 and 316L stainless steel.[2]

---

[1]G. A. Reimann, Fuels and Materials Development Program Quart. Progr. Rept. June 30, 1968, ORNL-4330, pp. 175–176.

[2]E. E. Bloom, "Radiation Effects in Type 316 and Titanium-Modified Type 316 Stainless Steel," pp. 152–155, this report.

Table 8.1. Grain Size Measurements After Mandrel Drawing in Tubing of Type 304L Stainless Steel Modified with 0.2% Ti

Batch	Condition	ASTM Grain Size
First	After pass 26	
	Plus 13% cold work	6 to 7
	Plus annealing for 40 min at 1200°C	7
	Final size (after pass 30)	
	Plus 12% cold work and annealing for 40 min at 1200°C	5 to 6
	Plus 24% cold work	5 1/2
	Plus annealing for 40 min at 1200°C	7
	Plus 43% cold work	7
	Plus annealing for 40 min at 1200°C	7
Second[a]	2-1	
	Plus last 30% cold work	7 1/2
	Plus annealing for 1 hr at 925°C	8
	Plus 5% work by plug drawing	8
	2-2	
	Plus last 15% cold work	6 1/2 to 7 1/2
	Plus annealing for 1 hr at 925°C	7 1/2
	Plus 5% work by plug drawing	7 1/2

[a]2-1 and 2-2 correspond to the drawing schedules with 30 and 15% reduction, respectively, between anneals. All anneals, except where otherwise noted, are at 1200°C for 1 hr.

Figure 8.1 shows the effect of titanium content on the tensile ductility at 650°C and a strain rate of 0.002 min^{-1}. For each carbon content, alloys containing between about 0.1 and 0.3 wt % Ti exhibit significantly higher postirradiation ductility than alloys containing larger or smaller amounts of Ti.

Creep-rupture tests at 650°C and a range of stresses are being conducted. Ductility is shown in Fig. 8.2 as a function of titanium content for tests at 30,000 psi. On the basis of these preliminary results the following qualitative trends are observed: (1) for this

Table 8.2. Composition of 50-lb Heats, Melted by Vacuum Induction, of Titanium-Modified Types 316 and 316L Stainless Steel

Alloy Designation	Content, wt %							
	C	Cr	Ni	Mo	Ti	Mg	Si	B
R1	0.06	17	12	2.4	0.23	0.5	0.4	0.0007
S1	0.05	17	12	2.4	0.33	0.4	0.4	0.0007
T1	0.05	17	12	2.4	0.46	0.3	0.4	0.0005
U1	0.05	17	13	2.5	0.60	0.2	0.4	0.0005
H1	0.02	16	13	2.6	0.04	0.6	0.3	0.0010
J1	0.007	16	12	2.5	0.09	0.3	0.3	0.0008
K1	0.006	16	12	2.5	0.14	0.2	0.3	0.0010
L1	0.012	17	12	2.6	0.21	1.8	0.4	0.0007
M1	0.023	17	11	2.5	0.30	1.8	0.4	0.0008
N1	0.023	17	12	2.6	0.46	1.7	0.4	0.0005

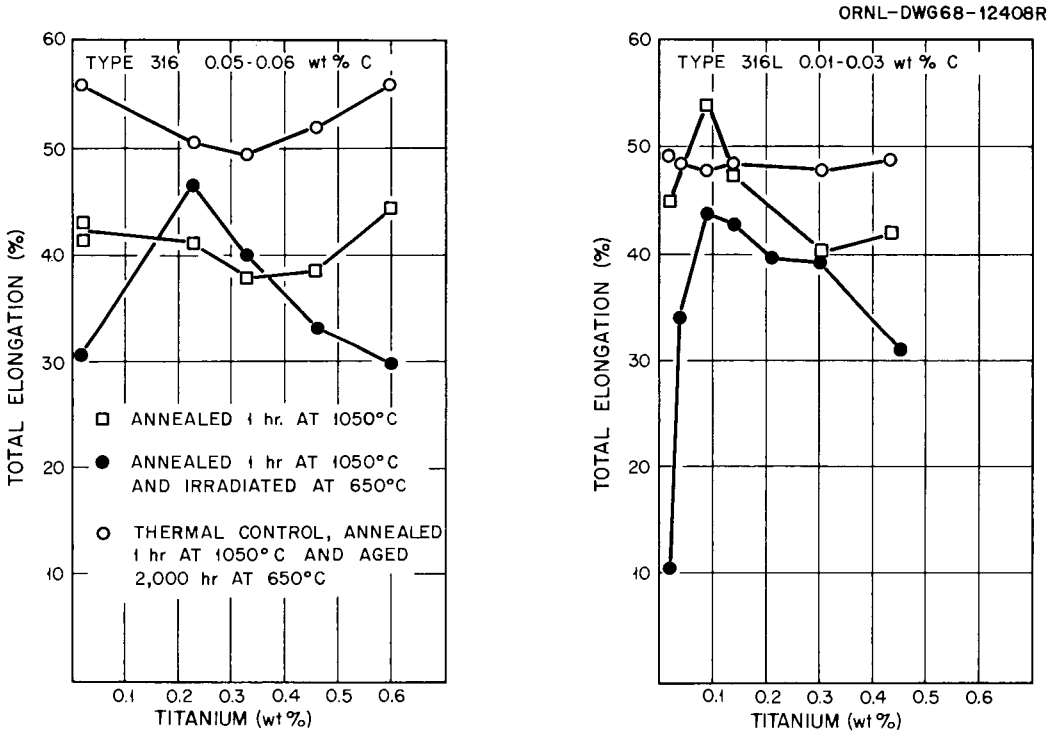

Fig. 8.1. Effect of Titanium Content on the Tensile Ductility of Types 316 and 316L Stainless Steel. Strain rate 0.002 min^{-1}. Irradiation conditions: about 2200 hr at 650°C, 9×10^{20} neutrons/cm^2 (thermal) and 7×10^{20} neutrons/cm^2 (> 1 Mev).

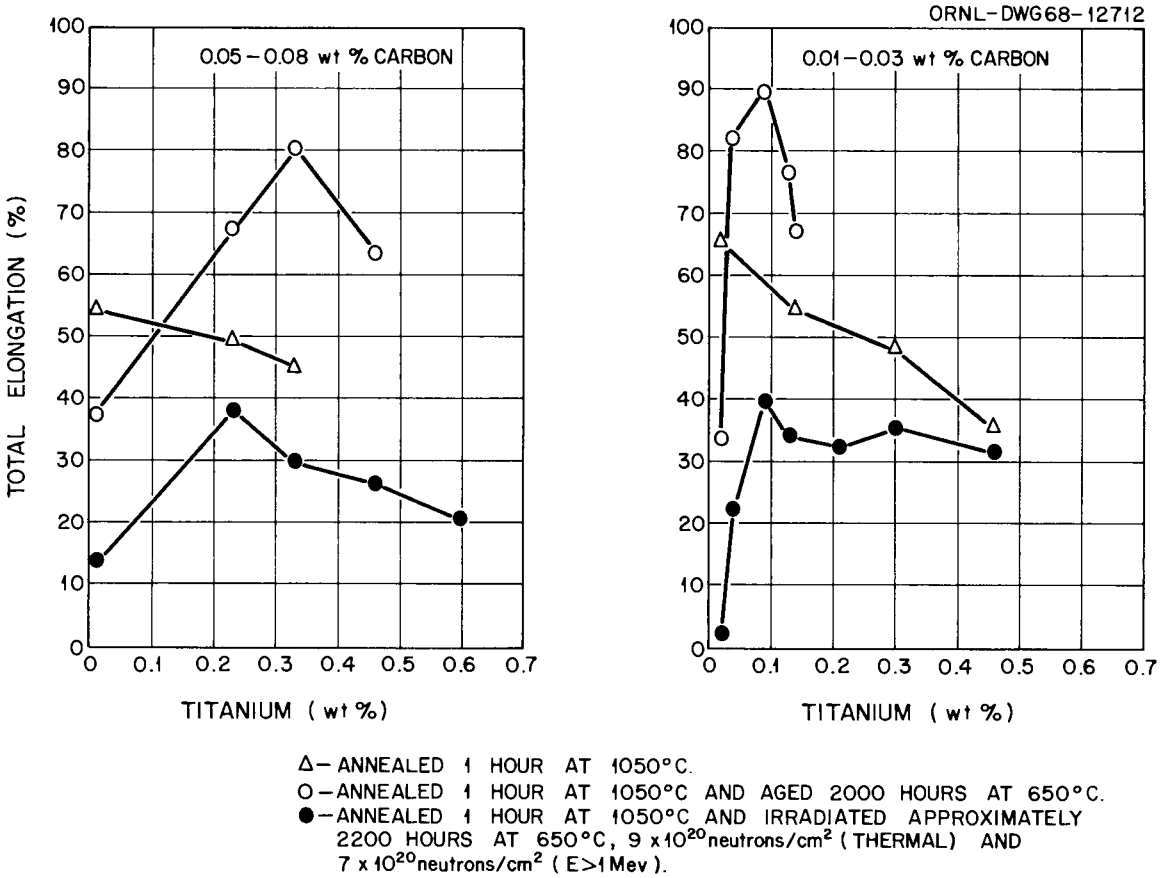

Fig. 8.2. Ductility as a Function of Titanium Content in Type 316 Stainless Steel Tested at 650°C at a Stress of 30,000 psi.

test condition, the ductility in the annealed condition appears to decrease with increasing titanium content; (2) aging the titanium-modified alloys results in an increased ductility; (3) for the series with 0.05 to 0.08 wt % C, maximum postirradiation ductility occurred in the alloy containing 0.23 wt % Ti; (4) in the series with 0.01 to 0.03 wt % C, the postirradiation ductility was significantly improved and essentially constant for alloys containing between 0.1 and 0.46 wt % Ti.

Radiation Effects in Type 316 and Titanium-Modified Type 316 Stainless Steel

E. E. Bloom

Our investigation of the effects of neutron irradiation on the mechanical properties of type 316 stainless steel and titanium-modified

type 316 stainless steel involves tensile and creep-rupture tests on specimens in three conditions: (1) annealed, (2) annealed and irradiated, and (3) annealed and aged at the irradiation temperature for the irradiation time. Variables under investigation include: (1) preirradiation heat treatment, (2) irradiation temperature, and (3) postirradiation test conditions, such as test temperature and strain rate.

The chemical compositions of the two heats of material now being investigated are listed in Table 8.3. Specimens of type 316 stainless steel have been annealed 1 hr at 1050°C and irradiated for about 2200 hr at temperatures of 550, 650, and 750°C. The neutron fluences in this experiment were about 9×10^{20} neutrons/cm^2 (thermal) and 7×10^{20} neutrons/cm^2 (> 1 Mev). Postirradiation tensile properties were determined at test temperatures of 550, 650, and 750°C. Results have indicated that irradiation at these conditions caused a significant decrease in both uniform and total elongation. The decrease in tensile ductility parameters was, however, independent of irradiation temperature over the range investigated. Postirradiation creep-rupture properties were dependent on irradiation temperature. As the irradiation temperature was increased in the range of 550 to 750°C, the creep rate and ductility increased as measured by postirradiation creep-rupture tests at 650°C.

Postirradiation testing of types 316 and 316L stainless steel irradiated at 650°C is continuing. Tensile properties of specimens tested in the unirradiated and irradiated conditions are shown in Figs. 8.3 and 8.4. The yield strength of the irradiated specimens of

Table 8.3. Chemical Composition of Types 316 and 316L Stainless Steel

	Content, wt %								
	C	Cr	Ni	Mo	Mg	Si	P	S	B
Type 316 Stainless Steel	0.068	17.2	12.5	2.06	1.9	0.5	0.039	0.004	0.0005
Type 316L Stainless Steel	0.02	16.9	12.7	2.7	2.3	0.58	0.013	0.015	0.0002

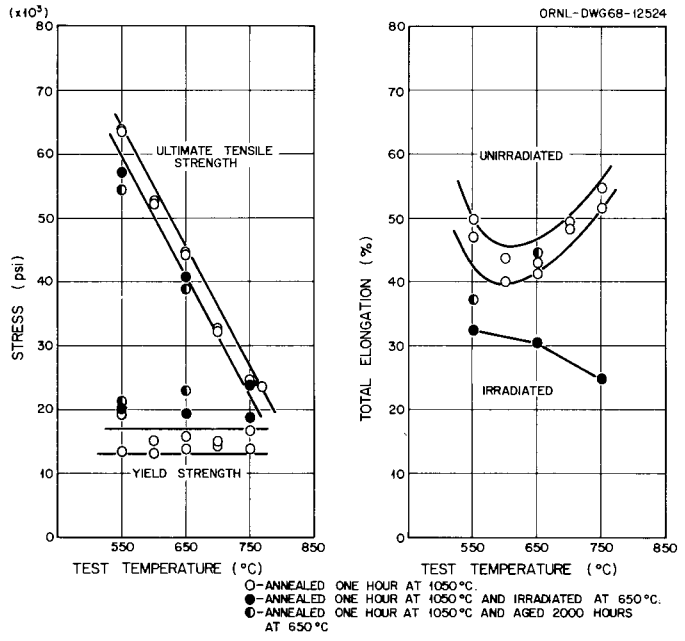

Fig. 8.3. Elevated Temperature Tensile Properties of Type 316 Stainless Steel in the Unirradiated Condition and After Irradiation at 650°C to About 9×10^{20} neutrons/cm^2 (Thermal) and 7×10^{20} neutrons/cm^2 (> 1 Mev). Strain rate: 0.002 min^{-1}.

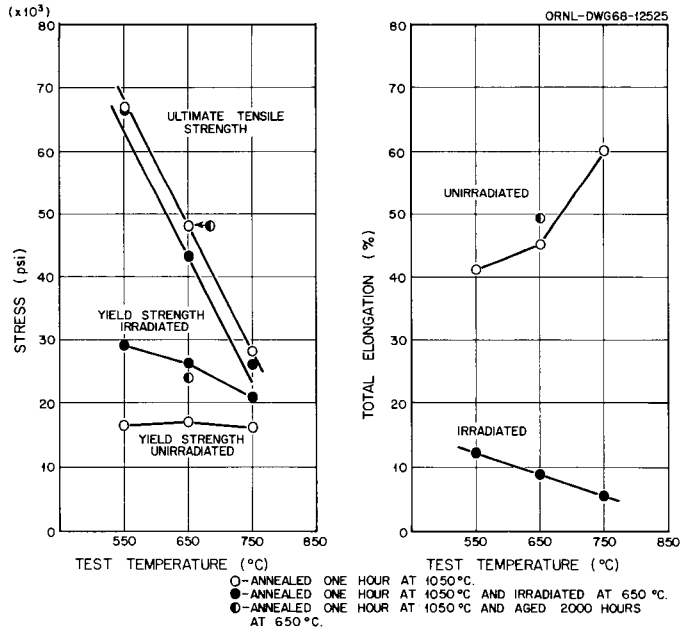

Fig. 8.4. Elevated Temperature Tensile Properties of Type 316L Stainless Steel in the Unirradiated Condition and After Irradiation at 650°C to About 9×10^{20} neutrons/cm^2 (Thermal) and 7×10^{20} neutrons/cm^2 (> 1 Mev). Strain rate: 0.002 min^{-1}.

both alloys was higher than that of annealed specimens. This increase appears to result from thermal aging rather than the irradiation, since specimens aged 2000 hr at 650°C also exhibit increased yield strength. There also appears to be a trend for both irradiated and thermal control specimens to have slightly lower ultimate tensile strengths than the as-annealed specimens. Over the range of test temperatures between 550 and 750°C, there is a significant reduction in total elongation that is greater for the low-carbon alloy than for the high-carbon alloy, even though the low-carbon alloy had a somewhat lower boron content and finer grain size. This suggests that differences in microstructure, such as the distribution of carbide precipitate, are important.

A comparison of the creep-rupture properties of these two alloys at 650°C is shown in Fig. 8.5. The life to rupture of both alloys is reduced by neutron irradiation. Irradiated specimens of type 316 stainless steel exhibited both reduced ductility and an increased minimum creep rate as compared to specimens in the as-annealed condition. The thermal control tests completed to date indicate that the increased creep rate is a result of thermal aging and that the reduced ductility is a result of neutron irradiation. For type 316L stainless steel irradiated under the same conditions, the minimum creep rates of annealed, irradiated, and thermal control specimens were comparable for the stresses investigated, and the reduced life to rupture results from a large reduction in ductility. Figure 8.6 compares the ductility of these two alloys as a function of strain rate for tests at 650°C. At high strain rates, the postirradiation ductility of type 316 stainless steel is significantly higher than that of type 316L stainless steel, while at lower strain rates, the ductilities of the two alloys are comparable.

Effects of Titanium and Carbon Variations in Incoloy 800

D. G. Harman

We determined the tensile properties of specimens from several experimental heats at 20 to 900°C and a strain rate of 0.02 min^{-1}. We heat

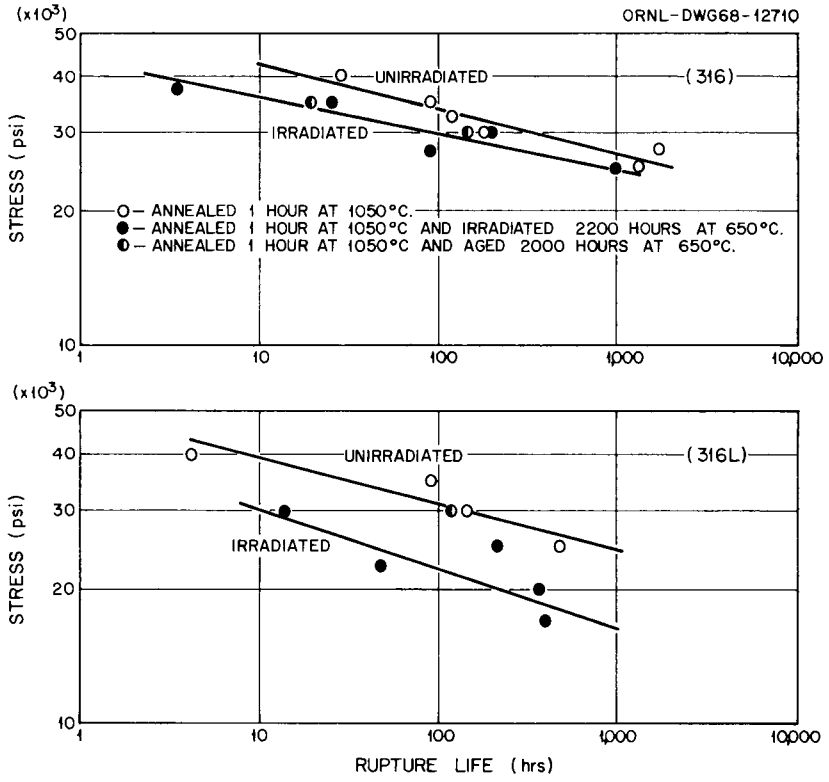

Fig. 8.5. Effect of Irradiation on the Rupture Life of Types 316 and 316L Stainless Steel at 650°C. Specimens were irradiated for about 2200 hr at 650°C to 9×10^{20} neutrons/cm^2 (thermal) and 7×10^{20} neutrons/cm^2 (> 1 Mev).

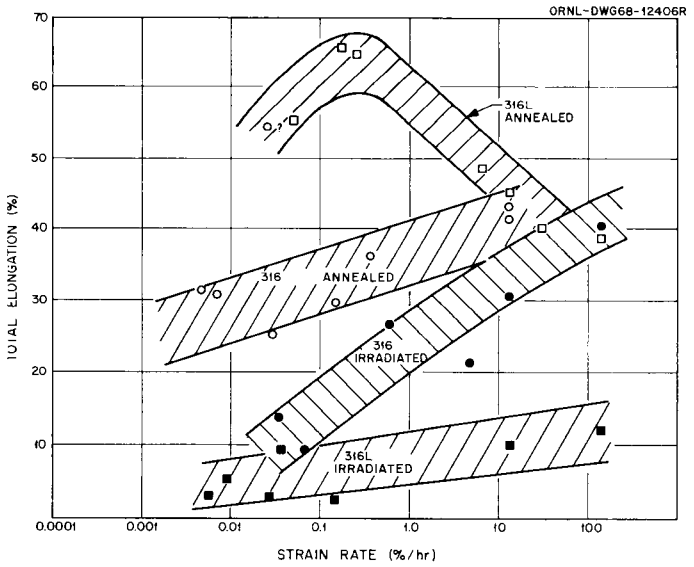

Fig. 8.6. Comparison of the Ductilities of Types 316 and 316L Stainless Steel at 650°C. One hour at 1050°C, pretest and preirradiation anneal. Irradiation conditions: 2200 hr at 650°C, 9×10^{20} neutrons/cm^2 (thermal) and 7×10^{20} neutrons/cm^2 (> 1 Mev).

treated the specimens to produce the mill-annealed condition. The heats containing 0.03 wt % C were held at 982°C for 30 min and those containing 0.12 wt % C were held at 1038°C for 30 min. Figures 8.7 through 8.9 show, respectively, the ultimate tensile strength, the 0.2% yield strength, and the total elongation plotted against the test temperature. In each case, the property curve from International Nickel Company's commercial Incoloy 800 is shown for comparison.

The yield strength values shown in Fig. 8.8 are particularly important, since design stresses based on the ASME Boiler and Pressure Vessel Code utilize yield strength values at temperatures below about 650°C for this alloy. Figure 8.8 shows the significantly higher yield strength of the high-carbon alloys as compared to the alloys of the low-carbon content typical of current commercial Incoloy 800. Although solution annealed material will, in general, have a lower yield strength, we expect the high-carbon alloy to show a strength advantage.

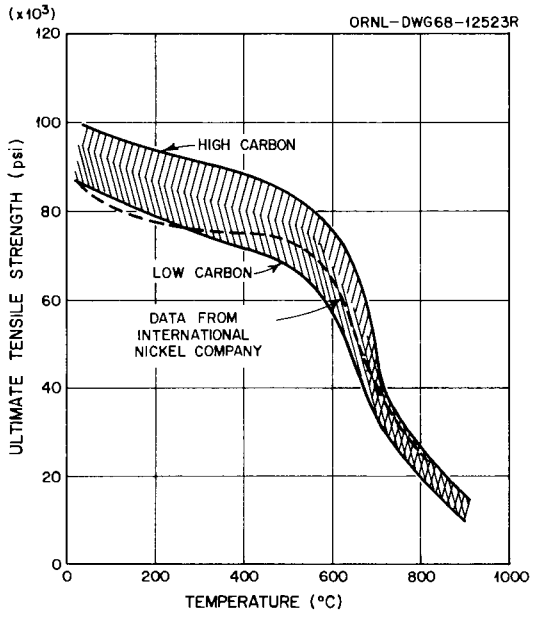

Fig. 8.7. Tensile Strength of Several Heats of Incoloy 800 Versus Test Temperature. Specimens were held at 982°C (low carbon) or 1038°C (high carbon) for 30 min and tested at 0.02 min^{-1}. Data from the International Nickel Company on mill-annealed (982°C) hot-rolled rod are shown for comparison. [Ref. Engineering Properties of Incoloy Alloy 800, Technical Bulletin T-40, The International Nickel Company (1964).]

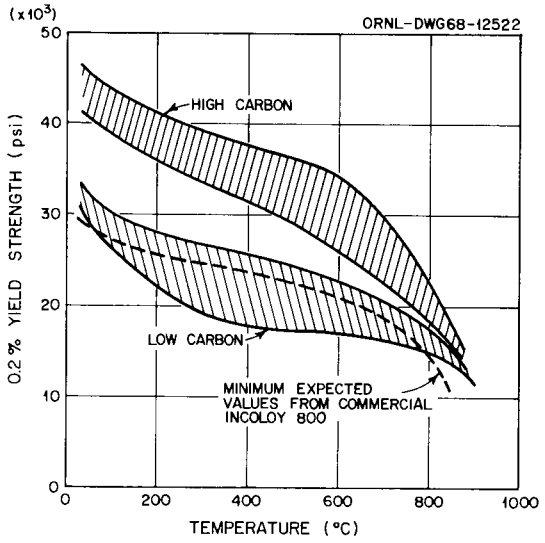

Fig. 8.8. Yield Strength of Several Heats of Incoloy 800 Versus Test Temperature. Specimens were heat treated and tested as indicated in Fig. 8.7. Data from International Nickel Company are the minimum values expected from mill-annealed hot-rolled rod. [Ref. Incoloy-800 for Nuclear Fuel Sheaths (A Monograph), C. N. Spalaris, Comp., GEAP-4633 (July 1964).]

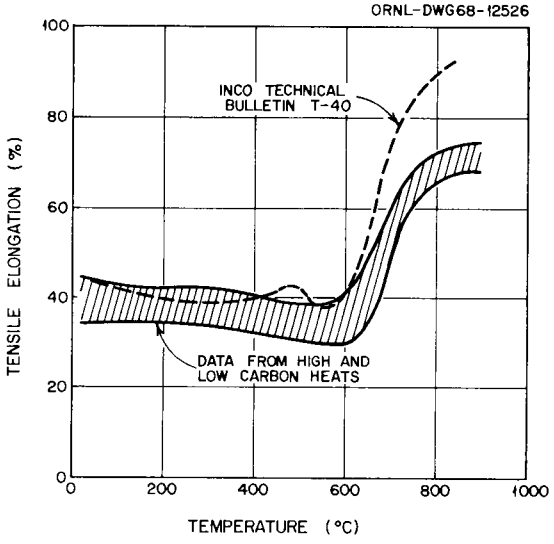

Fig. 8.9. Tensile Ductility of Several Heats of Incoloy 800 Versus Test Temperature. Specimens were heat treated and tested as indicated in Fig. 8.7. Data from International Nickel Company are as indicated in Fig. 8.7.

However, yield strength values should not affect design stresses for strictly creep situations. Further efforts will be directed toward evaluating unirradiated Incoloy 800 as a high-temperature structural material.

Radiation Damage in Incoloy 800

D. G. Harman

We are continuing our evaluation of the irradiation experiment comparing four heats of Incoloy 800 over a range of grain sizes. Samples containing 0.03 and 0.12% C and 0.1 and 0.3% Ti were irradiated at 700°C after being heat treated to provide the desired grain sizes.

We reported[3] tensile data for both the irradiated and control specimens and creep-rupture data for the irradiated specimens only. Several of the control creep tests have been completed, and Table 8.4 shows the current status.

As expected, the irradiated specimens showed about the same minimum creep rate as did the control specimens. In general, the creep rate decreased with increasing grain size. For the low-carbon heats, in which the spread in grain size was larger, this amounted to a difference of an order of magnitude.

Figure 8.10 shows the minimum creep rate versus the approximate grain diameter for the tests at 12,000 psi. Both the low-carbon alloys showed the same relationship of creep rate with grain size, but the heat with 0.1% Ti consistently showed twice the creep rate of that with 0.3% Ti. This was also true to some extent for the two high-carbon heats.

The low-carbon heats showed lower creep rates than did the high-carbon heats with the smaller grain sizes, but this was not true for the larger grain sizes. An extrapolation of the data to larger grain sizes (higher solution temperature) would indicate the high-carbon material to

---

[3]D. G. Harman, Fuels and Materials Development Program Quart. Progr. Rept. June 30, 1968, ORNL-4330, pp. 188–195.

Table 8.4. Creep-Rupture Properties of Four Incoloy 800 Heats[a] at 700°C

Annealing Temperature (°C)	Stress (psi)	Rupture Time, hr		Creep Elongation, %		Minimum Creep Rate, %/hr	
		Control	Irradiated	Control	Irradiated	Control	Irradiated
			0.1% Ti, 0.03% C				
900	12,000	67.0	79	89.3	54.2	0.43	0.29
925	12,000	88.9	103	113.7	60.6	0.33	0.19
950	12,000	125.1	95	99.6	63.0	0.23	0.23
980	12,000		419		57.8		0.05
1000	12,000		640		40.0		0.04
900	10,000	134	130	163.8	~ 100	0.25	0.19
925	10,000		144		68.2		0.16
950	10,000		230		87.3		0.10
980	10,000		676		58.6		0.03
			0.3% Ti, 0.03% C				
900	12,000		74		29.5		0.20
925	12,000		103		23.4		0.09
950	12,000		165		12.0		0.47
980	12,000		307		12.2		0.03
1000	12,000		260		9.9		0.03
900	10,000		215		33.5		0.07
925	10,000		86		19.6		0.14
950	10,000		233		19.8		0.05
980	10,000		507		15.4		0.02
			0.1% Ti, 0.12% C				
975	12,000	61.8	48	89.6	63.3	0.53	0.54
1000	12,000	54.4	51	57.2	36.8	0.53	0.49
1025	12,000	74	77	116.6	53.1	0.47	0.31
1040	12,000	134.4	108	101.8	50.7	0.26	0.20
1100	12,000	547.7	390	81.9	57.5	0.06	0.06

Table 8.4. (Continued)

Annealing Temperature (°C)	Stress (psi)	Rupture Time, hr		Creep Elongation, %		Minimum Creep Rate, %/hr	
		Control	Irradiated	Control	Irradiated	Control	Irradiated
			0.1% Ti, 0.12% C (continued)				
975	10,000	115.7	90	132.6	85.5	0.30	0.37
1000	10,000	181	125	113	100.3	0.21	0.23
1025	10,000	176	158	76.9	71.3	0.18	0.18
1040	10,000	224	247	137.5	79.7	0.16	0.11
			0.3% Ti, 0.12% C				
975	12,000	59.8	27	107.0	27.7	0.53	0.58
1000	12,000	64.9	36	118.0	27.0	0.49	0.40
1025	12,000	99.7	54	52.1	24.2	0.26	0.29
1040	12,000	135.8	72	111.7	21.8	0.22	0.18
1100	12,000	In test 760	408	In test 23	19.0	In test	0.03
975	10,000	112.3	76	79.5	33.4	0.28	0.25
1000	10,000	154.4	77	84.0	32.2	0.19	0.23
1025	10,000	191.0	56	134.0	26.7	0.16	0.27
1040	10,000	250.7	141	103.6	27.0	0.10	0.11

[a]Specimens heat treated 30 min at indicated temperature, then irradiated at 700°C to 2 to 3 × 10^{20} neutrons/cm^2 (thermal) or held at 700°C in the laboratory (controls) for 1100 hr.

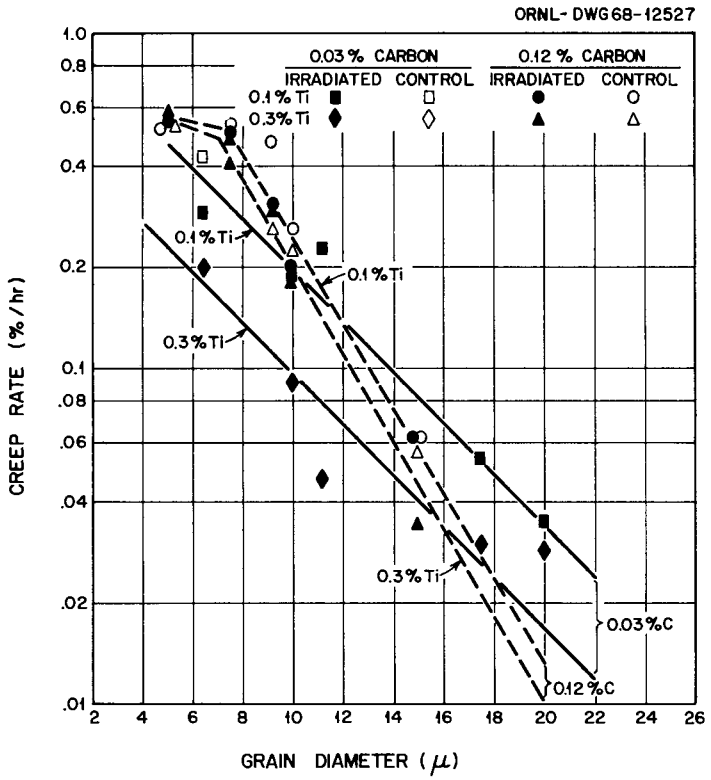

Fig. 8.10. Minimum Creep Rate at 12,000 psi for Four Incoloy 800 Heats at 700°C. Specimens were heat treated to indicated grain sizes and irradiated at 700°C to 2 to 3 × 10^{20} neutrons/cm^2 (thermal) or held at 700°C in the laboratory (controls) for 1100 hr.

be superior. This might be expected because more C would be in solution.

Table 8.4 shows that for the samples with 0.1% Ti the irradiation caused essentially no loss in rupture time for the 10,000-psi tests. Slight losses were obtained at the higher stress of 12,000 psi. The material with 0.3% Ti, on the other hand, showed appreciable losses at both stresses.

The control specimens with 0.3% Ti showed ductility similar to that of those with 0.1% Ti. After irradiation, however, the heats with 0.1% Ti were superior, as was reported previously. A more complete analysis of this experiment will be available for the next report.

Mechanical Properties of Hastelloy N and Related Compositions

C. E. Sessions H. E. McCoy R. E. Gehlbach

The aim of our current program is the development of a titanium-modified Hastelloy N with improved resistance to radiation damage. We have reported on the progress of our scaleup to 100-lb commercial melts,[4] in which both the irradiated and unirradiated mechanical behavior is superior to that of standard Hastelloy N. We are evaluating the thermal stability of the modified alloy since the addition of Ti to this Ni-Mo-Cr system could well influence the aging tendency of the alloy. We here report studies on aging, irradiation damage, and electron microscopy that relate to the metallurgical stability of the titanium-modified compositions at elevated temperatures.

Aging of Titanium-Modified Hastelloy N

Since the presence of Ti may affect the aging tendency of the alloy system, we are conducting an aging study on four commercial heats. Each alloy nominally contains Ni–12% Mo–7% Cr–0.2% Mn–0.06% C, with titanium concentration (0.15, 0.27, 0.45, and 1.2%) being the only significant variable. We are using the change in the tensile properties at 650°C and a strain rate of 0.002 min^{-1} to measure aging. Aging temperatures of 760 and 650°C are examined for three heat treatments before aging: 1 hr at 1177°C, 1 hr at 1260°C, and 1 hr at 1177°C plus 10% prestrain at room temperature. We shall eventually have data for aging times of 1500, 3000, and 10,000 hr; at present, however, only the results for 3000-hr aging are complete.

The changes in the yield strength and the total elongation due to aging following our standard solution anneal of 1 hr at 1177°C are shown in Fig. 8.11. The yield strength increases after aging at 650 and 760°C, the increase being greater for the 650°C aging treatment.

---

[4]H. E. McCoy and J. R. Weir, Quarterly Progress Report: Irradiation Effects on Reactor Structural Materials, August, September, October, 1967, BNL-678, pp. 11.14–11.19.

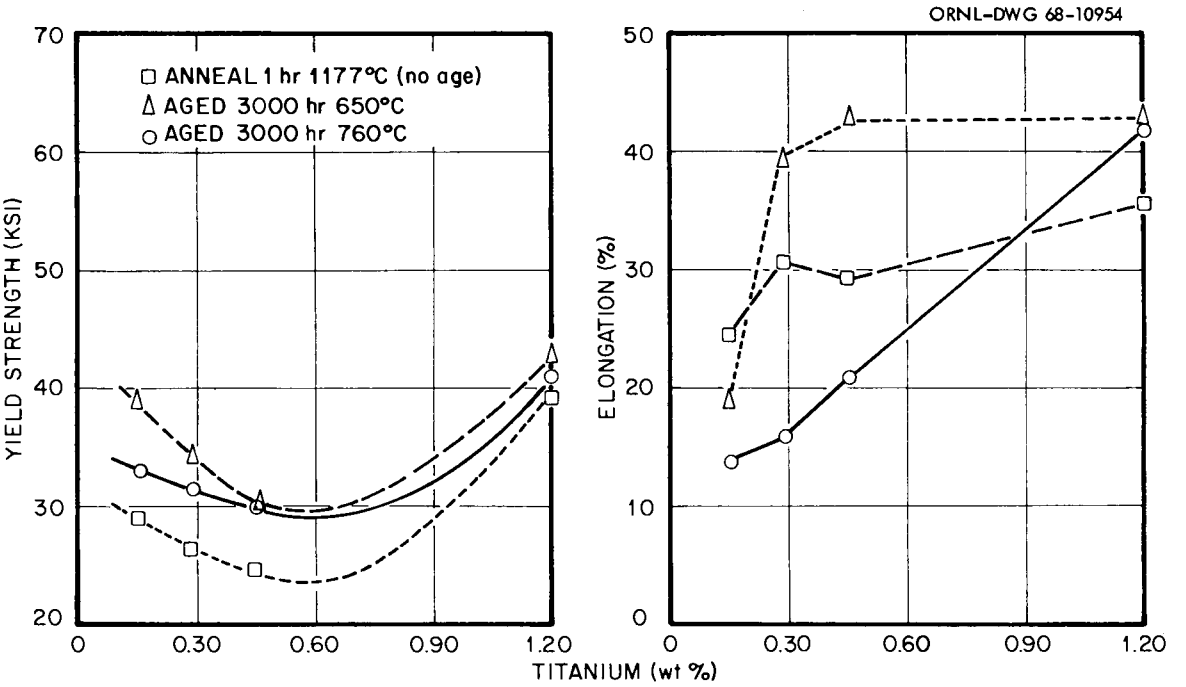

Fig. 8.11. Dependence of Strength and Ductility on Titanium Content of Modified Hastelloy N.

The change in the elongation at fracture is dependent on both the titanium content and the aging temperature. Aging at 650°C results in an increase in total elongation from about 30 to 40% for the three higher titanium levels and a decrease for the lowest titanium level. However, the 760°C aging temperature results in a decrease in tensile elongation from about 30 to about 15% at 650°C for the three lower titanium levels and an increase at the 1.2% Ti level.

Figures 8.12 and 8.13 summarize the property changes that result from several heat treatments and aging at 650 or 760°C. Here we have plotted the fractional change in total elongation and 0.2% yield strength based on the unaged samples with positive values indicating improvement and negative values indicating reduction in property with aging. Thus, each point should represent a percentage change due to aging alone. After aging at 650°C, the ductility varies appreciably with titanium content. Generally, at low levels the ductility is reduced, at 0.5% Ti the ductility increases, and at 1.2% Ti the ductility is improved by aging provided the treatment before aging did not involve annealing above 1177°C. The yield strength increases due to aging, the magnitude

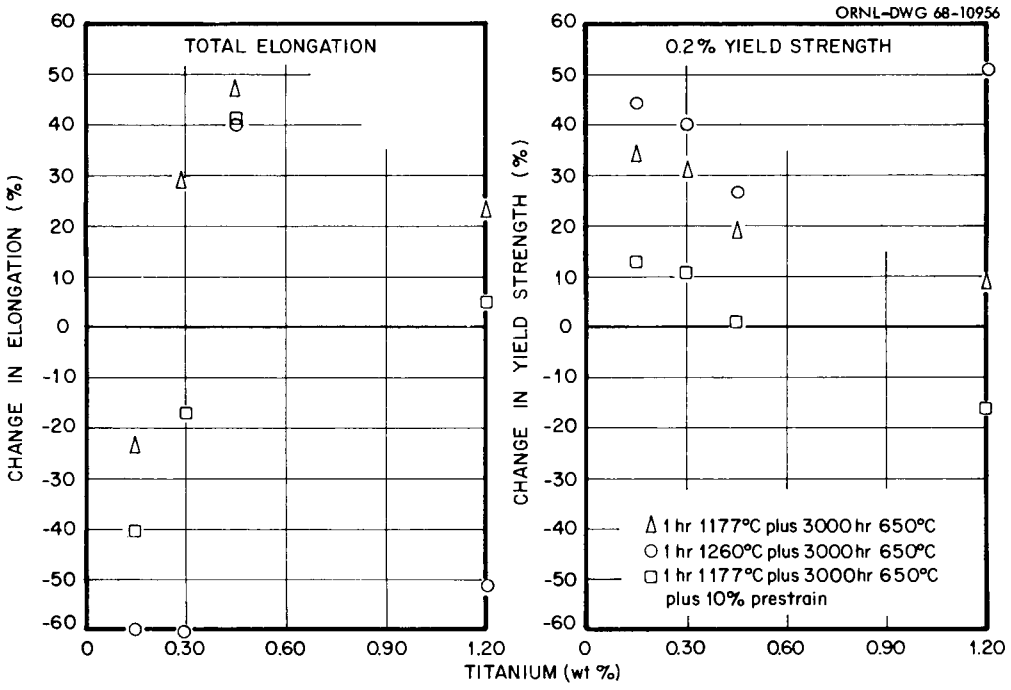

Fig. 8.12. Variation of Aging Response at 650°C for Titanium-Modified Hastelloy N with Titanium Content and Treatments Before Aging.

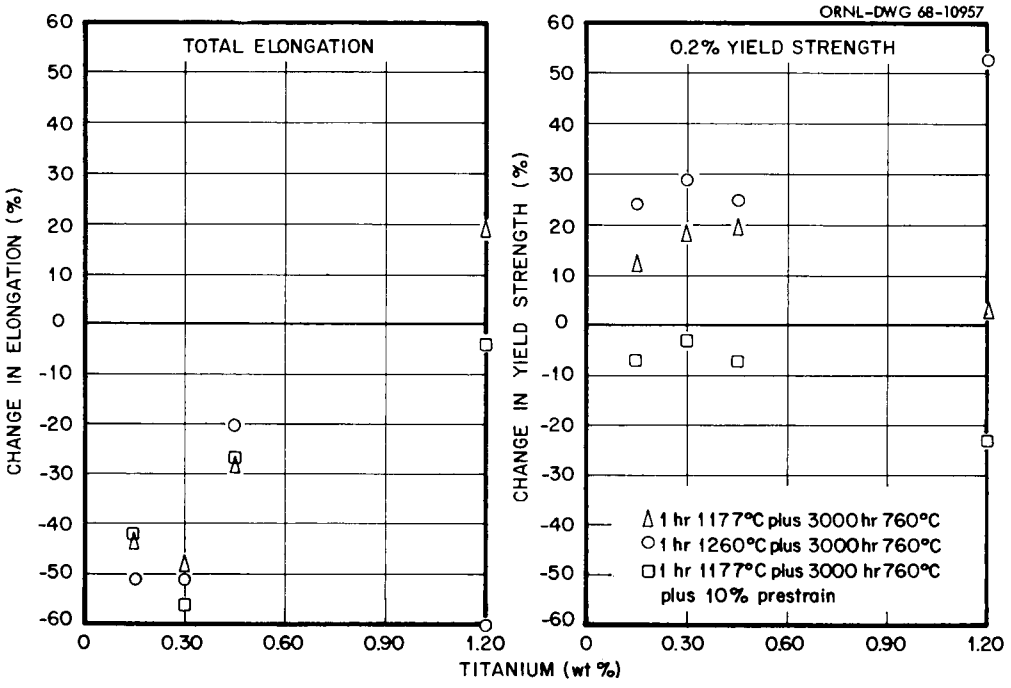

Fig. 8.13. Variation of Aging Response at 760°C for Titanium-Modified Hastelloy N with Titanium Content and Treatments Before Aging. Properties measured at 650°C.

of the increase diminishing with increasing titanium content. Using either a higher temperature for solution annealing (1260°C) or room-temperature prestraining before aging generally results in higher strengths and lower ductilities for samples both before and after aging.

As shown in Fig. 8.13, the aging at 760°C has resulted in a large (30 to 60%) loss in ductility for each heat treatment except at the 1.2% Ti level. The yield strengths increase on aging at 760°C except for the sample prestrained 10% before aging.

The microstructures of the three lower titanium levels appear similar, and the properties of each were also equivalent. However, the sample with 1.2% Ti exhibits precipitation, primarily along bands that probably resulted from fabrication. The large variation in properties of this heat with heat treatments (Figs. 8.12 and 8.13) may be partly attributable to local inhomogeneities within the original ingot that are evident as localized stringers of precipitate particles.

The magnitude of the observed aging effect at 760°C after 3000 hr is cause for some concern because we expect creep conditions and neutron irradiation to further reduce the fracture ductility. The role of Ti in the aging process is somewhat confusing, and it appears that Ti may actually be inhibiting rather than causing the aging.

Effects of Irradiation Temperature

Our first tests of mechanical properties of the titanium-modified Hastelloy N used samples that had been irradiated at 650°C. We found the properties excellent at test temperatures of 760 and 650°C. In additional experiments, we have irradiated samples over a broad temperature range for 1000 hr to a thermal fluence of 3×10^{20} neutrons/cm^2 and run postirradiation creep tests at 650 and 760°C. The stress-rupture properties of these samples at 650°C are shown in Fig. 8.14. Three heats of material were involved, each having the nominal composition Ni–12% Mo–7% Cr–0.2% Mn–0.05% C–0.5% Ti. Heat 104 is a 2-lb laboratory melt made by arc melting virgin stock, and heats 21545 and 66-548 are 100-lb melts from two different commercial vendors. All three materials have better stress-rupture properties than irradiated standard Hastelloy N at 650°C as long as the irradiation temperature is 660°C or lower. The

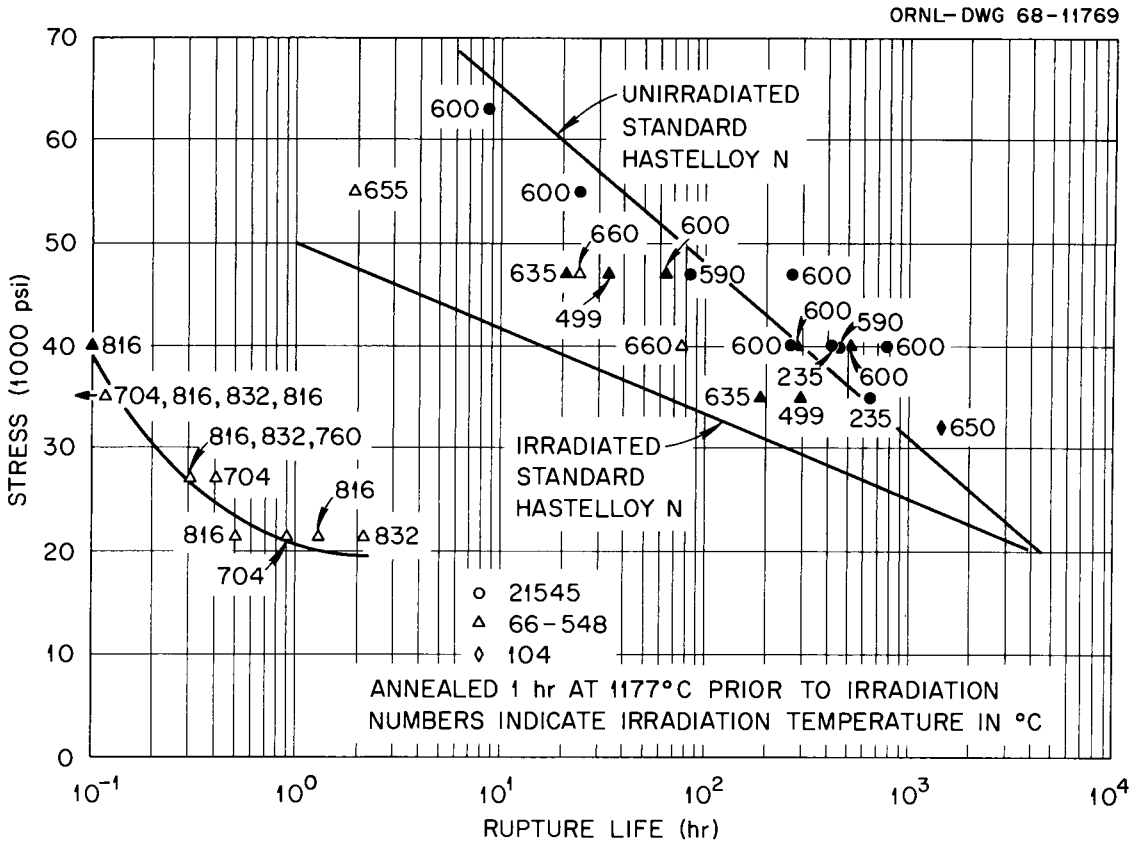

Fig. 8.14. Postirradiation Creep-Rupture Properties of Titanium-Modified Hastelloy N at 650°C.

samples of heat 66-548 irradiated at higher temperatures failed in shorter times when irradiated at temperatures of 704°C and greater. In general, the minimum creep rate is not significantly different in the irradiated and unirradiated conditions as long as the irradiation temperature does not exceed 660°C. The postirradiation creep rate is increased in samples irradiated above 704°C. The creep-rupture properties of all the titanium-modified alloys are superior to those of irradiated standard Hastelloy N at 760°C. However, heats 66-548 and 21545 show a reduction in life to rupture as the temperature of irradiation is increased.

The fracture strains are shown in Fig. 8.15 as a function of the minimum creep rate for tests at 760 and 650°C. Previous studies have

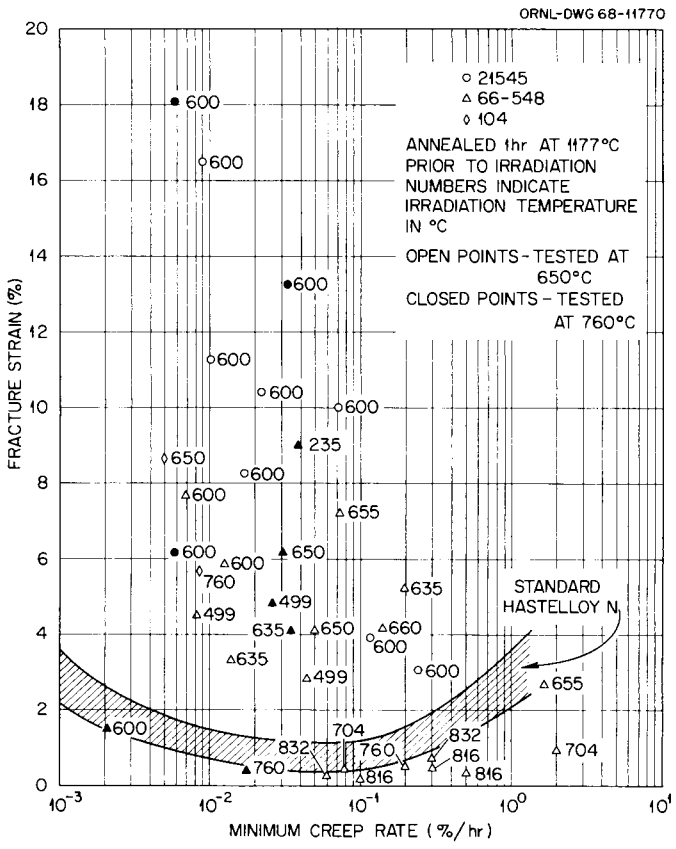

Fig. 8.15. Effect of Strain Rate on the Fracture Strain of Titanium-Modified Hastelloy N.

shown[5] that the scatterband in Fig. 8.14 holds for air- and vacuum-melted standard Hastelloy N when irradiated and tested at common temperatures of 650 or 760°C. Note the grouping of points for tests at 650°C on samples irradiated at 660°C or less and for tests at 760°C on samples irradiated at 760°C or less. All these samples show an improvement in fracture strain over that of irradiated standard Hastelloy N. The samples irradiated at 704°C and above and tested at 650°C fall below the scatterband for standard Hastelloy N. (These tests also show shorter rupture lives in Fig. 8.15 and higher creep rates.)

One further observation is that a heat of modified Hastelloy N (Ni–12% Mo–7% Cr–0.2% Mn–0.05% C) without the titanium addition also

[5]H. E. McCoy, MSR Program Semiann. Progr. Rept. Feb. 29, 1968, ORNL-4254, pp. 198–201.

showed a marked deterioration of postirradiation properties at 650°C when irradiated above 700°C. A significant difference in the behavior of the modified alloys with and without Ti is that the alloy without Ti (heat 21546) recovers its strength as the stress level is decreased. The samples of heat 21546 irradiated above 700°C that showed reduced rupture lives also had higher creep rates and lower fracture strains than samples irradiated at 650°C or lower.

Those observations have shown that the creep properties at 650°C of at least one 100-lb melt of titanium-modified Hastelloy N deteriorate when the irradiation temperature is above 700°C. This is of utmost concern since we want to use this alloy at 700°C. We have also found that a similar alloy without Ti shows similar behavior. This led us to question whether such effects are universal for Hastelloy N. We have never performed an experiment directed at evaluating the effects of irradiation temperature on the creep-rupture properties of Hastelloy N. We have found that the properties at 650 and 760°C are not affected markedly by irradiation temperature between 43 and 650°C, but we have never tested at 650°C a sample irradiated at 760°C. Such an experiment is now being carried out.

Electron Microscopy Studies

Hastelloy N. — We have found that the types and behavior of precipitated phases in Hastelloy N are closely related to the concentration of Si in the alloy.[6] The presence of more than about 0.2% Si in the melt causes increasing enrichment of the Si in the M_6C-type precipitates. The role of Si appears to be that of substituting for metal in the precipitates, resulting in a silicon-rich M_6C that is stable at temperatures higher than the true M_6C (ref. 7). However, the silicon-rich M_6C phase transforms to the Mo_2Ni_3Si intermetallic at temperatures above 1300°C. We

---

[6]R. E. Gehlbach, MSR Program Semiann. Progr. Rept. Feb. 29, 1968, ORNL-4254, pp. 206–213.

[7]R. E. Gehlbach and H. E. McCoy, "Phase Instability in Hastelloy N," paper presented at the International Symposium on Structural Stability in Superalloys, Seven Springs, Pennsylvania, September 4–6, 1968. To be published in the proceedings.

have not evaluated the kinetics of the transformation or the subsequent decomposition on exposure to lower temperatures. Preliminary investigations indicate that decomposition occurs with the formation of at least M_6C and Mo_2C. The high-temperature Mo_2Ni_3Si intermetallic has been identified both by x-ray diffraction and electron-probe microanalysis from extracted particles.

In alloys containing about 0.2% Si some true M_6C is formed, which can be put into solid solution at high annealing temperatures. The high-temperature silicide phase is not formed. We have found that decreasing either the Si or Mo causes the precipitation of Mo_2C as well as the M_6C type. Alloys with trace levels of Si have only Mo_2C after extended exposure at elevated temperatures.

Titanium-Modified Hastelloy N. — The microstructure of the titanium-modified alloy is quite different from that of the standard material. Two of the major compositional changes that affect the microstructure and precipitates that form are a decrease in Mo from 16 to 12% and a decrease in Si from 0.6 to 0.02% or less. As a result, precipitates of the M_6C type, which compromise the stringer and grain-boundary phases in the original version of the alloy, are absent.

Unlike what happens in the standard alloy, precipitates in the modified Hastelloy N are put into solid solution at normal annealing temperatures. Exposure at temperatures similar to those expected in service results in precipitation both at the grain boundary and in the matrix. Figure 8.16(a) shows the typical mode of precipitation in and adjacent to the grain boundaries after aging at 650°C for 1500 hr. Preliminary indications suggest that the precipitates are of the Mo_2C type. We observed [Fig. 8.16(b)] fewer precipitates of slightly different morphology after exposure at 760°C. The tensile ductility corresponding to this structure was lower than that of the unaged specimen.

The differences in precipitate morphology and amounts formed at 650 and 760°C are evident in Fig. 8.16. We know, from the results of tensile tests of aged specimens and from the postirradiation creep-rupture tests discussed above, that the loss of strength and ductility coincides with the higher temperatures where fewer precipitates are

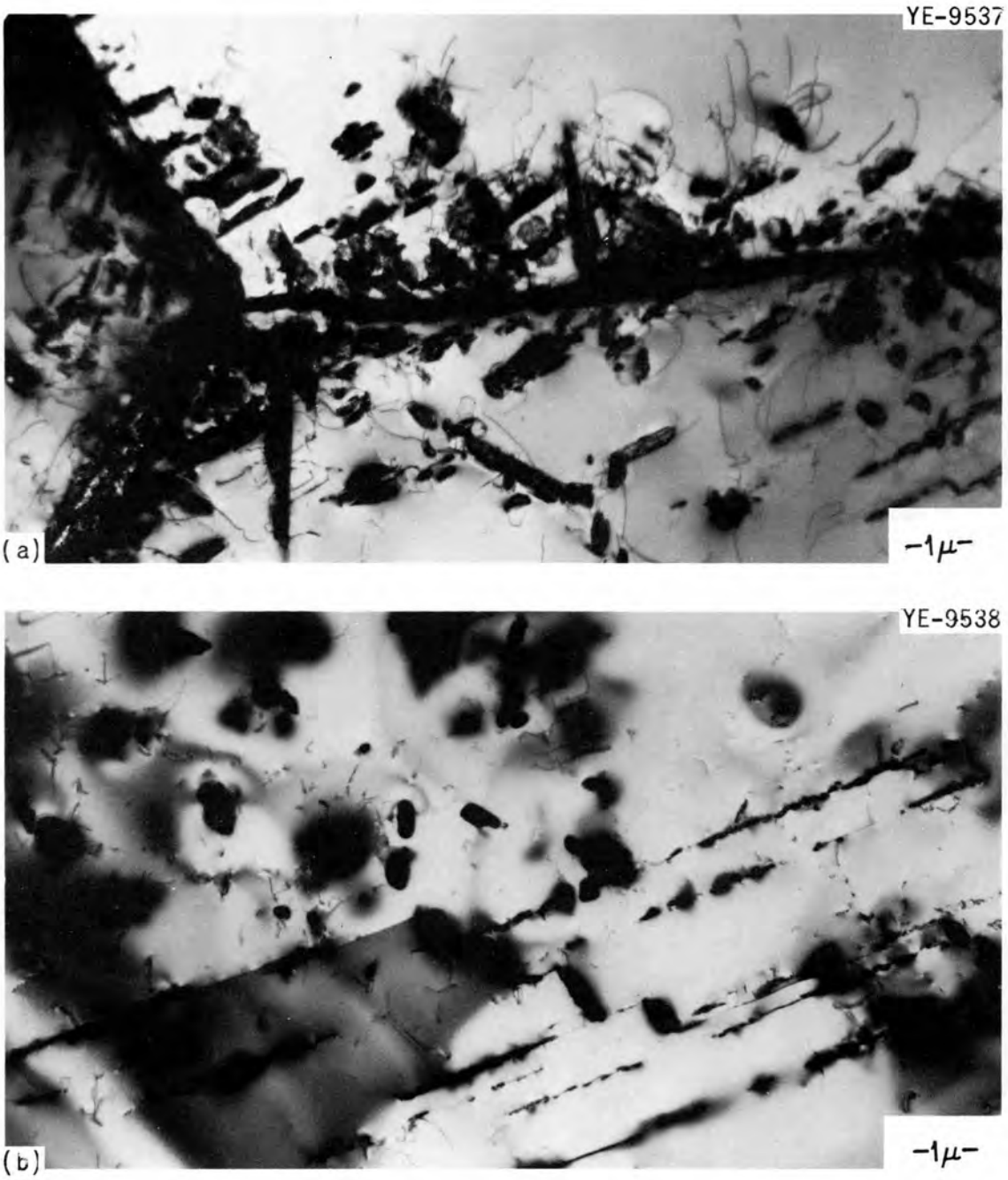

Fig. 8.16. Precipitation in Titanium-Modified Hastelloy N at 650 and 760°C. (a) Grain-boundary precipitation after aging at 650°C for 1500 hr, solution annealed 1 hr at 1177°C. (b) Precipitation after aging at 760°C for 1500 hr, solution annealed 1 hr at 1177°C.

present near grain boundaries. This undoubtedly indicates that gross precipitation at grain boundaries is beneficial in creep or that the reduction in the concentration of solute in the matrix at 650°C changes the deformation characteristics of the matrix so that it is able to deform more easily than if precipitation had not occurred.

Figure 8.17 illustrates the differences in substructure for irradiated and unirradiated creep specimens examined in transmission. Figure 8.17(b) shows a typical grain boundary in an alloy (heat 66-548) containing 0.48% Ti that was irradiated for 1128 hr at 635°C and tested in creep at 650°C and 47,000 psi to a rupture life of 20.7 hr and fracture strain of 5.2%. The grain boundaries are quite irregular and contain an appreciable amount of precipitate. A considerable amount of the fine, highly oriented Mo_2C precipitate is formed in the matrix [Fig. 8.17(c)], induced by strain and/or radiation. There is more of this precipitate in the irradiated and stressed specimen than in the one stressed at 650°C for 1438 hr without irradiation. These structures, observed after creep testing of the unirradiated and the irradiated material, do not show a large difference in precipitation. [Compare Fig. 8.17(a) and (b).]

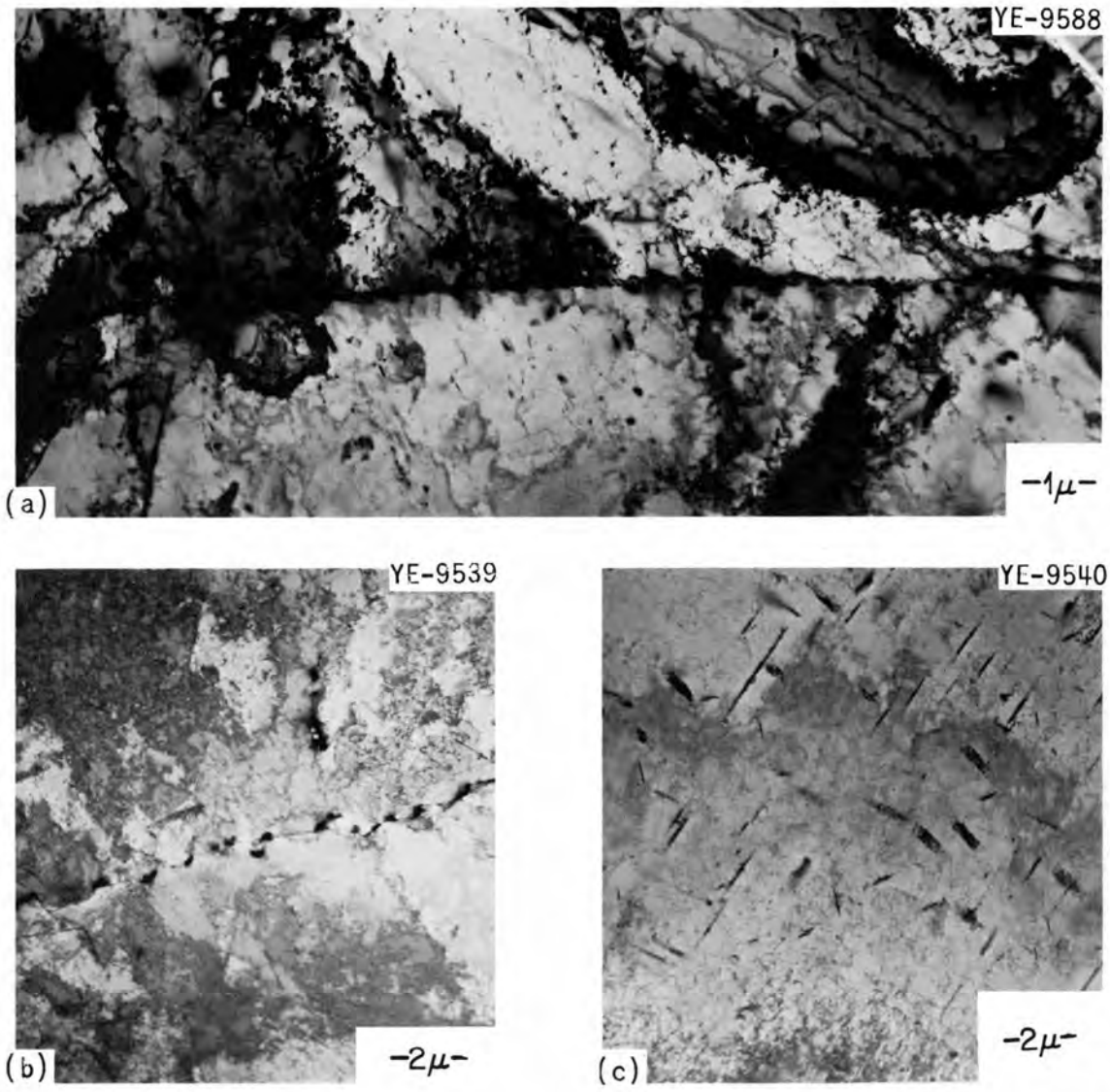

Fig. 8.17. Comparison of Unirradiated and Irradiated Hastelloy N, Heat 66-548. (a) Unirradiated creep specimens tested 1438 hr at 650°C. (b) Grain-boundary precipitate after irradiation at 635°C and creep testing at 47,000 psi at 650°C. (c) Matrix precipitation in irradiated and tested sample.

9. RADIATION EFFECTS IN ALLOYS AND STRUCTURAL MATERIALS

M. S. Wechsler

The object of this program is to investigate the underlying causes of the embrittlement of metals and structural alloys by radiation. Because of the critical importance of reactor pressure vessels, the program is particularly concerned with reactor irradiation effects in Fe and pressure-vessel steels.

The materials under study are base metal, heat-affected zones, and the weld metal in the commercial ASTM pressure-vessel alloys such as A 212-B, A 302-B, A 533-B, and A 543. The variables being investigated are material history, composition, the irradiation neutron flux and spectrum, and the irradiation temperature.

To enlarge the understanding of the effects produced by the interaction of the irradiation-induced defects and impurities in the commercial steels, we include studies of the effects of irradiation on Fe and V.

Radiation Effects on Pressure-Vessel Steels

Radiation Hardening and Embrittlement in ASTM A 212-B Steel (N. E. Hinkle, R. G. Berggren, W. J. Stelzman, T. N. Jones, M. S. Wechsler, and C. R. Case II[1])

In a previous report[2] we described an attempt to relate radiation hardening, as determined by measurements of tensile yield and fracture stress, to radiation embrittlement exhibited by Charpy notch-impact specimens of ASTM A 212-B pressure-vessel steel. Through the use of an estimated correction of strain rate, a calculated triaxiality factor,[3]

---

[1]Summer Trainee from University of Wisconsin, Oshkosh, Wisconsin, sponsored by Oak Ridge Associated Universities.

[2]M. S. Wechsler, N. E. Hinkle, R. G. Berggren, and W. J. Stelzman, Radiation Metallurgy Section Solid State Division Progress Report for Period Ending January 1968, ORNL-4246, pp. 6–27.

[3]T. R. Wilshaw and P. L. Pratt, "The Effect of Temperature and Strain Rate on the Deformation and Fracture of Mild-Steel Charpy Samples," pp. 973–991 in Proceedings First International Conference on Fracture, Vol. 2, The Japanese Society for Strength and Fracture of Materials, Japan, 1966.

and the assumption of a cleavage fracture load independent of temperature and strain rate, we found that the radiation hardening was more than sufficient to cause the observed shift in ductile-to-brittle transition temperature (DBTT). In order to define this relationship more precisely, we have extended our investigation of the effect of strain rate on yielding and fracture in the notched specimens. To do this, it was necessary to obtain quantitative measurements of the load applied to Charpy notched-bar specimens as a function of strain rate and temperature. Two approaches were taken to measure the loads applied to the notched-bar samples. First, the strikers of the impact machines were fitted with strain sensors whose outputs were calibrated to yield the loads applied to the samples during the impact test. Second, slow-bend tests were performed at a low strain rate on the notched-bar samples loaded in three-point bending. The loads were measured in an Instron machine in tests conducted as a function of temperature in a test chamber cooled by liquid N. To elucidate the strain pattern near the root of the notch, we attempted to reveal yield zones by etching.

Although most of our earlier work has been devoted to the ASTM A 212-B steel, our studies have now been extended to include ASTM A 533-B pressure-vessel steel. This is described in another section of this report.[4]

The information that can be determined from a standard impact test includes the total energy to fracture, fracture appearance, and lateral expansion and contraction; but no details of the deformation during the test are provided. Wilshaw and Pratt,[3] Fearnehough and Hoy,[5] and Tetelman and McEvily[6] have shown that the load and energy absorbed by a Charpy notch-impact specimen can be determined at any time during the test with an impact machine instrumented with strain sensors. We believe

---

[4]R. G. Berggren et al., "Radiation Hardening and Embrittlement in ASTM A 533-B Steel," pp. 189–194, this report.

[5]G. D. Fearnehough and C. J. Hoy, J. Iron Steel Inst. (London) 202, 912–920 (November 1964).

[6]A. S. Tetelman and A. J. McEvily, Jr., Fracture of Structural Materials, pp. 322–325, Wiley, New York, 1967.

that the instrumented Charpy impact test provides a favorable tool for studying the relationship between radiation hardening and embrittlement.

We have completed the instrumentation of two impact machines, one for use in a hot cell and one for use in the laboratory. The laboratory machine was equipped with a strain-gage bridge network consisting of a pair of Baldwin-Lima-Hamilton foil strain gages (type FAE-50-35S6, 0.5-in. gage length). These were placed in recesses on the sides of the Charpy striker along the center of the impact to serve as the active bridge element. A pair of identical gages for temperature compensation, located on the striker flange, served as the inactive bridge elements.

The impact machine used in the hot cell has a pair of Budd He-121-R2TC strain gages placed in recesses on the sides of the striker. These are high-elongation, rosette foil gages with a two-element 90° rectangular grid of 1/8-in. gage length. They are oriented to provide strain measurements parallel and normal to the direction of impact. All four sensor elements are active in this bridge network.

A Tektronix Model 543 oscilloscope, equipped with a Type Q plug-in module, provides the alternating-current excitation voltage for the strain-gage bridge. The output voltage of the bridge network is displayed on the oscilloscope screen. The oscilloscope has a single-sweep internal triggering mode that is armed manually as the pendulum descends at the start of a test. The oscilloscope traces are photographed with a Polaroid camera (see Fig. 9.1).

Both systems were calibrated statically for load on an Instron tensile machine. The load was applied to the striker via a standard Charpy notch-impact specimen properly positioned at the point of contact at the leading edge of the striker. The strain in the striker, as detected by the strain gages and traced on the oscilloscope screen, is directly proportional to the applied load, which is detected by the load cell of the tensile machine and graphically displayed on a strip-chart recorder. As an indication of the reliability of the oscilloscope traces and the load calibration, the fracture energies of a series of tests have been derived from the traces. These are compared in Fig. 9.2 with the fracture energies obtained from the scale on the impact machine.

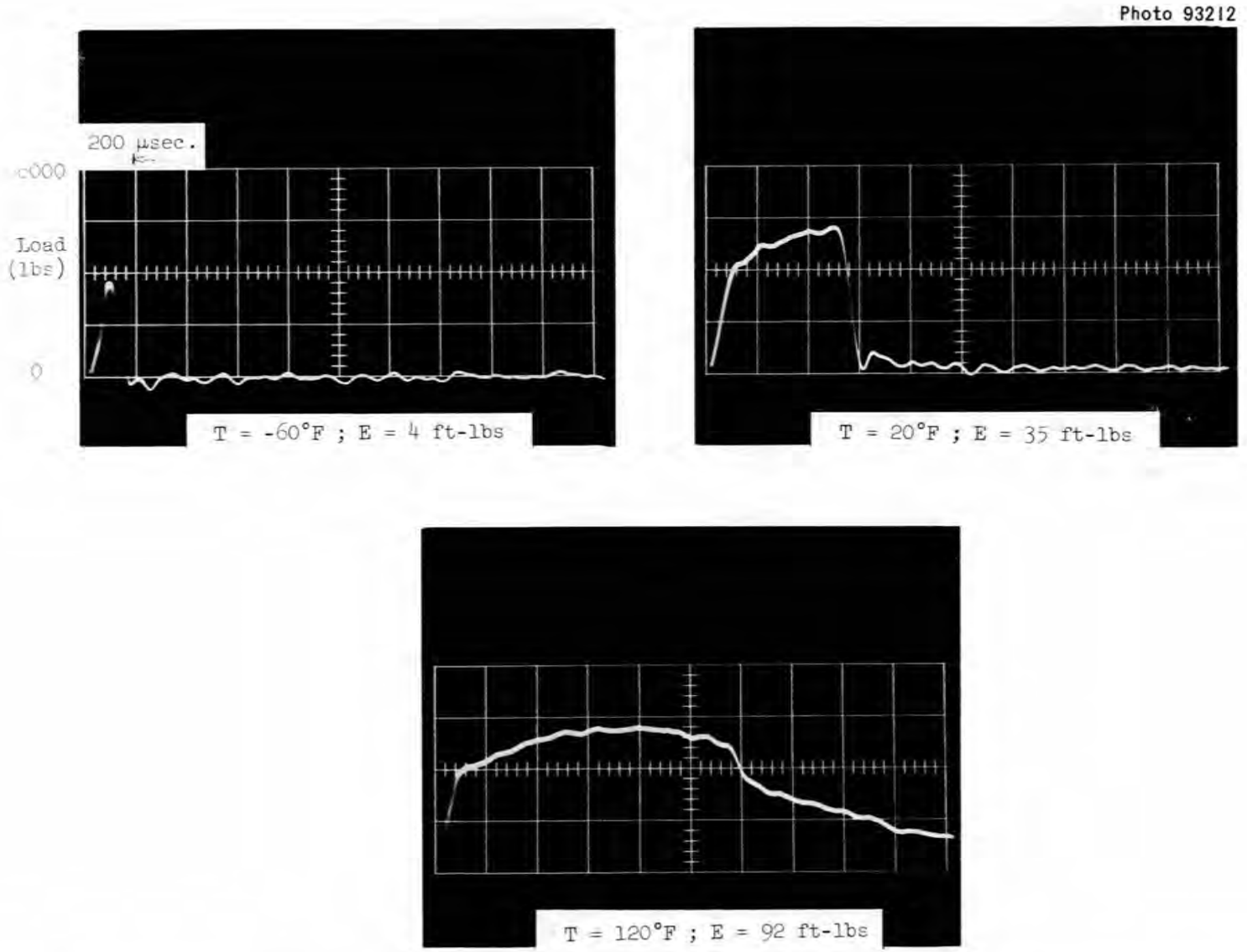

Fig. 9.1. Oscilloscope Traces of the Output of the Strain Gages Mounted on the Striker of the Impact Machine.

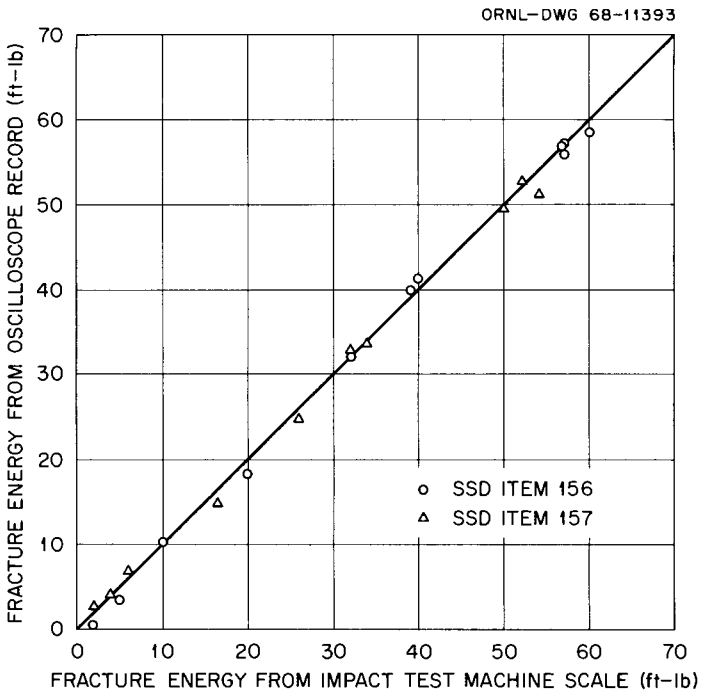

Fig. 9.2. Comparison of the Fracture Energy Measured by the Impact Machine with the Fracture Energy Calculated from the Oscilloscope Traces.

Charpy notch-impact specimens were also bend tested at low strain rate in a three-point-bend test apparatus mounted on an Instron tensile machine. The sample holder for the bend tests has the same shape as the anvil and striker of the impact machine.

The general yield load and fracture load for the impact tests on the A 212-B steel (Solid State Division Item 156) as measured with the strain-gage instrumentation are shown as a function of temperature in Fig. 9.3 (open and closed squares, respectively). The corresponding quantities for the slow-bend tests as measured on the tensile machine are also shown (open and closed circles, respectively). We see that the curves for impact tests are shifted about 150°C upward on the temperature scale with respect to the curves for slow-bend tests. The fracture load curves for impact and slow-bend tests have a similar shape, but the general yield curve for slow-bend tests appears to decrease more rapidly with increasing temperature than that for the impact tests.

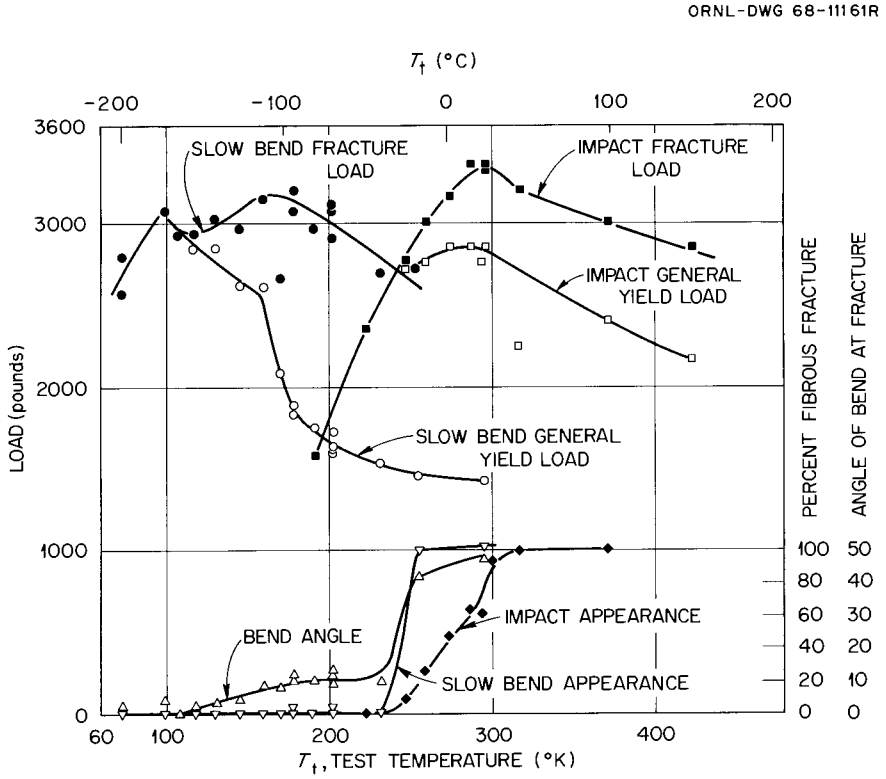

Fig. 9.3. The General Yield Load and Fracture Load from Impact and Slow-Bend Tests as a Function of Test Temperature. Also shown are the percent fibrous-fracture appearance for impact and slow-bend tests and the bend angle at fracture for the slow-bend tests. Unirradiated Charpy V-notch samples of A 212-B steel, SSD Item 156.

In the earlier work,[7] the criterion used for the critical cleavage stress, σ_c, was the point of intersection of the yield and fracture stresses as determined from tensile tests at low strain rates on smooth samples. The σ_c thus determined was assumed to be independent of strain rate. Applying this criterion to the results of the notched-bar tests in Fig. 9.3, we find the σ_c for slow bend to correspond to a load of about 2900 lb (at 110 K) and for impact tests, 2750 lb (at 240 K). Thus, the σ_c does indeed appear to be quite insensitive to strain rate.

---

[7]M. S. Wechsler, N. E. Hinkle, R. G. Berggren, and W. J. Stelzman, Radiation Metallurgy Section Solid State Division Progress Report for Period Ending January 1968, ORNL-4246, pp. 6–27.

The fracture surfaces of the impact and slow-bend specimens appeared somewhat different, probably due to the differences in strain rate and temperature. At temperatures just above the DBTT, the fracture surface of the impact specimen has the usual crystalline appearance (indicative of cleavage fracture) at the center, surrounded by a border of fibrous appearance (indicative of shear fracture) at the edges of the fracture surface. The slow-bend specimens, on the other hand, show fibrous-fracture appearance only near the root of the notch, with the crystalline appearance extending completely to the other three edges of the fracture surface.

As shown in Fig. 9.3, the change in the appearance of the fracture surface of impact specimens from 100% fibrous to 100% crystalline occurs in the temperature range where the impact fracture load reaches a maximum and the impact general yield load intersects the fracture load [i.e., from 295 K (22°C) to 250 K (−23°C)]. The DBTT determined by the impact energy criterion occurs in the same temperature range as that determined by the change in fracture appearance. Thus, the percent of fibrous-fracture appearance correlates with both the impact energy transition and the intersection of the curves of yield and fracture loads. However, the fracture-appearance transition of the slow-bend specimens, which occurs between 230 K (−43°C) and 255 K (−18°C), does not match the DBTT indicated by the intersection of the curves for slow-bend general yield and fracture load at 110 K (−163°C). These results indicate that the fracture appearance is not a positive indicator of the DBTT for tests of Charpy notch-impact specimens at low strain rates.

Figure 9.3 also shows the bend angles of the slow-bend specimens at fracture. The bend angle increases slowly from 0° near 110 K (−163°C), where the curves for general yield and fracture load intersect, to about 10° at the fracture-appearance transition temperature, 230 K (−43°C). The energy of deformation during slow bend has been calculated, and, as with the bend angle, it also increases gradually from near 110 K to about 230 K, where gross shear deformation becomes the controlling mechanism.

In summary, if the DBTT is defined as that temperature at which the fibrous-fracture appearance is essentially zero,[7,8] this is seen to be the temperature at which curves for the impact general yield and fracture loads intersect. For the slow-bend tests, however, this criterion is not applicable. We find instead that the DBTT of slow-bend tests is better defined by a bend angle of 0° at fracture.

In our previous work on the relationship between radiation hardening and embrittlement,[7,8] we also found that the DBTT of the irradiated impact specimens could be predicted from the tensile results if it were assumed that the maximum triaxiality correction factor,[9] used to obtain reasonably good agreement for unirradiated specimens, was reduced as a result of the irradiation. A decrease in the maximum triaxiality correction factor implies that the plastic zone, developed at the root of the notch before cleavage fracture is initiated, has been decreased. Using notch-impact specimens of A 212-B (Solid State Division Item 156) and the slow-bend technique, we attempted to study the development of the plastic zone at the root of the notch. Specimens were subjected to various loads up to the fracture or general yield loads near the DBTT and then etched to reveal the plastic zone and the development of the plastic hinges. We found it relatively easy to see the plastic hinges at the general yield load without etching, but at the lower stresses we were unable to observe the development of the plastic zone at the root of the notch even after using variations of Fry's reagent with or without thermal aging. Apparently the A 212-B steel is insensitive to this reagent because there is insufficient free N and C to decorate the dislocation lines. Because of this negative result, a similar study of irradiated specimens has not been undertaken.

---

[8]M. S. Wechsler, R. G. Berggren, N. E. Hinkle, and W. J. Stelzman, "Radiation Hardening and Embrittlement in a Low-Carbon Pressure Vessel Steel," paper presented at the Symposium on the Effects of Radiation on Structural Metals, June 26–28, 1968, San Francisco, California. To be published in the proceedings.

[9]T. R. Wilshaw and P. L. Pratt, "The Effect of Temperature and Strain Rate on the Deformation and Fracture of Mild-Steel Charpy Samples," pp. 973–991 in Proceedings First International Conference on Fracture, Vol. 2, The Japanese Society for Strength and Fracture of Materials, Japan, 1966.

The new techniques described above, along with recent improvements in older equipment, are being used to study the properties of irradiated A 212-B and A 533-B pressure-vessel steels. A major goal of these studies is to determine whether the principal effect of irradiation is to cause a change in the initiation or the propagation of cleavage fracture. The broader approach that is now available to us should make it possible to gain a deeper understanding of the effect of neutron irradiation on the phenomenon of brittle fracture.

Electron Fractography of Irradiated A 212-B Pressure-Vessel Steel
(C. R. Brooks,[10] J. L. Miller, M. S. Wechsler)

The hardening and embrittlement of A 212-B pressure-vessel steel upon neutron irradiation have been reported previously.[7,8] Tensile and impact properties were determined as a function of temperature for the unirradiated and irradiated base-plate material. These results show a radiation-induced increase in both the tensile yield stress and the DBTT of the steel as shown in Figs. 9.4 and 9.5. From the analysis of results, we concluded that the steel is embrittled because the irradiation has increased the yield strength without appreciably changing the fracture stress; that is, in the irradiated condition the steel begins to deform plastically at a higher stress level, but fracture occurs at the same stress for both conditions. Such behavior can be interpreted to mean that the irradiation has induced lattice defects that impede dislocation movement, but that the basic mechanism of the initiation and propagation of cracks is unaffected by the irradiation. If this is true, the morphology of the fracture surfaces should be identical for both conditions.

The morphology of brittle-fracture surfaces of ferritic steels is quite complex, consisting of a very fine structure of features (scale about 100 A) created by the complicated process of rapid propagation of cracks in a brittle, two-phase structure. Therefore, it is difficult

[10]Department of Chemical and Metallurgical Engineering, the University of Tennessee.

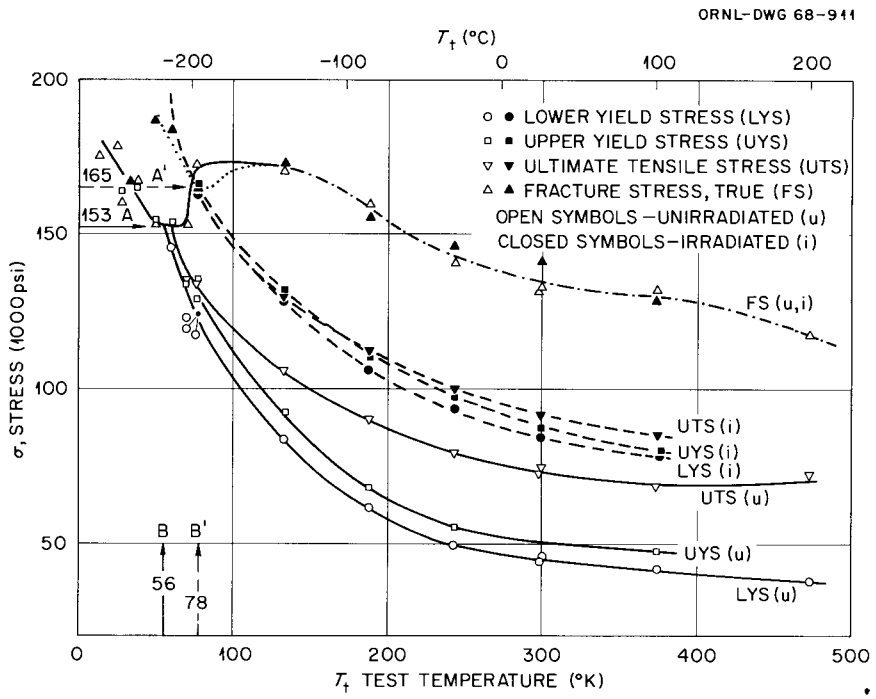

Fig. 9.4. Stress Versus Test Temperature for Tensile Tests on Unirradiated and Irradiated A 212-B Steel. Fluence, 1.0×10^{19} neutrons/cm^2, (> 1 Mev). Irradiation temperature, 60°C. Strain rate, 2.7×10^{-4} sec^{-1}. Ref.: M. S. Wechsler, R. G. Berggren, N. E. Hinkle, and W. J. Stelzman, "Radiation Hardening and Embrittlement in a Low-Carbon Pressure Vessel Steel," paper presented at the Symposium on the Effects of Radiation on Structural Metals, June 26–28, 1968, San Francisco, California. To be published in the proceedings.

to determine the sequence of events taking place as the steel fractures or to draw conclusions concerning the mechanism of initiation and growth of cracks. However, it is useful to characterize certain morphological features common on brittle-fracture surfaces, such as river patterns (see Ref. 11), as a function of the variables of heat treatment and irradiation.

Details of the fine structure of fracture surfaces can be obtained by electron fractography. This involves replicating the surface with plastic tape, coating the replica with C, shadowing with a metal such as Pt to improve contrast, and then dissolving the plastic. The secondary replica is thin enough to transmit electrons in the electron

[11] Electron Fractography, Am. Soc. Testing Mater. Spec. Tech. Publ. 436, American Society for Testing and Materials, Philadelphia, Pennsylvania, 1967.

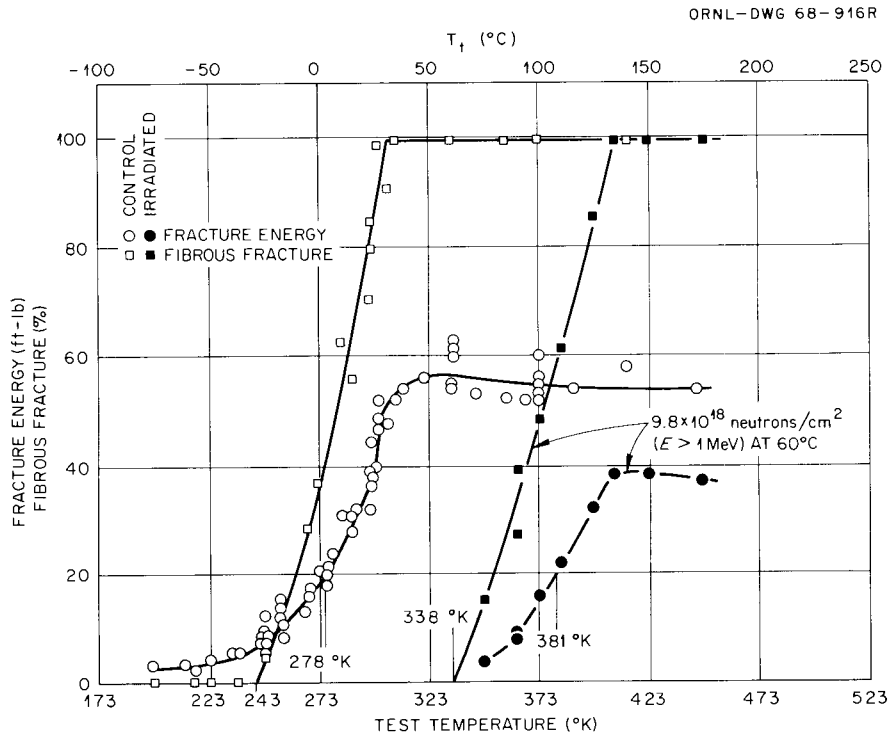

Fig. 9.5. Fracture Energy and Fibrous Fracture Appearance Versus Test Temperature for Impact Tests on Unirradiated and Irradiated A 212-B Steel. Ref., M. S. Wechsler, R. G. Berggren, N. E. Hinkle, and W. J. Stelzman, "Radiation Hardening and Embrittlement in a Low-Carbon Pressure Vessel Steel," paper presented at the Symposium on the Effects of Radiation on Structural Metals, June 26–28, 1968, San Francisco, California. To be published in the proceedings.

microscope, and an image of the surface that has good contrast is generated. The resolution of the image is limited by the plastic replica itself to about 100 A; the depth of field of the electron microscope allows the uneven surface to remain in focus. Thus, by electron fractography, we observe a replica of the fracture surface that reveals the fine details of the surface morphology.

We observed specimens from two heats of ASTM A 212-B steel, for which chemical analyses and heat treatments are given in Table 9.1. The heat treatments produced a soft steel with a microstructure of free ferrite and regions of rather coarse pearlite. Optical and electron micrographs of the microstructure of the unirradiated base plate are shown in Fig. 9.6. A comparison of microstructures for the unirradiated and irradiated steel is shown in the electron micrographs of Fig. 9.7;

Table 9.1. ASTM A 212-B Pressure-Vessel Steel[a]

Heat	Chemical Composition, wt %				
	C	Mn	Ph	S	Si
Item 157	0.36	0.62	0.012	0.033	0.18
Item 147	0.25	0.74	0.013	0.025	0.20

[a]Heat treatment: 2 3/4-in.-thick plate was normalized at about 900°C, cooled by water spray to 260°C, and stress relieved at 650 to 680°C; all specimens for impact and tensile tests were taken from quarter thickness.

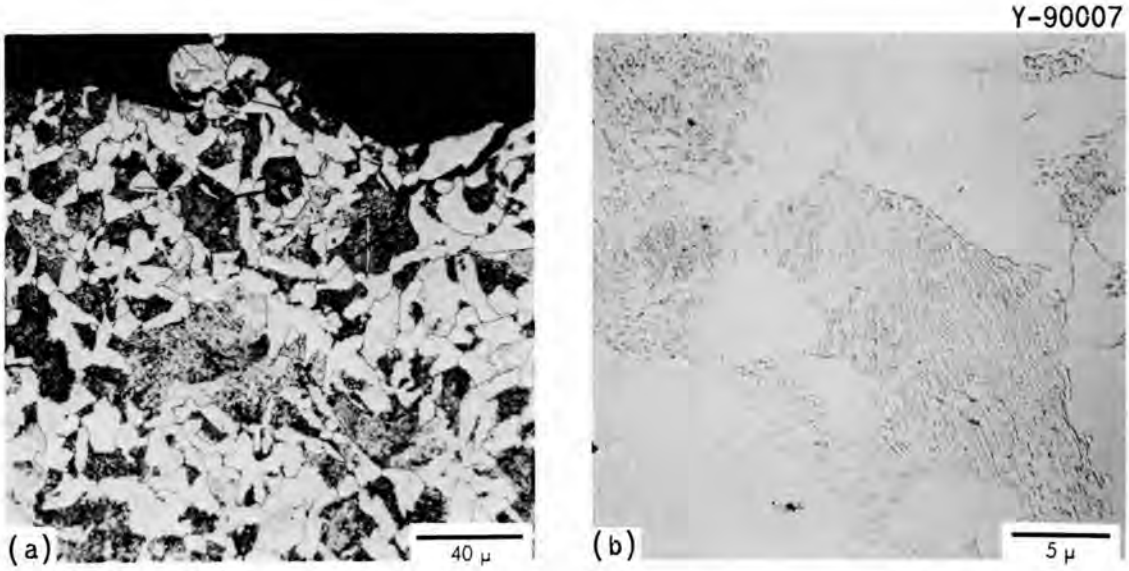

Fig. 9.6. Microstructure of Unirradiated ASTM A 212-B Pressure-Vessel Steel. (a) Optical micrograph showing edge of fracture surface of Charpy V-notch specimen. (b) Electron micrograph of replica of etched microstructure.

these were obtained by replicating polished and etched longitudinal sections near the fracture surfaces of tensile samples tested at low temperatures. No gross features distinguish the irradiated microstructure from the unirradiated one, except possibly for slight difference in the etching behavior that give rise to small pockmarks within ferrite grains in the irradiated steel.

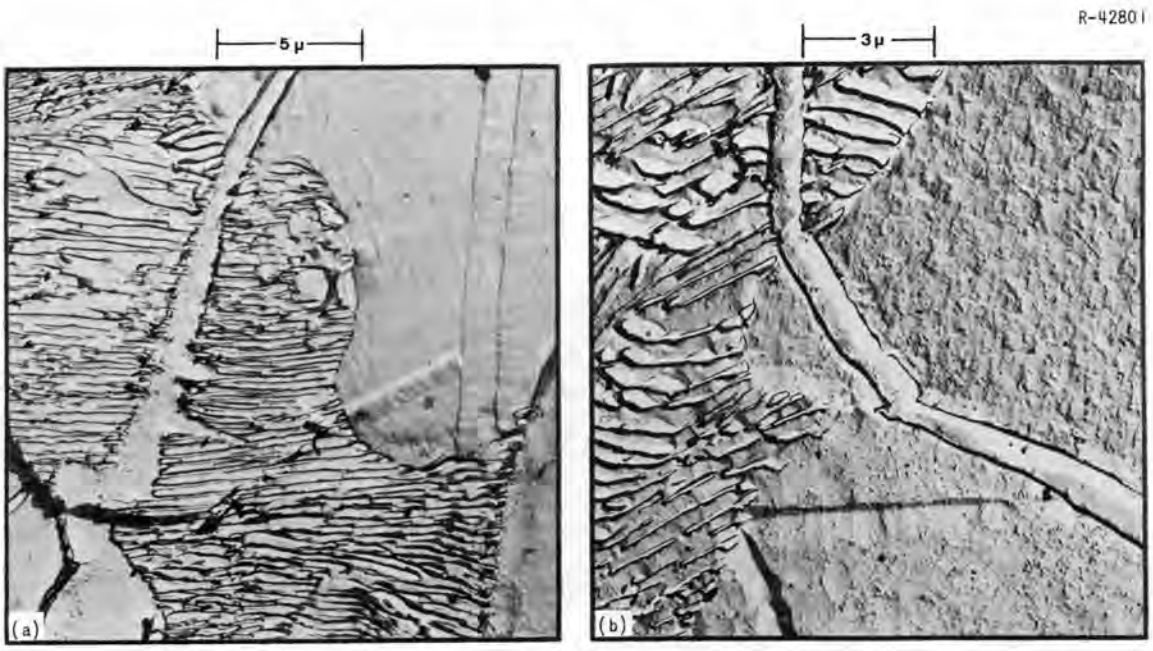

Fig. 9.7. Electron Micrographs of a Polished and Etched Section near the Fracture of Unirradiated and Irradiated Tensile Specimens of A 212-B Steel. (a) Unirradiated, T_t = 50 K. (b) Irradiated, T_t = 34 K, $\Phi = 1.0 \times 10^{19}$ neutrons/cm^2 at 60°C.

Electron fractographs were obtained on tensile and impact specimens irradiated near 60°C to a fluence of 1×10^{19} neutrons/cm^2 (> 1 Mev). The irradiation produced an increase in DBTT of 95°C (Fig. 9.5). The fractographs of the unirradiated tensile specimen tested at 77 K (−196°C) and the irradiated tensile specimen tested at 34 K (−239°C) are shown in Fig. 9.8; both specimens fractured brittlely (i.e., before a lower yield stress was reached). The pearlite platelets are clearly revealed in both cases, and no obvious differences are apparent in the morphologies of the unirradiated and irradiated fracture surfaces. Electron fractographs for impact specimens from Item 147 (Table 9.1) are shown in Figs. 9.9 and 9.10. The irradiations in this case were carried to 8×10^{18} neutrons/cm^2 (> 1 Mev) at 340°C, and despite the high irradiation temperature, the DBTT was increased about 30°C. All specimens were tested at temperatures below the DBTT. Figure 9.9 compares the unetched fracture surfaces of unirradiated and irradiated specimens; the fracture surfaces look quite similar. Figure 9.10 shows the surfaces in the etched condition. The microstructure is more clearly revealed in this

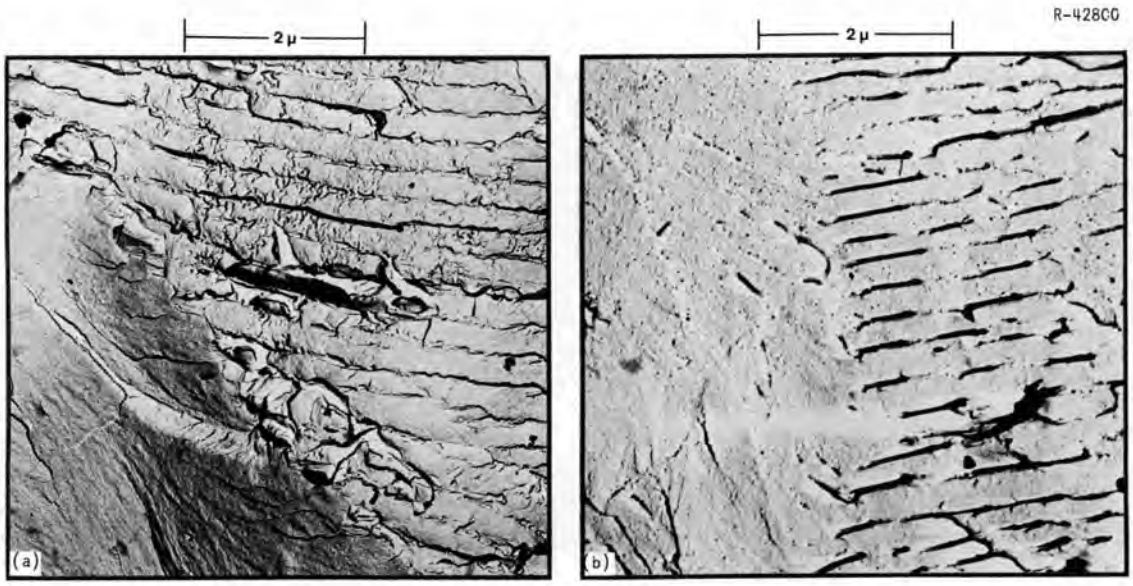

Fig. 9.8. Electron Fractographs of Unirradiated and Irradiated Tensile Specimens of A 212-B Steel. (a) Unirradiated, T_t = 77 K. (b) Irradiated, T_t = 34 K. $\Phi = 1.0 \times 10^{19}$ neutrons/cm^2 at 60°C.

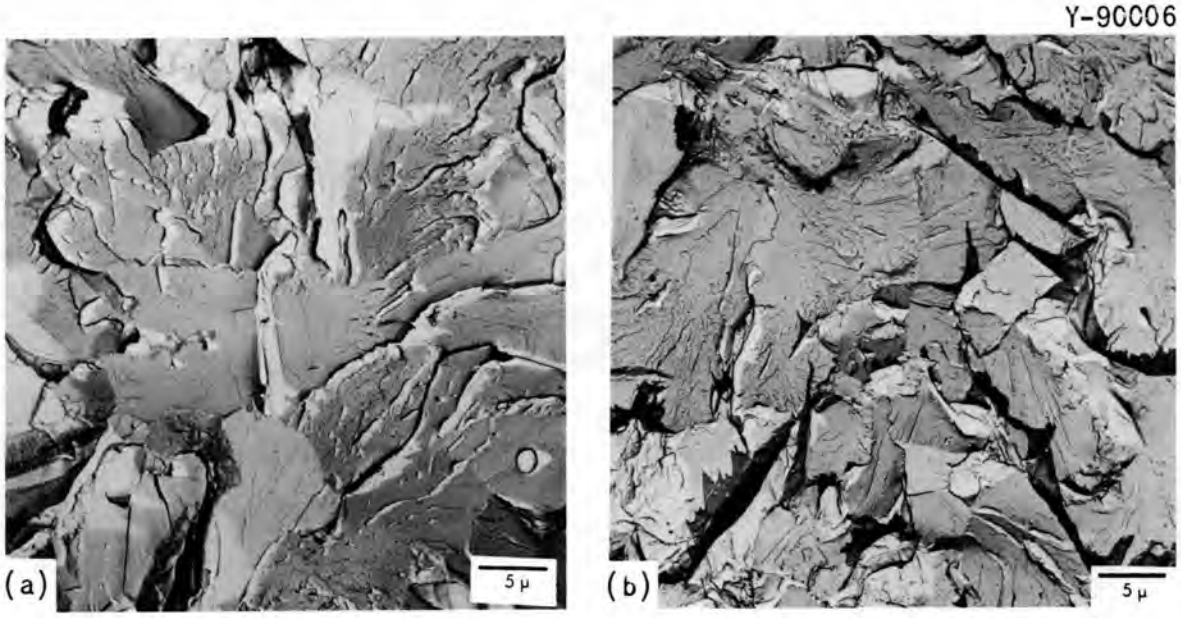

Fig. 9.9. Electron Micrographs of Replicas of Unetched Fracture Surface of Charpy V-Notch Impact Specimens of Unirradiated and Irradiated A 212-B Steel (Item 147). (a) Unirradiated, fractured at −60°C, 3 ft-lb. (b) Irradiated, 8.3×10^{18} neutrons/cm^2 at 340°C for 45 days, fractured at −40°C, 2 ft-lb.

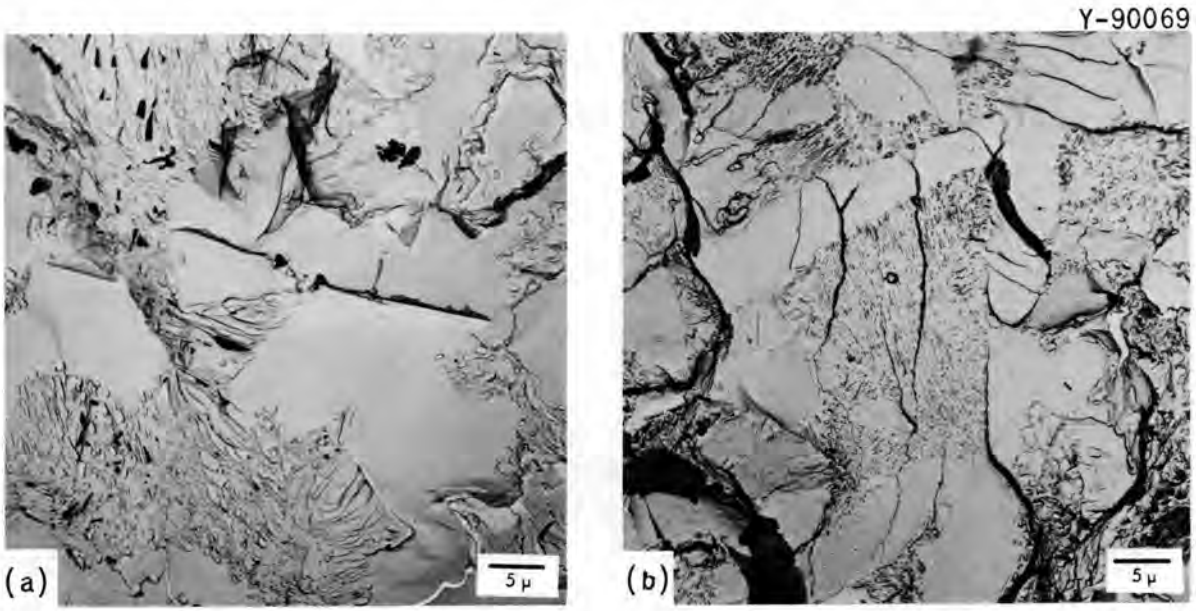

Fig. 9.10. Electron Micrographs of Replicas of Etched Fracture Surface of Charpy V-Notch Impact Specimens of Unirradiated and Irradiated A 212-B Steel (Item 147). (a) Unirradiated, fractured at −60°C, 3 ft-lb. (b) Irradiated, 8.3×10^{18} neutrons/cm^2 at 340°C for 45 days, fractured at −40°C, 2 ft-lb. Etched.

case, but again no gross difference is visible in the fracture morphology upon irradiation.

Transmission electron microscopy is another technique we have applied to the irradiated pressure-vessel steels. Figure 9.11 shows electron transmission micrographs for unirradiated and irradiated [8×10^{18} neutrons/cm^2, (> 1 Mev) at 70°C] foils from Item 147 (Table 9.1) taken with a Hitachi 200 kev electron microscope. The foils were deformed about 5% by rolling before chemical thinning. The micrograph (Fig. 9.11) for the irradiated foil does not indicate any defect clusters or spot contrast, as has been observed for many other irradiated metals. In a similar attempt, Birkle and Rall[12] were also unable to observe defect clusters produced by irradiation of A 212-B steel. Some differences in the dislocation configurations for the unirradiated and irradiated foils are apparent, however, in Fig. 9.11. The dislocations

[12]A. J. Birkle and W. Rall, Trans. Met. Soc. AIME 230, 156–163 (1964).

Photo 93213

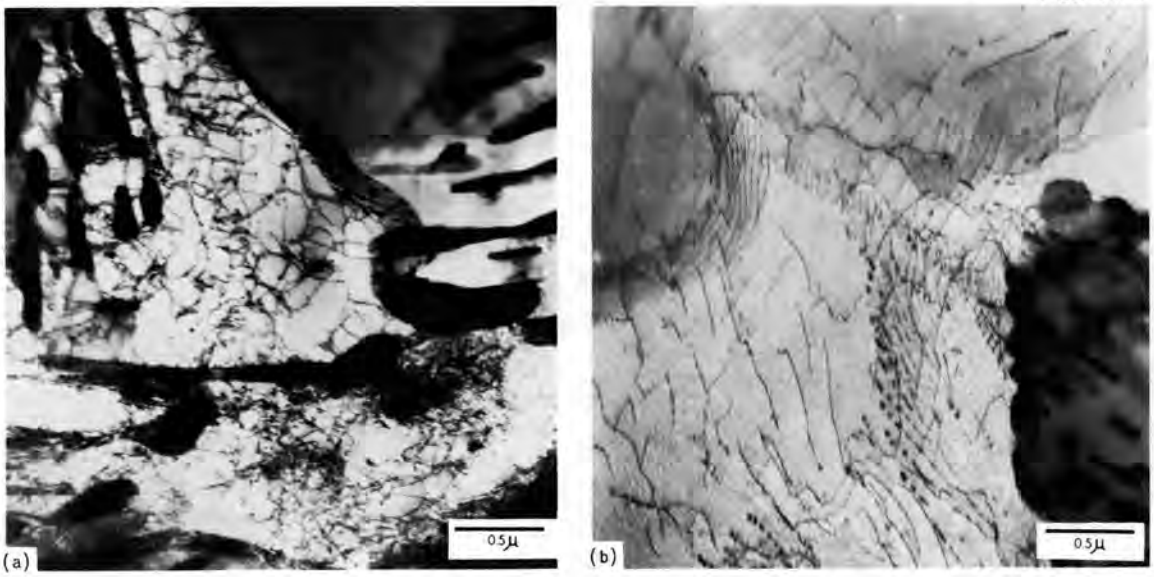

Fig. 9.11. Transmission Electron Micrographs of Unirradiated and Irradiated A 212-B Steel Strained about 5%. (a) Unirradiated. (b) Irradiated, 8×10^{18} neutrons/cm^2, 70°C.

generated by the rolling treatment appear somewhat clustered and tangled for the unirradiated foil, whereas for the irradiated one they lie in long strands along crystallographic directions. This is probably due to a type of dislocation channeling, such as that observed by Mastel et al.[13] for Mo or Tucker et al.[14] for Nb, but the absence of visible defect clusters in the transmission electron micrographs makes a study of the phenomenon considerably more difficult in ferritic steels.

Radiation Hardening and Embrittlement in ASTM A 533-B Steel
(R. G. Berggren, W. J. Stelzman, T. N. Jones, M. S. Wechsler)

Specimens for tensile and Charpy V-notch impact tests were taken from the surface, quarter-thickness, and midthickness locations of HSST (Heavy Section Steel Technology) Plate 01, a 12-in.-thick ASTM A 533-B Class 1 manganese-molybdenum-nickel steel plate. All specimens were of longitudinal orientation; that is, the tension axis of each specimen

---

[13]B. Mastel, H. E. Kissinger, J. A. Laidler, and T. K. Bierlein, J. Appl. Phys. 34, 3637–3638 (1963).

[14]R. P. Tucker, M. S. Wechsler, and S. M. Ohr, "Dislocation Channeling in Neutron-Irradiated Niobium," to be published in Journal of Applied Physics.

Table 9.2. Tensile Properties of Irradiated 12-in.-Thick A 533-B Steel[a] from Heat A-1008-1, HSST Plate 01

Specimen Number	Fluence [neutrons/cm^2 (> 1 Mev)]	Irradiation Temperature (°C)	Strength Properties, psi			Elongation, %	
			Upper Yield	Lower Yield	Ultimate[b] Tensile	Uniform	Total[c]
	× 10^{18}		× 10^3	× 10^3	× 10^3		
		Quarter-Thickness Specimens					
6000			70.7	68.5	90.2	8.9	17.6
6001			69.9	69.1	90.8	10.0	18.3
6036			69.8	68.6	90.3	10.0	18.8
6037			69.4	68.6	89.7	9.6	19.2
6054			69.7	68.1	89.2	10.7	22.1
6055			69.2	67.9	89.8	9.5	19.4
6064			69.1	67.5	89.2	10.2	21.4
6065			68.4	67.8	89.3	9.6	18.9
Average			69.5	68.3	89.8	9.8	19.5
6061	7.2	63	104.0	101.1	102.2	5.2	13.6
6033	7.7	65	107.0	102.4	103.6	4.2	13.0
6060	8.6	232	94.8	92.8	107.7	9.0	16.2
6032	8.9	232	96.1	94.7	108.8	8.7	15.5
6034	11.8	288	90.2	87.6	106.5	9.5	16.8
		Midthickness Specimens					
6077			69.6	68.2	90.1	9.4	18.0
6078			69.1	68.1	89.9	9.6	18.0
6112				68.1	89.8	8.3	17.4
6113			68.2	67.8	90.1	9.9	18.8
Average			69.0	68.0	90.0	9.3	18.0
6086	6.9	65	106.6	102.4	103.2	4.5	12.3
6092	7.6	65	108.4	104.2	105.3	4.9	11.8
6079	7.7	232	95.2	94.6	108.9	7.8	14.5
6085	8.8	232	96.6	95.9	110.7	7.5	14.1
6093	10.3	288	87.8	86.7	106.5	9.1	15.8
6099	11.6	288	88.5	86.1	105.6	7.8	14.7

[a] All specimens are of longitudinal orientation, tested at 27°C.

[b] Ultimate tensile strength is here defined as the maximum load after the yield point divided by original area of cross section.

[c] Length-to-diameter ratio: 7.

was parallel to the rolling direction. These specimens were irradiated to fast-neutron fluences of 5 to 11 $\times$ 10^{18} neutrons/cm^2 (> 1 Mev) at temperatures of 66, 232, 288, and 343°C.

Results of tensile tests on specimens from quarter-thickness and midthickness, irradiated at 66, 232, and 288°C and tested at room temperature, are presented in Table 9.2. Results from impact tests of Charpy V-notch quarter-thickness specimens, irradiated at 68, 232, and 293°C, are presented in Fig. 9.12.

The purpose of these tensile and impact tests was to determine the effect of varying the irradiation temperature over the range cited above. However, because of flux variations in the irradiation capsules and differences in core loading from one experiment to the other, it was necessary to accept the differences in fluences noted in Table 9.2 and Fig. 9.12. To correct for the differences in fluence, we assumed that the increase in yield stress and the increase in DBTT are proportional to the square root of the fluence. On this basis, the increase in yield stress upon irradiation at 232 and 288°C are about 74 and 42%, respectively, of the increase in yield stress for the 68°C irradiation. The effect of irradiation temperature, analyzed in this way, was about the same for quarter-thickness and midthickness specimens, although the increases in yield stress normalized to a given fluence were slightly greater for midthickness specimens.

For impact results (Fig. 9.12) it is difficult to make a similar comparison because the impact curves are not parallel and because the comparison would depend on the fracture energy at which the transition temperature were fixed. It turns out that for a 25 ft-lb criterion the increases in DBTT upon irradiation at 232 and 288°C are about 87 and 43%, respectively, of the increase in DBTT for the 68°C irradiation. These percentages are roughly in agreement with those for the tensile tests, but the agreement is somewhat fortuitous for the reason mentioned above.

It was stated earlier in this report[15] that the cleavage fracture stress under impact conditions may be determined by the intersection of

---

[15]N. E. Hinkle et al., "Radiation Hardening and Embrittlement in ASTM A 212-B Steel," pp. 174–182, this report.

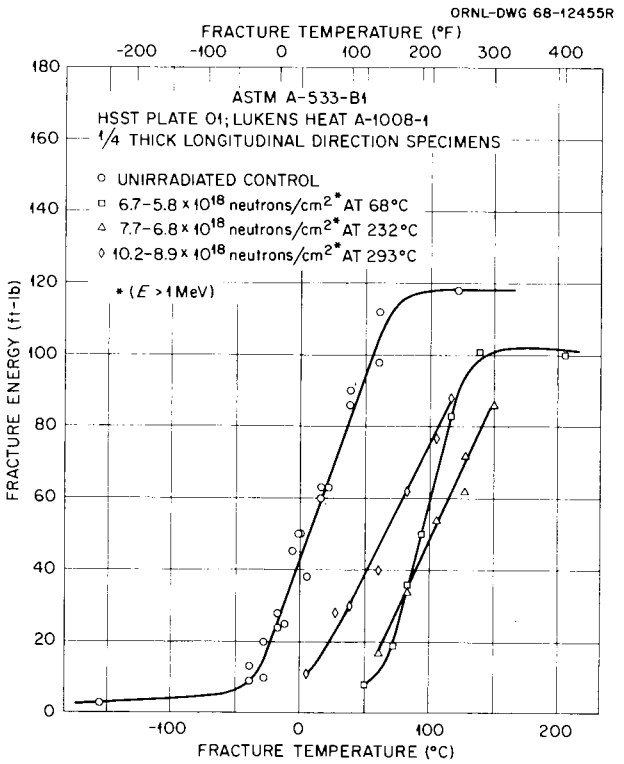

Fig. 9.12. Effect of Neutron Irradiation at Three Temperatures on the Notch-Impact Properties of Quarter-Thickness Specimens from a 12-in.-Thick Plate of Manganese-Molybdenum-Nickel Steel (ASTM A 533-B Class 1, HSST Plate 01).

general yield load and maximum (or fracture) load curves. Furthermore, one criterion for the DBTT is that temperature at which the yield stress reaches the cleavage-fracture stress. Hence, the DBTT is given by the temperature where the curves for general yield load and maximum load intersect. To determine this DBTT, oscilloscope records of load versus time during impact were obtained for most of the impact tests presented above. General yield loads and maximum loads obtained from these records are presented in Fig. 9.13. Zero-ductility transition temperatures may be determined by extrapolating to zero energy the steep portion of the curves for fracture energy in Fig. 9.12. These transition temperatures may be compared with those obtained from the intersection of the plots of the maximum load and general yield load recorded by the oscilloscope during notch-impact testing. Such results are given in Table 9.3. The data now available show that the transition temperatures

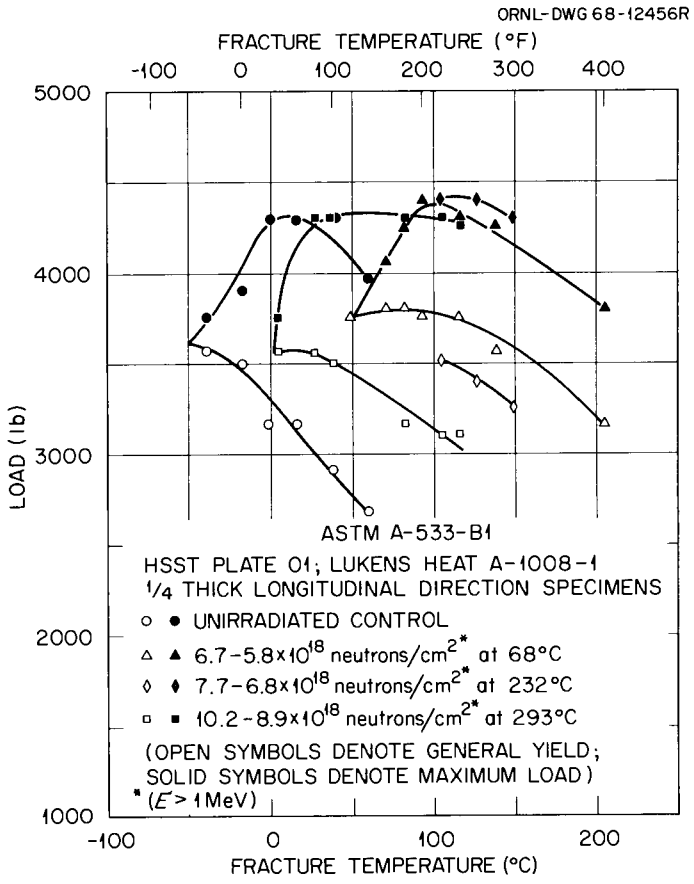

Fig. 9.13. General Yield and Maximum Loads During Notch-Impact Testing of Quarter-Thickness Specimens from a 12-in.-Thick Plate of Manganese-Molybdenum-Nickel Steel (ASTM A 533-B Class 1, HSST Plate 01).

Table 9.3. Comparison of Transition Temperatures of Irradiated ASTM A 533-B Class 1 Steel (Quarter-Thickness Charpy V-Notch Impact Specimens from HSST Plate 01)

Specimen Condition	Temperature, °C	
	At Zero Fracture Energy Intercept	Intersection of General Yield Load and Maximum Load Curves
Unirradiated	−44	−51
Irradiated to 6×10^{18} neutrons/cm^2 (> 1 Mev) at 68°C	58	49
Irradiated to 1×10^{19} neutrons/cm^2 at 293°C	−1	4

obtained by these two methods agree within the probable accuracy of the analysis. The present results indicate that the relationship between radiation hardening and embrittlement developed[16,17] for a different steel (ASTM A 212-B) will probably also apply to this ASTM A 533-B Class 1 steel.

Properties of 12-in.-Thick ASTM A 533-B Class 1 and Class 2 Steels
(R. G. Berggren, T. N. Jones)

Characterization tests continue on unirradiated 12-in.-thick plates of ASTM A 533-B (Manganese-Molybdenum-Nickel Steel Plate, Quenched and Tempered for Pressure Vessels). A portion of this material is included in several studies of radiation effects.

The first three plates (HSST plates 01, 02, and 03) were produced by Lukens Steel Company and heat treated to Class 1 specifications: The first two were heat treated by Combustion Engineering, Inc., and the third was heat treated by Lukens Steel Company. The HSST plates 01 and 02 were heat treated as identically as possible: both plates were dip quenched, edge down, in agitated water. The HSST plate 03 was flat quenched in agitated water so that possible effects of steam binding during quenching could be determined.

Test results for the central region of HSST plate 01 have been reported previously,[18,19] and those for the central region of HSST plate 02 have now been obtained. Tensile test results (ASTM standard 0.505-in.-diam specimens) for HSST plate 02 are presented in Table 9.4.

---

[16]M. S. Wechsler, N. E. Hinkle, R. G. Berggren, and W. J. Stelzman, Radiation Metallurgy Section Solid State Division Progress Report for Period Ending January 1968, ORNL-4246, pp. 6–27.

[17]M. S. Wechsler, R. G. Berggren, N. E. Hinkle, and W. J. Stelzman, "Radiation Hardening and Embrittlement in a Low-Carbon Pressure Vessel Steel," paper presented at the Symposium on the Effects of Radiation on Structural Metals, June 26–28, 1968, San Francisco, California. To be published in the proceedings.

[18]R. G. Berggren and T. N. Jones, Radiation Metallurgy Section Solid State Division Progress Report for Period Ending January 1968, ORNL-4246, pp. 38–41.

[19]F. J. Witt, Heavy Section Steel Technology Program Semiann. Progr. Rept. Feb. 29, 1968, ORNL-4315, pp. 19–28.

Table 9.4. Tensile Properties of 12-in.-Thick A 533-B Class 1 Steel from Heat 1195-1, HSST Plate 02

Specimen Number	Test Temperature (°C)	Strength Properties, psi				Percent	
		Upper Yield	Lower Yield	Ultimate Tensile	True Fracture	Total Elongation	Reduction in Area
		× 10^3	× 10^3	× 10^3	× 10^3		
Top-Surface Specimens — Longitudinal[a]							
6440	24	85.8	80.9	96.95	199.1	29.0	69.9
6441	24	85.8	81.0	96.95	197.9	29.2	69.5
6442	232	71.8	70.9	91.2	189.9	23.8	67.9
6443	232	71.3	70.3	92.25	189.4	23.8	66.8
6444	288		70.9[b]	96.55	168.8	23.8	58.6
6445	288		70.8[b]	96.3	174.5	23.8	61.1
6446	343		68.4[b]	91.75	172.6	25.0	65.9
6447	343		67.9[b]	91.35	163.7	28.0	64.0
Quarter-Thickness Specimens — Longitudinal[a]							
6448	24	72.3	69.9	91.05	180.6	26.0	67.9
6449	24	72.1	69.85	91.15	174.4	26.0	65.6
6450	232	61.4	61.0	86.4	180.4	25.0	66.8
6451	232	61.5	61.2	86.2	178.9	23.4	66.8
6452	288		61.9[b]	89.85	166.4	23.5	61.6
6453	288		62.4[b]	89.8	144.4	23.5	55.7
6454	343		60.4[b]	87.6	157.4	27.6	62.6
6455	343		60.9[b]	87.3	156.0	27.0	61.6
Midthickness Specimens — Longitudinal[a]							
6456	24	68.3	67.9	89.15	76.5	23.5	51.7
6457	24	69.55	68.6	89.4	152.5	25.2	56.8
6458	232	60.2	59.9	84.8	136.4	22.2	51.7
6459	288		62.4[b]	88.85	139.9	21.2	48.6
6460	288		61.4[b]	87.7	135.5	21.0	48.0
6461	343		59.9[b]	85.8	107.1	23.5	41.3
Top-Surface Specimens — Transverse[c]							
6467	24	87.5	80.4	97.1	194.1	28.4	63.0
6468	24	86.9	80.9	97.05	191.2	28.4	66.6
6472	288		70.9[b]	96.45	161.8	23.8	58.3
6475	288		70.7[b]	95.9	133.6	19.2	40.7

Table 9.4 (continued)

Specimen Number	Test Temperature (°C)	Strength Properties, psi				Percent	
		Upper Yield	Lower Yield	Ultimate Tensile	True Fracture	Total Elongation	Reduction in Area
		× 10^3	× 10^3	× 10^3	× 10^3		
Quarter-Thickness Specimens — Transverse[c]							
6464	24	71.85	69.1	91.0	170.2	26.5	63.0
6465	24	71.4	69.2	91.35	160.7	24.6	60.8
6473	288		62.4[b]	89.9	131.9	19.2	42.5
6476	288		62.4[b]	90.4	159.6	23.0	56.5
Midthickness Specimens — Transverse[c]							
6466	24	68.75	67.75	88.5	65.6	13.6	25.8
6469	24		70.2	91.3	64.3	19.8	38.1
6474	288		62.4[b]	87.7	130.5	19.8	43.4
6477	288		61.9[b]	84.2	73.9	9.2	21.6
Quarter-Thickness Specimens — Perpendicular[d]							
6470	24	71.1	69.0	91.05	136.7	23.8	57.3
6478	24	70.4	69.0	91.0	136.6	23.2	50.5
6471	288		62.9[b]	88.9	139.9	19.0	45.7
6479	288		63.15[b]	89.65	152.1	21.0	51.6

[a]Longitudinal specimen: tension axis parallel to rolling direction.

[b]Lower yield stress reported is 0.2% offset yield strength.

[c]Transverse specimen: tension axis transverse to the rolling direction and in the rolling plane.

[d]Perpendicular specimen: tension axis perpendicular to the rolling plane (plate surface).

The yield and ultimate strengths were found to be insensitive to specimen orientation. True fracture stress, elongation, and reduction of area were dependent on specimen orientation, the greatest orientation effect being at the half-thickness level due to the higher concentration of inclusions in the center of the plate thickness.

Charpy V-notch impact tests were conducted on HSST plate 02; the results are shown in Table 9.5 and Figs. 9.14 and 9.15. The major effect of specimen orientation was to lower fracture energies in the ductile portion of the energy-temperature curve (ductile shelf) for the transverse and perpendicular orientations. This is shown in Table 9.5 and Fig. 9.14. As observed for HSST plate 01, the energy-temperature curves for quarter-thickness and midthickness specimens were identical (Fig. 9.15), and a lower transition temperature was observed for surface specimens. The lower transition temperature of surface specimens is a result of the higher cooling rates near the surface of the plate during quenching.

Table 9.5. Drop Weight and Charpy-V Impact Properties of 12-in.-Thick ASTM A 533-B Class 1 Steel from Heat No. 1105-1, HSST Plate 02

Level in Plate	Orientation[a]	Temperature, °C		Energy, ft-lb	
		Drop-Weight Nil-Ductility[b]	Charpy-V Transition[c]	Ductile Shelf	Nil-Ductility Transition Correlation
Surface	L		−84	105	50
	T	−68	−73	85	35
Quarter-thickness	L		−7	115	25
	T	−15	−1	95	25
	P		10	80	18
Half-thickness	L		−7	95	25
	T	−12	16	90	15

[a] L: long axis of specimen longitudinal (parallel to plate surface).
T: Long axis of specimen transverse to rolling direction and parallel to plate surface.
P: long axis of specimen perpendicular to plate surface.

[b] P-3 drop-weight specimens.

[c] Transition temperature for 32 ft-lb fracture energy.

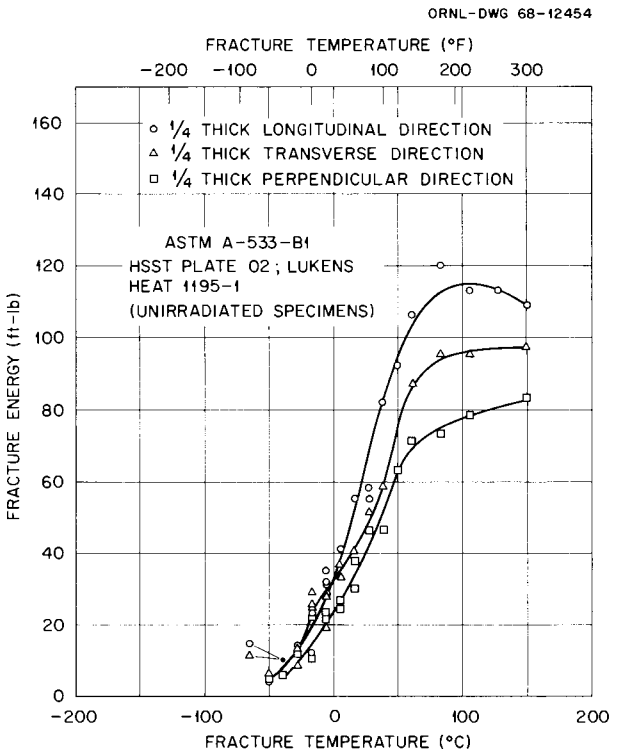

Fig. 9.14. Charpy V-Notch Impact Test Results for Three Specimen Orientations at the Quarter-Thickness Level in a 12-in.-Thick Plate of Manganese-Molybdenum-Nickel Steel (ASTM A 533-B Class 1, HSST Plate 02).

Drop-weight tests were also performed on surface, quarter-thickness, and midthickness specimens of transverse orientation. These results are given in Table 9.5. The effect of depth in plate agreed with the results from the Charpy tests: the surface specimens had a lower nil-ductility transition (NDT) temperature than quarter-thickness or midthickness specimens, and quarter-thickness and midthickness specimens had essentially the same NDT.

Several mechanical properties of HSST plates 01 and 02 are compared in Fig. 9.16 (properties of HSST plate 04, included in this figure, are discussed separately). These results show that the mechanical properties of HSST plates 01 and 02 are almost identical. Both plates meet the ASTM specifications and are uniform in properties through the central 8 in. with the exception of lower ductilities in the central 1 in. Material from these plates is satisfactory for studies of radiation effects. Material from HSST plate 01 is being used in one series of studies of radiation effects, and the results from this series should

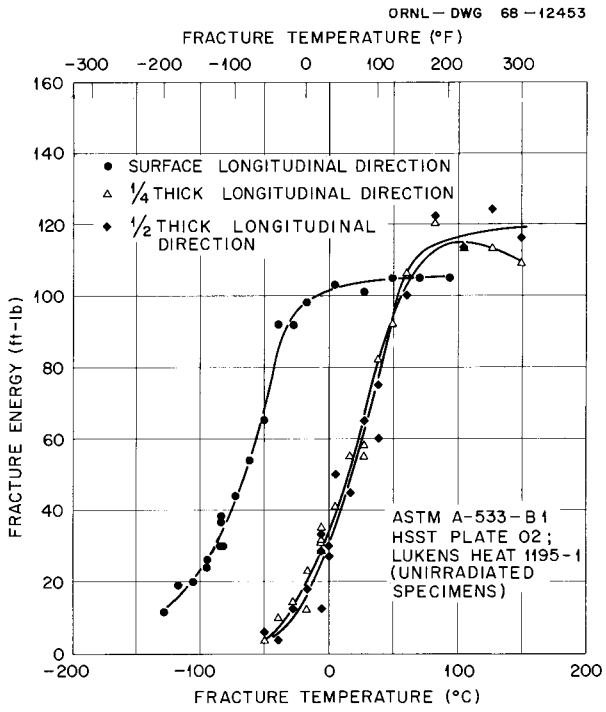

Fig. 9.15. Charpy V-Notch Impact Test Results for Specimens from Three Depth Levels in a 12-in.-Thick Plate of Manganese-Molybdenum-Nickel Steel (ASTM A 533-B Class 1, HSST Plate 02).

be comparable to results from studies using HSST plate 02 material, since the two plates are almost identical in unirradiated properties.

Test specimens are now being machined from HSST plate 03 (which was flat quenched).

The fourth 12-in.-thick A 533 plate (HSST plate 04) produced by Lukens Steel Company for the HSST program was cut into several sections, and parts were rerolled to 4- and 8-in. thicknesses. Segments of 4-, 8-, and 12-in. thickness were then heat treated by Lukens to ASTM A 533-B Class 2 properties. Mechanical testing by Lukens showed that the ASTM specifications could be attained but that ASME Section III toughness requirements could only be met in the 4- and 8-in.-thick plates. These segments of HSST plate 04 were flat quenched. One segment of the 12-in.-thick plate was retained in the mill-annealed condition for study of heat-treatment parameters.

We have obtained preliminary results of tensile and notch-impact tests for material near a corner (one plate thickness from edges) of

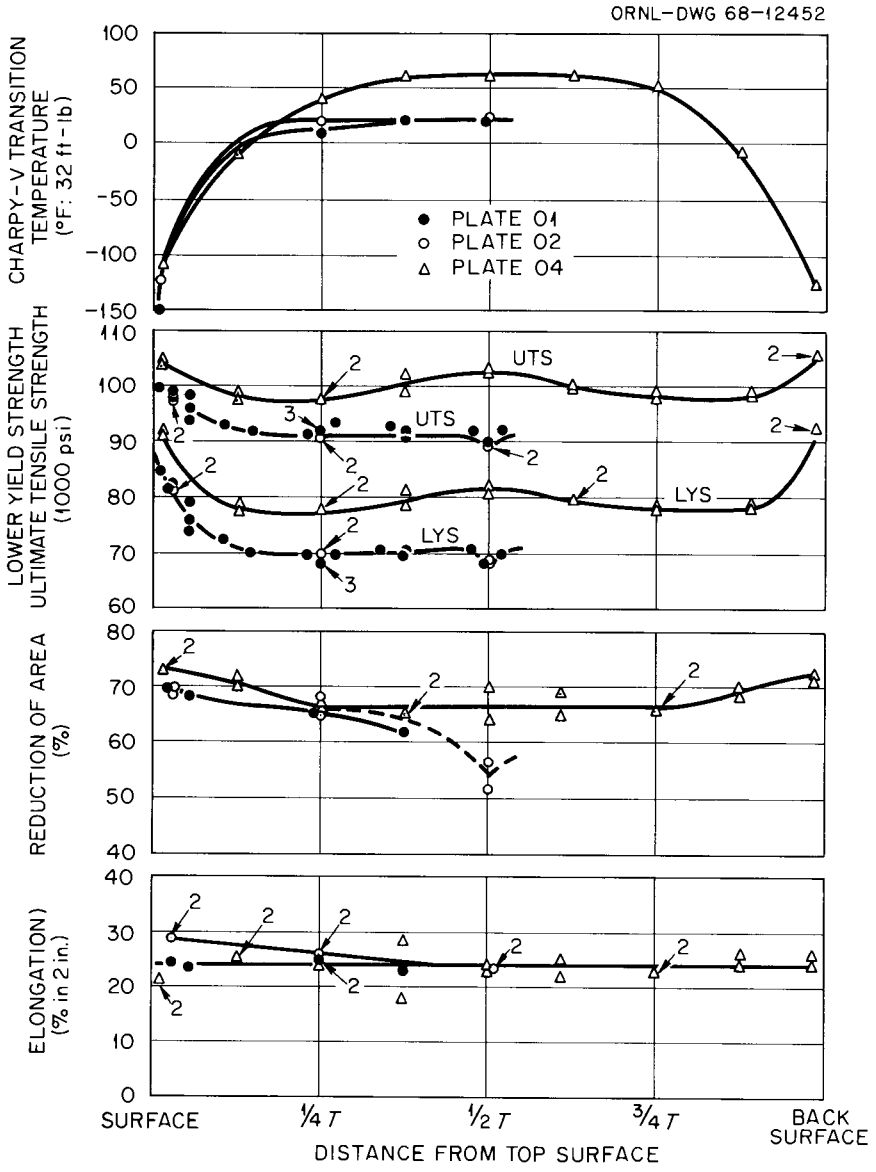

Fig. 9.16. Comparison of Mechanical Properties of Several Levels in Three 12-in.-Thick Plates of Manganese-Molybdenum-Nickel Steel (ASTM A 533-B Classes 1 and 2, HSST Plates 01, 02, and 04).

Table 9.6. Tensile Properties of 12-in.-Thick A 533-B Class 2 Steel[a] from Heat C-2748-2, HSST Plate 04

Specimen Number	Strength Properties, psi				Total Elongation[b] (%)	Reduction in Area (%)
	Upper Yield	Lower Yield	Ultimate Tensile	True Fracture		
	$\times 10^3$	$\times 10^3$	$\times 10^3$	$\times 10^3$		
Top-Surface Specimens						
04-2040		90.7	103.5	230.0	21.4	73
04-2041		91.6	104.1	236.0	21.6	73
One-Eighth-Thickness Specimens						
04-2042	79.0	78.4	98.7	208.0	24.9	71
04-2043	79.2	77.4	97.5	199.0	25.4	70
Quarter-Thickness Specimens						
04-2044		77.5	97.4	186.0	23.6	66
04-2045	78.4	77.6	97.2	191.0	23.9	67
Three-Eighths-Thickness Specimens						
04-2046		81.0	101.7	179.0	18.3	65
04-2047	79.3	78.3	98.6	188.0	28.4	65
Midthickness Specimens						
04-2048	82.6	81.6	102.7	230.0	24.0	70
04-2049	82.1	81.0	102.1	193.0	22.7	64
Five-Eighths-Thickness Specimens						
04-2050	80.6	79.6	100.2	216.0	21.9	69
04-2051	80.6	79.2	99.5	187.0	25.3	65
Three-Quarter-Thickness Specimens						
04-2052	78.7	78.3	98.7	186.0	23.1	66
04-2053	78.3	77.7	97.7	186.0	22.9	66
Seven-Eighths-Thickness Specimens						
04-2054	79.4	78.4	98.5	185.0	26.4	68
04-2055		77.9	97.8	202.0	23.9	70
Back-Surface Specimens						
04-2056	93.6	92.0	105.5	222.0	23.9	71
04-2057	93.4	92.0	105.3	231.0	25.9	72

[a]All specimens of longitudinal orientation (tension axis parallel to rolling direction), tested at 24°C.

[b]Elongation for length-to-diameter ratio (L:D) of 4; calculated from measurements for L:D ratio of 7.

the heat-treated 12-in.-thick segment of HSST plate 04. The tensile properties are presented in Table 9.6 and Fig. 9.16. Results of Charpy V-notch impact tests are also presented in Fig. 9.16. The mechanical properties are symmetric about the midthickness even though the plate was flat quenched.

Mill test reports, heat-treatment details, and detailed mechanical properties of HSST materials have been reported[20,21] and will be reported in the Heavy Section Steel Technology Program Semiannual Progress Report series.

Radiation Effects in Iron

Radiation Hardening in Iron (S. M. Ohr, N. E. Hinkle, M. S. Wechsler)

Temperature Dependence. — The change in the temperature dependence of the yield stress in Fe following neutron irradiation is of considerable interest because it is a manifestation of the nature of the defects responsible for radiation hardening and because it reflects the relative importance of the defects produced by radiation as barriers to dislocation motion compared to the preirradiation barriers. We have investigated[22,23] the temperature and strain rate dependencies of yield stress in Fe irradiated to a relatively low fluence of 1.2×10^{16} neutrons/cm^2 (> 1 Mev). We observed that the overall effect of neutron irradiation was an upward shift of the curve for yield stress versus test temperature without an appreciable change in its shape. We have now extended the study to a fluence of 2.7×10^{19} neutrons/cm^2 (> 1 Mev).

---

[20] F. J. Witt, Heavy Section Steel Technology Program Semiann. Progr. Rept. Feb. 29, 1968, ORNL-4315.

[21] F. J. Witt, Heavy Section Steel Technology Program Semiann. Progr. Rept. Aug. 31, 1967, ORNL-4176.

[22] S. M. Ohr and E. D. Bolling, Radiation Metallurgy Section Solid State Division Progress Report for Period Ending January 1967, ORNL-4097, pp. 13–24.

[23] S. M. Ohr, R. P. Tucker, and M. S. Wechsler, "Radiation Hardening in bcc Metals Niobium and Iron," pp. 187–192 in Proceedings of the International Conference on the Strength of Metals and Alloys, Tokyo, September 4–8, 1967, Vol. 9, Supplement to the Transactions of the Japan Institute of Metals, 1968.

The starting material for this study was 1 1/4-in. bar stock of Ferrovac-E Fe (Table 9.7). The bar was cold rolled to 0.01-in.-thick sheet from which tensile samples of 1/2-in. gage length were punched. These samples were annealed in vacuum to achieve a uniform grain diameter of about 30 μ. The tensile samples, shielded with Cd, were irradiated at temperatures between 52 and 77°C in the poolside facility of the ORR to a fluence of 2.7×10^{19} neutrons/cm^2 (> 1 Mev).

Table 9.7. Chemical Analysis of As-Received Ferrovac-E Iron

Element	Concentration (ppm by weight)	
	Original Mill Analysis	ORNL Analysis
Fe	Base metal	Base metal
C	40	50–100
O	65	50–130
N	1	5–15
H	0.3	< 1
S	70	10
P	50	10
B		10–20
Co	70	20
Cr	100	10–30
Cu	50	20
Mo	100	10
Ni	350	400
Si	60	200
Mn	10	10
V	40	1

Figure 9.17 shows the dependence of the lower yield stress on the test temperature obtained in this study as well as the curves for Fe both unirradiated and neutron irradiated to 1.2×10^{16} neutrons/cm^2. Note that the hardening is relatively insensitive to test temperature in samples irradiated to 1.2×10^{16} neutrons/cm^2. However, the samples irradiated to 2.7×10^{19} neutrons/cm^2 show greater hardening at low test temperatures. Similar observation has been made in Nb by Wechsler *et al.*[24]

[24] M. S. Wechsler, R. P. Tucker, and R. Bode, "Radiation Hardening in Single Crystal Niobium — The Temperature Dependence of Yielding." To be published in Acta Metallurgica.

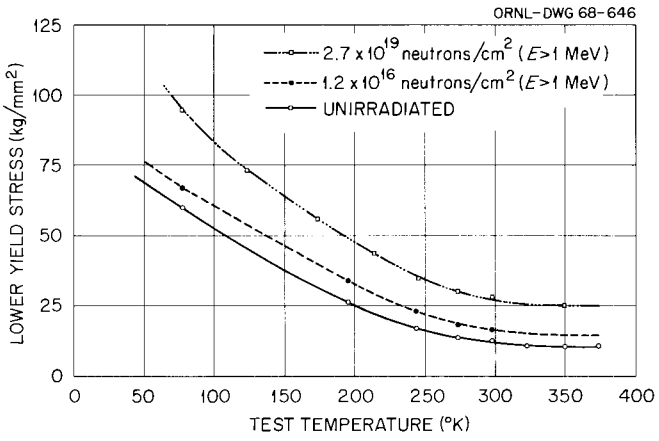

Fig. 9.17. The Temperature Dependence of Lower Yield Stress in Ferrovac-E Iron Unirradiated and Neutron Irradiated to Two Fluences.

They also pointed out that the hardening observed at lower test temperatures is in disagreement with a theory of radiation hardening proposed by Arsenault[25] which predicts a greater hardening at higher test temperatures. It is not clearly understood how an addition of new defects can give rise to a hardening that increases with decreasing test temperature. One of the difficulties associated with the problem is a lack of understanding of the nature of barriers present in Fe before irradiation.

Fluence Dependence. – It is well known that the presence of interstitial impurities can greatly influence the mechanical properties of Fe. It has also been suggested[26] that the irradiation hardening of Fe is sensitive to the content of interstitial impurities. Our study investigates the effect of impurity atoms (primarily interstitial C) on the dependence of radiation hardening on fluence.

The sample materials were vacuum-melted Ferrovac-E Fe with about 50 ppm C by weight, zone-refined Fe with 30 ppm C by weight, and decarburized Ferrovac-E Fe. Tensile samples with 1/2-in.-gage length were prepared from cold-rolled sheets 0.01 in. thick. Samples of zone-refined Fe, annealed in vacuum at 650°C for 20 min, gave a uniform grain size of 30 μ. Samples of Ferrovac-E Fe were similarly annealed at 750°C

[25]R. J. Arsenault, Acta Met. 15, 1853–1859 (1967).

[26]S. B. McRickard and J.G.Y. Chow, Acta Met. 14, 1195–2000 (1966).

for 6 hr to achieve a matching grain size of 30 μ. Samples of decarburized Fe were prepared from Ferrovac-E Fe by annealing the samples in an atmosphere of purified dry H_2 at 800°C for 72 hr. Following the decarburization treatment, the amount of C in solution as determined by measurements of internal friction was below 2 ppm, and the grain size was about 250 μ. A second group of Ferrovac-E Fe samples, annealed in vacuum at 870°C for 10 hr, resulted in a matching grain size of about 250 μ.

The samples of Fe with various interstitial impurity contents were irradiated at temperatures between 52 and 90°C in the poolside facility of the ORR at a flux of about 3×10^{12} neutrons cm^{-2} sec^{-1} (> 1 Mev) to a range of fluences between 1.2×10^{16} and 2.7×10^{19} neutrons/cm^2 (> 1 Mev).

Figure 9.18 shows the dependence of the lower yield stress on the square root of neutron fluence. The most noticeable feature is the rapid increase in yield stress for the Ferrovac-E Fe with a relatively high content of interstitial impurities at low neutron fluences. The rate of increase in yield stress decreases with increasing neutron fluence for all the samples studied. Note also the quick saturation of radiation hardening for Ferrovac-E Fe with the larger grain size.

It was suggested recently[27] that the barriers responsible for radiation hardening in Fe are complexes consisting of atoms of C and point defects produced by irradiation. Our observation is partly in agreement with such a mechanism in that rapid and greater hardening is attained in samples containing more C. It should be noted, however, that the samples of decarburized Fe also exhibit considerable hardening in the range of neutron fluences studied.

---

[27]J. Diehl, G. P. Seidel, and M. Weller, "Neutron Irradiation Hardening of Iron Single Crystals Containing Small Amounts of Carbon," pp. 219–225 in Proceedings of the International Conference on the Strength of Metals and Alloys, Tokyo, September 4–8, 1967, Vol. 9, Supplement to the Transactions of the Japan Institute of Metals, 1968.

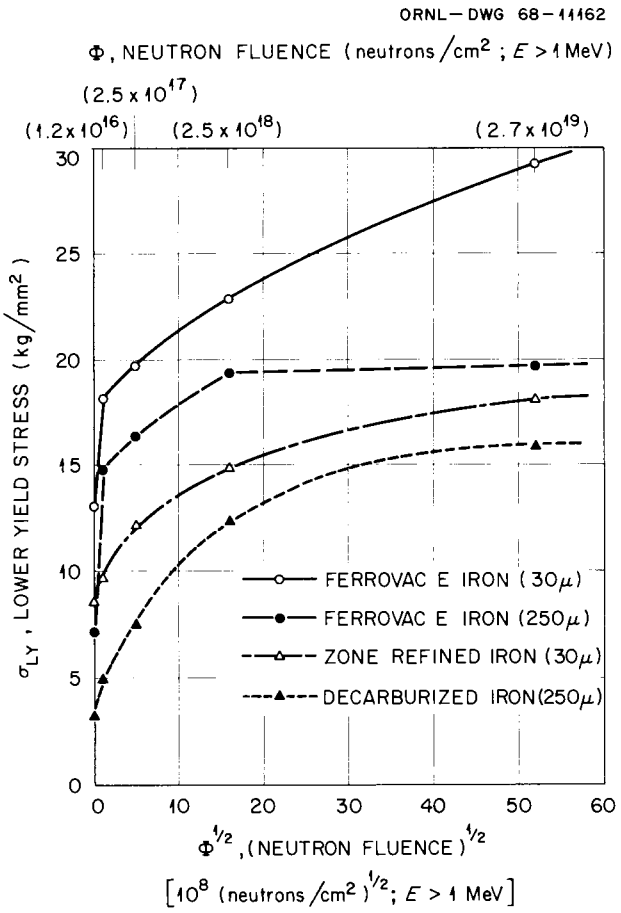

Fig. 9.18. The Lower Yield Stress Plotted Versus the Square Root of the Neutron Fluence for Ferrovac-E Iron of Two Grain Sizes, Zone-Refined Iron, and Decarburized Iron.

Effect of Interstitial Solutes. – Measurements of the mechanical properties of irradiated Fe (ref. 28), Nb (ref. 29), Mo (ref. 30), and W and Mo (ref. 31) have shown that there is an additional hardening of these metals as a result of postirradiation annealing at about 15% of the absolute melting temperature (0.15 T_m), when the irradiation temperature is below this value. It has been suggested that interstitial

[28]N. E. Hinkle and N. K. Smith, Radiation Metallurgy Section Solid State Division Progress Report for Period Ending January 1967, ORNL-4097, pp. 7–13.

[29]M. J. Makin and F. J. Minter, Acta Met. 7, 361–366 (1959).

[30]A. S. Wronski and A. A. Johnson, Phil. Mag. 8, 1067–1070 (1963).

[31]J. Moteff, "Radiation Damage in Body-Centered Cubic Metals and Alloys," p. 727 in Radiation Effects, Gordon and Breach, New York, 1967.

impurities may be contributing to this "radiation-anneal hardening" by interacting with the defects induced by irradiation to produce stronger barriers to dislocation motion. However, none of these measurements were made in studies that used supplemental techniques to determine which interstitial element was involved. Therefore, a detailed investigation[32] was begun to determine by suitable techniques which interstitial element contributes to the radiation-anneal hardening in Fe and to obtain an understanding of the mechanism of the interaction between interstitial atoms and defects induced by irradiation. Information gained from this study should be of great value in understanding the radiation hardening and embrittlement of steel.

Barton, Harries, and Mogford[33] observed differences in the magnitude of the radiation effect in steels produced by different methods. They suggested that the variability of the radiation hardening might be associated with the differences in the concentration of interstitial N, which is dependent on the method of steelmaking used (i.e., on the chemistry of the final product). As a result of their work and the fact that the effect of interstitial C on the radiation effect has been extensively studied,[34–36] we decided to study the effect of interstitial N on radiation effects in Fe.

The starting material for this study was Ferrovac-E Fe (Table 9.7) swaged from 1 1/4-in.-diam bar to 1/16 in. in diameter and decarburized and denitrogenized in dry H_2 at 800°C for about 96 hr. This material was further swaged and drawn to 0.050 in. in diameter, and pieces were

---

[32]N. E. Hinkle, J. M. Williams, W. E. Brundage, and J. T. Stanley, Radiation Metallurgy Section Solid State Division Progress Report for Period Ending July 1967, ORNL-4195, pp. 15–21.

[33]P. J. Barton, D. R. Harries, and I. L. Mogford, J. Iron Steel Inst. (London) 203, 507–510 (1965).

[34]H. Wagenblast and A. C. Damask, Phys. Chem. Solids 23, 221–227 (1962).

[35]F. E. Fujita and A. C. Damask, Acta Met. 12, 331–339 (1964).

[36]J.G.Y. Chow and S. B. McRickard, "Low-Temperature Embrittlement of Iron, Iron Alloys, and Steels by Neutron Irradiations," pp. 120–130 in Flow and Fracture of Metals and Alloys in Nuclear Environments, Am. Soc. Testing Mater. Spec. Tech. Publ. 380, American Society for Testing and Materials, Philadelphia, Pennsylvania, 1965.

cut for resistivity, internal-friction, and tensile specimens. The shoulders of the tensile specimens were fabricated by cold-upsetting the ends of 1 1/2-in.-long wire blanks in a double-ended, hydraulically operated die.

The specimens were heat treated 4 hr in dry H_2 at 700 and 800°C and then cooled in the furnace to establish grain sizes of 30 and 130 μ. Specimens of each grain size were further heat treated at 590°C for 10 hr, quenched in water, and stored in liquid N. In this heat treatment, one group of specimens of each grain size had about 20 ppm N by weight added by treatment in a hydrogen-ammonia atmosphere; a second control group was treated in an atmosphere of pure H_2. These materials are identified as Fe-20N and Fe, respectively. The concentration of N in solid solution was verified by measurements of internal friction. Less than 1 ppm N by weight was detected in the Fe material. The C in solution was below 2 ppm by weight as determined by measurements of internal friction and confirmed by measurements of the magnetic aftereffect. However, chemical methods indicated a concentration of 50 to 100 ppm C by weight. Therefore, the C in the Fe and Fe-20N materials is believed to be present in the form of carbides or segregated at grain boundaries, where it makes little contribution to the yield or flow stresses.

As previously reported,[32] the neutron irradiations were performed at temperatures between −50 and −100°C in a liquid-nitrogen-cooled cryostat positioned against one side of the ORNL Bulk Shielding Reactor. The neutron flux in this facility was about 3×10^{12} neutrons cm^{-2} sec^{-1} (> 1 Mev). For the results reported below, the specimens were irradiated to a fluence of 4×10^{17} neutrons/cm^2 (> 1 Mev).

After the irradiation, the assemblies were removed from the irradiation facility without exceeding the irradiation temperature and stored in liquid N for a period of radioactivity decay. Then the assemblies were taken apart in a bath of liquid N and stored in liquid N until testing began. The unirradiated specimens were also stored in liquid N while they awaited testing.

The irradiated specimens were annealed 15 min at temperatures from −36 to 250°C and quenched in liquid N. After this postirradiation anneal, the specimens were tested at −36°C at a strain rate of 0.02 min^{-1} to a strain of 0.04. At given amounts of strain in this range, the strain rate was momentarily changed to 0.002 min^{-1}. Next, the samples were aged for 20 hr at 40°C to permit the complete precipitation of any free nitrogen and carbon interstitials and tensile tested an additional 4% at −36°C according to the same pattern of strain rates. We expected the aging response to be a quantitative measure of the interstitial atoms remaining in solid solution following the postirradiation anneal. In Figs. 9.19 and 9.20 we show typical stress-strain curves for the Fe and Fe-20N materials. In these figures, we can observe the

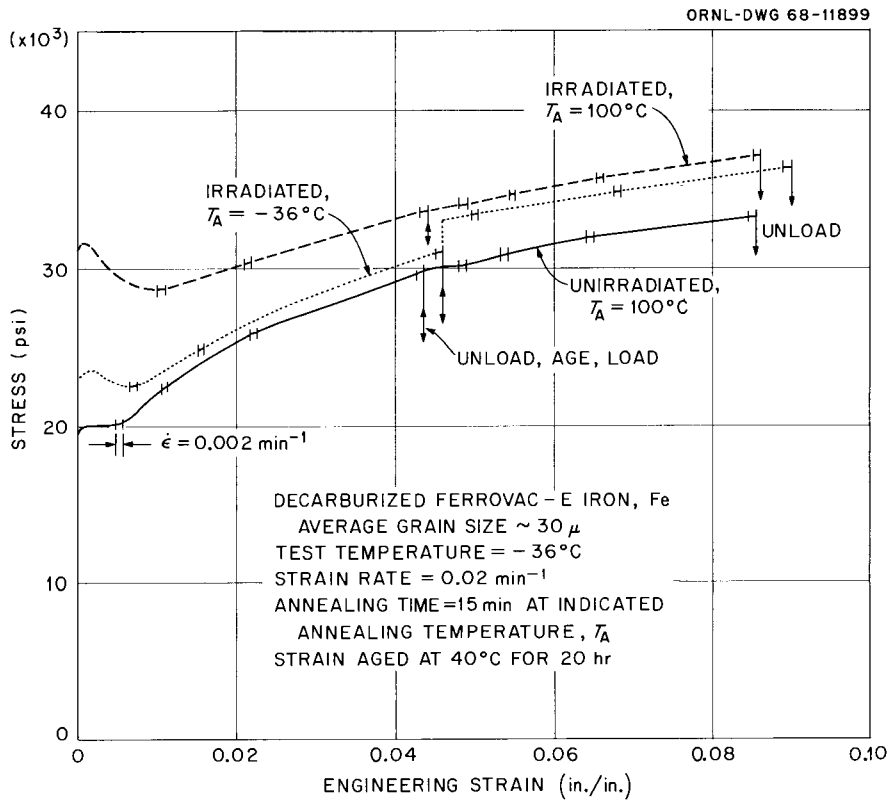

Fig. 9.19. Stress-Strain Curves at −36°C for Material Fe Showing the Effect of Irradiation, Postirradiation Annealing, and Strain Aging.

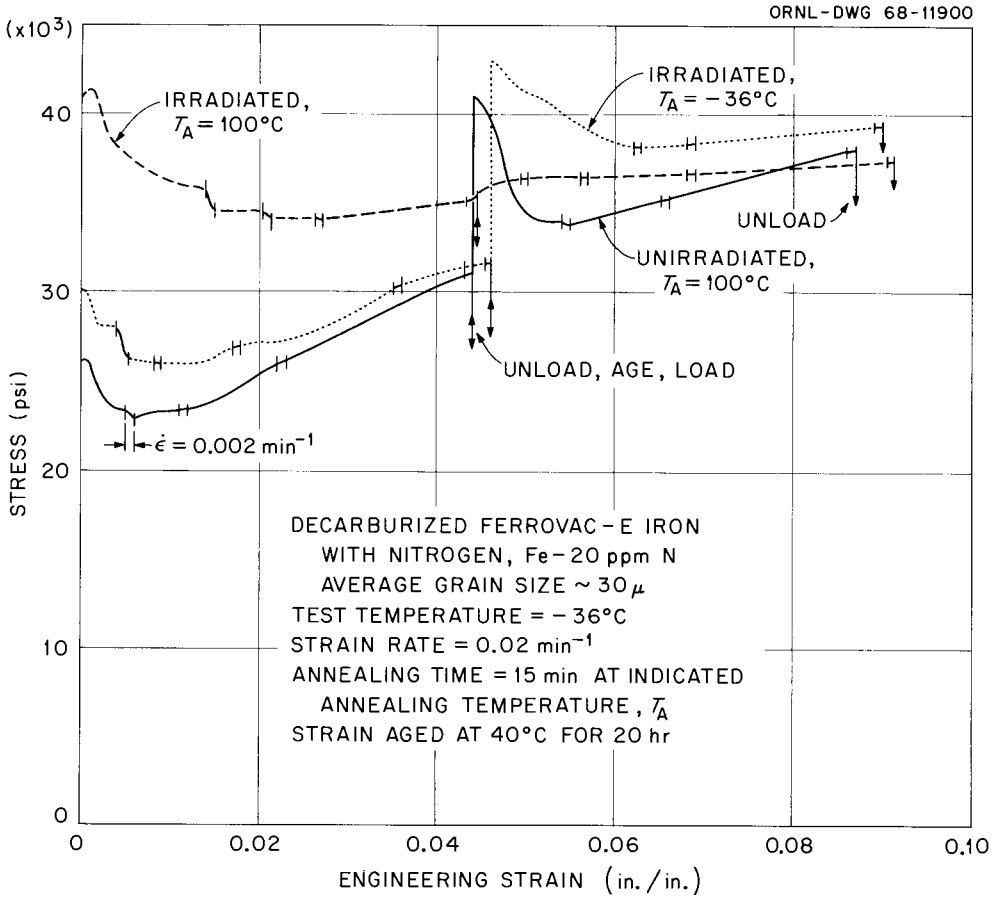

Fig. 9.20. Stress-Strain Curves at −36°C for Material Fe-20N Showing the Effect of Irradiation, Postirradiation Annealing, and Strain.

increase in yield stress upon irradiation, the radiation-anneal hardening, and the strain aging response. Also indicated are the strains where the strain rate was momentarily decreased to 0.002 min^{-1}.

In Figs. 9.21 and 9.22 we show the increase in lower yield stress as a function of postirradiation annealing temperature for fine- and coarse-grained materials. The Fe and Fe-20N of both grain sizes exhibit radiation-anneal hardening which appears to begin at or below 0°C in both grain sizes. In the fine-grained Fe, the radiation-anneal hardening is completed at 100°C, but appears to extend to about 150°C with a slightly greater magnitude for the Fe-20N, as seen in Fig. 9.21. But the results for the coarse-grained material, shown in Fig. 9.22, do not indicate any difference in the magnitude or temperature range of

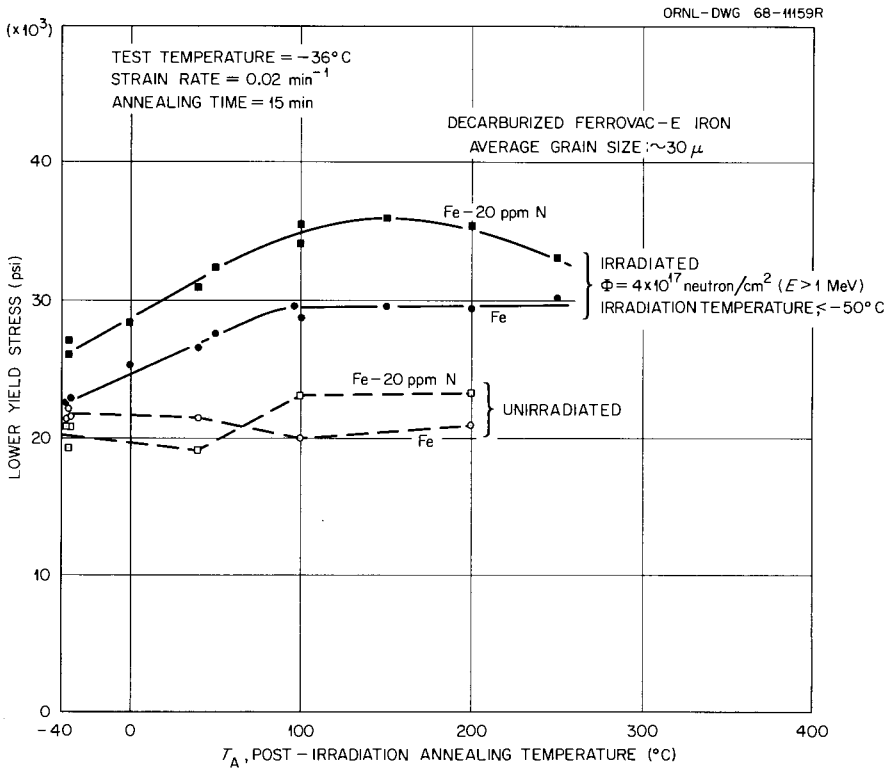

Fig. 9.21. Effect of Postirradiation Annealing on Separate Tensile Specimens.

the radiation-anneal hardening. There is an indication that softening is beginning at an annealing temperature of 200 to 250°C.

The increase in flow stress upon aging 20 hr at 40°C is shown in Fig. 9.23 as a function of the postirradiation annealing temperature before aging. The heights of curves in Fig. 9.23 are a measure of the amounts of interstitial impurities present in solid solution (and therefore able to participate in the strain aging) after the 15-min anneals at temperatures indicated on the abscissa. The most prominent feature in Fig. 9.23 is the decrease in the aging response of Fe-20N between 0 and 100°C, which reaches a minimum near zero aging response at about 100°C, whereas no minimum is seen for the Fe. The minimum for Fe-20N but not for Fe is also illustrated in Fig. 9.24, where we show the yield drop after aging the fine-grained materials. Since the magnitude of the yield drop is associated with the concentration of interstitial atoms in solution available to pin dislocation sources,

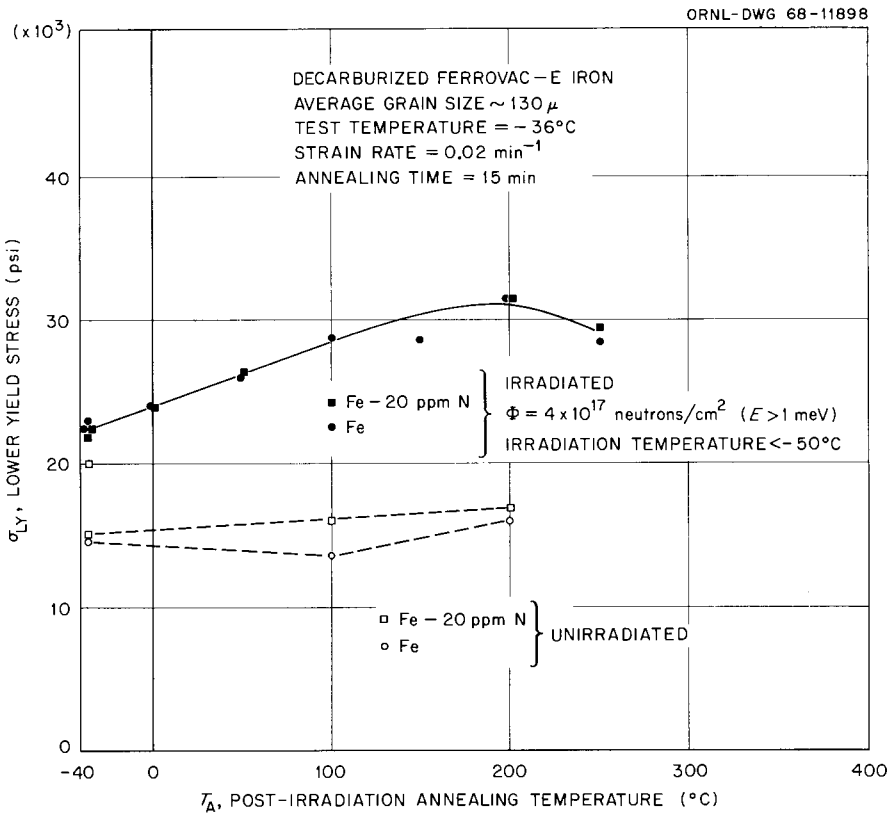

Fig. 9.22. Effect of Postirradiation Annealing on Separate Tensile Specimens.

the minimum in the aging response in Fig. 9.23 is evidence again that the N in solution is decreased during the postirradiation anneal at 100°C in Fe-20N. These results are in accord with our previous studies of resistivity and internal friction,[37] which indicated an annealing stage of 0 to 100°C in irradiated Fe-20N but no such stage for Fe.

Upon postirradiation annealing above 100°C, the aging response returns in Fe-20N, as shown in Fig. 9.23 for the flow stress increase upon aging and in Fig. 9.24 for the yield drop. The previous resistivity measurements[37] showed that the resistivity of Fe-20N decreased less than that of Fe in the postirradiation annealing temperature range 100 to 200°C, indicating some return of N to solid solution at these temperatures.

---

[37]N. E. Hinkle, J. M. Williams, W. E. Brundage, and J. T. Stanley, Radiation Metallurgy Section Solid State Division Progress Report for Period Ending July 1967, ORNL-4195, pp. 15–21.

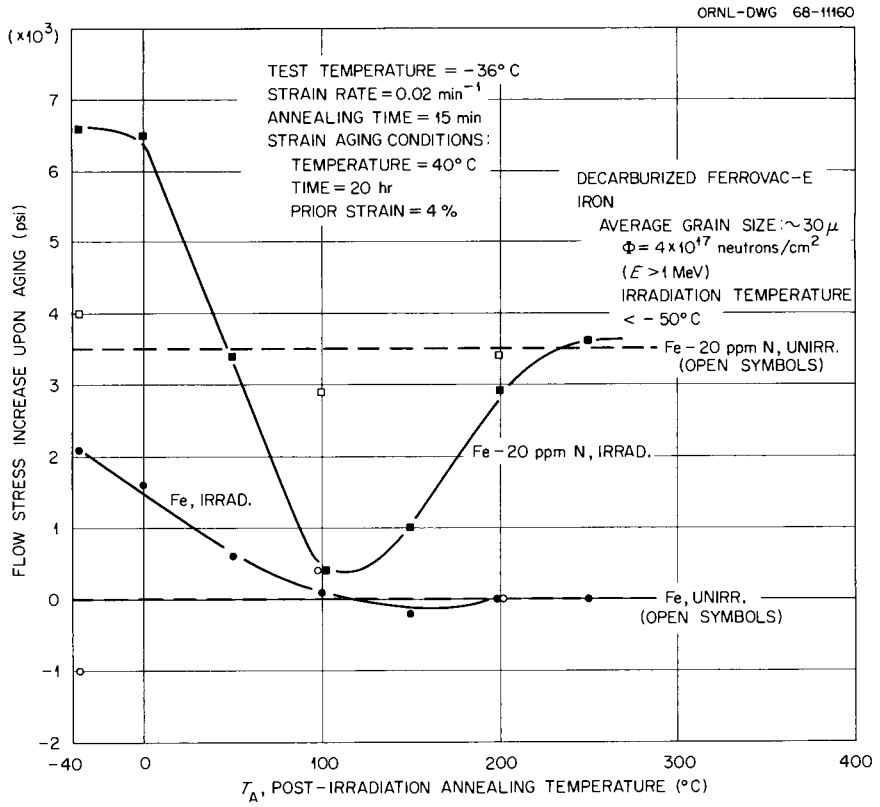

Fig. 9.23. The Increase in the Flow Stress for Tensile Specimens of Fine-Grain Fe and Fe-20N.

For mild steel irradiated at 45°C, Harries and Little[38] showed that the increase in the aging response for the same aging treatment (20 hr at 40°C) occurs at 300 to 400°C.

In comparing Figs. 9.23 and 9.24, note an increase in flow stress for the as-irradiated Fe upon aging for 20 hr at 40°C (Fig. 9.23), but no yield drop (Fig. 9.24). We believe the increase in flow stress is due to radiation-anneal hardening taking place during the aging treatment. Figure 9.21 shows that the radiation-anneal hardening of Fe goes to completion at about 100°C. This is consistent with the curve for Fe

---

D. R. Harries and E. A. Little, "Effect of Interstitial Nitrogen on Radiation Hardening in Mild Steels," paper presented at ASTM Fourth International Symposium on the Effects of Radiation on Structural Metals held in San Francisco, California, June 26–28, 1968, to be published in the proceedings.

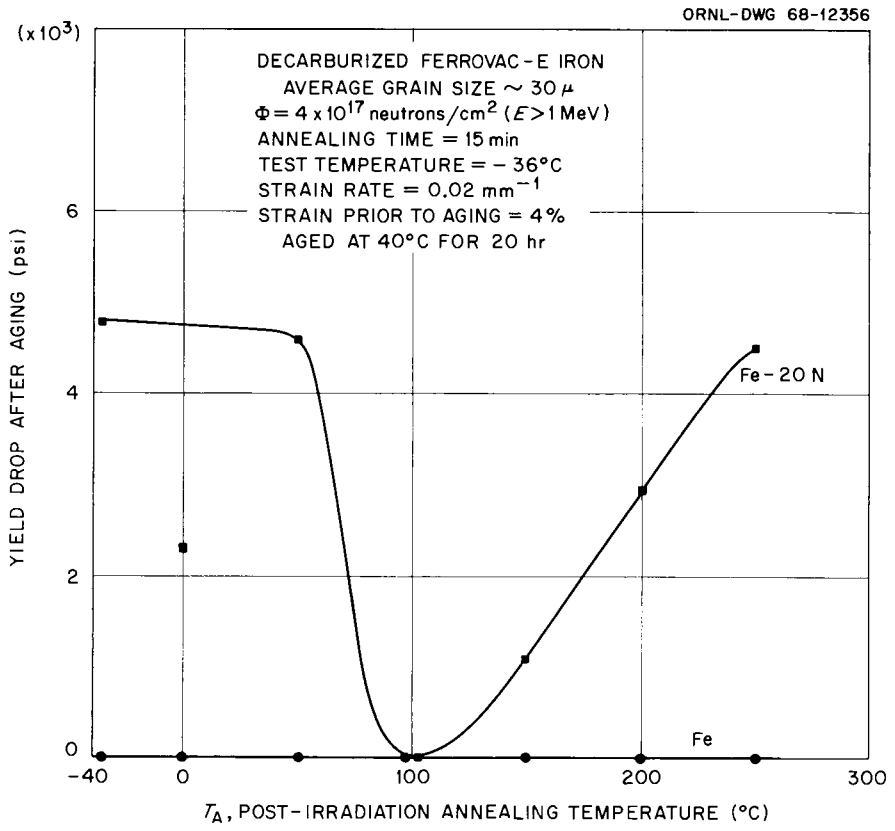

Fig. 9.24. The Yield Drop Observed for Fine-Grain Fe and Fe-20N after an Aging Treatment of 40°C for 20 hr.

in Fig. 9.23 in that the flow stress increase upon aging goes to zero for specimens annealed at about 100°C.

The observation that the Fe material exhibits radiation-anneal hardening to only a slightly lesser degree than the Fe-20N material (Fig. 9.21) suggests that N is not a major contributing factor to the radiation-anneal hardening. On the other hand, the strain aging results (Figs. 9.23 and 9.24), supported by earlier studies of resistivity and internal friction,[37] show that N is indeed removed from solid solution, presumably at defects produced by the irradiation. Thus, we conclude that the nitrogen-defect complexes do not have a hardening effect. This is further indicated by the recovery to the unirradiated strain aging response for flow stress (Fig. 9.23) and yield drop (Fig. 9.24) after annealing to 250°C, whereas the yield stress still exhibits the radiation-anneal-hardened value after annealing to this temperature.

Radiation Effects in Vanadium

Trapping of Interstitial Impurities in Vanadium Defects Produced by Radiation (J. M. Williams, W. E. Brundage, J. T. Stanley)

For the past two years, the Radiation Metallurgy Section has had under way a study of the effect of interstitial impurities on post-irradiation annealing phenomena in refractory metals, particularly Nb (refs. 39–42). The results obtained to date for Nb indicate that annealing effects above room temperature are possibly dominated and at the very least markedly influenced by the interaction of interstitial impurities with defects produced by radiation. In particular, the effects observed so far include (a) segregation of O in solution to radiation-produced dislocation loops in the 100 to 200°C range[39,40,43] and subsequent return to solution upon annealing at higher temperature[40,41] and (b) precipitation of C, possibly at dislocation loops.[42] These effects appear to account for the phenomenon known as "radiation-anneal hardening," first observed by Makin and Minter[44] in Nb. Indeed, Ohr and Tucker[45] have found that the anneal hardening is a two-stage process where the lower temperature stage is attributable to O and the higher temperature stage to C.

---

[39]J. M. Williams, J. T. Stanley, and W. E. Brundage, Radiation Metallurgy Section Solid State Division Progress Report for Period Ending January 1967, ORNL-4097, pp. 30–41.

[40]J. T. Stanley, J. M. Williams, and W. E. Brundage, Radiation Metallurgy Section Solid State Division Progress Report for Period Ending July 1967, ORNL-4195, pp. 26–34.

[41]J. T. Stanley, J. M. Williams, and W. E. Brundage, Radiation Metallurgy Section Solid State Division Progress Report for Period Ending January 1968, ORNL-4246, pp. 42–51.

[42]J. M. Williams, J. T. Stanley, and W. E. Brundage, Radiation Metallurgy Section Solid State Division Progress Report for Period Ending July 1968, ORNL-4334, pp. 9–20.

[43]R. Bullough, J. T. Stanley, and J. M. Williams, Metal Sci. J. 2, 93–96 (1968).

[44]M. J. Makin and F. J. Minter, Acta Met. 7, 361–366 (1959).

[45]S. M. Ohr and R. P. Tucker, Radiation Metallurgy Section Solid State Division Progress Report for Period Ending July 1968, ORNL-4334, pp. 29–33.

In view of the fact that V and its alloys are receiving more consideration as potential reactor materials than is Nb, we decided to undertake studies in V to ascertain the extent to which the effects in V parallel those in Nb. Vanadium, like Nb, is a Group VA metal in which the impurities O and N are highly soluble. The solubility of C is quite low. Vanadium, however, has a considerably lower melting point than Nb and is therefore more difficult to purify. Furthermore, C and O move in the same temperature range with nearly the same activation energies.[46]

Sample Preparation. – Two materials labeled VC and VD were used in this study. The starting material for each was 0.032-in.-diam wire obtained from the Materials Research Corporation. The final preparation procedure for each of the materials was an annealing and outgassing treatment by resistive heating of the wires in a high-vacuum bell jar. Material VC was annealed at about 1400°C for about 2.5 hr, and the final vacuum achieved was 6×10^{-9} torr. Material VD was annealed at about 1200°C for about 1 hr, and the final vacuum achieved was 3×10^{-8} torr. Thus, we expected VC to be the purer material. We cut the resulting wires into a number of resistivity and internal-friction samples. The internal-friction samples were 4 in. long, and the resistivity samples were 2 in. long with gage lengths of about 1 in.

Measurement Techniques. – The internal friction was measured using an inverted-torsion pendulum at 1.12 Hz. The resistivity was measured with a thermo-free microvolt potentiometer with the samples immersed in liquid He inside a superconducting solenoid set at 5 kilogauss. The direction of current in the sample was parallel to the magnetic field. Potential contacts to the resistivity samples were made by spot welding 0.005-in.-diam Fe wires to the samples. These contacts were used for the preirradiation measurements but were replaced with platinum contacts before the postirradiation measurements were made. Thus the gage lengths were not precisely constant between the preirradiation and postirradiation measurements. However, the gage lengths were measured as accurately as

---

[46]R. W. Powers and M. V. Doyle, J. Appl. Phys. 30, 514–524 (1949).

was possible without abusing the samples (±1%) for both sets of potential contacts.

Irradiation Procedures. — The materials VC and VD were irradiated simultaneously in a helium atmosphere in position CP-15 of the ORNL Bulk Shielding Reactor. The temperature of irradiation (60°C) was measured with a thermocouple spot-welded to a dummy sample in the assembly. The neutron fluence was 7×10^{17} neutrons/cm^2 (≥ 1.0 Mev).

Annealing Procedures. — Internal-friction samples were annealed in place in the torsion pendulum. Resistivity samples were postirradiation annealed by immersing the sample holder in a silicone oil bath, temperature controlled to ±0.2°C. Following each anneal, the samples were cooled rather rapidly to room temperature, and the oil was removed simultaneously by immersing them in Freon 11. Then, for the measurement at liquid-helium temperature, the samples were cooled slowly to near liquid-nitrogen temperature by passing cooled nitrogen gas over them and were inserted slowly into the liquid-helium-cooled magnet. This slow-cooling procedure was followed because we found that rapid cooling to liquid-nitrogen temperature seemed to introduce scatter into the data. Westlake[47] has found resistivity anomalies between measurements at room temperature and at liquid-nitrogen temperature that he attributes to precipitation of H. If H had been introduced into our materials during irradiation, such a phenomenon could possibly account for the sensitivity of our data to the procedural details in this experiment. It should be emphasized, however, that only the apparent scatter in the data and not the main effects reported in our results were affected by the procedures.

Figure 9.25 shows results from preirradiation measurements of internal friction between 100 and 340°C. The oxygen and nitrogen peaks are identified on the basis of the data of Powers and Doyle.[46] Table 9.8 shows the corresponding oxygen and nitrogen concentrations calculated from the data of Powers and Doyle, together with the residual resistivity values for the two materials. The resistivity

[47]D. G. Westlake, Phil. Mag. 16, 905–908 (1967).

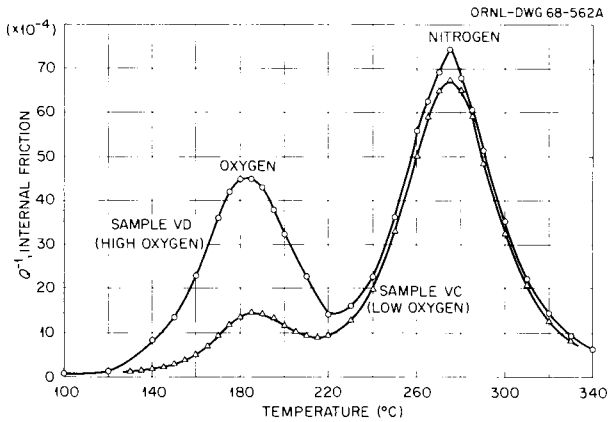

Fig. 9.25. Internal Friction of Unirradiated Vanadium Materials as a Function of Temperature. Frequency = 1.12 Hz.

Table 9.8. Characteristics of Vanadium Materials

Material	Concentration, at. ppm		Resistivity ($\mu\Omega$-cm)
	Oxygen	Nitrogen	
VC	83	1770	1.32 ± 0.02
VD	257	1940	1.59 ± 0.02

values represent the average of measurements on three samples of each material, and the error limits shown probably arise from inconsistencies in the geometrical measurements. We have been unable to locate literature giving the resistivity contributions of interstitial impurities in V, but the resistivity values given in Table 9.8 are reasonable if it is assumed that the resistivity contributions for O and N are in the range 5 to 10 $\mu\Omega$-cm/at. %. This range of values is typical of interstitial impurities in body-centered cubic metals. If the resistivity difference of 0.27 $\mu\Omega$-cm between the two samples is attributed to the interstitial impurity difference of 344 ppm (atomic), we get a resistivity of 7.8 $\mu\Omega$-cm/at.% interstitial impurities, making no distinction between O and N as to effect on resistivity.

After irradiation, an internal-friction sample from material VD was annealed first at the oxygen-peak temperature (185°C) and then at the nitrogen-peak temperature (275°C), and internal friction was measured as a function of time at the two temperatures. Figure 9.26

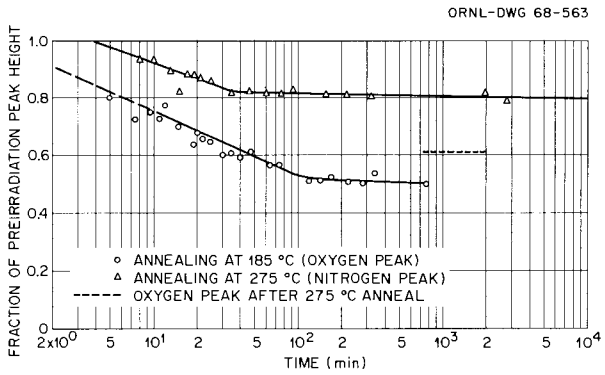

Fig. 9.26. Fractional Decrease of Internal-Friction Peaks Due to Oxygen and Nitrogen in Vanadium Material VD as a Function of Annealing Time at the Peak Temperatures.

shows the results of this experiment. The oxygen peak had decreased by about 50% after 100 min annealing at 185°C. The nitrogen peak decreased about 20% during the anneal at 275°C. After the anneal at 275°C, the sample was returned to 185°C, and some recovery of the decrease in the oxygen peak was noted.

Figure 9.27 shows results of postirradiation isochronal annealing for materials VC and VD over the range 60 to 220°C. The change in resistivity is taken with respect to the unirradiated resistivity. Thus the samples increased in resistivity by about 0.035 μΩ-cm upon irradiation and decreased as shown in the figure upon isochronal annealing.

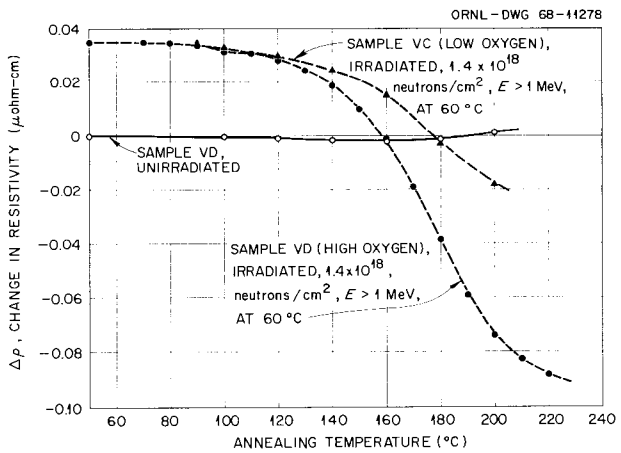

Fig. 9.27. Changes in Resistivity of Vanadium upon Isochronal Annealing. Materials VD-irradiated and VC-irradiated were annealed for 1-hr periods at 20°C intervals.

However, since the gage lengths were not precisely the same for the preirradiation and postirradiation measurements, an explanation of the way in which we arrived at the increase of 0.035 μΩ-cm is needed. For four samples (two each of VC and VD) the resistivity increase upon irradiation was found to range from 0.025 to 0.049 μΩ-cm with an average of 0.035 μΩ-cm, and these measurements included the error associated with changing and remeasuring the gage length. Thus, for purposes of presenting the magnitudes of the effects in these samples on some absolute basis, we assumed the resistivity increased by 0.035 μΩ-cm upon irradiation in all the samples. The principal feature illustrated in Fig. 9.27 is that both materials exhibit a large decrease in resistivity between 100 and 200°C, but the decrease is much smaller in material VC (low oxygen content) than in VD (high oxygen content). Furthermore, the resistivity goes below the preirradiation value. In view of the problem of gage length, we would not argue that the appearance of going below the preirradiation value is necessarily real in material VC, but it decidedly is real in VD. Unirradiated material VD exhibits a slight decrease in resistivity up to 140°C and thereafter increases slightly. This increase appears to be reversible. The resistivity decreases again when we return the sample to 140°C after annealing it at 200°C. However, the magnitudes of the effects in unirradiated VD are much smaller than in the irradiated material.

The data represented as 1-hr isochronal annealing data in Fig. 9.27 are in fact the end points of a series of 1-hr isothermal anneals on one sample at successively increasing temperatures, where measurements were made as a function of time during the 1-hr period. From this type of measurement, the activation energy of the process can be determined from the change in slope attendant upon changing the temperature abruptly from T_1 to T_2. Figure 9.28 shows the series of isothermal anneals obtained on VC. The activation energies that were calculated from the changes in slope are tabulated in Table 9.9. It is difficult to estimate the error in this method of determining activation energy, but by drawing various curves through the data in Fig. 9.28, we estimate that the scatter in the data warrants assignment of an error band no greater

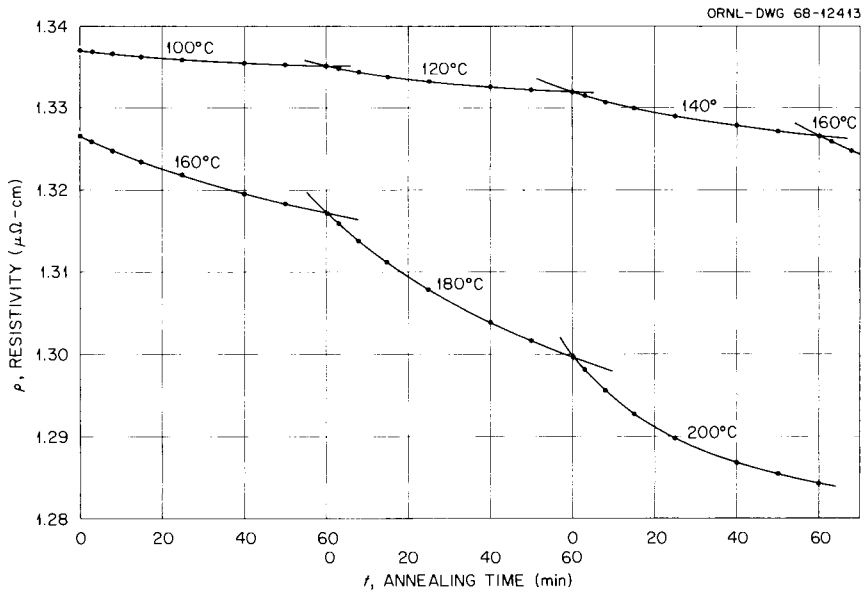

Fig. 9.28. Resistivity as a Function of Annealing Time at Successively Increasing Temperatures in an Irradiated Sample of Vanadium Material VC.

Table 9.9. Activation Energies Obtained from Ratio-of-Slopes Method

Annealing Temperatures, °C		E_m Activation Energy (ev)
T_1	T_2	
100	120	1.23
120	140	1.24
140	160	1.14
160	180	1.32
180	200	1.02

than ±0.12 ev to any one determination, assuming all the apparent scatter is indeed random. The values are in reasonably good agreement except for the value 1.02 ev obtained for the last temperature transition from 180 to 200°C. In Nb, it has been found that the apparent activation energy for Stage III falls off as the measurements are made at higher

temperatures.[48,49] This is attributed to the concept that the saturation value is strongly temperature dependent, a circumstance that would invalidate most methods of determining activation energy as saturation is approached.

We shall first discuss the annealing effects between 100 and 220°C, but before proceeding, perhaps some background information on previous annealing studies in this temperature region in body-centered cubic metals will help facilitate discussion. Pronounced resistivity annealing stages in this temperature region have been observed in both neutron-irradiated and deformed body-centered cubic metals,[50–53] and because irradiation is known to produce point defects, these stages were first attributed to annealing of point defects and called Stage III annealing. Now, however, there is mounting evidence that in the Group VA metals these resistivity decreases are caused by the migration of interstitial impurities to defect structures produced by irradiation or deformation. The evidence that this is the case in Nb and Ta appears quite conclusive.[48,49,54,55] Earlier, Köthe and Schlät[56] observed that the

---

[48]J. M. Williams, J. T. Stanley, and W. E. Brundage, Metal Sci. J. 2, 100–104 (1968).

[49]A. Köthe, Acta Met. 16, 357–367 (1968).

[50]D. E. Peacock and A. A. Johnson, Phil. Mag. 8, 563–577 (1963).

[51]J. Moteff and J. P. Smith, "Recovery of Defects in Neutron-Irradiated Tungsten," pp. 171–187 in Flow and Fracture of Metals and Alloys in Nuclear Environments, Am. Soc. Testing Mater. Spec. Tech. Publ. 380, American Society for Testing and Materials, Philadelphia, Pennsylvania, 1965.

[52]D. G. Martin, Acta Met. 5, 371–376 (1957).

[53]L. Stals and J. Nihoul, Phys. Status Solidi 8, 785–793 (1965).

[54]R. Bullough, J. T. Stanley, and J. M. Williams, Metal Sci. J. 2, 93–96 (1968).

[55]Z. C. Szkopiak and B. Pouzet, "Effect of Oxygen on 'Stage III' Recovery in Cold-Worked Niobium," pp. 709–723 in International Conference on Vacancies and Interstitials in Metals, Vol. II, Jülich, Germany, September 1968.

[56]A. Köthe and F. Schlät, J. Mater. Sci. 2, 201–205 (1967).

magnitude of the annealing effects in deformed V decreased with decreasing oxygen content and concluded that effects in V are analogous to those in Nb and Ta. This interpretation has recently been questioned by Perepezko et al.[57] on the basis of an activation energy determination. These workers observed annealing effects between 100 and 200°C in both deformed and neutron-irradiated V that closely resemble those of Köthe and Schlät in deformed material and those of the present work in irradiated material. Perepezko et al.[57] measured activation energies of 0.87 ± 0.07 ev and 0.79 ± 0.09 ev for the annealing stage in deformed and irradiated materials, respectively. Since these activation energies are lower than the diffusion activation energies of either C, O, or N and greater than the diffusion activation energy of H, they conclude that the annealing stage should be attributed to annealing of lattice vacancies, possibly to impurity traps. It would appear that the activation energies of about 0.8 ev are somewhat lower than is usually measured for an annealing process in this temperature region; as the authors point out,[57] an enormous number of jumps (about 10^8) of the migrating species is implied.

In view of the considerably larger activation energy measured in the present experiment, we submit that the mechanism of migration of interstitial impurities to radiation-produced defects, probably dislocation loops, still provides a simple and satisfactory explanation of events in this temperature region. First of all, the effect takes place in the temperature region where internal-friction measurements indicate O first becomes highly mobile, whether it migrates to radiation-produced defects or not. Thus, we prefer to attribute the internal-friction decrease at the oxygen-peak temperature to migration of O to some site where it is effectively removed from interstitial solid solution. This interpretation and the notion that the resistivity decrease is connected with the internal-friction decrease are supported by the fact that the activation energy for the resistivity decrease measured in this experiment (Table 9.9) agrees with the diffusion activation energy of O (1.25 ev) (ref. 58).

---

[57]J. H. Perepezko, R. F. Murphy, and A. A. Johnson, "Point Defects in Vanadium." To be published in The Philosophical Magazine.

[58]R. W. Powers and M. V. Doyle, J. Appl. Phys. 30, 514–524 (1949).

The magnitude of the resistivity decrease and the fact that the resistivity drops below the preirradiation value are readily accounted for on the basis of this mechanism. The internal-friction decrease (Fig. 9.26) indicates that about 50% of the O or 130 ppm (atomic) is removed from solution in material VD. The magnitude of the resistivity decrease for this material, 0.125 μΩ-cm, divided by the above-mentioned figure, 7.8 μΩ-cm at. %, would suggest removal of about 160 ppm (atomic), which is basically in good agreement considering that the figure 7.8 μΩ-cm at. % represents about an average of the resistivity contributions of O and N rather than the contribution of O specifically. Since most of the residual resistivity is caused by interstitial impurities, any effect involving a sizable fraction of these impurities is likely to override the relatively small increase in resistivity caused by irradiation. It is to be expected that material containing less O will exhibit a smaller resistivity decrease, as was the case in this experiment (Fig. 9.27).

Resistivity annealing studies were not made above 220°C, but the fact that the nitrogen peak decreases with time at the nitrogen-peak temperature (275°C) indicates that the behavior of N is similar to that of O and that a large resistivity decrease should be expected in this temperature region as well. Köthe and Schlät observed such a resistivity decrease centered at 265°C in deformed V containing 1000 ppm N (ref. 56).

In the discussion so far we have ignored possible effects due to C, but because the diffusion activation energy for C (1.18 ev) is only slightly lower than that for O (1.26 ev), involvement of C in the annealing effect below 200°C cannot be ruled out. The width of the 100 to 200°C annealing stage in V is somewhat greater than the corresponding stage in Nb (ref. 59), and this suggests that the effect might involve the migration of both O and C. However, the solubility of C in equilibrium solid solution in V is thought to be quite low, and the absence of

---

[59] J. T. Stanley, J. M. Williams, and W. E. Brundage, Radiation Metallurgy Section Solid State Division Progress Report for Period Ending July 1967, ORNL-4195, pp. 26–34.

any major resistivity decrease upon annealing in the unirradiated V (Fig. 9.27) shows that almost all the C is in equilibrium before irradiation. Furthermore, the 182°C internal-friction peak (Fig. 9.25) is stable and fairly narrow, suggesting a single relaxation due to O alone.

PART IV.

TECHNIQUES OF FABRICATION AND TESTING

10. TUNGSTEN METALLURGY

W. O. Harms

The object of this program is to develop economical methods for producing high-quality tungsten and tungsten-alloy tubing with good creep-rupture properties at high temperatures, good microstructural stability, good ductility at low temperatures, and good weldability. We fabricate tubing both by modification of conventional techniques based on extrusion, tube reduction, and warm drawing and by direct chemical vapor deposition (CVD) through the hydrogen reduction of heavy-metal halides. Our program includes complete physical and metallurgical evaluation of both fabrication processes.

Primary and Secondary Working of Tungsten Alloys

W. R. Martin

Extrusion of Tungsten (R. E. McDonald)

Four duplex billets have been fabricated from a primary tungsten tube shell and molybdenum bar stock. Using these billets, we are studying the effects of prior work and extrusion preheat temperature on the structure of the final extruded tube. Because of temperature variations during extrusion, a primary tungsten tube shell extruded above 1700°C usually has three different microstructures: the nose of the tube shell is fully recrystallized, the tail is a wrought structure, and the center is a mixture of the two.

We machined a ring sample from each of four primary tungsten tube-shell sleeves before assembling the duplex billets. The ring has been sectioned: one section will be heat treated to duplicate the time and temperature treatment of the extruded duplex billet, and the other section will represent the condition of the primary extrusion billet. The billets will be extruded at a constant extrusion ratio of 3 between 1200 and 1700°C.

Installation of New Tube Reducer (R. E. McDonald)

The Materials Processing group has received the new tube reducer. It is being installed and is expected to be operational by mid-November. The Aetna-Standard Company, Pittsburgh, designed and built the machine to our specifications. Figure 10.1 is an overall view from the exit table towards the feed end of the tube reducer. The roll carriage is powered by a 400-rpm 150-hp direct-current motor that will allow the stroke speed to be varied from 10 to 30 strokes/min. The feed can be adjusted from 0 to 1/2 in. per stroke, and the tube can be rotated from 0 to 180° per stroke. This flexibility will allow us to reduce a variety of materials on a single machine and study the effects of feed, speed, and rotation on the finished tube. The designed parting force is 450,000 lb, and the 4-hi design will allow us to reduce a tube shell 2 in. in outside diameter and 1/4 in. in wall thickness in a single operation to a tube 1 in. in outside diameter and 0.100 in. in wall thickness.

Chemical Vapor Deposition of Tungsten and Vanadium Alloys

W. R. Martin

Deposition of Tungsten-Rhenium Alloys (J. I. Federer)

The object of current tungsten-rhenium codeposition experiments is to prepare sheet stock nominally containing 5% Re. The alloy is being deposited on resistance-heated sheet substrates. After deposition, the deposit is sectioned, and the substrate (Mo—0.5% Ti) is dissolved in acid, leaving the deposit unattacked. Electrical connections are made to the substrate by means of water-cooled copper electrodes that impose a temperature gradient along the length of the substrate, the highest temperature being in the center. As a result, previous deposits have usually had a higher rhenium content on the ends, while the thickest deposit was always in the center. We minimized this temperature gradient by reducing the width of the substrate at both ends, resulting in increased heat generation and decreased heat flow into the electrodes. The most satisfactory substrate, which was obtained by trial and error,

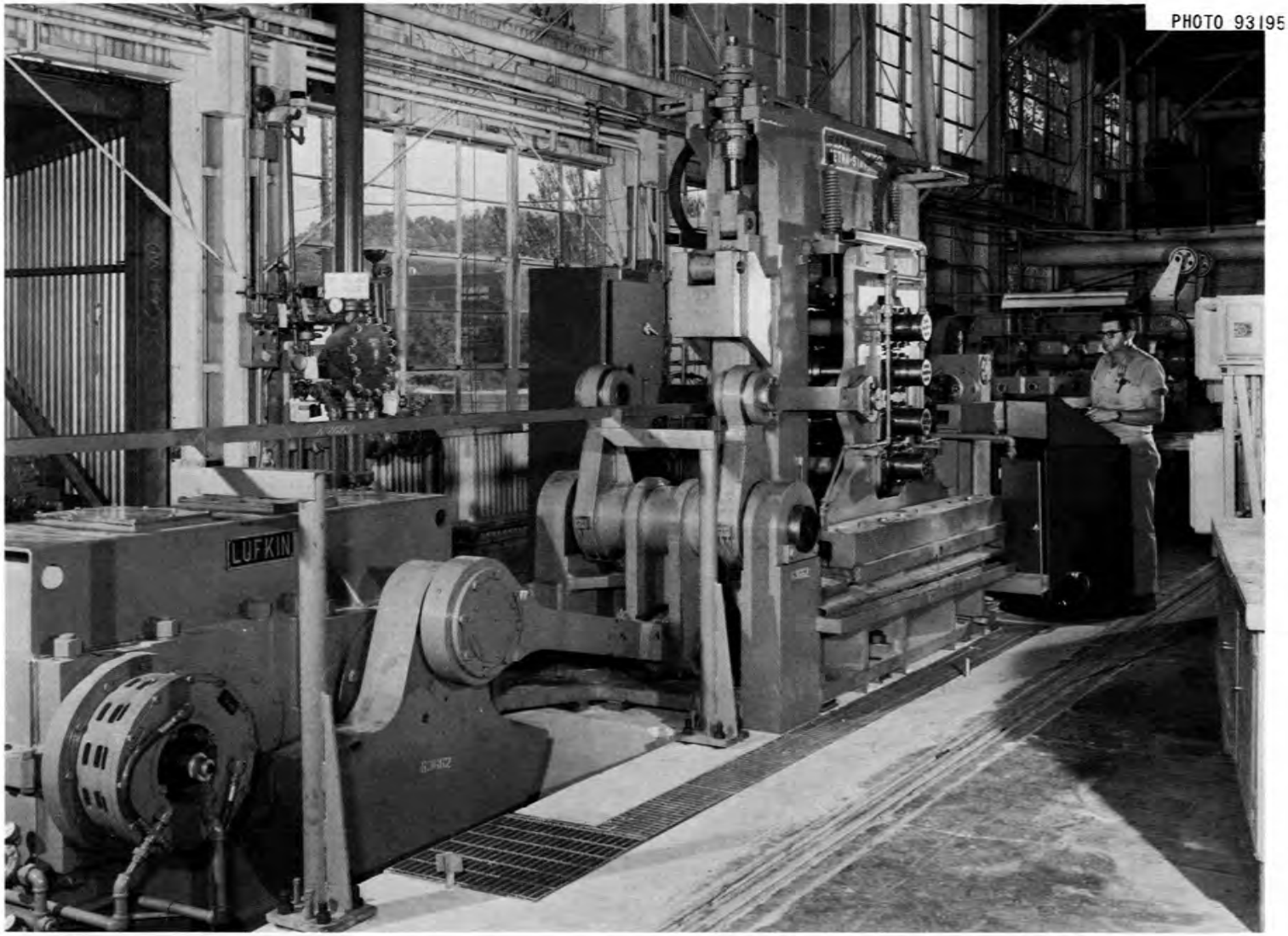

Fig. 10.1. View of New Experimental Tube Reducer.

measures 3.25 × 0.025 × 14 in. with 1.5-in.-long end sections that are 2 in. wide. This provides about 100 $in.^2$ of deposit. With the substrate mounted in a Pyrex glass chamber rather than the usual metal chamber, we measured the temperature distribution along the length of the substrate with an optical pyrometer. In a typical case, the temperature was 750 ± 5°C over about 12 in. of the 14-in.-long section but was hotter on the ends. Hydrogen flow rates up to 3000 cm^3/min at 10 torr did not impose a temperature gradient along the substrate.

Several attempts to deposit W–5% Re sheet stock ended prematurely due to equipment failure before a successful deposit was obtained. The alloy was successfully deposited at 750°C, 10 torr, and a $H_2/(WF_6+ReF_6)$ ratio of 12. The direction of gas flow was reversed every 30 min during the 16 hr deposition in an effort to improve thickness uniformity. The average thickness on both sides of the substrate and the rhenium content along the length of the deposit were as follows:

Location, in.	0	3	6	9	12	14
Rhenium, %	5.1	3.8	4.0	4.1	3.8	5.9
Thickness, in.	0.049	0.041	0.034	0.033	0.040	0.062

Although the substrate was hotter on the ends, the rhenium content was unexpectedly high in those positions. The rhenium content was more uniform over the bulk of the deposit. We attribute the greater thickness on the ends partly to the higher temperature but mostly to gas depletion. This phenomenon might be overcome by using higher flow rates, but that would lower efficiency. In this experiment, 89% of the metal content of the metered fluorides was recovered in the deposit.

The deposit was cut into pieces about 3 × 3 in., and the substrate was dissolved in an acid solution that was 45% HNO_3, 45% H_2O, and 10% H_2SO_4. The deposit from one side of the substrate was stress-relieved for 2 hr at 1100°C and 1×10^{-6} torr. Specimens for bend tests are being prepared from both the as-deposited and stress-relieved portions of the substrate.

Deposition of Vanadium Alloys (W. C. Robinson, Jr.)

We have begun an investigation of the feasibility of depositing vanadium metal. Vanadium is considered a candidate for cladding advanced fast reactor fuels.

Efforts to deposit V from the pentafluoride (VF_5) resulted in the formation of a stable intermediate, VF_3, which precipitated as a green solid in the reaction zone. Thermodynamic considerations indicated a borderline chance that the metal might be produced by hydrogen reaction with the vanadium chlorides. The reaction becomes more feasible at elevated temperatures, with the free energy of reaction of H_2 with UCl_3 being zero at about 1350°C and negative beyond that. This is not usually a desirable indication, since most reactions in CVD have a −20 or −30 kcal ΔF^0 at the deposition temperature. In spite of this, we considered it worthwhile at least to attempt deposition under these conditions.

Two types of chloride were obtained: VCl_4 and VCl_3. The tetrachloride is a fuming, dark-brown liquid that is stored under Cl_2 and reacts violently with air or water. The difficulty of transferring this material into a container adaptable to one of our deposition rigs discouraged us from viewing it as a primary source of vanadium metal. Furthermore, it evidently decomposes spontaneously to VCl_3 when the chlorine atmosphere is reduced above it, and this solid VCl_3 clogs the transfer line. As a result, in a deposition attempt at 950°C only about 2 g of material was transferred, leaving a very thin, unidentifiable film on the stainless steel mandrel. Therefore the VCl_3, a purple solid, was loaded into one of our containers and transferred by argon entrainment. Twelve grams of material was moved into the 950°C reaction zone along with H_2, and a somewhat thicker deposit was made on the stainless steel mandrel. This deposit was identified as principally VCl_2, which is evidently a stable intermediate for which no thermodynamic data are available. Higher temperatures are obviously required, but 950°C was the limit of the resistance-heated surface being used. Therefore, we are now installing a high-temperature induction-heated deposition rig that will allow us to deposit V at higher temperatures.

Metallurgical Properties of Tungsten Alloys

A. C. Schaffhauser

Recrystallization of Wrought CVD Tungsten

We are continuing our studies to determine the recrystallization behavior of wrought CVD tungsten. Previously we showed that recrystallization of material containing 25 ppm F is retarded by small gas bubbles and/or unprecipitated fluorine impurities.[1] If the material is preannealed before rolling to precipitate impurities in the form of large gas bubbles, recrystallization occurs at much lower temperatures. This behavior is observed in the hardness data shown in Fig. 10.2. The material with no preanneal shows a gradual softening at 1800°C due to slow recrystallization and precipitation of fluorine impurities. The material that was preannealed at 2500°C before rolling exhibits a very rapid drop in hardness in the first few hours of annealing at 1200°C due to rapid recrystallization.

We determined the kinetics of recrystallization from measurements by a point-counting analysis of the volume fraction of recrystallized material. The point-counting array, defined by line intersections on a square grid, was superimposed on a minimum of nine photomicrographs from each sample, and the volume fraction of recrystallized material was taken as equal to the fraction of points falling within the recrystallized regions. Hilliard[2] has shown that the maximum reliability and efficiency of this technique is achieved when the average number of points falling in any one recrystallized region does not greatly exceed unity. This condition was difficult to meet in samples that had a large fraction of recrystallized area because of the heterogeneous nature of recrystallization in this material (Fig. 10.3). Therefore, data from

---

[1]A. C. Schaffhauser and K. Farrell, Fuels and Materials Development Program Quart. Progr. Rept. June 30, 1968, ORNL-4330, pp. 286–294.

[2]J. E. Hilliard, "Applications of Quantitative Metallography in Recrystallization Studies," p. 267 in Recrystallization, Grain Growth, and Textures, American Society for Metals, Metals Park, Ohio, 1966.

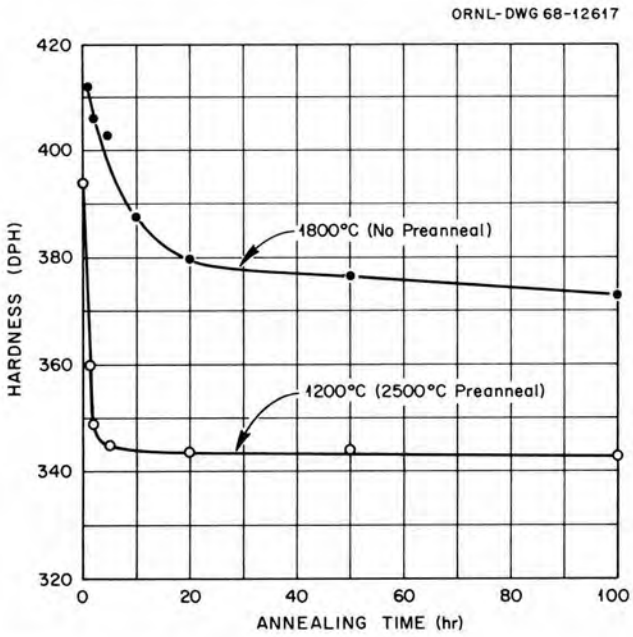

Fig. 10.2. Effect of Annealing Time on the Hardness of Wrought CVD Tungsten.

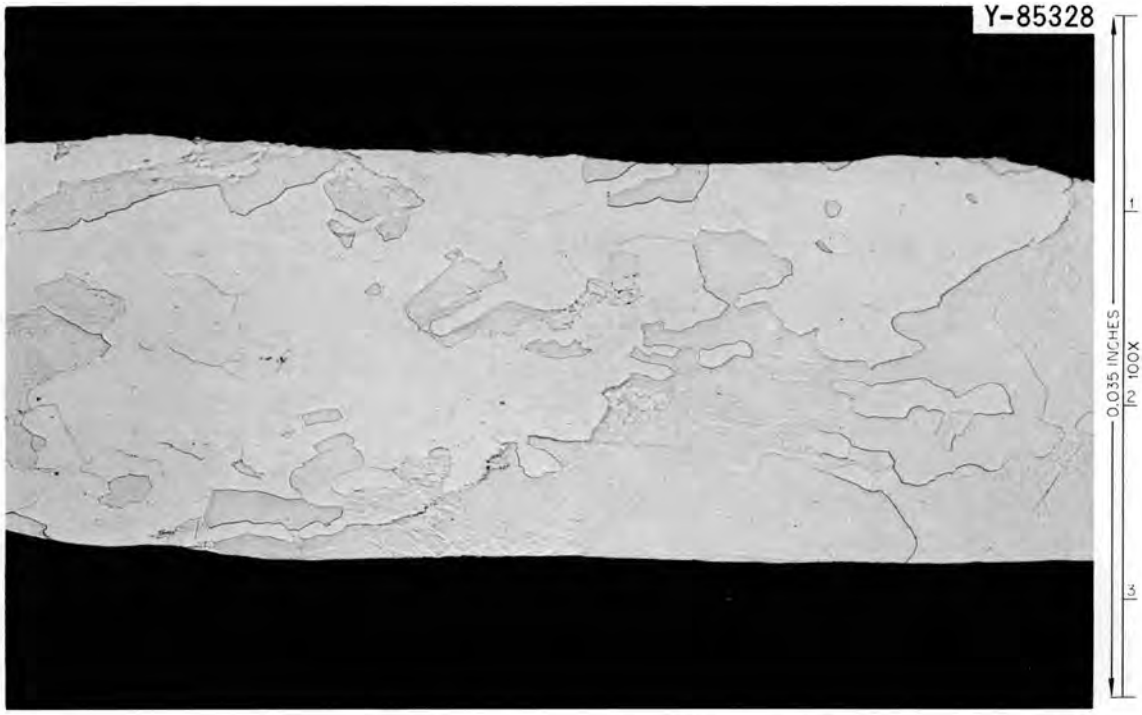

Fig. 10.3. Wrought CVD Tungsten Annealed 1 hr at 1200°C (Preannealed 1 hr at 2500°C Before Rolling).

two different point arrays were compared, and the data shown in Fig. 10.4 indicate that with less than 50% recrystallized area the 80-point grid gives more consistent results.

Figure 10.4 shows that the fraction of recrystallized material increases logarithmically with increasing annealing time. The rate constant at 1800°C for the material not preannealed before rolling is 8.8 log hr^{-1} compared to 49 log hr^{-1} at 1200°C for the preannealed material. The large difference in the recrystallization rates of material that was preannealed and material that was not preannealed clearly shows that the large bubbles (> 1000 A) produced by preannealing are not effective in retarding recrystallization in this material. This observation could account for the conflicting results on the effect of gas bubbles on recrystallization in irradiated materials.[3]

[3]B. Russell, J. Australian Inst. Metals 11, 18 (1966).

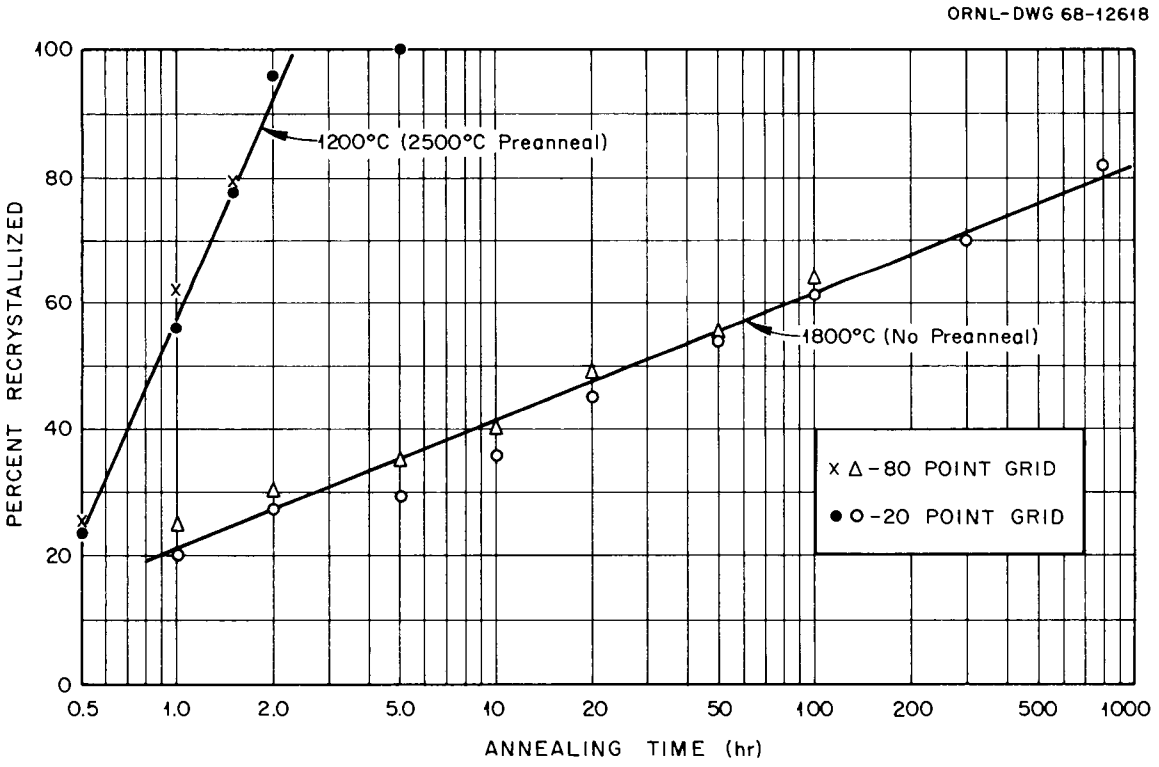

Fig. 10.4. Rate of Recrystallization of Wrought CVD Tungsten.

The Properties of CVD Tungsten Deposited from WCl_6

We have observed great differences in the grain structure and effects of annealing in CVD tungsten deposited from WF_6 (fluoride tungsten) and material deposited from WCl_x (chloride tungsten).[4,5] A significant increase in the efficiency of thermionic emitters made from chloride tungsten rather than fluoride tungsten has also been shown.[5] Thus, the determination of the metallurgical properties of chloride tungsten is of great importance for thermionic applications. This study was initiated to determine the properties of chloride tungsten, as we have done for fluoride tungsten, and to elucidate the mechanisms responsible for the differences in behavior.

The preliminary results given in this report were obtained from a small quantity of material produced by San Fernando Laboratories and given to us by Dr. Ling Yang of Gulf General Atomic. Future studies will be conducted on materials from a variety of sources.

Previously, we showed that two very important properties for high-temperature applications, the grain stability and bubble formation, are directly related to fluorine impurities in fluoride tungsten. An example of this behavior is shown in Fig. 10.5 in material containing 6 ppm F. Very few bubbles are observed by electron microscopy on the grain boundaries of this material after annealing at 1800°C, and some grain growth has occurred. At higher annealing temperatures extensive grain growth takes place, and bubbles with an average diameter of 1.7 μ cover about 18% of the grain boundary area at 2500°C. No grain growth is

---

[4]A. C. Schaffhauser and R. L. Heestand, "Effect of Fluorine Impurities on the Grain Stability of Thermochemically Deposited Tungsten," p. 222 in 1966 IEEE Conference Record of the Thermionic Conversion Specialist Conference, Institute of Electrical and Electronic Engineers, New York, 1966.

[5]L. Yang and R. G. Hudson, "Evaluation of Chemically Vapor Deposited Tungsten as Electron Emitters for Nuclear Thermionic Application," p. 329 in Proceedings of the Conference on Chemical Vapor Deposition of Refractory Metals, Alloys, and Compounds, Gatlinburg, Tennessee, September 12–14, 1967, ed. by A. C. Schaffhauser, American Nuclear Society, Hinsdale, Illinois.

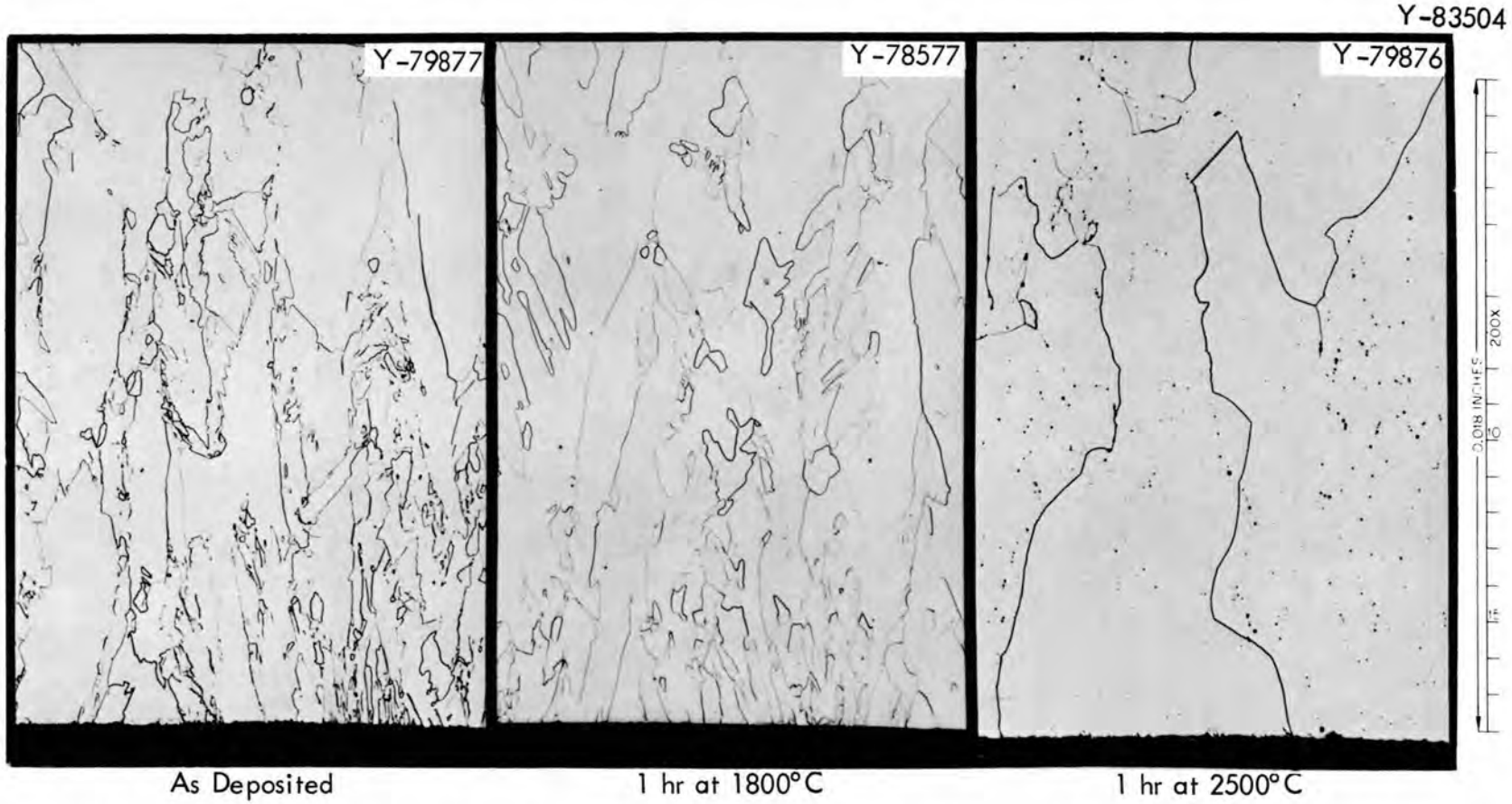

Fig. 10.5. Effect of Annealing Temperature on the Microstructure of CVD Tungsten Deposited from WF_6 Containing 6 ppm F. Deposit S82-1. Etchant: NH_4OH and H_2O_2. 13.5% reduction.

observed at 2500°C in fluoride tungsten containing 30 ppm F, in which bubbles with an average diameter of 2.3 μ cover about 38% of the boundary area.[6]

High-purity chloride tungsten, obtained by chlorinating fluoride tungsten scrap, also contains residual fluorine impurities. Upon annealing, however, much greater grain growth occurs in the chloride material, apparently independent of the fluorine content, and little or no bubble formation is observed by electron microscopy. The extensive grain growth in the chloride material we have tested, which contains 7 ppm F, is shown in Fig. 10.6. The reasons for this anomalous behavior are not known, but they may result from a difference in the nature of the fluorine impurities in the chloride material due to the difference in deposition conditions. Chloride tungsten is usually deposited between 900 and 1100°C, whereas fluoride tungsten is normally deposited between 500 and 700°C. The reaction product of the fluoride deposit is HF and that of chloride deposits is HCl. The trace impurities in the deposition system are very likely different, too.

The increased performance of thermionic emitters made from chloride-tungsten is due to the higher bare-work function of the (110) preferred orientation that, as shown in Table 10.1, can be obtained under special deposition conditions in this material.[5] Fluoride tungsten normally has a (100) preferred orientation that approaches a more random structure for those deposition conditions that produce a lower fluorine content, as is also shown in Table 10.1. We expect that a detailed study of the effects of deposition temperature and composition of the gaseous phase at the deposition surface on the surface energy and growth morphology of deposits will be necessary to understand the differences in orientation of these materials.

---

[6]K. Farrell, J. T. Houston, and A. C. Schaffhauser, "The Growth of Grain Boundary Gas Bubbles in Chemically Vapor Deposited Tungsten," p. 363 in Proceedings of the Conference on Chemical Vapor Deposition of Refractory Metals, Alloys, and Compounds, Gatlinburg, Tennessee, September 12–14, 1967, ed. by A. C. Schaffhauser, American Nuclear Society, Hinsdale, Illinois.

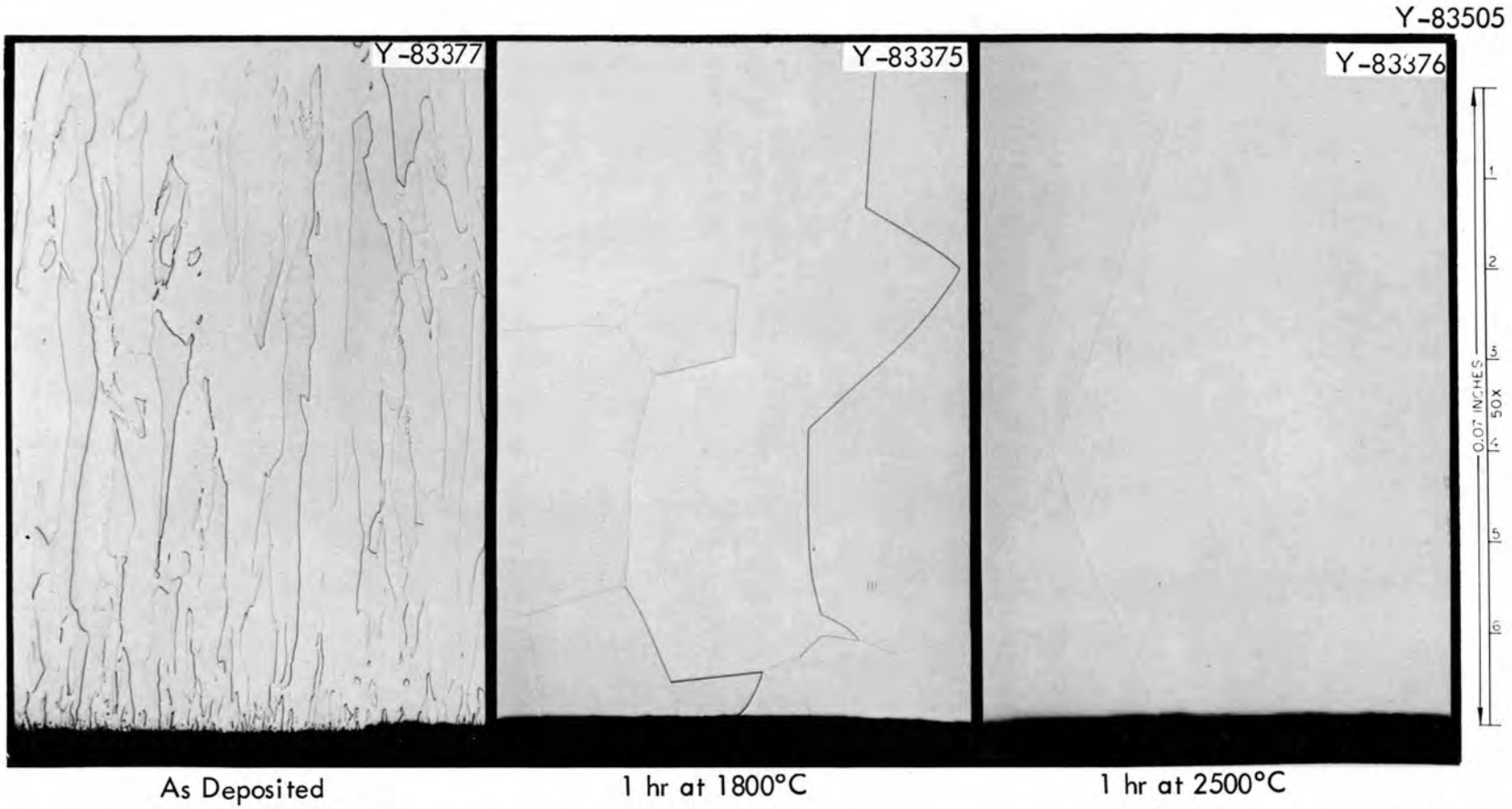

Fig. 10.6. Effect of Annealing Temperature on the Microstructure of CVD Tungsten Deposited from WCl_6 Containing 7 ppm F. Deposit SFL-GA1. Etchant: NH_4OH and H_2O_2. 13% reduction.

Table 10.1. Preferred Orientation of CVD Tungsten Deposits

Sample Number	Feed Gas	Fluorine Content (ppm)	Relative Diffraction Intensity, I_s/I_r (110)	(200)	(211)	(310)	(222)	(321)
SFL-GA1	WCl_6	7	84	1	0	0	0	2
S90-I	WF_6	30–31	0	73	0	0	0	0
S90-O	WF_6	17–20	0	90	0	0	0	0
S82-O	WF_6	4–5	0.5	15	0.5	1	0	0.5
S83-O	WF_6	< 1	2	6	1	2	0	1

11. NONDESTRUCTIVE TEST DEVELOPMENT

R. W. McClung

The purpose of this program is to improve the present methods, techniques, and apparatus for nondestructive evaluation of nuclear reactor materials and components or to develop new ones. Mechanical and electronic devices for nondestructive testing, precise calibration procedures, and reference standards are being developed.

Electromagnetic Inspection Methods (Eddy Currents)

C. V. Dodd, J. W. Luquire, W. E. Deeds, and W. G. Spoeri

We continued research and development on both analytical and empirical bases.

Analytical Studies

In our analytical research we are continuing to derive integral equations for problems of interest and are using our computer programs to generate numerical solutions directly applicable to actual eddy-current tests. A paper[1] with the following abstract was presented at the 8th Symposium on Physics and Nondestructive Testing:

> We have obtained integral representations for the vector potential produced by a circular coil for a number of different geometrical configurations. From the vector potential we can calculate any observable electromagnetic induction phenomena. Our present solutions are limited to cases with axial symmetry and linear media. The solutions are in the form of multiple integrals of ordinary and modified Bessel functions.

---

[1] C. V. Dodd, W. E. Deeds and J. W. Luquire, "Integral Solutions to Some Eddy Current Problems," paper presented at the 8th Symposium on Physics and Nondestructive Testing, Schiller Park, Illinois, September 24–26, 1968. To be published in proceedings of the meeting.

The configurations which we have already solved include coils with rectangular cross sections in the following locations: above or on each side of a two-conductor sheet bounded by parallel planes, between two parallel plane conductors, encircling a tube or a rod consisting of one metal clad on another, and inside a tube. The electromagnetic phenomena which we have calculated include the coil impedance, the phase and amplitude of the voltage induced in pickup coils, the effects of small spheroidal defects on the impedance and phase, and the forces generated in a metal by the eddy currents. The agreement between calculated and measured phenomena is excellent in most cases and within experimental error in all cases.

We have calculated and measured the voltage induced in a pickup coil by an electromagnetic wave transmitted through a conducting plate. Figure 11.1 shows variations in the calculated and measured values of the magnitude of the voltage as the plate thickness is increased. The agreement is good within the limits of experimental error.

We have modified existing ORNL computer programs to plot contours of the defect sensitivity factor[2] for various configurations of eddy-current coil and conductor. These plots are made on the cathode ray tube plotter. Figure 11.2 shows how the sensitivity to defects varies with position in a conductor for a coil above a conducting plate.

Probe Development

We have constructed several high-temperature reflection coils for use with the phase-sensitive eddy-current instrument. These probes were constructed to measure the level of liquid sodium in a stainless steel tube. The coils were wound from Teflon-coated wire, the probe was potted with high-temperature epoxy, and all joints were made with high-temperature solder. When a constant driving current is used on the portable phase-sensitive eddy-current instrument, the probe will operate from room temperature to 175°C with only minor thermal drift.

---

[2]C. V. Dodd, Fuels and Materials Development Program Quart. Progr. Rept., June 30, 1968, ORNL-4330, pp. 302–305.

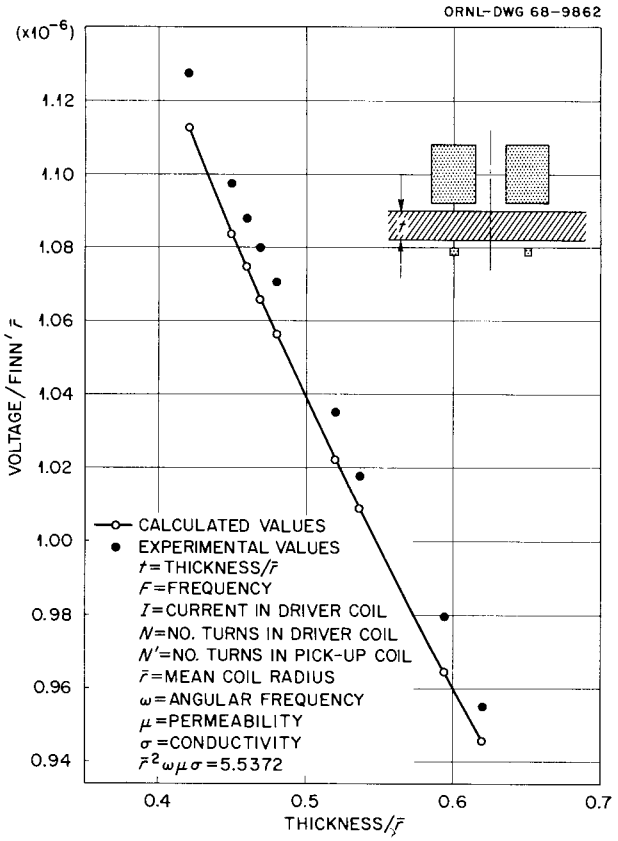

Fig. 11.1. Calculated and Measured Value of Induced Voltage in the Through-Transmission Mode as Plate Thickness Varies.

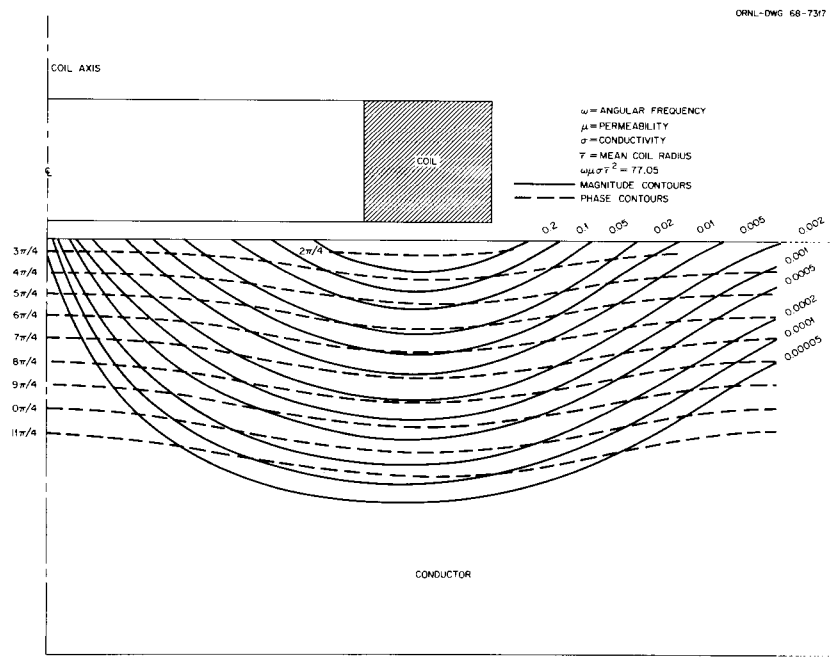

Fig. 11.2. Contours of the Defect Sensitivity Factor in a Conducting Plate.

Ultrasonic Inspection Methods

K. V. Cook and H. L. Whaley

Optical Visualization of Ultrasound

We made a brief series of observations with the recently constructed mirror schlieren system (diagrammed schematically in Fig. 11.3) to evaluate its sensitivity, stability, and ease of operation. We observed (1) interaction of pulses and continuous beams of ultrasound with metal specimens of various shapes; (2) ultrasound transmitted through the wall and into the bore of both plexiglas and metal tubing; and (3) ultrasound inside a compression-molded polystyrene block. These observations confirmed expected improvements in sensitivity, stability, resolution of detail, and ease of operation. Because of the greater sensitivity, the slight outward bowing of the glass walls of the water tank when filled (which was acceptable with the lens system) cannot be tolerated with the mirror system. A new, improved tank with 3/8-in.-thick sides of Pyrex plate glass is being fabricated to eliminate this problem.

We formulated long-range plans for applying the schlieren system to the ultrasonic inspection of welds, a nondestructive testing problem for which it has unique potential. A schlieren study of this problem will

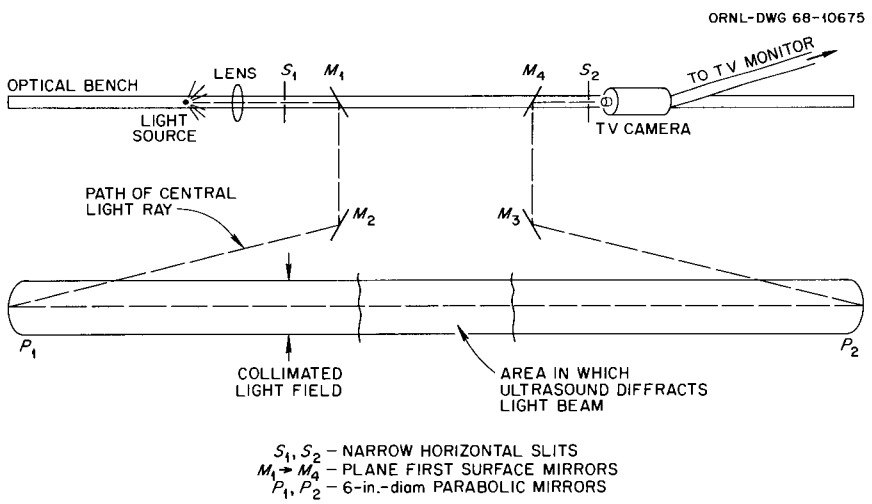

Fig. 11.3. Diagram of the Parabolic-Mirror Schlieren System for Viewing Ultrasonic Energy.

increase our knowledge of conventional testing techniques and possibly contribute to the development of new ones.

Frequency Analysis

The frequency-analysis system has been applied to investigate the spatial amplitude and frequency dependence of the energy patterns radiated from various types of ultrasonic transducers. The transducer was moved with respect to a small, fixed, spherical reflector so as to receive a reflection from the desired spot in its radiation pattern. This was equivalent to moving a point sensor from location to location in the beam pattern. When possible, small air bubbles generated on the end of hypodermic tubing were used as reflectors since they provided extremely sharp pulses for analysis. Three main types of analysis were made: (1) analysis of the spectrum at points along a line intersecting and perpendicular to the transducer axis (i.e., plots of frequency versus amplitude at discrete points); (2) scans in the same direction as in (1) but at single, fixed frequencies that produce plots of amplitude versus distance from the axis; and (3) scans along the transducer axis at single, fixed frequencies to produce curves of amplitude versus distance from the transducer. In analyses (2) and (3), the fixed frequency was chosen by inspection of the total frequency spectrum of a pulse reflected from a large, flat block. We examined the beam structures of focused and collimated as well as of flat transducers. Where a comparison could be made, the experimental results agreed quite well with the Fresnel-zone theory. Knowledge of the beam structure as a function of both frequency and intensity can tell us such things as optimum water column (transducer to specimen distance), the location of the focal point of a focused transducer, the effective size of the transducer element, the degree of symmetry of the radiation pattern, and the effective width of the ultrasound beam at any distance from the transducer. Furthermore, beam analysis can serve as a "fingerprint" of a transducer, providing a dynamic, quantitative description by which any changes can be immediately detected.

We have also used the system to study frequency effects caused by some of the important variables in ultrasonic tests. One of these is orientation of the transducer axis with respect to a reflecting surface. Figure 11.4 shows the drastic loss of higher frequencies resulting from a slight transducer misalignment. (The curves have been normalized). Figure 11.5 shows the effect of length of water column on the frequency spectrum of a pulse reflected from the surface of a large, flat plate (again, all curves have been normalized). Another variable, the effects of which we can now see and measure directly, is "tuning" or impedance matching between the transducer and the output of the ultrasonic pulser. For example, if we wish to use 5 Mhz as the test frequency, we can observe the frequency spectrum of the transducer and tune the impedance-matching network until we get the maximum response at 5 Mhz. We have also observed changes in the frequency spectrum of a pulse reflected in turn from various sizes of artificial discontinuities in a metal plate (flat-bottomed drilled holes), but background noise must be reduced to obtain better reproducibility.

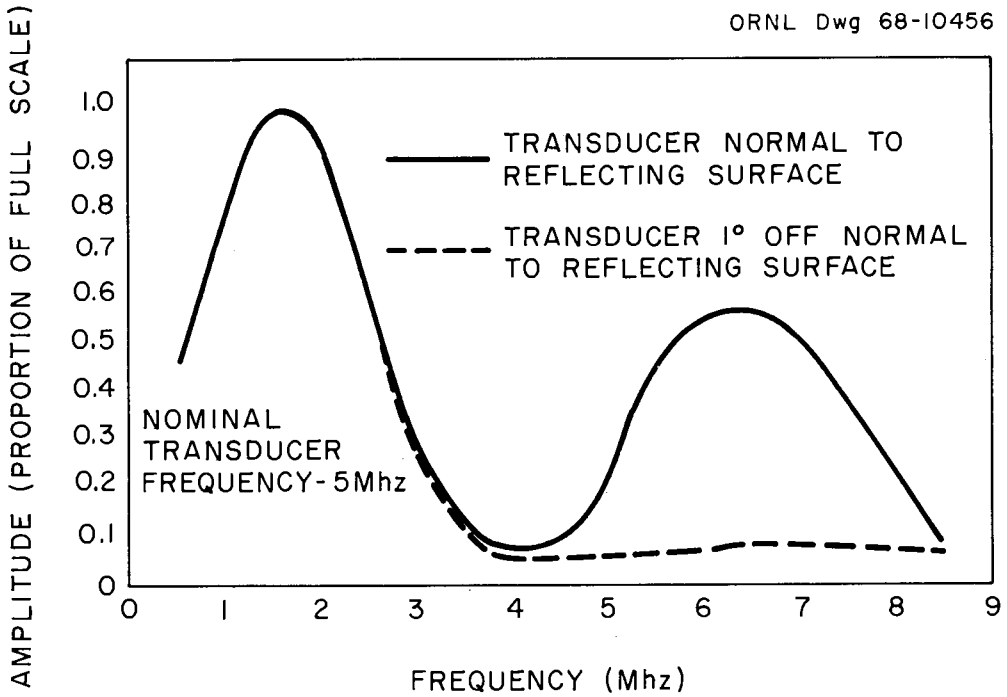

Fig. 11.4. Frequency Spectra Changes Due to Misalignment of Ultrasonic Beam 1° from Normal.

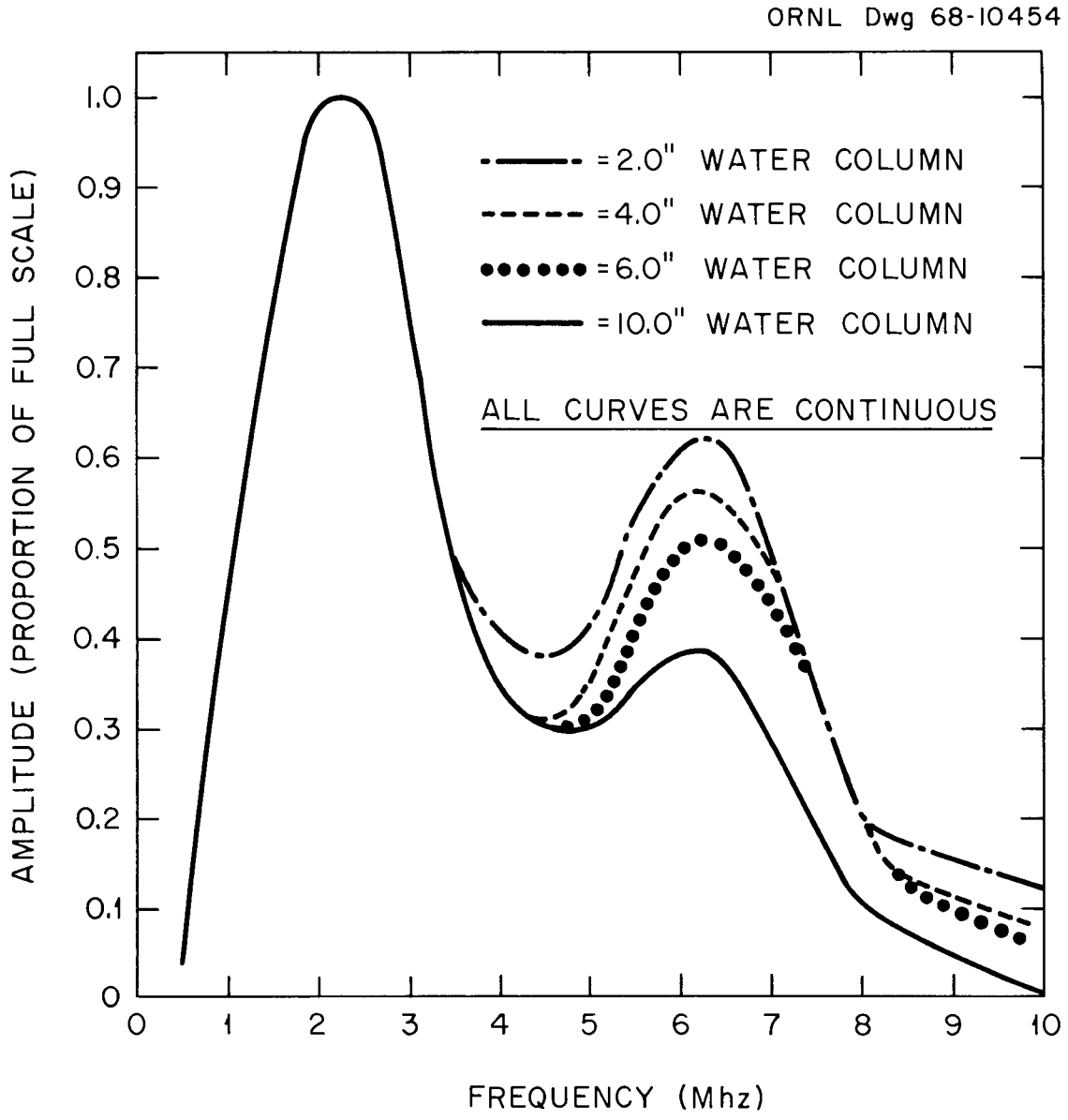

Fig. 11.5. Frequency Spectra Changes Due to Increasing Water Column Between Ultrasonic Transducer and Specimen.

12. JOINING RESEARCH ON NUCLEAR MATERIALS

G. M. Slaughter

The purpose of this program is to gather fundamental and applied data needed for a better understanding of the weldability of materials that are either being considered or currently used for nuclear applications. The fundamental aspects of the program are concerned with the effects of minor variations in amount and type of alloying elements and impurities on the behavior of weldments. Specific alloys of interest include the austenitic stainless steels and the nickel-rich alloys such as Incoloy 800 and Inconel 600. Our applied studies emphasize the application of stainless steels in the Fast Flux Test Facility (FFTF). These project-oriented investigations will help define the influence of welding process, parameters, and postweld treatments on the microstructure and mechanical properties of irradiated and unirradiated weldments. A modest program concerned with the influence of weld defects will provide base-line results in this much-talked-about but little-investigated field.

We hope this broad-based program will develop the modifications in both chemical analysis and procedures necessary to produce the high-quality weldments needed for the various programs of the Commission. These data will be immediately and directly applicable to such components as the Fast Test Reactor vessel by providing the capability to predict the effects of chemical composition and welding procedure on overall welding behavior.

The Effect of Minor Variations in Chemical Composition on Weldability

In our continuing investigation of the effect of small variations in the minor elements usually present in structural materials, we have emphasized Al, Ti, S, and P in Incoloy 800, and S in Inconel 600. This work has been reported previously and is continuing.

Subcontract work at Rensselaer Polytechnic Institute has investigated the effects of minor elements on the hot cracking of Inconel 600. At ORNL, we have begun work on the effect of minor variations of chemical composition on the weldability of austenitic stainless steels.

The Effect of Minor Elements on the Hot-Cracking Tendencies of Inconel 600 (G. M. Goodwin, W. F. Savage[1])

This investigation was undertaken to determine the effect of six minor elements (S, P, Si, Mn, Ti, and Al) on the hot-cracking propensity of Inconel, a solid-solution-strengthened nickel-base alloy.

In order to determine the effects of these six elements, we developed a new test for evaluating weldability, the "TIGAMAJIG" test. An outgrowth of the VARESTRAINT test, the TIGAMAJIG test combines the advantages of its predecessor with reduced specimen size and ease of specimen preparation. A technique was developed that allows preparing a large number of specimens of systematically varied composition by incorporating compacted and sintered powder inserts that contain the desired "impurity" additions.

We performed a full factorial experiment, using all of the 64 possible combinations of the six elements. The entire testing program was replicated at two levels of augmented strain, thereby providing an accurate estimate of error.

Using the method of Yates[2] and the analysis of variance, we determined the significant effects of the six minor elements for three cracking parameters: the total, maximum, and average crack length.

We also found that some of the minor elements had significant effects on the cross-sectional area and depth of penetration into the weld pads into which the powder inserts had been incorporated. We postulated that this resulted from the effect of these elements on the

---

[1]W. F. Savage, Dept. of Materials Engineering, Rensselaer Polytechnic Institute, Troy, New York; G. M. Goodwin, formerly of Rensselaer, now a member of the staff of ORNL.

[2]F. Yates, Design and Analysis of Factorial Experiments, Imperial Bureau of Soil Science, London, 1937.

potential drop, E_a, at the anode. In general, it appeared that those elements that have a low value of the work function, ϕ, on a high ratio of secondary electron emission, θ, could increase E_a due to a change in the size of the negative space charge near the anode. The subsequent increase in kinetic energy of the incident electrons would then result in increased penetration and a greater cross-sectional area.

Cross sections of each of the weld pads are shown in Fig. 12.1. The welds were prepared under identical welding conditions (current, voltage, travel speed, etc.), and as may be seen from the figure, wide variations in depth of penetration and cross-sectional area result. Note that none of the intentional "impurity" additions exceeded the commercial specifications for Inconel 600. The advantage of using a precise mathematical analysis of the data, such as the method of Yates, and the

Fig. 12.1. Weld Penetration Studies in Inconel Welds. Only minor variations in base-metal analysis produced widely varying weld-zone geometries and depths. (Rensselaer Polytechnic Institute figure).

analysis of variance is also obvious from Fig. 12.1: it is extremely difficult to draw reasonable conclusions about the effects and interaction effects of the various elements merely from visual observation of the cross sections. A statistical analysis of the data shows that Si, Ti, and P increase the cross-sectional area and depth of penetration, while Al decreases both these parameters. Strong interaction effects exist between S and Si and between Ti and Al.

We found S and P to be highly detrimental to all three of the cracking parameters. We attribute this to a high degree of segregation and the subsequent reduction in the effective solidus and liquidus, coupled with a decrease in the solid-liquid interfacial energy that permits wetting of the grain and subgrain boundaries and the subsequent formation of grain-boundary films.

We found that both Mn and Si reduced the detrimental effect of S, due in part at least to an increase in the solid-liquid interfacial energy. However, a significant Si-Mn interaction effect indicated that these two elements, when present together, were not as effective in reducing the effect of S as was either one alone.

We also found that Ti and Al reduced the hot-cracking propensity of Inconel. We believe that the effect of Ti and Al and, in part, the effect of Mn and Si was due to the excellent deoxidizing capabilities of these four elements.

We showed that such large-scale factorial experiments could be used successfully to identify the significant effects of minor elements on the hot-cracking propensity of Inconel and therefore proposed that this technique be applied to study other minor elements and other alloy systems.

Weldability of 18% Cr–8% Ni Class Stainless Steels (W. J. Werner, D. A. Canonico)

We have expanded the program on the weldability of nickel-base alloys to include the effects of minor variations in composition on the weldability of the 18% Cr–8% Ni class of steels. As a general rule, alloys of this class are welded with a type 308 or 308L stainless steel filler

wire. Hot cracking is controlled by the delta ferrite content of the weld metal, and most welding filler wires of this class are specified to contain a certain percentage of delta ferrite in accordance with the Schaeffler diagram.[3] This is achieved through rigid control of composition during processing. Canonico and Martin,[4] however, showed that both the delta ferrite content and the strength of a weldment can be markedly influenced by heat input during welding. The purpose of this phase of our program is to gain additional insight into the interrelationship of composition, welding procedure, and weldability.

We are preparing the series of alloys shown in Table 12.1. Included in the table for reference purposes are the ASTM specification limits for type 308L alloys; these are designed to delineate the possible limits of ferrite composition in the weld metal. Figure 12.2 shows their approximate positions on the Schaeffler diagram. After arc melting and

[3]A. L. Schaeffler, Welding J. 26(10) 601-s–620-s (1947).

[4]D. A. Canonico and W. R. Martin, Metals and Ceramics Div. Ann. Progr. Rept. June 30, 1967, ORNL-4170, pp. 139–141.

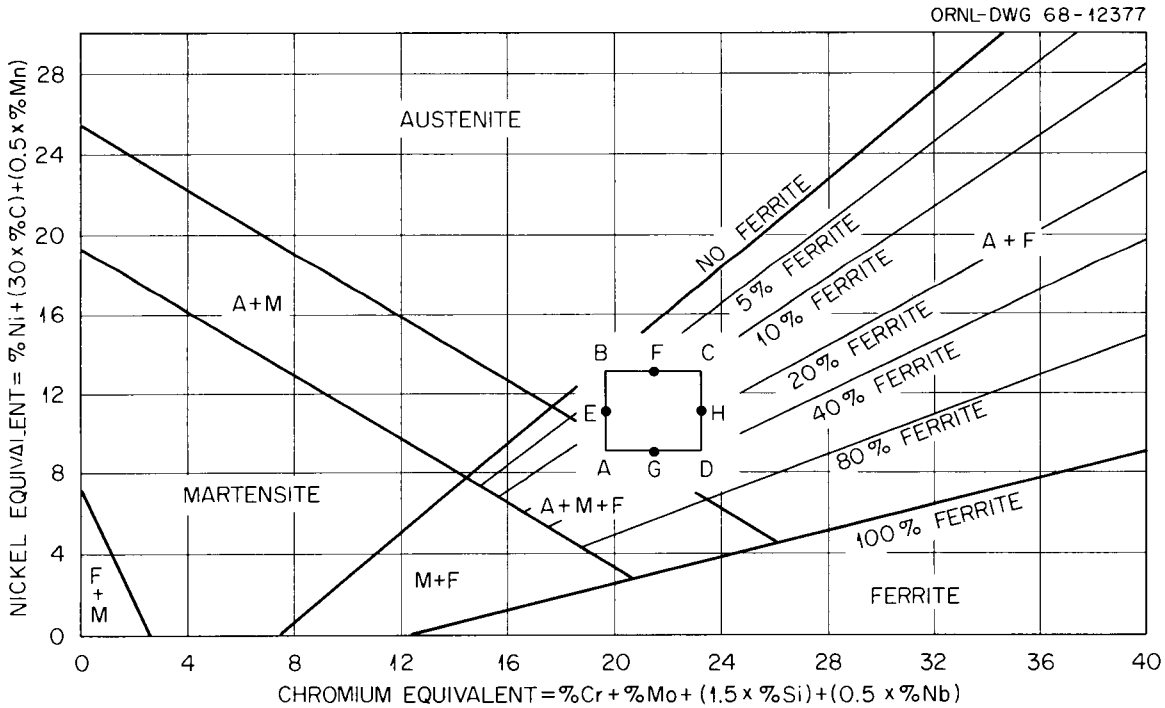

Fig. 12.2. Positions of Experimental Alloys on the Schaeffler Diagram.

Table 12.1. Compositions of Special Type 308L Stainless Steel Alloys for Weldability Studies

Alloy Designation	Composition, wt %							
	Cr	Ni	Mn	Si	C	Mo	S	P
A	19.5	9	a	a	a	a	a	a
B	19.5	11	2.5	a	0.03	a	a	a
C	22	11	2.5	0.60	0.03	0.25	a	a
D	22	9	a	0.60	a	0.25	a	a
E	19.5	9	a	a	0.03	a	a	a
F	19.5	11	2.5	0.60	0.03	a	a	a
G	19.5	9	a	0.60	a	a	a	a
H	22	9	a	0.60	0.03	0.25	a	a
ASTM Specifications	19.5–22	9–11	1.0–2.5	0.25–0.60	0.03[b]	a	0.03[b]	0.03[b]

[a]Nominally zero.

[b]Maximum.

drop casting into water-cooled copper molds, the resulting ingots (3/8 in. × 1 in. × 6 in.) will be hot rolled to 1/8-in. plate.

Initial studies will be aimed toward determining the ferrite contents as a function of heat input in bead-on-plate welds made by the gas tungsten-arc process.

Development of Welding Procedures for Commercial and Modified Alloys

Joining Development in Support of Fast Flux Test Facility (G. M. Goodwin, G. M. Slaughter)

We have begun our efforts with a special emphasis on the joining development required in support of the FFTF pressure vessel. This vessel is to be fabricated from relatively thick-walled type 304 stainless steel. There appears to be a dearth of information regarding the

properties of stainless steel weldments at elevated temperatures both in the irradiated and unirradiated condition, and the optimum welding process for joining the vessel components remains unknown. We are supplying PNL with machined specimens of welds for their irradiation studies of the effects of welding process and composition of filler metal on stainless steel weldments. We are also questioning vendors to determine industrial experience in the welding of large stainless steel vessels and have under way a program to fill in weldability data in those particular areas where basic information is most needed.

The 1500-amp Linde submerged-arc welder has been put into operation, and its range of welding parameters has been determined. The unit has been set up to produce a 4-ft butt weld in the 1-in.-thick plate of type 304 stainless steel to be supplied by PNL. We are also installing equipment to deposit butt welds by the gas-shielded arc processes. Production will begin as soon as the process/filler wire combinations to be used are determined. To this end, a meeting of representatives from ORNL, PNL, and RDT has been arranged for October 1 and 2.

We have discussed with Combustion Engineering, Inc., and with Babcock and Wilcox Company the welding procedures that might typically be used by potential fabricators of FFTF vessels.

At Combustion Engineering, we discussed in detail several specific processes — including submerged-arc, gas-metal arc, gas-tungsten arc, and manual-metal arc — with regard to their applicability to several combinations of base metal and filler wire. The bulk of their experience in welding stainless steel has been with submerged-arc overlays on carbon and low-alloy steels. For this and other reasons, they would prefer to use the submerged-arc process for fabricating heavy-walled stainless steel vessels.

Combustion Engineering noted that they have had little experience with the 16 wt % Cr–8 wt % Ni–2 wt % Mo filler wire that has been proposed as a filler material for the FFTF vessel except in instances when the customer specifically requested it. Personnel at their Research and Development Laboratory were especially concerned that so little is known about the mechanical properties of austenitic weld metal in the creep range (480°C and above). This is particularly important

since some suppliers of wire begin with rod stock in which trace elements vary widely and in which there is often poor control of residuals and deoxidizers.

On the other hand, there has been considerable experience at Babcock and Wilcox with the 16 wt % Cr–8 wt % Ni–2 wt % Mo filler material. They developed it and have used it on a variety of stainless steels. They indicated that the creep-rupture properties of this material are superior to those of other stainless steel weld metals. Although the submerged-arc process would probably be their first choice for fabricating the FFTF vessel, they noted that the electroslag welding process has been qualified for austenitic stainless steels. Thus, they would not eliminate it as a possibility for use.

The Effects of Defects on Mechanical Properties of Weldments

C. D. Lunden[5]

This task was also begun this quarter. It is established that discontinuities exist in weldments, and some cursory work has been done to characterize both the discontinuities and their effects. For example, the ASME Boiler Code, Sections 3 and 9, permits a maximum size indication in the base metal and weld metal. Furthermore, the tools for determining the presence of indications are such that, through their own limitations, they permit the acceptance of discontinuities of a given size. Since a 2% resolution is considered acceptable in radiography, one of the most commonly used nondestructive inspection tools, a discontinuity of something less than this could be present in all welded structures examined by radiography and yet be undetected.

We want to determine when a discontinuity becomes a flaw. We intend to characterize various discontinuities and establish their effects on

[5]Consultant from the University of Tennessee Department of Chemical and Metallurgical Engineering.

the mechanical properties of the materials being joined. From a fracture-mechanics point of view, we know that a discontinuity size that is acceptable in a low-alloy steel can lead to a catastrophic failure in an ultra high-strength steel. Hence, not only must one consider the discontinuity size per se, but he must relate this to the material and to the service conditions to which that material will be exposed.

The initial stages of our investigation have been aimed at producing discontinuities typical of those found in actual weldments. These must be capable of being reproduced with a reasonable certainty and must be detectable by nondestructive testing methods. Also, the defect orientation or shape must be capable of being altered with regard to the specimen geometry. Last, the mechanical testing method for evaluating the effects of the discontinuities must be considered with regard to the expected service conditions.

We successfully produced discontinuities in Inconel 600 by the electron-beam welding process and an overlapping weld pass technique. Sixteen overlapping full-penetration weld passes have been made with the electron beam at right angles to the sheet surface. The resultant fused zone is about 1/4 in. long, and the discontinuities lie with their long axis in the plane of the sheet in the fusion and heat-affected zones. Figure 12.3, a photomicrograph of a cross section of such a weld in Inconel 600, shows some typical discontinuities. Specimens that will

Fig. 12.3. Inconel-600 Weld with Discontinuities Having Long Axes in Plane of Sheet. Etchant: glyceria regia. 26×.

be machined from these welds will be ultrasonically tested to locate accurately the discontinuities and then mechanically tested to determine the effects of the discontinuities. The orientation of the discontinuities with respect to the sheet surface can be altered by changing the angle of impingement of the electron beam. A cross section of a weld made with the electron beam oriented at 45° to the sheet surface is shown in Fig. 12.4; the discontinuity is oriented at an angle of 45° to the sheet surface. Thus, by varying the beam angle, we can, it appears, vary the defect orientation to suit the testing procedure.

Further studies have been undertaken with a scanning electron microscope to characterize discontinuities by direct observation of the surface of the discontinuity. This procedure promises to define more clearly the type of discontinuities being produced. A scanning electron micrograph of the surface of a hot crack (discontinuity) in nickel is shown in Fig. 12.5. It is evident by the appearance of the cellular dendritic structure that a liquid film existed at the time the discontinuity was formed; note the rounded, featureless surface of the fractured cellular dendrites.

Fig. 12.4. Inconel-600 Weld with Discontinuities Oriented at 45° to the Sheet Surface. Etchant: glyceria regia. 26X.

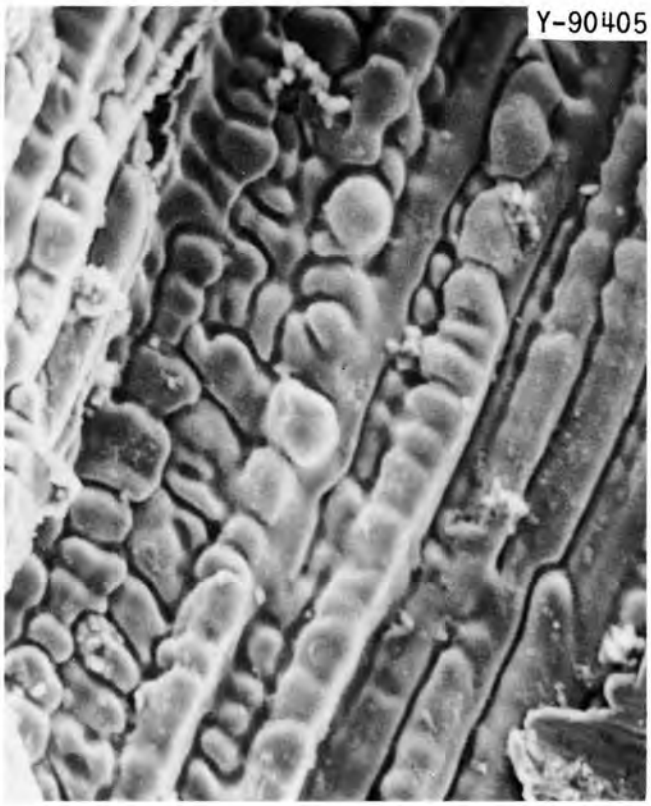

Fig. 12.5. Scanning Electron Micrograph of the Surface of a Hot Crack in Nickel. The cellular dendritic structure indicates that a liquid film existed at the time the crack was formed. Etchant: glyceria regia. 1000×.

13. FUEL ELEMENT FABRICATION DEVELOPMENT

G. M. Adamson, Jr.

The purpose of this program is to devise new combinations of materials or new fabrication techniques to advance the technology for fabricating fuel elements for research reactors. We are attempting to improve the performance of advanced research reactors, such as HFIR and ATR, by developing fuel elements with lower production costs, longer lives, increased safety or reliability, or all three. The studies include factors affecting both fabrication and irradiation performance. We must also develop sufficient knowledge of the processes used for fabricating aluminum-based dispersion fuel elements so that we can adequately assist commercial fabricators, purchasers, specification writers, and technical inspectors. Other studies are aimed at improving the reliability and reducing the cost of the required nondestructive inspection techniques. Because of the overlapping nature of the programs, this section includes some work supported by the AEC Technical Assistance Program.

Irradiation Studies of Dispersion Plates

M. M. Martin, J. H. Erwin, A. E. Richt
W. R. Martin K. V. Cook

We have finished fabricating both sample and instrumented miniature fuel plates[1] for the G-12 loop experiment in ETR cycles 99 and 100. The effect of powder fines on the performance of burned and hi-fired U_3O_8 fuels will be investigated in this two-cycle experiment. The plates for irradiation, as well as the standby plates, are described in Table 13.1. Two levels of fuel loading are given: 0-67 and 0-68 compositions. The lower U_3O_8 concentration compares to that of HFIR, while the upper represents a 25% increase.

---

[1]M. M. Martin, W. J. Werner, and C. F. Leitten, Jr., Fabrication of Aluminum-Base Irradiation Test Plates, ORNL-TM-1377 (February 1966).

Table 13.1. Miniature Test Plates for ETR G-12 Loop Irradiations in Cycles 99 and 100

Plate Reference Number	Fuel Dispersoid[a]			Location in G-12 Loop	
	Powder Blend Designation	Core Concentration (wt %)	Loading of ^{235}U (g)	Tier	Slot
	Burned U_3O_8 Test Plates				
0-68-1622	PB5	49.28	2.448	3	1[b]
0-68-997	PB4	49.28	2.456	3	2
0-68-1605	PB5	49.28	2.451	3	3
0-68-1607	PB6	49.28	2.462	3	4
	Hi-Fired U_3O_8 Test Plates				
0-67-1617	PB2	40.21	1.944	4	1[b]
0-67-974	PB1	40.21	1.947	4	2
0-67-982	PB2	40.21	1.957	4	3
0-67-986	PB3	40.21	1.949	4	4
	Burned U_3O_8 Standby Plates				
0-68-1621	PB5	49.28	2.450	3	1[b]
0-68-1600	PB4	49.28	2.456	3	2
0-68-1602	PB5	49.28	2.454	3	3
0-68-1608	PB6	49.28	2.463	3	4
	Hi-Fired U_3O_8 Standby Plates				
0-67-1616	PB2	40.21	1.947	4	1[b]
0-67-976	PB1	40.21	1.944	4	2
0-67-979	PB2	40.21	1.957	4	3
0-67-984	PB3	40.21	1.948	4	4

[a] Alcoa 101 aluminum matrix.

[b] Instrumented plate.

Characteristics of the two grades of U_3O_8 used in fabricating the plates are tabulated in Table 13.2. The hi-fired and burned oxides are comparable to the previously irradiated fuels that contained 3 wt % powder fines of −325 mesh. The levels of fines in the various powder fuel blends (PB1–PB6) are 10, 25, and 50 wt %. The lower limit corresponds to the present maximum permissible content for HFIR, while the upper represents the normal yield in manufacturing the oxides.

Table 13.2. Characterization of Fuel Core Components

	Hi-Fired U_3O_8 (Batches 30-2602 and 30-2616)			Burned U_3O_8 (Batch 30-2615)			Matrix Aluminum
Powder blend designation	PB1	PB2	PB3	PB4	PB5	PB6	
Uranium, wt %	84.54	84.23	84.48	84.28	84.39	84.14	
^{235}U in uranium, wt %	93.20	93.16	93.23	93.16	93.16	93.16	
Toluene density, g/cm^3	8.221	8.247	8.258	7.641	7.647	7.653	2.719
Surface area, m^2/g	0.050	0.064	0.066	0.341	0.382	0.352	0.195
Sieve analysis, wt %							
+140	0.0	0.0	0.0	0.0	0.0	0.0	0.0
−140 +170	0.2	0.2	0.1	0.0	0.0	0.0	0.0
−170 +200	23.9	19.9	13.4	23.0	19.7	3.8	0.1
−200 +230	22.5	18.2	9.9	22.3	17.5	19.6	0.2
−230 +270	24.4	20.3	12.8	21.5	17.6	10.8	2.2
−270 +325	19.1	16.0	13.1	22.3	19.0	12.0	9.2
−325 + dust	9.9	25.4	50.7	10.9	26.2	53.8	88.3

The fabrication of the miniature test plates did not proceed smoothly. For example, to promote bonding, the cover plates and frames of type 6061 aluminum are pickled in an "Oakite" solution immediately before the billet assembly and rolling operations. As indicated in Table 13.3, five plates from each of the two fuel compositions were rejected for nonbonds detected visually. We believe that these nonbonds resulted from overuse and consequent exhaustion of the cleaning baths. Cladding components prepared from fresh solutions bonded adequately.

In addition to the visual examination, the plates were ultrasonically evaluated for nonbond by through-transmission techniques. Due to the irradiation schedule, new standards were not developed. However, approximation references were a HFIR standard containing 1/16-, 3/32-, and 1/8-in.-diam flat-bottom holes for the sample plates and a piece of type 6061 aluminum for the instrumented plates. These references serve only as good approximations, for plates with different types of cores can have different attenuation properties. We found higher and more variable attenuation in plates containing the burned U_3O_8. With

Table 13.3. Summary of Fuel Plate Yield[a]

Inspections	Composition			
	0-67		0-68	
	Number Rejected	Percentage	Number Rejected	Percentage
Plate dimensions	1	4	2	8
Core dimensions	2	8	1	4
Core location	3	12	2	8
Visually detected nonbonds	5	20	5	20
Ultrasonically detected nonbonds	0	0	3	12
Uranium homogeneity[b]	1	4	0	0
TOTAL REJECTED	12	48	13	52

[a]Total of 25 plates of each composition.

[b]Spot indication of 0.005 $in.^2$ greater than 25% above nominal loading.

hi-fired U_3O_8, the 25 and 50% levels of powder fines also appear to increase the attenuation.

The results of the ultrasonic inspection are summarized in Table 13.4. For insertion into the G-12 loop experiment, the plates must exhibit less attenuation of ultrasound than that from the reference, the 1/8-in.-diam flat-bottom hole. All of the sample and instrumented plates that contained hi-fired U_3O_8 passed the test for 3/32-in.-diam defect nonbonds. The failure of the plates at calibrations of 1/16-, 3/32-, and/or 1/8-in.-diam indications may be associated with the type of U_3O_8 and level of fuel powder fines. We note that burned U_3O_8 copiously fragments during plate fabrication. Fragmentation should produce higher and more variable attenuation of ultrasound and increase the spurious rejection rate through reduced nonbond detection sensitivity. We shall examine this more thoroughly.

The rolled density, densification during rolling, and fabrication voids of the fuel core in the sample plates appear to be independent of the initial fines content of the U_3O_8. Average values for these parameters are presented in Table 13.5. One can note that the void volumes

Table 13.4. Results of Ultrasonic Inspection

Type of Plate	Fuel Powder Fines (wt %)	Number Inspected	Number Failing Test, References[a] (in.) 1/16	3/32	1/8
		Hi-Fired U_3O_8			
Instrumented	25	5	0	0	b
Sample	10	5	0	b	b
Sample	25	5	2	0	b
Sample	50	5	5	0	b
		Burned U_3O_8			
Instrumented	25	4	4	b	0
Sample	10	5	5	5	3
Sample	25	5	5	5	0
Sample	50	4	4	4	0

[a]Diameters of flat-bottomed reference holes for calibration.

[b]Does not apply.

Table 13.5. Fines Content, Voids, and Density of the Core in Sample Plates Containing Hi-Fired and Burned U_3O_8

Number of Plates	Fines Content of U_3O_8 Powder (wt %)	Concentration (vol %) U_3O_8	Fabrication Voids	Density Core (g/cm^2)	Change During Rolling (%)
		Hi-Fired U_3O_8			
5	9.9	17.56	3.29	3.5992	2.75
5	25.4	17.60	3.05	3.6081	2.91
5	50.7	17.60	3.03	3.6089	2.89
	Average	17.59	3.12	3.6054	2.85
		Burned U_3O_8			
5	10.9	23.62	8.00	3.6652	3.58
5	26.2	23.61	8.06	3.6634	2.89
4	53.8	23.54	8.30	3.6536	3.18
	Average	23.59	8.11	3.6612	3.22

of plates containing burned U_3O_8 are considerably higher than those of the hi-fired U_3O_8. We conclude, considering void volume alone, that the plates containing burned U_3O_8 should exhibit superior irradiation performance.

We shipped the test and standby plates for ETR cycles 99 and 100 in early September. As in previous G-12 irradiation experiments, the loop for these irradiations will be shared with Idaho Nuclear Corporation. The personnel there will also supervise the running of the loop, insertion and removal of the plates, and return of the plates to ORNL for postirradiation examination.

The test plates irradiated in ETR cycles 93, 94, and 96 arrived at ORNL September 27. These plates are scheduled for immediate postirradiation examination.

Fabrication of Fuel Plates

W. R. Martin

Investigations of Nonuniform Deformation in Simulated Fuel Plates (J. H. Erwin, W. R. Martin)

We are studying models of why nonuniform deformation (dogboning) occurs in fuel plates. We think the basic causes are the differences in compressive strengths of the fuel core, frame, and cladding material, and the force distribution along the deformation zone while the core-frame interface is being deformed. It is this force distribution that we now believe can explain dogboning on the leading and trailing edges of composite fuel plates and that predicts the variations in shape noted for the frame, coverplate, and core. We are attempting to install numerous microstrain gages within simulated fuel plates to determine the force distribution during the rolling of composite plates.

Study of the Fit of Fuel Compact to Frame Cavity (J. H. Erwin, M. M. Martin)

Aluminum-base fuel plates for research reactors are usually produced by the roll bonding of cored and clad picture frames. Before rolling the compacts, our practice is to vacuum degas the fuel compacts

to remove adsorbed gases and pressing lubricants. If inconsistent dimensional changes occur during heat treatment, the fit between the compact and frame cavity may be altered unless tailored parts are used. We are investigating the effects of various dimensional misfits on final plate quality and fabrication parameters.

In the investigation, we fabricated 68 dispersion fuel plates, using the fuel compact dimensions for the HFIR outer annulus. No fuel gradient was used, however. Thirty-four compacts of hi-fired U_3O_8 dispersed in Al and an equal number of arc-cast hypostoichiometric UAl_3 in Al were clad with alloy 6061. Each compact contained 37 g U depleted in ^{235}U. Average attributes of the degassed compacts are recorded in Table 13.6.

Table 13.6. Record of Compacts Fabricated for Study of Fit of Compact to Frame Cavity

	Average Attributes of Compacts[a]	
Materials		
Dispersoid	Hi-fired U_3O_8	Hypostoichiometric UAl_3
Matrix aluminum	101	101
Degassed composition		
Dispersoid, %		
By weight	45.99	52.48
By volume	20.7	27.9
Voids, vol %		
Estimate of standard deviation	0.158	0.279
Degassed physical properties		
Weight, g	93.788	94.271
Density, g/cm^3	3.7254	3.7061
Dimensions, in.		
Width	2.6467	2.6587
Length	2.1691	2.1799
Thickness	0.2676	0.2678
Changes from degassing operation		
Dimensions, mils		
Width	+2.0	+14.6
Length	+1.1	+11.4
Thickness	+1.3	+4.5
Weight, mg	−30	+2
Density, %	−0.631	±2.719
Estimate of standard deviation	0.112	0.218

[a]Compacts degassed for 1 hr at 500°C, pressed at 30 tsi.

The dimensions of the rectangular parallelepiped compacts are given in Table 13.6. The frames were machined to the following differential differences between the cavity and the degassed dispersions: (1) length differences of +1, −0.5, and −4%; (2) width differences of +1, −0.5, and and −4%; and (3) thickness differences of +5, 0, and −5%. When we changed one of the three dimensional variables, the other two matched the standard dimensions of the frame cavity. All cover plates were 0.108 in. thick, and all frames were 0.265 in. thick except those used for the differential thickness variables.

After being rolled to a total reduction in thickness of 89.60%, the fuel plates were inspected for (1) visual and ultrasonic indications of nonbonds, (2) fuel-core dimensions, and (3) x-ray attenuation indications of excessive fuel concentrations near the core ends. We interpret the latter inspection as an indication of dogboning.

Surprisingly, no plate exhibited a blister or ultrasonic nonbond that could be attributed to the misfit between the frame cavity and compact. In fact, only one blister developed, and it was located at the core end in a UAl_3-bearing plate in which the experimental variables matched the dimensions of the frame cavity and fuel compact. We conclude that within the range investigated blistering in these plates is independent of the degree of fit between the frame cavity and fuel compact.

The x-ray attenuation measurements indicated little fuel-core thickening (dogboning) near the ends of the rolled dispersions. As shown in Table 13.7, the values for plates containing U_3O_8 were consistently less than 15%; one UAl_3-bearing plate exhibited dogboning greater than 30%. The degree of core thickening, however, does appear to decrease with decreasing fit ratio of compact to cavity. In comparison to ATR plate 19, which usually shows severe dogboning, perhaps the relatively thin cover plates (0.011 in.) over our cores may account for the limited amount of thickening indicated. We are studying the effect of the ratio of cover-plate thickness to frame thickness on special ATR fuel plates.

Table 13.7. Effect of Fit of Compact to Cavity Upon the Degree of Core Thickening in U_3O_8- and UAl_x-Bearing Fuel Plates

Variable		Degree of Core Thickening,[a] %	
Changed Dimension	Fit Ratio, Compact/Cavity	45 wt % U_3O_8-Al Cores	52 wt % UAl_x-Al Cores
Thickness	1.050	0	22
	0.000	b	18
	0.950	b	15
Length	1.010	15	25
	0.995	b	18
	0.960	b	0
Width	1.010	b	35
	0.995	b	<15
	0.960	b	0

[a]Based on x-ray attenuation measurements.

[b]Dogboning was always less than 10 to 15%, and exact numbers were not determined.

The spread of the fuel core during rolling did depend on the degree of fit between the fuel compact and frame cavity:

$$S = \frac{W_2 - W_1}{W_2} 100 , \qquad (13.1)$$

where

S = spread, %,

W = width of fuel compact, in.

Subscripts 1 and 2 indicate the degassed and rolled values, respectively. The elongation of the core during rolling is defined similarly. Table 13.8 shows typical values for spread and elongation as a function of the various fit variables. Decreases in core thickness result in a decrease in plate width and little change in length; a decrease in core width and core length has little effect on the opposite dimension; but the spread increases with decreasing width, while the elongation shows

Table 13.8. Effect of Fit of Fuel Compact to Frame Cavity Upon the Spread and Elongation of U_3O_8- and UAl_x-Bearing Fuel Plates After Rolling[a]

Variable		45 wt % U_3O_8-Al Cores				52 wt % UAl_x-Al Cores			
Changed Dimension	Fit Ratio, Compact/Cavity	Length (in.)	Width (in.)	Spread (%)	Elongation (in.)	Length (in.)	Width (in.)	Spread (%)	Elongation (in.)
Thickness	1.050	20.21	2.751	3.78	89.27	19.91	2.754	3.45	89.05
	0.000	20.08	2.735	3.22	89.20	19.85	2.760	3.66	89.02
	0.950	20.11	2.717	2.58	89.21	20.05	2.715	2.06	89.13
Length	1.010	20.02	2.751	3.78	89.17	19.79	2.753	3.41	88.98
	0.995	20.40	2.734	3.18	89.37	19.89	2.746	3.17	89.04
	0.980	20.34	2.735	3.22	89.34	20.00	2.748	3.24	89.10
	0.960	20.45	2.734	3.18	89.39	20.18	2.749	3.28	89.20
Width	1.010	20.18	2.738	3.33	89.25	20.06	2.740	2.96	89.13
	0.995	20.15	2.758	4.02	89.24	19.84	2.765	3.75	89.01
	0.980	20.22	2.778	4.72	89.27	19.82	2.777	4.25	89.00
	0.960	19.83	2.823	6.23	89.06	19.72	2.809	5.34	88.95

[a]All plates were hot rolled to 0.0625 in. and then annealed and cold reduced to 0.050 in.

little effect from core length variations. As expected from consideration of the volume of matrix available for deformation, the U_3O_8-Al compacts widen and elongate slightly more than the UAl_3-Al dispersions of similar uranium content. Flaking of fuel particles beyond the core ends, which were essentially square, was not observed in radiographs of the plates. Two of the U_3O_8-bearing plates, however, showed flash or fuel tapering about 0.19 in. long at the core ends. The flash in the remainder of the U_3O_8 and all of the UAl_x fuel plates was less than 0.06 in. long.

This study did not show the blister problem to be singularly dependent upon the misfit between compact and frame. Misfit did affect the degree of core spreading during rolling. Dogboning was less for plates containing U_3O_8 than for plates containing UAl_x and appeared to depend somewhat upon the misfit. But the magnitude of dogboning in both types of plate was low and may have been due to the relative thinness of the cladding compared to the thickness of the core.

Grinding and Crushing of UAl_x Fuel (G. L. Copeland, M. M. Martin)

A major problem in the preparation of UAl_x particles is the crushing of the arc-melted buttons to particles of usable size without excessive production of particles below the 325 mesh size. Present ATR specifications require −100 mesh particles with a maximum of 25 wt % being −325 mesh. While plates may be satisfactorily fabricated with larger amounts of fines, the irradiation behavior of plates with such particle distributions is unknown.

We prepared hypostoichiometric (75 wt % U) and hyperstoichiometric (68 wt % U) UAl_3 for fabrication studies. Crushing devices such as jaw crushers, rod mills, hammer mills, disk crushers, mullers, and diamond mortar and pestles generally yield about 50% fines (−325 mesh) in the −100 mesh product. We investigated several alternate methods of crushing in an attempt to improve the yield of material in the usable size range. The arc-cast material was rough crushed to about 10 mesh for the following experiments. A sample of each composition was annealed to improve the homogeneity.

Roll Crusher. — The roll crusher should be ideal for minimizing fines, for material finer than the roll spacing should fall through unhindered if the feed rate is relatively slow. The crusher is very fast and easily set up for automatic feeding, screening, etc., for production use. Our roll crusher has 12-in.-diam rolls that are spring loaded so that the rolls are not damaged if large, tough chunks are accidentally fed through. This crusher is normally operated in an inert atmosphere, but it is now operating in air. Therefore, we concentrated on the less pyrophoric hyperstoichiometric UAl_3 with a very slow feeding rate to minimize dusting. We did, however, make two small runs with the annealed hypostoichiometric UAl_3 although an abundance of sparks was produced.

The hypostoichiometric material was passed through the crusher only once — one sample at a roll spacing of 0.010 in. and the other at 0.006 in. The results are in Table 13.9.

Table 13.9. Size Distribution[a] by Weight of Annealed[b] Hypostoichiometric UAl_3 After Roll Crushing

U.S. Standard Mesh Size	Through 0.010-in. Roll Spacing[c]		Through 0.006-in. Roll Spacing	
	(g)	(%)	(g)	(%)
+100	34.455	85.0	6.322	45.5
−100 +140	2.005	4.93	1.557	11.3
−140 +200	1.462	3.60	1.387	9.96
−200 +270	0.620	1.53	0.615	4.42
−270 +325	0.520	1.28	0.659	4.73
−325	1.488	3.67[d]	3.375	24.3[e]
TOTAL	40.550	100.01	13.914	100.21

[a]Sieved 15 min on Ro-Tap.

[b]Annealed for 2 hr at 1300°C in argon.

[c]One pass through indicated roll spacing.

[d]Fines (−325 mesh) in −100 mesh fraction: 24.5%.

[e]Fines (−325 mesh) in −100 mesh fraction: 44.5%.

The hyperstoichiometric material was crushed in both the annealed and the as-cast condition. The sample was passed through the crusher at a roll spacing of 0.010 in. The −100 mesh fraction was removed, and the +100 mesh fraction was then passed through a 0.006-in. roll spacing. The −100 mesh fraction was again removed, and the oversize material was passed through a 0.003-in. roll spacing. The size distributions of the combined samples after this sequence are given in Table 13.10. The results are very encouraging. The percentage of fines is lower than with any other method attempted thus far. One potential problem with the hyperstoichiometric UAl_3 is that the +100 mesh fraction tends to flake, probably due to deformation of the more malleable aluminum-rich areas. The annealing treatment greatly decreases the amount of flaking, as would be expected. Some possibilities for further improving the yield with the hyperstoichiometric UAl_3 are

1. breaking up the flakes with a hammer mill (the flakes are quite brittle after passing through the 0.003-in. roll spacing) or
2. longer annealing times or slight increases in the uranium content to eliminate the aluminum-rich areas.

The material is being characterized chemically and metallographically. Further experiments on larger lots are planned to confirm these results and to attempt to reduce the flaking of the hyperstoichiometric material.

Fluid Energy Mill. — A Trost Gem-T laboratory fluid energy mill is a very useful tool for grinding brittle ceramics. We evaluated this devise for use with both hypostoichiometric and hyperstoichiometric materials. It operates by suspending particles in high-velocity streams of argon and impelling them into each other. The particles then leave the grinding chamber and are carried around a classifiying loop that removes the fines and returns the larger particles to the grinding chamber. The only control over grinding size is the argon pressure applied to the nozzles. A lower pressure both decreases the impact velocities and allows larger particles to be removed from the apparatus during the classification.

Table 13.10. Size Distributions[a] by Weight of Hyperstoichiometric UAl_3 After Passing Through Roll Crusher[b]

U.S. Standard Mesh Size	As Arc Cast		Annealed[c]	
	(g)	(%)	(g)	(%)
+100	30.616	35.09	12.172	14.82
−100 +140	22.730	26.05	19.283	23.48
−140 +200	16.205	18.58	20.465	24.92
−200 +270	5.272	6.04	7.752	9.44
−270 +325	3.442	3.95	5.634	6.86
−325	8.974	10.29[d]	16.808	20.47[e]
TOTAL	87.239	100.00	82.114	99.99

[a]Sieved 15 min on Ro-Tap.

[b]Rough crushed material (−10 mesh) was successively passed through 0.010-, 0.006-, and 0.003-in. roll spacings. The −100 mesh fraction was removed after each pass.

[c]Annealed 72 hr at 600°C in argon.

[d]Fines (−325 mesh) in −100 mesh fraction: 15.9%.

[e]Fines (−325 mesh) in −100 mesh fraction: 24.1%.

Our first attempt was with hypostoichiometric UAl_3 at a gage pressure of 40 psi. The machine clogged frequently until the +16 mesh fraction of the material was removed. We used only the −16 mesh fraction of the starting material in subsequent runs. Production was very slow. Material leaving the apparatus was ultrafine during normal operation, but when the chamber became overloaded, coarser material was forced through. This is evident in the size distribution shown in Table 13.11: most of the material is either coarse or very fine. The −100 mesh fraction was about 62% fines for the first run. The gage pressure was lowered to 20 psi for the second run, but the grinding behavior was about the same. The annealed hypostoichiometric UAl_3 was used in the fourth run at varying pressures with essentially the same results.

Table 13.11. Size Distributions[a] by Weight of Hypostoichiometric UAl_3 Ground in Fluid Energy Mill

U.S. Standard Mesh Size	Run 1[b]		Run 2[b]		Run 4[c]	
	(g)	(%)	(g)	(%)	(g)	(%)
+60	33.263	47.88	4.890	42.52	18.365	71.5
−60 +100	15.400	22.16	1.840	16.00	2.481	9.62
−100 +140	3.945	5.68	0.400	3.48	0.616	2.40
−140 +200	2.270	3.27	0.340	2.96	0.576	2.24
−200 +270	0.910	1.31	0.190	1.65	0.343	1.34
−270 +325	0.835	1.20	0.225	1.87	0.308	1.20
−325	12.855	18.50[d]	3.625	31.52[e]	2.985	11.65[d]
TOTAL	69.478	100.00	11.500	100.00	25.674	100.00

[a]Sieved 15 min on Ro-Tap.

[b]As-cast hypostoichiometric UAl_3.

[c]Annealed hypostoichiometric UAl_3.

[d]Fines (−325 mesh) in −100 mesh fraction: 62%.

[e]Fines (−325 mesh) in −100 mesh fraction: 76%.

The hyperstoichiometric UAl_3 was used in the third run and the annealed hyperstoichiometric in the fifth run. We varied the pressures in an attempt to increase production. The gage pressure was maintained at 20 psi until the chamber began to overload, increased to about 60 psi to promote grinding, and then lowered to 10 psi or lower to promote removal of the material through the classifier. The size distributions are shown in Table 13.12. The results are the same as for the hypostoichiometric material. Part of the material becomes ultrafine, and part remains coarse; only a minor portion of the material is in the desired range of −100 +325 mesh. This type of distribution could be due to several factors:

1. The corners or small fragments could be knocked from the large particles.

2. The impact might be such that each particle crushed shatters into several small fragments.

Table 13.12. Size Distributions[a] by Weight of Hyperstoichiometric UAl_3 Ground in the Fluid Energy Mill

U.S. Standard Mesh Size	Run 3[b]		Run 5[c]	
	(g)	(%)	(g)	(%)
+60	16.116	68.77	13.937	57.1
−60 +100	3.244	13.85	2.044	8.4
−100 +140	0.956	4.08	0.740	3.03
−140 +200	0.643	2.74	0.629	2.57
−200 +270	0.332	1.42	0.366	1.50
−270 +325	0.286	1.22	0.328	1.34
−325	1.857	7.91[d]	6.395	26.2[e]
TOTAL	23.434	99.99	24.439	100.14

[a]Sieved 15 min on Ro-Tap.

[b]As-cast hyperstoichiometric UAl_3.

[c]Annealed hyperstoichiometric UAl_3.

[d]Fines (−325 mesh) in −100 mesh fraction: 45.6%.

[e]Fines (−325 mesh) in −100 mesh fraction: 75.6%.

3. The classification may be such that only the ultrafine particles are normally removed and overloading then sweeps the large particles through with very little attrition.

The third possibility is most likely. In this case, a machine such as the Majac Jet Pulverizer, with its independently controlled grinding chamber and classifier, would give improved performance. However, the grinding action of this type mill appears to be rather inefficient for UAl_3.

The Trost Gem-T fluid energy mill was not a good device for grinding UAl_3. Its poor particle distributions, excessive usage of Ar as the fluid medium, and long grinding times are significant disadvantages.

Mechanisms of Swelling in the UAl_x-Al Compacts (A. K. Chakraborty)

We are studying the swelling behavior of UAl_x dispersed in Al. The stability of the UAl_x fuel at elevated temperatures depends on the interaction of UAl_3 and Al to form UAl_4. Fuel particle size, fuel composition, temperature, storage history of the powders, and type of surface on the aluminum powders are factors that influence the swelling behavior.

Voids have been observed in the reaction zone between UAl_3 and Al. To determine the cause of this void formation, we constructed a diffusion couple between UAl_3 and Al and heat treated it for 1 hr at 600°C. After this heat treatment, we found a large interfacial area of UAl_4 between the UAl_3 and Al. Within the UAl_4 layer that was formerly UAl_3, many voids were found due to a Kirkendall effect. A similar diffusion couple was made using Al and an UAl_xZr_y fuel containing 14 wt % Zr. Even after an exposure of 20 hr at 600°C we found no voids and a very thin interfacial reaction zone in this diffusion couple. The latter shows that doping elements can very effectively retard the transformation of UAl_3 to UAl_4.

A report describing all aspects of our experiments on fuel swelling has been drafted.

Characterization of Sol-Gel U_3O_8 (M. M. Martin)

The performance of aluminum-based dispersion-type fuel plates in reactors may depend upon the amount and location of voids within the core that could provide a place to accommodate particle swelling and fission gases. The particular fuel and its method of manufacture and concentration in the fuel core establishes the quantity of voids that are retained and/or open to the matrix in a roll-bonded and annealed fuel plate.[2] In our search for an improved fuel for HFIR, we have found that U_3O_8 prepared by the sol-gel process[3] offers the additional

---

[2]M. M. Martin, J. H. Erwin, and W. R. Martin, Trans. Am. Nucl. Soc. 11(1), 107 (June 1968).

[3]R. G. Wymer, Laboratory and Engineering Studies of Sol-Gel Processes at Oak Ridge National Laboratory, ORNL-TM-2205 (May 1968).

desirable property of a larger and perhaps a controllable amount of closed porosity within the fuel particles.

Figure 13.1 shows the as-polished structure of U_3O_8 particles from three methods of preparation. Hi-fired U_3O_8 is comparable to that being used successfully in HFIR. The burned U_3O_8 is from an earlier stage of the hi-fired process and is made simply by burning uranium machining chips.

The photographs in Fig. 13.1 for burned (A,D) and hi-fired (B,E) oxides show materials that are depleted as well as enriched in ^{235}U. In comparing these, one sees differences of (1) pore size in the hi-fired and (2) agglomeration of fines in the burned oxides. These differences result primarily from a loosening of process control and metal purity requirements with the depleted materials. The sol-gel U_3O_8 shown in

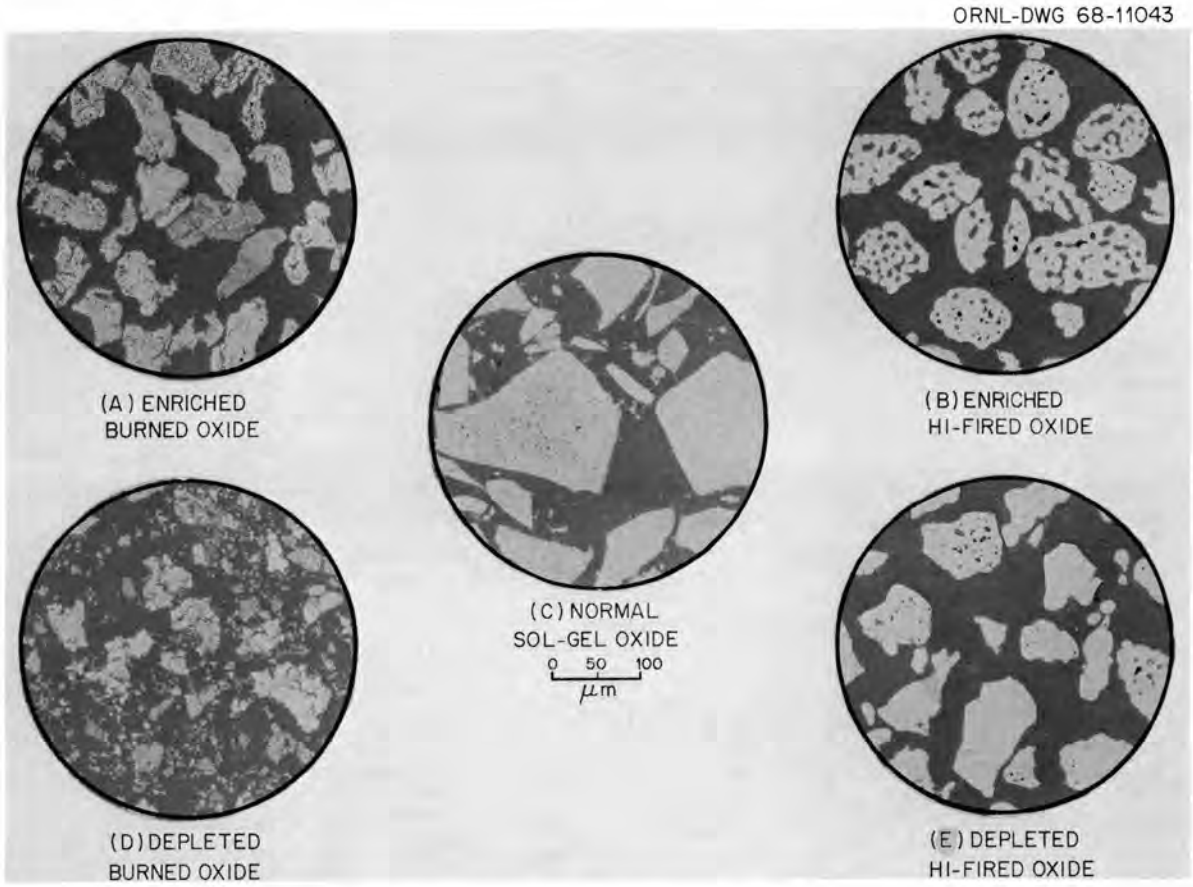

Fig. 13.1. As-Polished Structure of U_3O_8 Particles from Three Methods of Preparation.

(C) contains normal U. In contrast to the pores and cracks in hi-fired and burned materials, the sol-gel U_3O_8 particles have an abundance of minute voids distributed uniformly throughout the as-polished structure. The diameter of most of the voids is less than 1 μm.

The sol-gel U_3O_8 that was characterized came from the Chemical Technology Division at ORNL. Lines from a Debye-Scherrer powder camera sample were indexed to be the orthorhombic form of U_3O_8; two extra lines, however, indicated the presence of minor amounts of hexagonal U_3O_8. Spectrographic analysis revealed impurities of Al, B, Fe, Na, and Ni that exceeded the HFIR specification.[4] Closer control of starting materials should reduce these contaminants to an acceptable level. The results of other analyses are given in Table 13.13 which includes for comparison data for hi-fired and burned U_3O_8.

Note in Table 13.13 the excellent agreement between the values for toluene density and mercury density determined at 15,000 psi for the sol-gel material. The amount of closed porosity calculated from the toluene and x-ray densities is 12.4 vol %. The mercury and toluene densities for both burned and hi-fired materials, however, differ significantly. In fact, the toluene values for hi-fired particles are always near that for theoretically dense U_3O_8. We conclude that most of the pores and cracks depicted in Fig. 13.1 for the burned and hi-fired materials are open to the surface of the particles. The minute and finely distributed voids in sol-gel U_3O_8, however, are closed.

All of the above information gives a reasonably clear picture of sol-gel U_3O_8. The distribution of a relatively large volume of closed porosity appears to be its principal asset, since the material may be able to hold a significant quantity of fission gases. If the pores can be retained during plate fabrication and irradiation, sol-gel U_3O_8 should be an extremely attractive fuel for research reactors. The decision on whether or not it will perform adequately on HFIR fuel must be based on results from plate fabrication and irradiation experiments now being planned.

---

[4]R. W. Knight, J. Binns, and G. M. Adamson, Jr., Fabrication Procedures for Manufacturing High Flux Isotope Reactor Fuel Elements, ORNL-4242 (June 1968).

Table 13.13. Characterization of U_3O_8 Materials

	Method of Preparation				
	Burning of Metal Chips	Hi-firing	Sol-Gel	Burning of Metal Chips	Hi-firing
Uranium concentration, wt %	84.3	84.5	84.7	84.7	85.2
^{235}U assay, wt %	93.2 (enriched)	93.2 (enriched)	0.7 (normal)	0.2 (depleted)	0.2 (depleted)
Mercury density, g/cm^3					
at 29 psig	5.69	6.83	4.90	a	a
at 15,000 psig	7.06	7.63	7.29	a	a
Toluene density, g/cm^3	7.64	8.22	7.35	7.92	8.29
Closed porosity, vol %	7.8	0.8	12.4	5.6	1.2
Surface area, m^2/g	0.34	0.05	0.49	0.56	0.06
Major particle size range property analysis, μ	88–44	88–44	149–44	88–44	88–44
Amount <44 μ, wt %	11	10	27	b	3

[a]Not determined.

[b]Analysis generates fines.

Studies of Fuel Plate Surfaces

J. V. Cathcart

We have continued our efforts to develop an anodic film to coat the cladding of aluminum fuel elements in reactors such as the HFIR. One phase of the work involved a study of the effect of temperature of the anodizing bath on the protective qualities of the films. We previously demonstrated that a film formed on 99.999% pure Al at 4°C was an order of magnitude more protective in static corrosion tests at 200°C than one formed at room temperature. This behavior is apparently related to the influence of temperature on the pore structure of the films. Figure 13.2 is an electron micrograph of a cross section through an anodic film formed in an oxalic acid bath at 4°C. Note that the pore

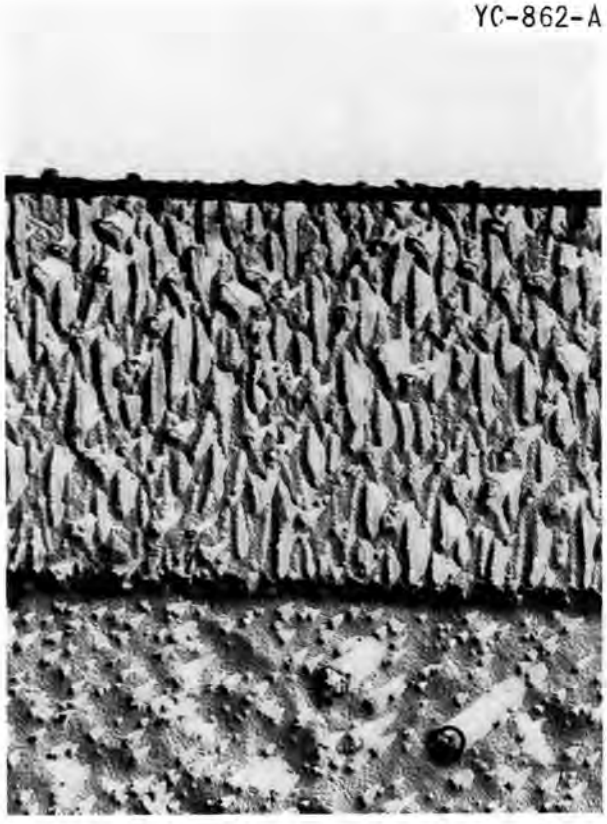

Fig. 13.2. Electron Micrograph of a Cross Section Through an Anodic Film Formed in Oxalic Acid at 4°C on a 99.999% pure Aluminum Specimen. 12,000×.

structure is still evident; however, the pore size has been considerably reduced, and the pore density and length and the degree to which the pores are interconnected are all less than the corresponding parameters for room-temperature films. We are also investigating the relationship between the initial thickness of these anodic films and the time in water at 200°C required for their breakdown.

We have studied the properties of anodic films formed in an anodizing bath containing 38 g $TiO(KC_2O_2)_2$, 1.2 g citric acid, and 1.0 g oxalic acid per liter of water. It is believed that films formed in this bath are tougher and more elastic than those formed in oxalic acid; hence, it is possible that they will better withstand the strain gradients that develop in tests where a high heat flux exists across the specimen-water interface.

The initial results of static, isothermal tests of these films on 99.999% pure Al at 200°C showed them to be at least as protective as low-temperature films formed in oxalic acid. Again, this behavior appears to be tied to the pore structure of the films, the pore spacing being wider than that for the room-temperature oxalic acid films.

In the last test, carried out by John Griess in a flowing loop rig, the test section of the loop was coated with an anodic film formed in oxalic acid at 16°C and exposed for 168 hr at an interface temperature of about 200°C. The thermal data from the loop indicated a reduction in the corrosion rate over the total time of the test; however, metallographic examination of the specimen after test failed to reveal any remnant of the original anodic film. It is clear that we need to improve further the protective qualitites of the anodic films in order to counteract the much more stringent corrosion conditions encountered in the flowing loop tests.

Two new test sections have been completed for the flowing loop. In light of the results described above, we plan to coat the first of these with an anodic film formed in the $TiO(KC_2O_2)_2$ bath.

Vapor Fabrication of Fuels and Reactor Materials

W. R. Martin

Vapor Fabrication of PuO_2 Powder from PuF_6 (W. C. Robinson, Jr.)

The following is the abstract of a report[5] issued this quarter:

> A program was undertaken to establish the feasibility of converting PuF_6 to PuO_2 in a one-step process by chemical vapor deposition techniques. The process is analogous to the UF_6 conversion process and involves the reaction of PuF_6 vapor, hydrogen, and H_2O. A remote apparatus with facilities for fluorination of PuF_4 to PuF_6 and subsequent conversion of PuF_6 to PuO_2 was designed, constructed, and the feasibility experiments were completed. X-ray analyses of the powder product confirmed the presence of PuO_2 only.

Work was begun to extend the investigation to the simultaneous conversion of PuF_6-UF_6 mixtures to the mixed oxide. This required apparatus modification to accommodate the concurrent metering of both fluoride gases. The fluorination system used for conversion of PuF_4 to PuF_6 will also be redesigned. This new design has been completed, and construction has begun.

Flame-Produced Material (J. I. Federer)

Preparation of UO_2. — In past experiments, UO_2 was usually prepared with large excesses of both H_2 and O_2 compared to the amount of UF_6 in the gas mixture.[6] These elements form water in excess of that required for reaction. In a commercial application of the process, gaseous HF, also formed in the reaction, would be recovered as salable hydrofluoric acid. The commercial composition of this acid is about 50 wt % HF and would be obtained by adding or extracting water. A mole ratio of $H_2:O_2:UF_6 = 3:1:1$ is needed for stoichiometric reaction; a ratio of

---

[5]W. C. Robinson, Jr., and W. R. Martin, A Feasibility Study of the Conversion of PuF_6 to PuO_2 by Chemical Vapor Deposition, ORNL-TM-2306 (August 1968).

[6]J. I. Federer, W. C. Robinson, Jr., and F. H. Patterson, Conversion of UF_6 to UO_2 in a Flame Reactor, ORNL-TM-2327 (October 1968).

about 16.3:4.3:1 is needed for reaction and to provide sufficient water for 50 wt % hydrofluoric acid. This consideration and the incentive to further characterize the flame-reactor process for making UO_2 resulted in a series of experiments in which the reacting gases contained smaller amounts of H_2 and O_2 than had been used previously. Recent experiments were conducted in which H_2 and O_2 were varied from stoichiometric to 2 and 20 times stoichiometric values, respectively. Thus, the possibility of producing UF_4 in an oxygen-starved system and UO_2F_2 in a hydrogen-starved system was examined. The conditions and results of these experiments are presented in Table 13.14.

Table 13.14. Conditions of Formation and X-Ray Analysis of Flame-Produced Powder

Gas Composition[a] (moles/mole UF_6)		Pressure (torr)	Location of Sample[b]	X-Ray Analysis[c]			
Hydrogen	Oxygen			UO_2	U_3O_8	UF_4	Other[d]
3	1	80	A	S	M	NF	M
			B	S	NF	NF	W
3	2	40	A	S	NF	NF	W
			B	S	NF	NF	W
3	10	30	A	NF	S	NF	S
			B	NF	M	NF	M
3	10	30	A	NF	S	NF	S
			B	NF	S	NF	S
3	20	60	A	S	M	NF	M
			B	S	NF	NF	M
6	2	60	A	S	W	NF	W
			B	S	NF	NF	W
6	1	70	A	S	W	NF	W
			B	S	W	NF	W

[a] Stoichiometric ratio: $H_2/O_2/UF_6 = 3:1:1$.

[b] A, reaction tube; B, powder trap.

[c] Amount of phases estimated from intensities of lines on x-ray powder patterns. S, strong; M, medium; W, weak; NF, none found.

[d] Unidentified compounds.

Table 13.14 shows that pressure, which was intended to be constant, varied from 30 to 80 torr. The pressure listed for any given experiment was necessary to maintain a stable flame. The pressure actually was constant except during the period at the beginning of the experiment when we were forced to seek by trial and error for that pressure necessary to keep the flame burning. In the first four experiments, O_2 was increased from the stoichiometric values to 20 times that value. Uranium dioxide was a principal product of each of these experiments except for an oxygen value of 10 times stoichiometric. In this experiment, and in another performed under similar conditions as a check, U_3O_8 formed instead of UO_2. Uranium dioxide was the principal product formed in the last two experiments for which the hydrogen content of the gases was two times stoichiometric. Neither UF_4 nor UO_2F_2 has been identified in the product from these experiments; however, either compound may be present in the other (unidentified) compounds present in every case. Attempts to index the weak and diffuse lines caused by these compounds on x-ray powder patterns have been unsuccessful. Tentative identification of UO_3, UO_2F_2, and $UF_4 \cdot 1\ 1/2\ H_2O$ was made in some cases. The results show that UO_2 can be prepared with a stoichiometric mixture of gases and mixtures containing small excesses of H_2 and O_2. These results and those from previous experiments[6] imply that a mixture can be used that would result in hydrofluoric acid of near commercial composition to be sold rather than discarded as waste. This will help solve a problem of waste disposal and will improve the economics of UF_6 conversion.

Characterization of Flame-Produced UO_2. — In a continuing effort to increase the particle size of flame-produced UO_2, we heat treated samples at 1100 and 1200°C in wet H_2 for 16 hr. Sieve analysis of as-prepared and heat-treated powders are shown in Table 13.15. These results show that heat-treated powder contains a larger fraction of −325 mesh material than does as-prepared powder. Similar results have been obtained after heat treatment at 1000°C and after conversion to U_3O_8

Table 13.15. Sieve Analyses of As-Prepared and Heat-Treated Powder Produced in the Flame Reactor

Mesh Size	As-Prepared	Heat Treated (wet H_2, 16 hr)	
		1100°C	1200°C
+60	5.2	0	0.1
−60 +80	18.6	0.1	0.2
−80 +100	12.1	2.3	0.7
−100 +120	9.9	6.3	4.2
−120 +140	8.1	12.7	10.6
−140 +170	4.5	8.3	8.3
−170 +200	5.0	8.9	10.2
−200 +230	2.7	4.0	5.3
−230 +270	5.1	7.8	9.5
−270 +325	5.8	10.5	11.2
−325	23.1	39.1	39.8

followed by reduction to UO_2 at 600°C (ref. 7). The increase in the amount of −325 mesh material is attributed to the breaking up of agglomerates present in as-prepared powder. At the same time, very little sintering of the powder occurs in a loosely packed bed.

Thermal Conductivity of UO_2-W Pellets. — Powder mixtures of UO_2 and $W_{20}O_{58}$ were prepared in the flame reactor from gas mixtures containing UF_6, WF_6, H_2, and O_2. The powders were sieved to obtain −200 mesh material and defluorinated (to 50 ppm F) in wet H_2 at 1000°C. This treatment also reduced $W_{20}O_{58}$ to metallic W. Pellets were prepared from the powders by uniaxially pressing at 10,000 psi followed by isostatically pressing at 50,000 psi and then sintering at 1750°C for 4 hr in dry H_2. The thermal conductivities of three UO_2-W pellets and a UO_2

[7] J. I. Federer and W. R. Martin, Fuels and Materials Development Program Quart. Progr. Rept. June 30, 1968, ORNL-4330, pp. 331–334.

pellet were measured between 25 and 90°C in a longitudinal heat-flow apparatus.[8] The thermal conductivities (λ) at 30°C are shown below:

Tungsten, wt %	0	18	33	52
λ, w cm^{-1} $°C^{-1}$	0.0459	0.0577	0.1055	0.1387

Polycrystalline UO_2 of 93% theoretical density has a λ value of 0.070 w cm^{-1} $°C^{-1}$; W has a λ of 1.7 w cm^{-1} $°C^{-1}$. The lower value of 0.0459 w cm^{-1} $°C^{-1}$ for the UO_2 pellet and lower than expected values for the UO_2-W pellets are probably due to cracks running perpendicular to the longitudinal (heat flow) axis of the pellets. These cracks and some voids, which were visible to the unaided eye, were also observed in radiographs and in metallographic sections.

In summary, the feasibility of preparing duplex UO_2-W powders in a flame reactor was demonstrated, and pellets pressed and sintered from these powders contained defects that resulted in low thermal conductivities even though W was the continuous phase in the two pellets with the highest content of W.

Chemical Vapor Deposition of Silicon Carbide from Silicon Tetrachloride-Methane-Hydrogen Mixtures (J. E. Spruiell[9])

A study was conducted to determine the effect of deposition parameters on the characteristics of silicon carbide deposits produced by chemical vapor deposition from silicon tetrachloride-methane-hydrogen mixtures. The deposits were characterized by determining (1) deposit density and soundness, (2) phases present, (3) surface appearance, (4) hardness, and (5) deposition rates.

The composition and surface morphology of the deposits varied markedly as a function of the operating parameters. Figure 13.3 depicts four deposits made under different experimental conditions. Figure 13.3(a) is a silicon-rich deposit formed at relatively low temperatures (1175°C), and Fig. 13.3(d) is a carbon-rich deposit formed at about 1400°C. Figure 13.3(b) and (c) are stoichiometric deposits formed

[8]D. L. McElroy and R. S. Graves, Private communication.

[9]Consultant from the University of Tennessee.

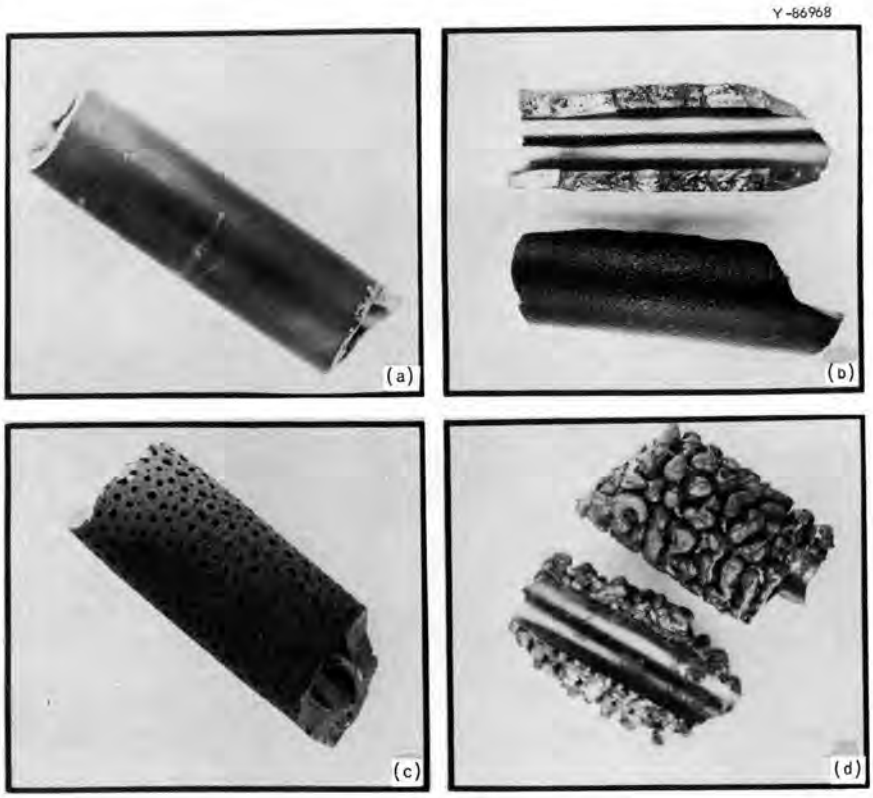

Fig. 13.3. Representative SiC Deposits. (a) Silicon-rich deposit formed at 1175°C; (b) and (c) pure SiC deposited at 1350°C; and (d) graphite-rich deposit formed at 1400°C.

at 1350°C. The primary parameter for this process is temperature. In general, the higher the deposition temperature, the more carbon-rich the deposit stoichiometry and the rougher the deposit morphology. The characteristics of the deposits over a range of deposition parameters and optimization of parameters for producing particular deposit properties were discussed previously.[10] This work on SiC has now been discontinued.

Development of Nondestructive Inspection Techniques

B. E. Foster S. D. Snyder

Work this quarter has involved scanner calibration and studies of radiographic densitometry for determination of fuel-plate homogeneity.

---

[10]J. E. Spruiell, Chemical Vapor Deposition of Silicon Carbide from Silicon-Tetrachloride-Methane-Hydrogen Mixtures, ORNL-4326 (in press).

Scanner Calibration Studies

We have continued our efforts to establish x-ray attenuation calibration curves of various U_3O_8 loadings of HFIR fuel plates. Thirty-two enriched fuel plates have been fabricated using frames, uranium oxide, and procedures from Metals and Controls, Inc. (the fabricator of HFIR fuel core). These plates are divided into four groups of eight plates each with each group having a different U_3O_8 particle size distribution as follows:

Group A: "as supplied"

Group B: (−170 +200)

Group C: distribution evenly divided between (−170 +325)

Group D: (−325 + dust).

Within each group there are pairs of both inner- and outer-annulus plates of nominal loading and 125% of nominal loading. Using this series of plates, we will be able to observe the effects of particle size on the x-ray attenutaion calibration for loadings from nominal to 125% of nominal.

Since x-ray attenuation is an exponential function, we lose sensitivity to fuel changes at our normal x-ray energy conditions of 50 kvcp and 2.5 ma for the plates with higher loadings. We regain the desired sensitivity by increasing the energy, so these plates are being scanned at both 50 and 55 kvcp. Over half the plates have been totally scanned at both energies. After the total scanning, we will select one inner- and one outer-annulus plate of nominal loading and 125% of nominal loading from each group for sample scanning, machining, and chemical analysis to establish the calibration curve relating milligrams of U per 5/64-in.-diam spot to attenuation.

Radiographic Densitometry

We are continuing our study of the use of radiography and densitometry to determine the qualitative and quantitative capabilities and limitations for the detection and measurement of fuel inhomogeneity in dispersion core fuel plates.

Figure 13.4 is a graph of film density plotted against aluminum thickness of typical data from a radiograph of the aluminum step wedge

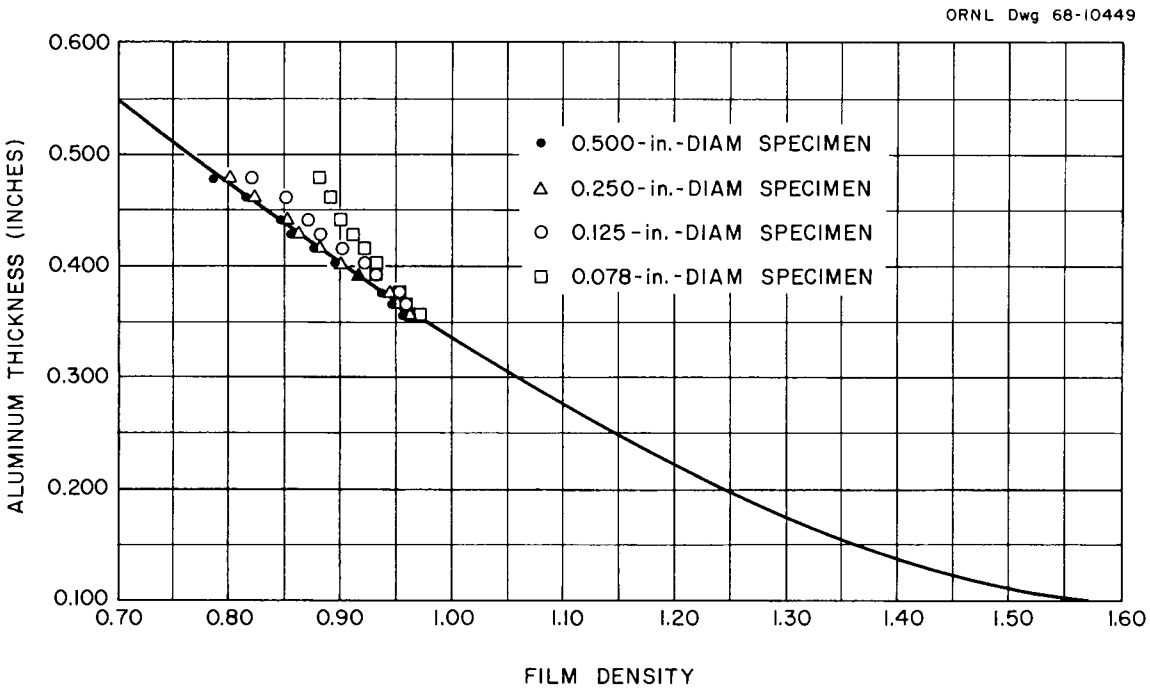

Fig. 13.4. Radiographic Density Curve for Aluminum Step Wedge and Simulated Excess Fuel in a Fuel Plate.

and small-diameter aluminum disks (representing excess fuel) when superimposed on a fuel plate. The aperture of the densitometer was 0.078 in. The graph clearly shows the bias in film density (and interpretation of fuel content) resulting when 0.078- and 0.125-in.-diam disks are measured. The error has been as much as 33%. This bias is not evident when measuring the film density for the 1/4- and 1/2-in.-diam specimens.

Computer programs have been developed to achieve the best least-squares-curve fit for the data from the film densitometry studies. Similar programs were also developed for curve fitting the data for the calibration curves from the x-ray attenuation scanning.

Additional work in the Nondestructive Testing Laboratory has been in conjunction with studies of fuel plate fabrication. Problems in ultrasonic scanning of plates are reported above.[11]

---

[11]M. M. Martin et al., "Irradiation Studies of Dispersion Plates," pp. 260–265, this report.

PART V.

ENGINEERING PROPERTIES OF REACTOR MATERIALS

14. PHYSICAL AND MECHANICAL METALLURGY OF REFRACTORY ALLOYS

W. O. Harms

The purpose of this program is to provide a broad, base-technology evaluation of high-temperature alloys for use in high-performance nuclear reactors and isotopic heat sources for advanced space, terrestrial, and civilian power applications. Principal emphasis is placed on materials problems involving tantalum-, niobium-, molybdenum-, and vanadium-base alloys for systems that use alkali metals as thermodynamic working fluids and heat-transfer media. Some work on superalloys is included because of the more immediate need for these materials in thermoelectric power devices.

Basic Physical Metallurgy Studies

H. Inouye

Solubility, Diffusivity, and Permeability of Interstitials in Refractory Metals (R. L. Wagner)

Our task is to measure the permeability of N through W to assess its ability to contain nitride fuels. We are measuring the rate at which N degasses from a tungsten wire. From this, we determine the solubility and diffusivity of N in W. The permeability in units of torr liter cm^{-3} $torr^{-\frac{1}{2}}$ is calculated from the relationship

$$K = DS \ , \tag{14.1}$$

where

K = permeability,

D = diffusivity,

S = solubility constant.

The following equation allows one to calculate the flux, J, of gas through the cladding walls:

$$J = \frac{K\Delta P^{\frac{1}{2}}}{d} , \qquad (14.2)$$

where

ΔP = the pressure differential from inside to outside of the cladding wall,

d = the thickness of the cladding wall.

The literature values for the solubility, diffusivity, and permeability of N in refractory metals and our results to date are presented in Table 14.1 along with the values for Mo and Ta. At the two temperatures presented, our values for diffusion of N in W are lower than the literature values by an order of magnitude, and our values for solubility are an order of magnitude higher. This results in our values for permeation and flux being slightly lower.

The permeability and flux values for Mo are about two to three orders of magnitude higher than those for W. The high solubility of Ta — six orders of magnitude higher than that of the others — results in its high values for permeability and flux in comparison with W.

The disagreement between our tungsten data and the published values is unresolved. Further experiments are being carried out to determine the diffusivity and solubility as a function of temperature.

Interaction of Stress and Vacuum on Properties of Superalloys at Elevated Temperatures (D. T. Bourgette)

The two objectives of this investigation are to determine the effects of evaporation losses on creep behavior and the effect of stress on the evaporation kinetics of superalloys. Haynes alloy No. 25 was selected for the initial tests.

Preliminary results showed that evaporation losses increased with stress at 785°C and 10^{-8} torr. Measurements of the BET surface area show that the higher stresses increased the evaporation area. Therefore,

Table 14.1. Solubility, Diffusivity, and Permeability of Nitrogen in Refractory Metals

Table 14.1 Solubility, Diffusivity, and Permeability of Nitrogen in Refractory Metals

Metal	Diffusivity (cm^2/sec)	Solubility Constant$_1$ (torr liter cm^{-3} $torr^{-\frac{1}{2}}$)	Nitrogen Solubility at 760 Torr N_2 (ppm)	Permeability (torr liter cm^{-1} sec^{-1} $torr^{-\frac{1}{2}}$)	Flux at 10^{-4} torr[a] (g cm^{-2} sec^{-1})
			1600°C		
W[b]	4.5×10^{-7}	9.5×10^{-5}	0.22	4.2×10^{-11}	7.1×10^{-16}
W[c]	4.0×10^{-7}	4.3×10^{-4}	1.0	1.7×10^{-10}	2.9×10^{-15}
W[d]	4.5×10^{-8}	5.1×10^{-4}	1.2	2.3×10^{-11}	3.8×10^{-16}
Mo[c]	4.0×10^{-6}	6.0×10^{-3}	26.6	2.4×10^{-8}	3.6×10^{-13}
Ta[e]	1.8×10^{-7}	4.4×10^{3}		7.9×10^{-4}	1.3×10^{-8}
			1800°C		
W[b]	1.4×10^{-6}	2.1×10^{-4}	0.5	3.0×10^{-10}	4.9×10^{-15}
W[c]	1.6×10^{-6}	3.4×10^{-4}	0.8	5.5×10^{-10}	9.0×10^{-15}
W[d]	8.9×10^{-8}	1.8×10^{-3}	4.2	1.6×10^{-10}	2.6×10^{-15}
Mo[c]	7.8×10^{-6}	7.7×10^{-3}	34	6.0×10^{-8}	9.9×10^{-13}
Ta[e]	4.2×10^{-7}	1.6×10^{-3}		6.7×10^{-4}	1.1×10^{-8}

[a] Based on thickness of 1 cm.

[b] F. J. Norton and A. L. Marshall, Trans. AIME 156, 351 (1944); S. Dushman, Scientific Foundations of Vacuum Technique, p. 562, Wiley, New York, 1962.

[c] R. Frauenfelder, Permeation, Diffusion, and Solution of Nitrogen in Tungsten and Molybdenum, Final Report, WERL-2823-28, (June 30, 1967).

[d] This study

[e] J. D. Fast, Interaction of Metals and Gasses, p. 215, Academic Press, New York, 1965.

calculations of weight loss based on the original geometric area would show an increase in evaporation losses with an increase in stress. Since specimens stressed at 2000 to 2500 psi contracted about 0.08% in 1000 hr, creep strain does not appear to be responsible for increasing the surface area.

Specimens with nominal thicknesses of 0.007, 0.012, and 0.030 in. were creep tested in high vacuum at 785°C and stress levels of 2100 to 15,000 psi. At a given stress, the thinner specimens were weaker because a larger volume fraction of the alloy was influenced by the evaporation losses. This behavior is illustrated in Table 14.2.

Table 14.2. Effect of Specimen Thickness on the Time to Produce 1% Plastic Strain in Haynes Alloy No. 25 at 785°C and Various Stresses in High Vacuum

Specimen Thickness, in.	Time (hr) to 1% Strain at Given Stress (psi): 15,000	10,000	5,000
0.007	10	40	460
0.012	14	53	600
0.030	24	200	4500[a]

[a]Extrapolated.

Development of Age-Hardening Refractory Alloys (C. T. Liu)

The purpose of this task is to develop age-hardening refractory alloys containing a uniform dispersion of fine particles throughout the matrix. We are studying the binary alloys listed below:

Nb–40 wt % Hf
Nb–53 wt % Hf
Nb–70 wt % Hf
Ta–29.5 wt % Hf
Ta–50.3 wt % Hf
Ta–35 wt % Hf
Ta–19.6 wt % Zr
Ta–24.6 wt % Zr

The aging characteristics of the Nb–53 wt % Hf, Ta–50.3 wt % Hf, and Ta–65 wt % Hf alloys after oil quenching were reported previously.[1]

In the literature, two types of Nb–Hf phase diagrams are reported: one contains the miscibility gap,[2] and the other does not.[3] Our work supports the miscibility gap. In order to further confirm the existence of two high-temperature phases, we heat treated several specimens of the Nb–Hf alloys listed in Table 14.3. We found that the rate of precipitation

[1]C. T. Liu, Fuels and Materials Development Program Quart. Progr. Rept. June 30, 1968, ORNL–4330, pp. 345–349.

[2]M. A. Tylkina, I. A. Tsyganona, and E. M. Savitskii, Russ. J. Inorg. Chem. 9, 893 (1964).

[3]A. Taylor and N. J. Doyle, J. Less-Common Metals 7, 37–53, (1964).

Table 14.3. The Effect of Cooling Rate on the Precipitation of Nb-Hf Alloys

Specimen Number	Composition, wt %		Heat Treatment	Microstructure
	Nb	Hf		
1	47	53	Oil quenched from 1820°C, aged 3 hr at 1000°C	Uniform precipitation of fine particles
2	47	53	Cooled from 1820 to 1000°C in 40 sec, aged 6 hr at 1000°C	Partial precipitation, mixture of fine and coarse star-shaped precipitates
3	47	53	96 hr at 1700°C, heated to 1850°C for 30 min, cooled to 1000°C in 5 min, aged 120 hr at 1000°C	Essentially single phase with very small amount of coarse precipitates within and on the grain boundaries.
4	60	40	Oil quenched from 1820°C, aged 6 hr at 1000°C	Same as Specimen 1
5	60	40	Same as specimen 3	Same as specimen 3

as well as the morphology were extremely sensitive to the rate at which the specimens were quenched (Fig. 14.1). This is due to the enormous number of extra vacancies, produced in quenching the samples to room temperature rather than allowing them to cool slowly, that govern the precipitation process.[4] Since the extra vacancies produced by quenching are not expected to change the features of the phase diagram, we believe that the simple phase diagram reported by Taylor and Doyle[3] may be a result of an aging time insufficient to introduce the two high-temperature phases.

A competitive mechanism of precipitation is observed in the Ta–29.5 wt % Hf alloy. As aging treatment proceeds, the uniformly dispersed phase produced by the mechanism of continuous precipitation is progressively replaced by the growth of the discontinuous precipitation at the grain boundaries, as is shown in Fig. 14.2.

The macrohardness data for Nb-Hf, Ta-Hf, and Ta-Zr binary alloys are shown as a function of aging temperature in Fig. 14.3. The Rockwell hardness values increase from about 20 to 60 as aging temperature decreases from 1100 to 600°C. The valleys between 1000 and 1200°C in the hardness plots correspond to the temperature of the highest rate of coarsening.

Preliminary tensile tests of the Nb–53 wt % Hf alloy show that the yield strengths vary from 65,000 to 100,000 psi, corresponding to different heat treatments. As a comparison,[5] the yield strength of unalloyed Nb is about 23,500 psi.

Thermodynamics of Spinodally Decomposed Alloys (C. T. Liu and B. T. Loh)

The existence of a miscibility gap in a phase diagram provides the necessary condition required for spinodal decomposition. The kinetic parameters associated with the spinodal decomposition, however, are closely

---

[4]A. Kelly and R. B. Nicolson, Progr. Mat. Sci. 10(3), 160–178 (1963).

[5]H. R. Babitzke, G. Asai, and H. Kato, Bureau of Mines, Report of Investigation No. 6101, (1962).

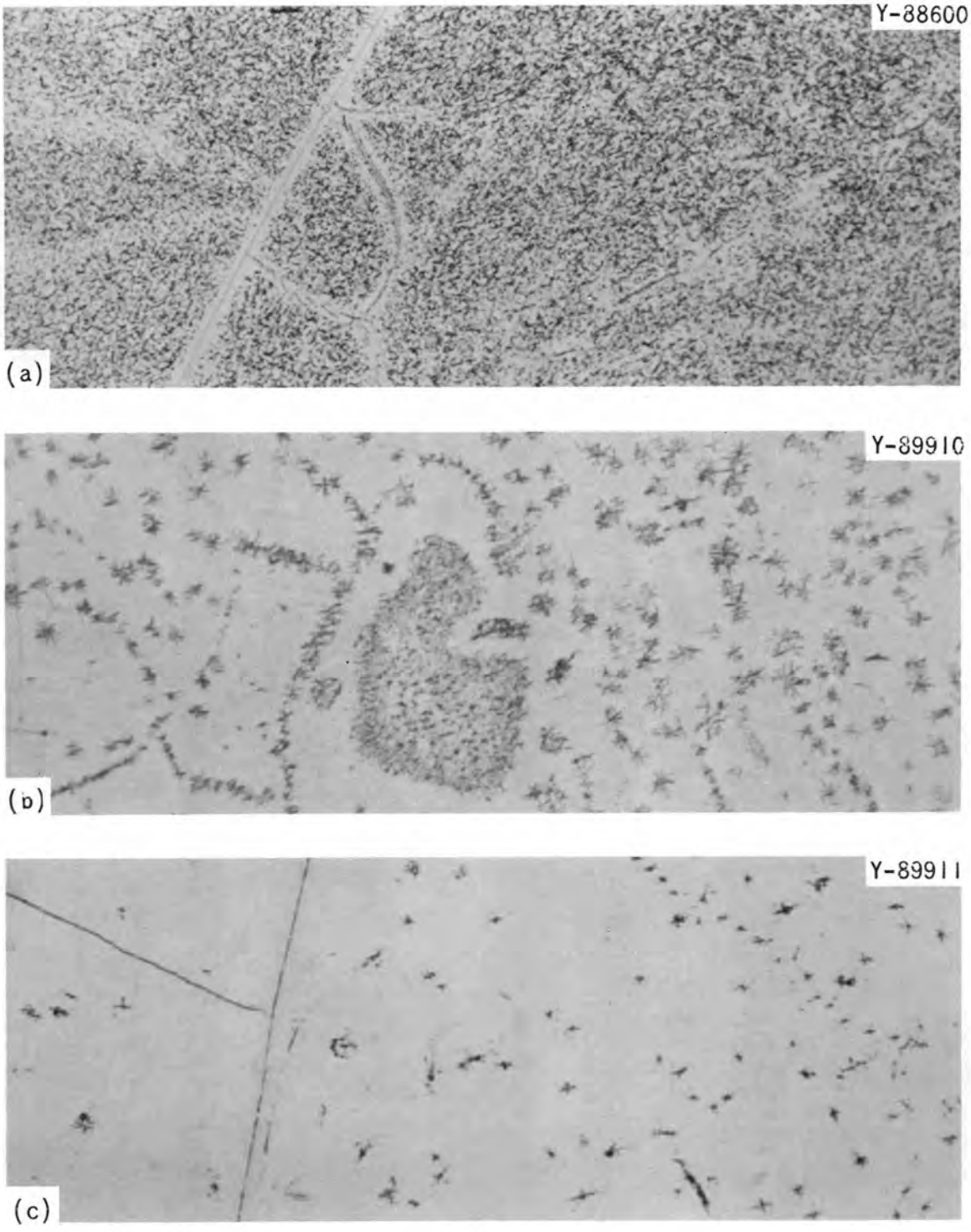

Fig. 14.1. The Effect of Cooling Rate on the Microstructure of Nb–53 wt % Hf. (a) Oil Quenched from 1820°C; aged 3 hr at 1000°C. 750×. (b) Cooled from 1820°C to 1000°C in 40 sec, aged 6 hr at 1000°C. 500×. (c) 96 hr at 1700°C; 1820°C for 1/2 hr; cool from 1850 to 1000°C 5 min; aged 120 hr at 1000°C. 500×. Etchant: 100 parts HNO_3, 50 parts H_2O, 10 parts HF acid.

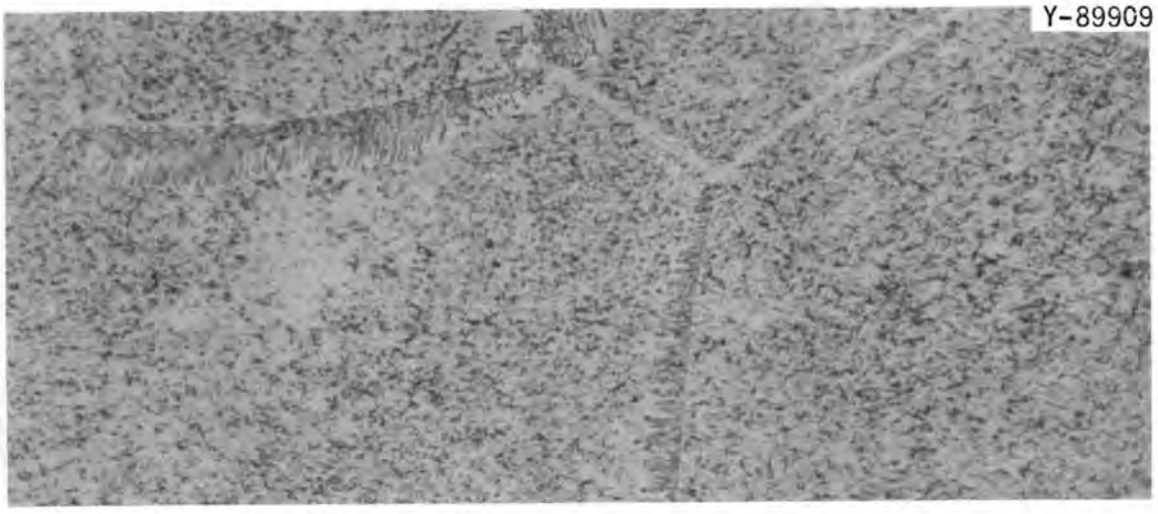

Fig. 14.2. Photomicrograph of Ta–29.5 wt % Hf Alloy Aged 4 hr at 1200°C. 750×. Etchant: 50 parts 30% H_2O_2, 10 parts HNO_3, 3 parts HF.

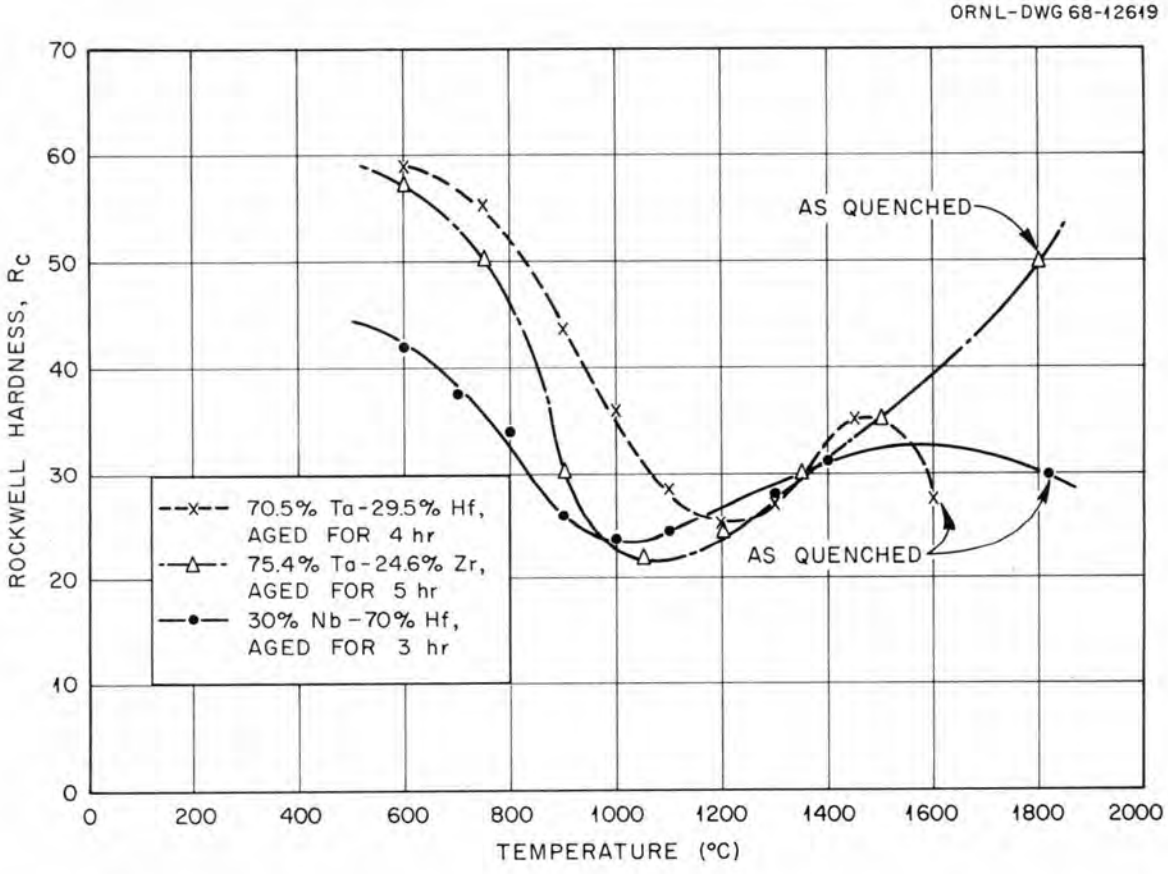

Fig. 14.3. A Plot of Rockwell Hardness Against Aging Temperature, for Nb-Hf, Ta-Hf, and Ta-Zr Alloys at Constant Time.

related to the free energy of mixing, ΔG_m, for a given alloy system. For example, the composition range where the spinodal reaction can occur is determined by a loci of $\frac{\partial^2 \Delta G_m}{\partial C^2} = 0$, and both the driving force for diffusion and the equilibrium wave length of the modulated structure in spinodal alloys are related to the value of $\frac{\partial^2 \Delta G_m}{\partial C^2}$ (ref. 6), where C is the concentration. Therefore, values of the free energy of a mixture are a very important part of the studies of spinodal decomposition.

Based on the quasi-chemical theory,[7] the ΔG_m of a solid solution containing N_A atoms of type A and N_B atoms of type B is given by

$$\Delta G_m = V\rho_{AB} - Tk(\ln W) , \qquad (14.3)$$

where

$V = H_{AB} - 1/2\ (H_{AA} + H_{BB})$

ρ_{AB} = total number of AB bonds

T = absolute temperature

k = Boltzmann's constant

k(lnW) = configurational entropy

H_{AA}, H_{AB} and H_{BB} = bond energies between atoms A-A, A-B, and B-B, respectively.

In the case of a regular solution, ρ_{AB} and lnW can be calculated by assuming a random arrangement of atoms. However, such an assumption is not justified for the spinodal alloys. Also, the consideration of only the first nearest neighbor bonds in Eq. (14.3) is not a good approximation for the body-centered cubic solid solutions where the distance between the first and second nearest neighbor atoms is small (about 13% difference).

By considering both the first and second nearest neighbor bonds and correcting for clustering[8] of similar atoms in spinodal alloys, we

---

[6]J. W. Cahn, Trans. Met. Soc. AIME 242, 166 (1968).

[7]R. A. Swalin, Thermodynamics of Solids, pp. 109–131, Wiley, New York, 1962.

can derive a general equation for the free energy of mixing from the statistical and thermodynamical calculations. The result is

$$\Delta G_m = -TNk \left[(Z_1 + Z_2 - 1)\{C(\ln C) + (1-C)\ln(1-C)\} - \frac{Z_1}{Z}\left\{ C\ln\left(C - \frac{2C(1-C)}{\sqrt{f_1}+1}\right) + (1-C)\ln\left(1-C-\frac{2C(1-C)}{\sqrt{f_1}+1}\right)\right\} - \frac{Z_2}{Z}\left\{ C\ln\left(C - \frac{2C(1-C)}{\sqrt{f_2}+1}\right) + (1-C)\ln\left(1-C-\frac{2C(1-C)}{\sqrt{f_2}+1}\right)\right\}\right], \quad (14.4)$$

where

Z = coordination number

$N = N_A + N_B$

$f_i = 1 + 4C(1-C)(e^{2vi/kT} - 1)$.

The subscript i here refers to the first and second nearest neighbor bonds (1 or 2), respectively. When V_1 and V_2 are given, Eq. (14.4) can be used to calculate the free energy of mixing as a function of temperature and composition. The free energy of mixing, in turn, determines the solubility of the miscibility gap for a given alloy system. Or, alternatively, the energy terms V_1 and V_2 can be determined from the critical condition of composition and temperature and solubility of miscibility gap in the phase diagram.

We are making calculations to apply Eq. (14.4) to the decomposition behavior of the experimental alloys of interest.

Welding and Brazing Development

G. M. Slaughter

Brazing Alloy Development (D. A. Canonico, N. C. Cole)

We have continued our efforts to develop high-temperature brazing alloys for joining refractory metals, ceramics, and graphite to themselves

[8] Y. Takagi, Proc. Phys.-Math. Soc. Japan. 23, 44 (1941).

and to each other. An integral phase of the alloy development is the determination of the mechanical properties of the alloys that have proven acceptable in wetting and flowing experiments. We have chosen to use the Miller-Peaslee shear test.[9] Tests at both ambient and elevated temperatures have been completed on Ta–10% W and TZM (Mo–0.5% Ti–0.1% Zr) base metals in the as-brazed condition. During the past quarter, we have also investigated the effect of prolonged exposures at elevated temperatures on the shear strengths of Ta–10% W joints. The Miller-Peaslee specimens were aged for 50 hr at a temperature representative of that at which these alloys may be employed in service. Table 14.4 shows the shear strengths obtained for the alloys investigated.

As expected, the results showed a definite relationship between the shear strength and the base metal. For instance, a given brazing alloy such as No. 4A at room temperature yielded shear strengths of 18,500 and 30,000 psi, respectively, for TZM and Ta–10% W base metals. Brazements on Ta–10% W base metal were stronger at room temperature with all the experimental brazing alloys. At elevated temperatures, the strength advantage of the Ta–10% W base metal brazed with alloys from the Ti-V systems (Nos. 11, 12, and 13) was not as impressive, and the brazes made with the Ti-Zr systems showed that the TZM joints were stronger than the Ta–10% W joints. We attribute this dependence of brazement strength on temperature and base metal to alloying effects. Note that, on the whole, strengths are good, even to temperatures within a couple of hundred degrees of the melting points of the brazing alloys.

The results of the high-temperature aging studies show that the brazes made with the alloys from the Ti-Zr systems (Nos. 4, 5, 6, 8, and 9) did not weaken noticeably due to the aging treatment. In fact, most of the brazements were stronger after aging. However, this was not the case for the Ti-V systems (Nos. 11, 12, and 13). These alloys all had lower shear strengths after aging. Note that although the deterioration was significant, the strengths are still actually quite high. In general, the mechanical properties of all of these brazed joints are very attractive.

---

[9]F. M. Miller and R. L. Peaslee, Welding J. (N.Y.) 37(4), 144-s–150-s (1958).

Table 14.4. Results of Mechanical Properties Studies on Brazed Joints at Ambient and Elevated Temperatures

Brazing Alloy Identification Number	Brazing Alloy Composition (wt %)	Melting Point (°C)	Test Temperature (°C)	Aging Temperature (°C)	Shear Strength (psi)		
					TZM Base Metal	Ta–10% W Base Metal As Brazed	Ta–10% W Base Metal Aged 50 hr
					× 10^3	× 10^3	× 10^3
4A	Ti–45Zr–10Ta	1550	RT[a]	1250	20[b]	38	30
			1250	1250	6.5	2.5	5.2
4E	Ti–42.5Zr–15Ta	1525	RT	1250	17[c]	37	29
			1250	1250	5.3		5.6
5A	Ti–49Zr–2Si	1250	RT	1000	25	33	40
			1000	1000	26	5	10
6A	Ti–40Zr–20Nb	1550	RT	1250	16	48	43
			1250	1250	10	4.7	6.3
8B	Ti–46Zr–8Ge	1250	RT	1000	36	55	53
			1000	1000	11	27	14
9C	Ti–35Zr–30Cr	1050	RT	1000	28	49	34
			1000	1000		13	6.7
10B	Ti–49Zr–2B	1250	RT		40	59	
			1000		36	42	
11F	Ti–26V–10Nb	1575	RT	1000	19	60	49
			1250	1000	19	51	15

Table 14.4. (Continued)

Brazing Alloy Identification Number	Brazing Alloy Composition (wt %)	Melting Point (°C)	Test Temperature (°C)	Aging Temperature (°C)	Shear Strength (psi)		
					TZM Base Metal	Ta–10% W Base Metal As Brazed	Ta–10% W Base Metal Aged 50 hr
					× 10^3	× 10^3	× 10^3
12A	Ti–26V–9Mo	1550	RT	1250	20	46	37
			1250	1250	8	20.684	12
12E	Ti–27V–5Mo	1525	RT	1250	12		50
			1250	1250	24	26	14
13E	Ti–25Cr–21V	1350	RT	1000	25	51	32
			1000	1000	19	33	13

[a]RT = room temperature

[b]TZM aged 50 hr at 1250°C, 19,000 psi.

[c]Specimen broke in base metal

Physical Properties of Refractory Materials

D. L. McElroy

Thermal Conductivity of Tungsten-Base Alloys (R. K. Williams, J. P. Moore, W. P. Murray)

Table 14.5 indicates the temperature ranges covered by our data for thermal conductivity and electrical resistivity on two relatively pure tungsten samples and four tungsten-base alloys, three of which are common thermoelements.

Table 14.5. Temperature Ranges for Which Data are Available for Estimates of Thermal Conductivity of Tungsten-Base Alloys

Material	Temperature Range, K	
	Thermal Conductivity[a]	Electrical Resistivity[b]
Electron-Beam-Melted W	80–350	80–1700
99.98% W (Radial)	80–1300	80–1700
W–2.8 wt % Re	80–350	80–1600
W–5.4 wt % Re	80–400	80–1700
W–26 wt % Re	300–400	300–1700
	573–2473[c]	573–2473[c]
W–1.5 wt % Ta	80–300	80–300

[a]Thermal conductivity data obtained using 3 apparatuses: 80–350 K, absolute longitudinal (±1.2% error); 300–400 K, comparative longitudinal (±3% error); 300–1300 K, radial heat flow (±1.5% error).

[b]Electrical resistivity data obtained using 2 apparatuses: 80–350 K, absolute longitudinal (±0.4% error); 300–1700 K, 4-probe Electrical Resistivity (±0.2% error).

[c]Data by A. D. Feith, Thermal Conductivity and Electrical Resistivity of Tungsten–26 wt % Rhenium, GEMP–562 (1967).

These data were used for testing several increasingly complex estimation methods for predicting the thermal conductivity of all six materials from 80 to 1700 K. Table 14.6 indicates the methods used and their limitations.

Table 14.6. Formulas Used for Thermal Conductivity Estimates

Number	Formula Tested[a]	Limitation
1	$L_o T \rho_A^{-1}$	L may not be equal to L_o, and phonon transport is neglected
2	$L_W T \rho_A^{-1}$	L may not be equal to $L_W = \left(\frac{\lambda_W \rho_W}{T}\right)$
3	$\frac{L_o T}{\rho_A} + \left(\lambda_W - \frac{L_o T}{\rho_W}\right)$	L is not equal to L_o for W, so braced term incorrectly estimates the phonon transport of the alloys, which should be less than for W
4	$\left(\frac{1.11\ L_o\ [1 - \exp(-T/77 + 0.214)]\ T}{\rho_A}\right) + \frac{93.5}{T} - \frac{4220}{T^2}$	Excellent fit for W when ($\rho_A = \rho_W$), but alloy content should alter both L and lattice portion
5	$\left[\frac{\rho_W}{(1.11\ L_o\ [1 - \exp(-T/77 + 0.214)]\ T} + \frac{\rho_A - \rho_W}{L_o T}\right]^{-1} + \frac{93.5}{T} - \frac{4220}{T^2} - 15.1X\left(\frac{93.5}{T} - \frac{4220}{T^2}\right)^2$	Allows L and lattice portion to be altered by alloying

[a]Nomenclature: T = Temperature, K
L_o = Sommerfeld limit, 2.443×10^{-8} V^2/K^2
ρ = measured electrical resistivity of the alloy
L = Weidemann-Franz ratio $\lambda_A \rho_A / T$
L_W = Weidemann-Franz ratio for 99.85% W; $\lambda_W \rho_W / T$
ρ_W = measured electrical resistivity of pure W

We found formula 5 (Table 14.6) to be the most satisfactory of those listed. Calculated and experimental thermal conductivity data are compared in Table 14.7 and Fig. 14.4. The estimation technique, which was developed from two different approaches to separate the phonon and electronic thermal conductivity components,[10] gives reasonably good values for the tungsten-base alloys, but further efforts may be justified. The two main areas for further study are (1) optimizing the parameters for better calculations at low temperatures and (2) obtaining high-temperature thermal conductivity data. Attempts to accomplish this are described below.

[10]R. K. Williams and W. Fulkerson, "Separation of the Electronic and Lattice Contributions to the Thermal Conductivity of Metals and Alloys," submitted to the Canadian Journal of Physics September 1968.

Table 14.7. Comparison of Estimated and Experimental Thermal Conductivity Values

Temperature (°K)	Percent Difference[a]					
	EBM[b] W	99.98% W	W–2.8% Re	W–5.4% Re	W–26% Re	W–1.5% Ta
100	+2.99	+0.06	+14.8	+5.1		+17.4
300	−2.2	−0.08	+ 3.0	+3.2	+3.4	+ 2.9
500		−0.16				
700		−0.28			−10.3	
900		−0.10			−4.9	
1100		+0.06			−0.8	
1300		+0.26			+1.5	
1500					+3.5	
1700					+5.1	

[a] $\left(\frac{\lambda_{calc} - \lambda_{expt}}{\lambda_{expt}}\right) \times 100$

[b]Electron-beam-melted

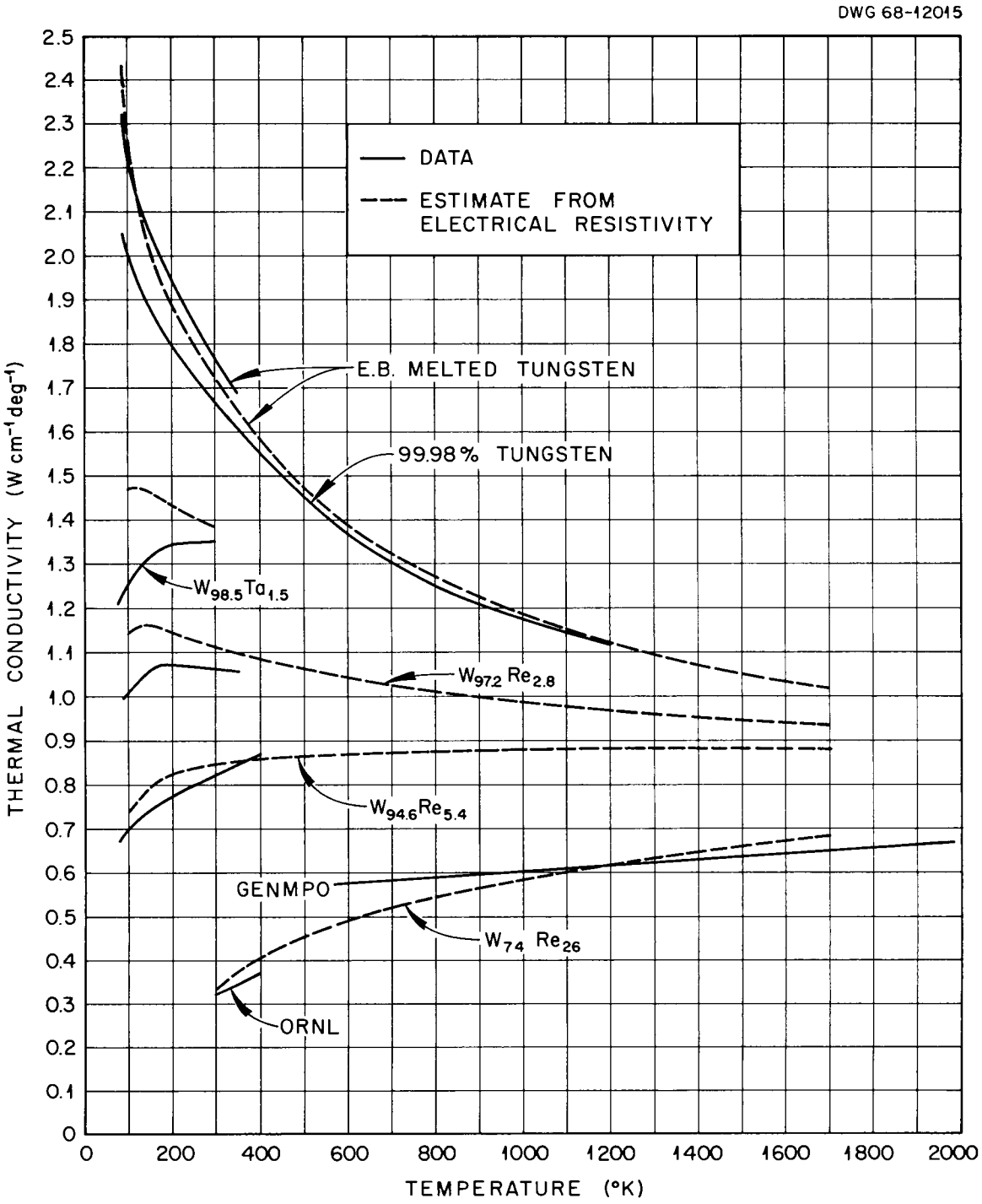

Fig. 14.4. Thermal Conductivity Measurements and Estimates of Tungsten and Several Tungsten-Base Alloys.

Development of a Thermal Conductivity Method Using Electrical Heating

(K.-H. Bode, R. K. Williams)

Our vacuum radial heat flow apparatus is being altered to develop a method to determine thermal conductivity from an electrically heated wire. We hope this will yield needed electrical resistivity and thermal conductivity data to 1700 K on electrically conducting samples that are small relative to radial heat flow specimens.

The following is the abstract of a paper[11] presented this quarter:

> When the ends of an electrically heated wire, placed in vacuo and surrounded by walls at uniform temperature, T_E, are held at the same temperature, $T_o (T_E \leq T_o)$, then a certain current can be found such that the temperature distribution is isothermal over the total length. Starting from these conditions, the thermal conductivity can be determined by variations of either currents or temperatures. Using the one-dimensional heat conduction equation for a current carrying wire, twelve exact relations for the thermal conductivity have been obtained in terms of measurable quantities. The thermal conductivity, the electrical resistivity, the thermal expansion, and the heat losses from the free sample surface, are assumed to be arbitrary functions of temperature only.
>
> When used with a single experimental arrangement thermal conductivity values can be determined in different ways. In addition, this arrangement allows thermal conductivity measurements using solutions derived by others, thus affording a comparison of different methods.

[11] K.-H. Bode, "Possibilities to Determine Thermal Conductivity using New Solution for Current-Carrying Electrical Conductors," paper presented at Eighth Conference on Thermal Conductivity, Purdue University, Lafayette, Indiana, October 7–10, 1968.

Previous reports in this series:

ORNL 4330 Period Ending June 30, 1968

ORNL-4350
UC-25 — Metals, Ceramics, and Materials

INTERNAL DISTRIBUTION

1–3. Central Research Library
4–5. ORNL — Y-12 Technical Library Document Reference Section
6–20. Laboratory Records Department
21. Laboratory Records, ORNL R.C.
22. ORNL Patent Office
23. G. M. Adamson, Jr.
24. T. E. Banks
25. J. H. Barrett
26. S. E. Beall
27. R. L. Beatty
28. R. J. Beaver
29. M. Bender
30. R. G. Berggren
31. D. S. Billington
32. E. E. Bloom
33. A. L. Boch
34. E. S. Bomar
35. B. S. Borie
36. D. T. Bourgette
37. G. E. Boyd
38. R. A. Bradley
39. R. J. Breeding
40. R. B. Briggs
41. R. E. Brooksbank
42. W. E. Brundage
43. D. A. Canonico
44. R. M. Carroll
45. J. V. Cathcart
46. A. K. Chakraborty
47. Ji Young Chang
48. D. L. Clark
49. G. W. Clark
50. N. C. Cole
51. K. V. Cook
52. W. H. Cook
53. G. L. Copeland
54. W. B. Cottrell
55. C. M. Cox
56. F. L. Culler
57. C. W. Cunningham
58. J. E. Cunningham
59. H. L. Davis
60. V. A. DeCarlo
61. J. H. DeVan
62. J. R. DiStefano
63. C. V. Dodd
64. R. G. Donnelly
65. D. A. Dyslin
66. W. S. Ernst
67. J. H. Erwin
68. K. Farrell
69. J. S. Faulkner
70. J. I. Federer
71. D. E. Ferguson
72. R. B. Fitts
73. B. Fleischer
74. B. E. Foster
75. A. P. Fraas
76. J. H Frye, Jr.
77. W. Fulkerson
78. L. C. Fuller
79. T. G. Godfrey, Jr.
80. J. M. Googan (Y-12)
81. R. J. Gray
82. W. R. Grimes
83. A. G. Grindell
84. H. D. Guberman
85. D. G. Harman
86. W. O. Harms
87–89. M. R. Hill
90. N. E. Hinkle
91. D. O. Hobson
92. H. W. Hoffman
93. R. W. Horton
94. W. R. Huntley
95. H. Inouye
96. D. H. Jansen
97. J. D. Jenkins
98. W. H. Jordan
99. G. W. Keilholtz
100. R. T. King
101. R. L. Klueh
102. J. Komatsu
103. J. A. Lane
104. J. M. Leitnaker
105. B. C. Leslie
106. T. B. Lindemer
107. A. P. Litman
108. C. T. Liu

109. H. R. Livesey
110. A. L. Lotts
111. R. N. Lyon
112. H. G. MacPherson
113. R. E. MacPherson
114. M. M. Martin
115. W. R. Martin
116. R. W. McClung
117. H. E. McCoy, Jr.
118. H. C. McCurdy
119. R. E. McDonald
120. W. T. McDuffie
121. D. L. McElroy
122. C. J. McHargue
123. F. R. McQuilkin
124. A. J. Miller
125. E. C. Miller
126. J. P. Moore
127. R. E. Moore
128. W. L. Moore
129. C. S. Morgan
130. J. G. Morgan
131. F. H. Neill
132. G. T. Newman
133. T. M. Nilsson
134. T. A. Nolan (K-25)
135. K. Notz
136. S. M. Ohr
137. A. R. Olsen
138. M. F. Osborne
139. P. Patriarca
140. W. H. Pechin
141. A. M. Perry
142. S. Peterson
143. R. A. Potter
144. R. B. Pratt
145. M. K. Preston
146. R. E. Reed
147. C. R. Reese
148. D. K. Reimann
149. G. A. Reimann
150. A. E. Richt
151. P. L. Rittenhouse
152. W. C. Robinson
153. M. W. Rosenthal
154. D. J. Rucker
155. C. F. Sanders
156. G. Samuels
157. A. W. Savolainen
158. J. E. Savolainen
159. A. C. Schaffhauser
160. J. L. Scott
161. J. D. Sease
162. C. E. Sessions
163. O. Sisman
164. G. M. Slaughter
165. S. D. Snyder
166. K. E. Spear
167. I. Spiewak
168. P. Spindler
169. J. E. Spruiell
170. W. J. Stelzman
171. R. L. Stephenson
172. J. O. Stiegler
173. D. A. Sundberg
174. E. J. Tenckhoff
175. D. B. Trauger
176. R. P. Tucker
177. G. M. Watson
178. S. C. Weaver
179. M. S. Wechsler
180. A. M. Weinberg
181. J. R. Weir, Jr.
182. W. J. Werner
183. H. L. Whaley
184. G. D. Whitman
185. F. W. Wiffen
186. J. M. Williams
187. R. K. Williams
188. R. O. Williams
189. J. C. Wilson
190. R. G. Wymer
191. F. W. Young, Jr.
192. C. S. Yust
193. A. F. Zulliger
194. C. M. Adams, Jr. (Consultant)
195. Leo Brewer (Consultant)
196. L. S. Darken (Consultant)
197. J. A. Krumhansl (Consultant)

EXTERNAL DISTRIBTUION

AIR FORCE MATERIALS LABORATORY, Wright-Patterson Air Force Base

198. C. H. Armbruster
199. H. M. Burte
200. G. Glenn
201. Technical Director

AIR FORCE WEAPONS LABORATORY, Kirtland Air Force Base

202. D. Brooks

AMES LABORATORY

203. O. N. Carlson
204. W. L. Larsen
205. M. Smutz
206. F. H. Spedding

ARGONNE NATIONAL LABORATORY

207. L. Baker
208. J. H. Kittel
209. M. V. Nevitt
210. P. G. Shewmon
211. R. C. Vogel

LMFBR PROGRAM OFFICE, Argonne National Laboratory

212. A. Amorosi
213. L. Burris
214. L. Kelman
215. J. M. McKee

AEC-RDT SITE REPRESENTATIVES

216. M. E. Jackson, Argonne National Laboratory
217. D. J. Wille, Atomic Power Development Associates
218. R. L. Morgan, Atomics International
219. J. V. Levy, General Electric, Cincinnati
220. J. F. Weissenberg, General Electric, Cincinnati
221. R. H. Ball, Gulf General Atomic
222. J. E. Hebert, Idaho
223. D. A. Moss, Idaho
224. K. A. Trickett, Idaho
225. D. F. Cope, Oak Ridge National Laboratory
226. C. L. Matthews, Oak Ridge National Laboratory
227. P. G. Holsted, Pacific Northwest Laboratory
228. J. Sako, Pacific Northwest Laboratory
229. Atomic Energy Commission Library, Washington

DIVISION OF NAVAL REACTORS, AEC, Washington

230. R. H. Steele

DIVISION OF REACTOR DEVELOPMENT AND TECHNOLOGY, AEC, Washington

231. J. C. Crawford, Jr.
232. G. W. Cunningham
233. A. Giambusso
234. H. G. Hembree
235. J. R. Hunter
236. E. E. Kintner
237. W. H. Layman
238. W. H. McVey
239. J. J. Morabito
240. R. E. Pahler
241. A. J. Pressesky
242. M. A. Rosen
243. J. M. Simmons
244. E. E. Sinclair
245. A. Taboada
246. A. N. Tardiff
247. A. Van Echo
248. C. E. Weber
249. M. J. Whitman

DIVISION OF RESEARCH, AEC, Washington

250. P. W. McDaniel
251. D. K. Stevens

DIVISION OF SPACE NUCLEAR SYSTEMS, AEC, Washington

252. R. E. Anderson
253. D. Beard
254. J. F. Griffo
255. C. E. Johnson
256. J. A. Powers
257. F. C. Schwenk

OAK RIDGE OPERATIONS OFFICE

258. W. J. Larkin
259. Laboratory and University Division

ATOMIC POWER DEVELOPMENT ASSOCIATES

260. E. C. Kovacic
261. A. A. Shoudy

ATOMICS INTERNATIONAL

262. H. Pearlman

BABCOCK AND WILCOX COMPANY, Lynchburg, Virginia 24505

263. C. Baroch
264. S. P. Grant
265. C. Johnson
266. L. Weissert

BATTELLE MEMORIAL INSTITUTE, Columbus, Ohio

267. W. Berry
268. D. Keller
269. S. J. Paprocki
270. Defense Materials Information Center

BATTELLE MEMORIAL INSTITUTE, PNL, Richland, Washington

271. A. L. Bement
272. J. J. Cadwell
273. T. T. Claudson
274. D. L. Condotta
275. E. Evans
276. B. R. Hayward
277. W. E. Roake
278. J. C. Tobin
279. R. G. Wheeler
280. Technical Information File

FAST FLUX TEST FACILITY, Battelle-Northwest

281. E. R. Astley

BROOKHAVEN NATIONAL LABORATORY

282. D. H. Gurinsky
283. C. Klamut

BUREAU OF MINES

284. Haruo Kato, Albany Metallurgy Research Center, P. O. Box 70, Albany, Oregon 97321
285. T. Sullivan, Bureau of Mines, Boulder City, Nevada 89005

COMBUSTION ENGINEERING

286. W. P. Chernock
287. S. S. Christopher

GENERAL ELECTRIC, Cincinnati

288. D. H. Ahmann
289. H. C. Brassfield
290. V. P. Calkins
291. E. Hoffman
292. J. McGurty
293. J. Moteff

GENERAL ELECTRIC, Nuclear Systems Programs, Cincinnati

294. E. E. Hoffman

GENERAL ELECTRIC, San Jose

295. R. Duncan
296. H. Klepfer

GENERAL ELECTRIC, Pleasanton

297. H. W. Alter

GENERAL ELECTRIC, Sunnyvale

298. K. P. Cohen
299. F. Comprelli
300. R. Skavdahl
301. C. Spalaris
302. E. L. Zebroski

GULF GENERAL ATOMIC

303. D. B. Coburn
304. A. J. Goodjohn
305. J. P. Howe
306. S. Jaye
307. J. F. Watson

IDAHO NUCLEAR CORPORATION

308. W. C. Francis

ILLINOIS INSTITUTE OF TECHNOLOGY RESEARCH INSTITUTE

309. D. J. McPherson

JET PROPULSION LABORATORY (NASA)

310. J. Davis

KNOLLS ATOMIC POWER LABORATORY

311. R. F. Wojciescak
312. Document Library

LOS ALAMOS SCIENTIFIC LABORATORY

313. R. D. Baker
314. D. B. Hall
315. J. A. Leary
316. R. Perkins
317. R. E. Peterson
318. Reports Library

MOUND LABORATORY

319. R. G. Grove

NASA, LEWIS RESEARCH CENTER

320. M. Ault
321. J.W.R. Creagh
322. J. J. Lombardo
323. T. P. Moffitt
324. T. A. Moss
325. F. E. Rom
326. L. Rosenblum
327. N. D. Sanders
328. N. Saunders
329. H. Schwartz

NAVAL RESEARCH LABORATORY

330. J. R. Hawthorne
331. C. Serpan
332. L. E. Steele

NORTH CAROLINA UNIVERSITY, Raleigh, North Carolina 27607

333. J. Beeler
334. R. E. Dahl

NUCLEAR MATERIALS AND EQUIPMENT CORPORATION

335. C. Caldwell
336. K. Puechl

OHIO STATE UNIVERSITY, Columbus, Ohio 43212

337. M. G. Fontana
338. R. W. Staehle

RENSSELAER POLYTECHNIC INSTITUTE

339. C. B. Willingham, Jr.

SANDIA CORPORATION

340. J. Read Holland
341. J. Jacobs
342. D. R. Johnson

SAVANNAH RIVER LABORATORY

343. P. H. Permar
344. S. P. Rideout

TRW SYSTEMS (NASA), Redondo Beach, California 90278

345. H. Lurie

UNION CARBIDE CORPORATION, New York

346. J. A. Swartout

UNION CARBIDE CORPORATION, Materials Systems Division, Indianapolis

347. C. F. Leitten, Jr.

UNITED NUCLEAR CORPORATION

348. A. Strasser

UNIVERSITY OF CALIFORNIA, Lawrence Radiation Laboratory, Livermore

349. W. R. Holman
350. J. S. Kane
351. L. W. Roberts
352. A. J. Rothman
353. B. Rubin

U.S. NAVAL AIR SYSTEM COMMAND (AIR-52031B)

354. T. Kearns
355. I. Machlin

USAEC Scientific Representative, American Embassy, Box 40 FPO, N. Y. 09510

356. W.L.R. Rice

WESTINGHOUSE, Advanced Reactor Division, Waltz Mill Site

357. E. C. Bishop
358. J.C.R. Kelly
359. P. J. Levine
360. P. Murray
361. W. E. Ray
362. G. A. Whitlow

WESTINGHOUSE, Astronuclear Laboratory

363. R. T. Begley
364. D. C. Goldberg

WESTINGHOUSE, Atomic Power Division

365. T. Stern

WESTINGHOUSE, Bettis

366. R. H. Fillnow
367. P. N. Gustafson
368. Westinghouse Bettis Laboratory Library

369–590. Given distribution as shown in TID-4500 under Metals, Ceramics, and Materials category (25 copies – CFSTI)